

STRUCTURE-BASED DRUG DESIGN OF NOVEL THERAPEUTICS TARGETING  
ONCOSTATIN M

by

Kelsey Skluzacek

A thesis

submitted in partial fulfillment

of the requirements for the degree of

Master of Science in Chemistry

Boise State University

December 2018

© 2018

Kelsey Skluzacek

ALL RIGHTS RESERVED

BOISE STATE UNIVERSITY GRADUATE COLLEGE

**DEFENSE COMMITTEE AND FINAL READING APPROVALS**

of the thesis submitted by

Kelsey Skluzacek

Thesis Title: Structure-Based Drug Design of Novel Therapeutics Targeting Oncostatin  
M

Date of Final Oral Examination: 19 October 2018

The following individuals read and discussed the thesis submitted by student Kelsey Skluzacek, and they evaluated her presentation and response to questions during the final oral examination. They found that the student passed the final oral examination.

Don Warner, Ph.D.	Chair, Supervisory Committee
Cheryl Jorcyk, Ph.D.	Member, Supervisory Committee
Matthew D. King, Ph.D.	Member, Supervisory Committee
Lisa Warner, Ph.D.	Member, Supervisory Committee

The final reading approval of the thesis was granted by Don Warner, Ph.D., Chair of the Supervisory Committee. The thesis was approved by the Graduate College.

## DEDICATION

I would like to dedicate this project to all of my family and friends. Specifically, I would like to thank my parents, Mary and David, who have been my biggest supporters my entire life and without whom I would not be the person I am today. Furthermore, my sincerest gratitude and appreciation for all the patience, love, and support I have received from my fiancé, Jerrett Holdaway, throughout this process.

## ACKNOWLEDGEMENTS

I would like to acknowledge Dr. Don Warner for allowing me to have the opportunity to work on this project and I am appreciative for all the guidance he gave me throughout my time in his lab. Additionally, I would like to gratefully acknowledge Dr. Lisa Warner for all the support and guidance she provided to me, particularly her assistance with the ITC experiments. Furthermore, the aid of Dr. Matthew King is acknowledged for his computational work. I would like to also acknowledge Dr. Cheryl Jorcyk and her students for their efforts in performing the ELISA and Western Blot analysis assays. Finally, I would like to thank Dr. Joe Dumais, Dr. Xinzhu Pu, Matthew Turner, Thaaer Muhammed, and Joey Tuccinardi for their help during the characterization of the compounds.

The work in this thesis was supported by the Institutional Development Awards (IDeA) from the National Institute of General Medical Sciences of the National Institutes of Health under Grants #P20GM103408 and P20GM109095. Support was also received from the Biomolecular Research Center at Boise State University with funding from the National Science Foundation, Grants #0619793 and #0923535; the MJ Murdock Charitable Trust; and the Idaho State Board of Education. The Boise State University NMR facility instrumentation was purchased through an NSF CRIF-MU/RUI, Grant #0639251 and departmental funding. I would also like to thank and acknowledge the support I received from the Department of Chemistry and Biochemistry at Boise State University for the financial support I received through teaching assistantships and summer fellowships.

## ABSTRACT

At 30% of all new diagnoses, the most prevalent malignancy for women is breast cancer, which in the United States will result in an estimated 266,000 new cases this year alone. Of the patients diagnosed with breast cancer, approximately 10-15% will develop distant metastases within three years of the initial detection of a primary tumor. For comparison, the five-year survival rate for localized breast cancer is 99%, whereas, the survival rate for metastatic breast cancer drops drastically to only 27%. The significant difference in survival rates is indicative of a need for a novel treatment strategy for metastatic breast cancer.

Oncostatin M (OSM), a member of the interleukin-6 family of cytokines, has been shown in the context of breast cancer to promote epithelial to mesenchymal transition (EMT), promote tumor cell detachment and invasiveness, increase circulating tumor cell (CTC) numbers, induce the expression of proangiogenic factors, and promote lung and bone metastases. For these reasons, the work presented describes the structure-based drug design, synthesis, and preliminary testing of small molecule inhibitors (SMIs) of OSM to be used as a therapeutic treatment method for metastatic breast carcinomas. Based on synthetic accessibility and computational screening, SMIs were synthesized and subsequently evaluated for inhibition of OSM-induced signaling using an enzyme-linked immunosorbent assay (ELISA). The SMIs were further assessed for binding affinity toward OSM using isothermal titration calorimetry (ITC). The results suggested that SMIs capable of inhibiting OSM-induced signaling also exhibited binding to OSM. Furthermore, SMIs

not able to bind to OSM correlated with poor inhibition of OSM-induced signaling. Therefore, the preliminary results suggest: specific SMI-OSM binding occurs, SMIs are capable of inhibiting OSM-induced signaling, and that additionally optimized SMIs have the potential to be used as novel therapeutic treatment options for metastatic breast cancer.

## TABLE OF CONTENTS

DEDICATION .....	iv
ACKNOWLEDGEMENTS .....	v
ABSTRACT .....	vi
LIST OF TABLES .....	xii
LIST OF FIGURES .....	xiii
LIST OF SCHEMES.....	xv
LIST OF ABBREVIATIONS.....	xvi
CHAPTER ONE: Introduction .....	1
1.1 Overview of Breast Cancer .....	1
1.1.1 Cancer .....	1
1.1.2 Breast Cancer .....	1
1.1.3 Metastasis.....	5
1.2 Oncostatin M.....	7
1.2.1 Interleukin-6 Family .....	7
1.2.2 Function of OSM .....	7
1.2.3 Role in Breast Cancer .....	9
1.2.4 OSM as a Therapeutic Target .....	11
1.3 Structure-Based Drug Design .....	11
1.4 Design of SMI-10 Analogs using SBDD.....	14

1.5 Concluding Remarks.....	16
1.6 References.....	17
<b>CHAPTER TWO: SYNTHESIS, CHARACTERIZATION, AND EVALUATION OF SMI-10 ANALOGS .....</b>	<b>23</b>
2.1 Introduction.....	23
2.1.1 Metastatic Breast Cancer .....	23
2.1.2 Oncostatin M as a Therapeutic Target .....	25
2.2 Design of SMI-10 Analogs .....	27
2.2.1 High-Throughput Virtual Screening .....	27
2.2.2 OSM Inhibition Assay .....	28
2.2.3 Optimization of Lead Compound .....	30
2.3 Results and Discussion .....	32
2.3.1 Synthesis of SMI-10 Analogs .....	32
2.3.2 Predicted Binding Affinity of SMI-10 Analogs.....	44
2.3.3 OSM Inhibition Assay .....	46
2.4 Concluding Remarks.....	48
2.5 Materials and Methods.....	48
2.5.1 Materials and Reagents .....	48
2.5.2 Equipment .....	49
2.5.3 Characterization .....	49
2.5.4 SMI-10 Analogs.....	49
2.5.5 Cell Cultures .....	63
2.5.6 OSM Inhibition Assays.....	63
2.6 References.....	64

CHAPTER THREE: BINDING AFFINITY OF SMI-10 ANALOGS .....	69
3.1 Introduction.....	69
3.1.1 Metastatic Breast Cancer and Oncostatin M.....	69
3.1.2 Design of SMI-10 Analogs .....	70
3.1.3 OSM Inhibition Assay .....	72
3.1.4 Isothermal Titration Calorimetry .....	73
3.1.5 Heteronuclear HSQC-detected Titrations .....	74
3.2 Results and Discussion .....	74
3.2.1 Isothermal Titration Calorimetry .....	74
3.2.2 Heteronuclear HSQC-detected Titrations .....	80
3.3 Concluding Remarks.....	81
3.4 Materials and Methods.....	81
3.4.1 Materials and Reagents .....	81
3.4.2 Equipment .....	82
3.4.3 OSM Inhibition Assays.....	82
3.4.4 Human Recombinant OSM.....	83
3.4.5 Isothermal Titration Calorimetry .....	85
3.4.6 Heteronuclear HSQC-detected Titrations .....	86
3.5 References.....	86
APPENDIX A: <sup>1</sup> H NMR Spectra .....	88
APPENDIX B: <sup>13</sup> C NMR Spectra .....	104
APPENDIX C: MASS SPECTROMETRY.....	120
APPENDIX D: INFRARED SPECTROSCOPY .....	136

APPENDIX E: ISOTHERMAL TITRATION CALORIMETRY .....	152
--	-----

## LIST OF TABLES

Table 1.1	Breast cancer subtypes .....	4
Table 2.1	Structures of SMI-10 analogs .....	34
Table 2.2	Electrostatic interactions of SMI-10 analogs .....	46
Table 3.1	Structures of SMI-10 analogs .....	71
Table 3.2	Thermodynamics of SMI-10 analogs.....	75

## LIST OF FIGURES

Figure 1.1	Progression of ductal carcinoma.....	3
Figure 1.2	Metastatic cascade of cancer.....	6
Figure 1.3	OSM induces the STAT3, PI3K, and MAPK pathways.....	9
Figure 1.4	Angiogenesis stimulated by secretion of VEGF from tumor cells .....	10
Figure 1.5	Process of structure-based drug design.....	14
Figure 1.6	Binding sites of OSM and SMI docked in binding pocket of OSM .....	15
Figure 1.7	Structure of SMI-10 .....	16
Figure 2.1	OSM induces the STAT3, PI3K, and MAPK pathways.....	26
Figure 2.2	Binding sites of OSM and SMI docked in binding pocket of OSM .....	27
Figure 2.3	Screening of SMIs via ELISA and Western Blot analysis .....	29
Figure 2.4	Structure of SMI-10 .....	30
Figure 2.5	SMI-10 in binding pocket of OSM.....	31
Figure 2.6	OSM-induced inhibition assay.....	47
Figure 3.1	OSM induces the STAT3, PI3K, and MAPK pathways.....	70
Figure 3.2	OSM-induced inhibition assay.....	72
Figure 3.3	ITC of SMI-10F .....	76
Figure 3.4	ITC of SMI-10G .....	77
Figure 3.5	Structure of SMI-10H .....	78
Figure 3.6	ITC of SMI-10I.....	79

Figure 3.7  $^1\text{H}$ - $^{15}\text{N}$  HSQC spectrum of OSM ..... 80

## LIST OF SCHEMES

Scheme 2.1	Overall synthetic route for SMI-10 analogs.....	33
Scheme 2.2	Synthetic route for <b>1</b> .....	35
Scheme 2.3	Synthetic route for SMI-10A.....	36
Scheme 2.4	Synthetic route for SMI-10B.....	37
Scheme 2.5	Proposed synthetic route for SMI-10D.....	38
Scheme 2.6	Proposed synthetic route for SMI-10C and -10D.....	39
Scheme 2.7	Synthetic route for SMI-10C and -10D.....	40
Scheme 2.8	Synthetic route for SMI-10E.....	41
Scheme 2.9	Synthetic route for SMI-10F and -10G.....	42
Scheme 2.10	Synthetic route for SMI-10H, -10I, and -10J.....	43
Scheme 2.11	Synthetic route for SMI-10K.....	44

## LIST OF ABBREVIATIONS

AKT	protein kinase B
CD44	cluster of differentiation 44
CDK	cyclin-dependent kinase
CTC	circulating tumor cell
DCIS	ductal carcinoma <i>in situ</i>
ELISA	enzyme-linked immunosorbent assay
EMT	epithelial to mesenchymal transition
ER	estrogen receptor
ERK	extracellular signal-regulated kinase
HER2	human epidermal growth factor receptor 2
HRMS	high resolution mass spectrometry
HSQC	heteronuclear single quantum correlation
IL-6	interleukin-6
IR	infrared
ITC	isothermal titration calorimetry
$K_D$	equilibrium dissociation constant
LIF	leukemia inhibitory factor
LIFR	leukemia inhibitory factor receptor
MAPK	mitogen-activated protein kinase

MET	mesenchymal to epithelial transition
mTOR	mammalian target of rapamycin
$n$	binding stoichiometry
NMR	nuclear magnetic resonance
OSM	oncostatin M
OSMR	oncostatin M receptor
PI3K	phosphatidylinositol-3-kinase
PR	progesterone receptor
pSTAT3	phosphorylated signal transducer and activator of transcription 3
SBDD	structure-based drug design
SMI	small molecule inhibitor
STAT3	signal transducer and activator of transcription 3
TNBC	triple negative breast cancer
VEGF	vascular endothelial growth factor
$\Delta G$	Gibbs free energy
$\Delta H$	change in enthalpy
$\Delta S$	change in entropy

## CHAPTER ONE: Introduction

### 1.1 Overview of Breast Cancer

#### 1.1.1 Cancer

Cancer is characterized as a collection of related diseases linked with accelerated cell cycles, genomic alterations, and the potential for invasive growth that when left untreated, ultimately leads to death. As such, cancer has become a major public health concern worldwide and is the second leading cause of death in the United States, after heart disease. In the United States, an estimated 1.7 million new cases of cancer will be diagnosed in 2018, resulting in approximately 600,000 deaths (Siegel, 2018). Fortunately, progress has been made against cancer, primarily due to advances in medical treatment and earlier diagnosis, which has been indicated by a decline in mortality by about 1.5% per year since the early 1990s (Siegel, 2018; DeSantis, 2014).

#### 1.1.2 Breast Cancer

For women, breast cancer is the most prevalent malignancy and accounts for 30% of all new diagnoses, producing an estimated 266,000 cases for 2018 alone (Siegel, 2018). The five-year survival rate for localized breast cancer is 99%, however, the survival rate for distant metastatic breast cancer drops to an abysmal 27% (Howlader, 2017). The drastic difference in post-metastatic survival rates is suggestive of a need for a novel treatment method.

Several factors affect the likelihood of developing breast cancer. In general, as many as 10% of breast cancer patients in developed countries result from genetic

predisposition, inherited as an autosomal dominant trait. (McPherson, 2000). Mutations in the *BRCA1* and *BRCA2* genes are known to increase the risk of developing breast cancer. Specifically, a study in Ashkenazi Jews found that carriers of these mutations developed breast cancer in 56% of participants by the age of 70 (Key, 2001). In addition to genetic predispositions, the chance of developing breast cancer increases with age, such that it doubles every 10 years until menopause, when the rate then slows dramatically. However, certain factors can reduce the risk for breast cancer. Notably, a full-term pregnancy provides a 25% reduction in risk for women as well as increasing protection with an increasing number of pregnancies (Key, 2001).

Breast carcinomas are generally classified as either ductal or lobular, depending on where the cancer originates. The most common histological classification is ductal carcinoma *in situ* (DCIS), which originates from cancer growth in the milk ducts (Malhotra, 2010). Within the United States, DCIS accounts for nearly 20% of all breast cancers detected via screening mammography (Burstein, 2004; Cowell, 2013). The progression toward DCIS begins with the formation of ductal hyperplasia, which occurs when there are too many cells present within the duct. Subsequently, when the cells begin to take on an abnormal appearance, it is termed atypical ductal hyperplasia. Finally, DCIS occurs when the cells exhibit cancerous features, but remain confined inside the duct. Upon breaking through the basement membrane, the DCIS is considered to progress to an invasive ductal carcinoma (Cowell, 2013) (Figure 1.1).

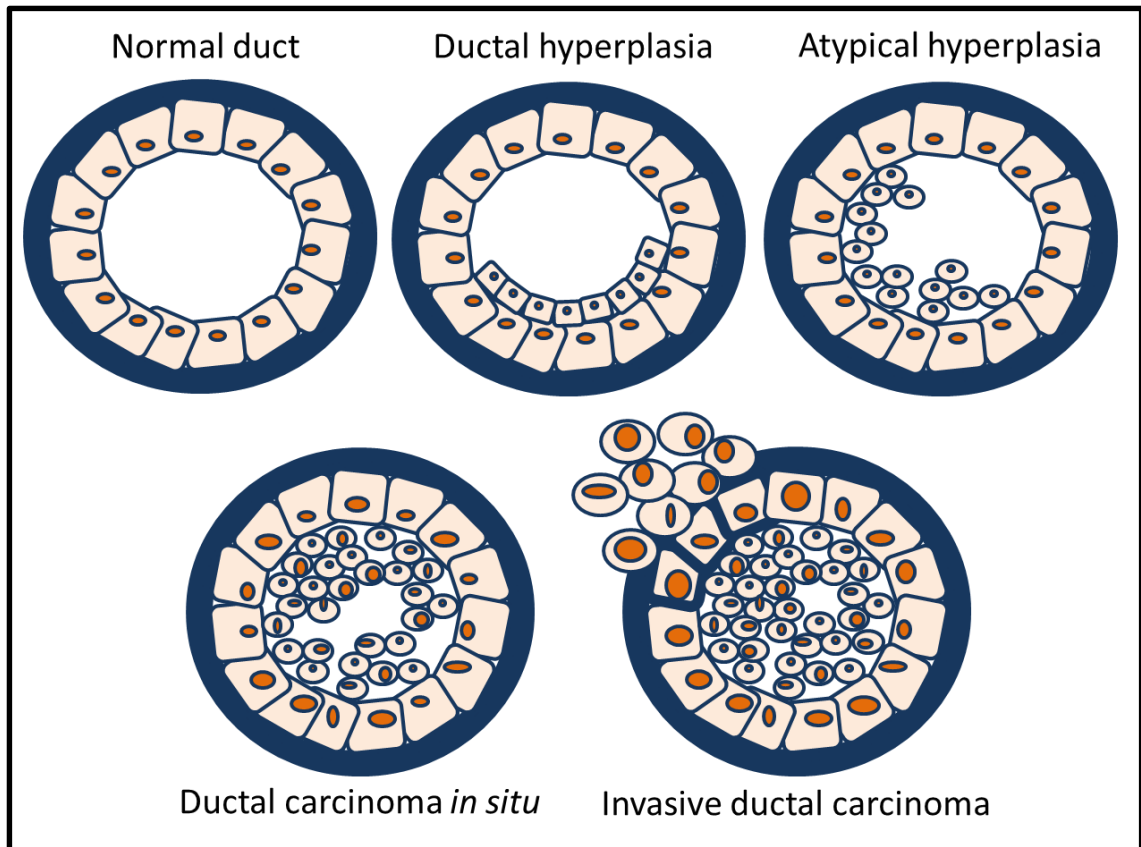


**Figure 1.1 Progression of ductal carcinoma.** When a normal duct generates too many cells, it becomes a ductal hyperplasia. Subsequently, atypical hyperplasia occurs when the cells become abnormal in appearance. As soon as the cells exhibit cancerous features, but remain confined inside the duct they become a DCIS. Finally, upon breaking through the basement membrane the cells are termed as an invasive ductal carcinoma.

Breast cancer is further categorized into four major subtypes: luminal A, luminal B, HER2-enriched, and triple negative breast cancer (TNBC). The subtypes are determined based on estrogen receptor (ER) status, progesterone receptor (PR) status, and the expression of human epidermal growth factor receptor 2 (HER2). At 40% of all diagnoses, the most prevalent is luminal A (ER+ and/or PR+, HER2-). It is the least aggressive in terms of growth rate and recurrence and also has the best prognosis of all the subtypes. Luminal B (ER+ and/or PR+, HER2+) and HER2-enriched (ER-, PR-, HER2+), which combined account for another 30-35% of diagnoses, are more aggressive than luminal A in terms of proliferation rates, but respond well to targeted therapies. The final subtype,

TNBC (ER-, PR-, HER2-), typically has a poor short-term prognosis and lacks targeted therapies (Anderson, 2014; Sharp, 2014) (Table 1.1).

**Table 1.1 Breast cancer subtypes.<sup>a</sup>**

	Luminal A	Luminal B	HER2-enriched	TNBC
Percentage of diagnosis	40%	20%	10-15%	15-20%
ER/PR status	Positive	Positive	Negative	Negative
HER2 status	Negative	Positive	Positive	Negative

<sup>a</sup>Of the four subtypes, luminal A is the most commonly diagnosed and least aggressive. At one third of diagnoses combined, luminal B and HER2-enriched typically respond well to treatment with targeted therapies. TNBC is the least treatable subtype and generally has a poor short-term prognosis.

Prognosis and treatment options for breast cancer patients are typically based upon tumor-node-metastasis staging. Stage 0 lobular carcinoma *in situ* originates from the glandular lobules of the breast and is unable to become invasive itself, but rather increases the risk for developing an invasive form of breast cancer by 7% (Maughan, 2010). Therefore, diagnosis with stage 0 lobular carcinoma *in situ* requires no treatment other than rigorous surveillance for the development of additional breast malignancies. Conversely, stage 0 DCIS is able to progress to invasive breast cancer and is typically treated by surgery followed by radiation therapy. Treatment for early-stage invasive breast cancer (stages I and II) generally involves breast-conserving surgery prior to radiation therapy. Additionally, adjuvant systemic therapies such as chemotherapy, endocrine therapy, and tissue-targeted therapies are used in patients with early-stage breast cancer to help decrease recurrence. The standard of care for patients diagnosed with stage III locally advanced breast cancer includes induction chemotherapy and subsequent local therapy, such as

surgery and/or radiation. Finally, stage IV metastatic breast cancer has the lowest five-year survival rate and is typically treated through a combination of adjuvant systemic therapies, mastectomy, and radiation therapies (Maughan, 2010).

### 1.1.3 Metastasis

Invasive breast cancer cells have the potential to become metastatic, which results in the formation of tumors at secondary sites in distant organs. Approximately 10-15% of patients diagnosed with breast cancer develop distant metastases within three years of the initial detection of the primary tumor (Weigelt, 2005). The multi-step process through which metastasis occurs is known as the metastatic cascade, involving the detachment of a tumor cell from the primary site and the ensuing formation of tumors at secondary sites. The first step toward detachment of tumor cells encompasses a phenotypic change known as an epithelial to mesenchymal transition (EMT), which allows the cells to change from an adherent, non-motile cell into an invasive, non-adherent, and vastly mobile cell (van Zijl, 2011). Following EMT, the tumor cells enter either the lymphatic or the blood circulatory system through a process called intravasation. Upon entering the circulatory system, the cells become designated as circulating tumor cells (CTCs) capable of migrating to target organs. When the CTCs reach the target organs, a process called extravasation can occur in which the cells exit the circulatory system through adjacent tissue. Interestingly, the majority of CTCs either undergo apoptosis or are destroyed by the immune system prior to extravasation. In fact, only 0.1% of CTCs are able to survive long enough to extravasate at target organs. Upon extravasation, a mesenchymal to epithelial transition (MET) occurs in which the cells undergo the reverse process from that of EMT (Fidler, 1970). Following MET, the tumor cells may either lay dormant or proliferate into a

secondary metastatic tumor (Price, 2016; Chaffer, 2006) (Figure 1.2). For breast cancer specifically, metastasis preferentially occurs in the bones, brain, lungs, and liver (Bolin, 2012; Bos, 2009; Weigelt, 2005).

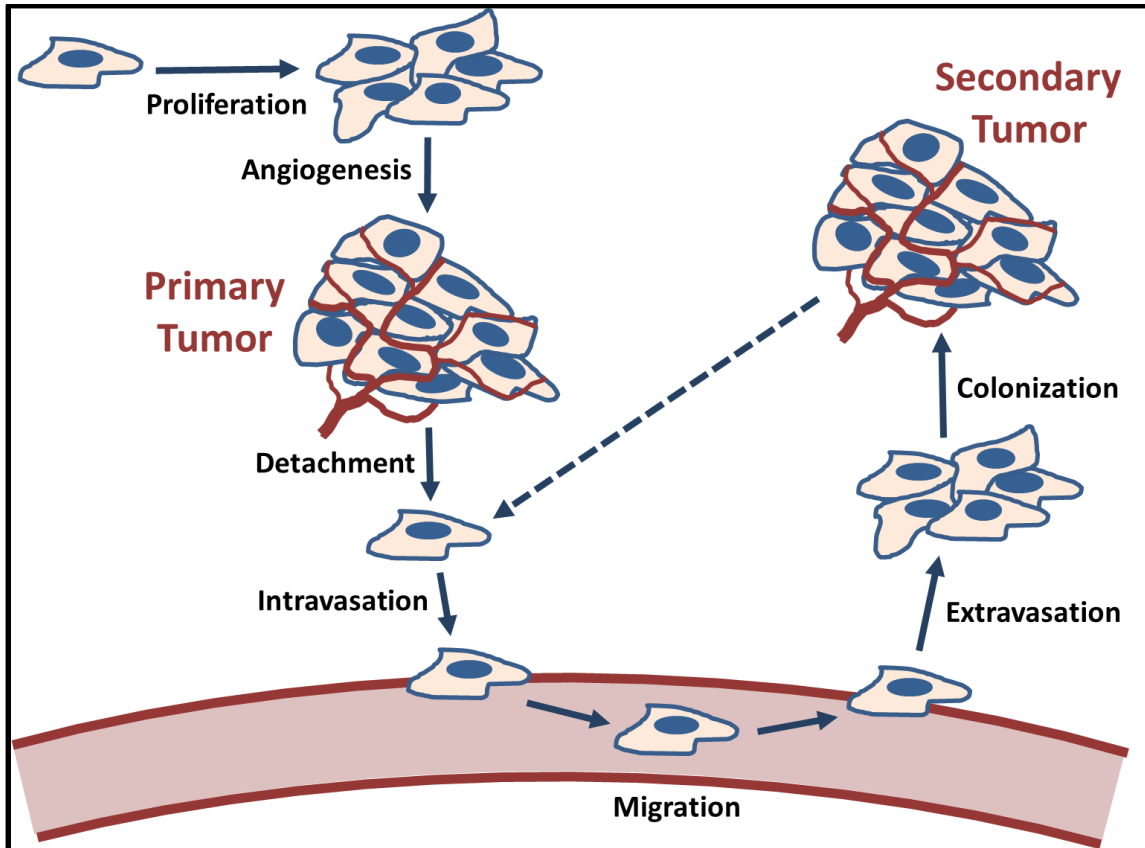


**Figure 1.2 Metastatic cascade of cancer.** Upon formation of the primary tumor, cells detach following EMT and intravasate into the circulatory system, where they become known as CTCs. The CTCs migrate to target organs, extravasate from the circulatory system, go through MET, and proliferate into a secondary metastatic tumor. The process is then able to repeat itself from the secondary tumor to develop additional tumors.

## **1.2 Oncostatin M**

### 1.2.1 Interleukin-6 Family

In general, cytokines such as the interleukin-6 (IL-6) family, bind to receptors on target cells and exhibit both tumor-promoting and inhibitory effects on breast cancer growth. IL-6 cytokines are important in regard to inducing the acute-phase response caused by inflammation that is associated with either infection or injury as well as controlling the immune system, which tends to be significantly impaired in breast cancer patients (Heinrich, 1990; Knüpfner, 2007). The pleiotropic IL-6 cytokines have been shown to inhibit apoptosis as well as promote metastasis through an increase in EMT, cell motility, and decrease of cell adhesion (Sullivan, 2009; Knüpfner, 2007). One particular member of the IL-6 family, oncostatin M (OSM), promotes breast cancer progression through the enhancement of angiogenesis and metastasis as well as the promotion of cell detachment and invasive capacity (Queen, 2005; Bolin, 2012).

### 1.2.2 Function of OSM

As a member of the IL-6 family of cytokines, the primary roles for OSM consist of cellular growth, differentiation, development, hematopoiesis, neurogenesis, bone homeostasis, liver function, immunomodulatory effects, and inflammatory response (Modur, 1997; Heinrich, 2003). OSM functions via binding to two types of transmembrane receptors: the leukemia inhibitory factor receptor (LIFR), composed of a glycoprotein gp130 and LIFR $\beta$  subunit, and the OSM-specific receptor (OSMR), which is made up of a gp130 and OSMR $\beta$  subunit (Liu, 1998; Heinrich, 2003).

Breast cancer is associated with several signaling pathways that are generally activated by inflammatory cytokines, such as OSM (Kim, 2015; Demyanets, 2011).

Specifically, the signal transducer and activator of transcription 3 (STAT3), phosphatidylinositol-3-kinase (PI3K), and the mitogen-activated protein kinase (MAPK) pathways are all involved in promoting the progression of breast cancer (Figure 1.3). The STAT3 signaling pathway increases the invasive potential of cancer cells as well as promotes EMT and migration (Tester, 2000). Additionally, the PI3K pathway is associated with increased cancer cell survival against chemotherapeutics (Chen, 2013). Furthermore, MAPK signaling induces migration and invasiveness of cancer cells and increases cellular proliferation and survival (Meng, 2013; Menendez, 2005). Ultimately, activation of the aforementioned pathways by OSM results in an increase in metastasis for breast cancer patients and thus a decrease in overall survival rates.

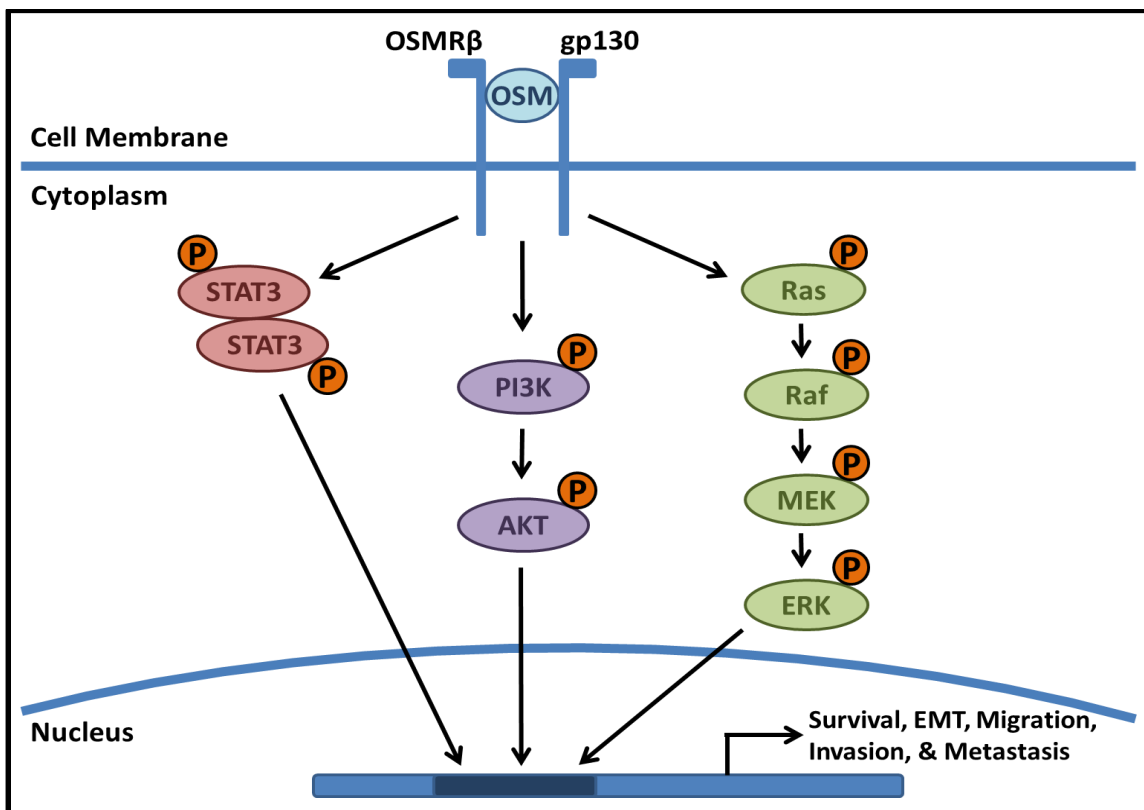


**Figure 1.3** OSM induces the STAT3, PI3K, and MAPK pathways. OSM induces activation of several signaling pathways that include STAT3, PI3K, and MAPK. Upon activation via phosphorylation of signaling proteins, the translocation of transcription factors into the nucleus allows for transcription of target genes responsible for the promotion of cancer metastasis.

### 1.2.3 Role in Breast Cancer

Although OSM was originally identified as an inhibitor of breast cancer cell proliferation *in vitro*, it has since been shown to play a role in cell detachment and angiogenesis and as such exhibits enhancement of tumor progression and metastasis *in vivo* (Queen, 2005; Bolin, 2012). Specifically, OSM has been implicated in inducing EMT, cell-substrate detachment, and increased invasiveness in breast carcinoma cells *in vitro*, which ultimately leads to enhanced metastatic potential (Bolin, 2012; Guo, 2013; Jorcyk, 2006).

One of the hallmarks of cancer progression is angiogenesis, a process by which new blood vessels form to provide oxygen and nutrients for the developing tumor (Figure 1.4).

This process transpires when the tumor reaches a size greater than one millimeter, which is the maximum distance that nutrients can efficiently diffuse from the adjacent capillaries. OSM is able to facilitate angiogenesis and thus promote tumor growth via activation of the STAT3 signaling pathway and the production of the proangiogenic vascular endothelial growth factor (VEGF) (Fossey, 2011; Weiss, 2011).

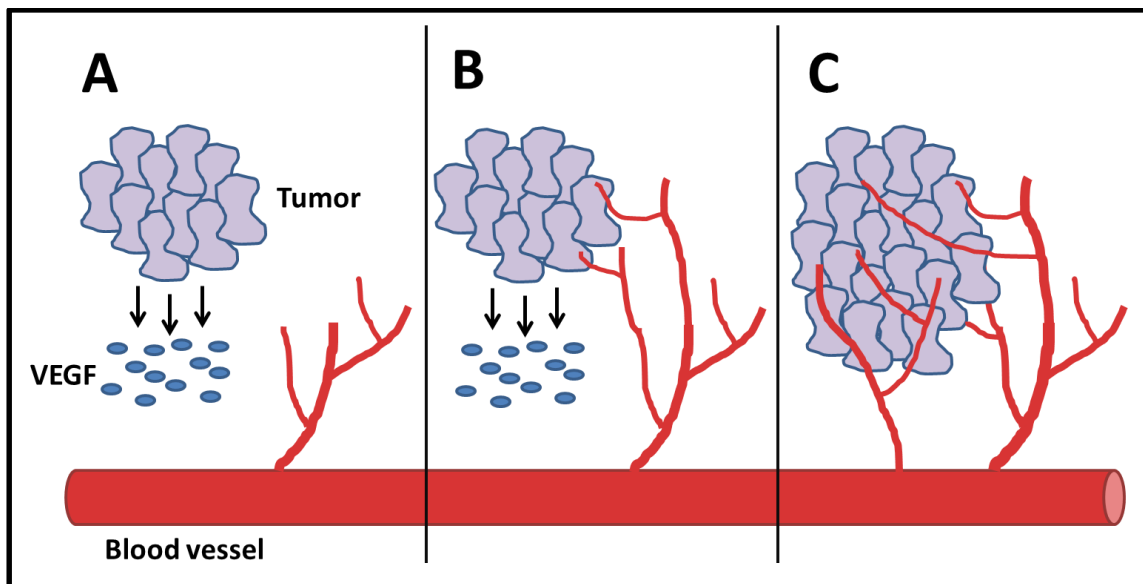


**Figure 1.4** Angiogenesis stimulated by secretion of VEGF from tumor cells. **A.** Upon reaching a size greater than one millimeter, the hypoxic tumor begins secreting proangiogenic VEGF. **B.** Release of VEGF is able to stimulate the growth of adjacent blood vessels into the tumor through a process known as angiogenesis. **C.** The formation of blood vessels to the tumor allows for oxygen and nutrient uptake, thus resulting in overall tumor growth.

Another important characteristic of cancer progression is the level of CTCs present within the circulatory system. CTCs are thought to be the principal method by which tumor metastasis to secondary sites occurs. Therefore, an elevated expression of CTCs has been associated with an unfavorable prognosis typically correlated to metastatic progression (Bednarz-Knoll, 2011; Cristofanilli, 2004). Furthermore, OSM has been shown to increase the number of CTCs (Tawara, 2018). Interestingly, evidence also suggests that through a

process called tumor self-seeding, CTCs are able to reenter an established primary tumor and enrich it with cells that are more aggressive. This self-seeding process, facilitated through IL-6 cytokines, allows for accelerated tumor growth and increased angiogenesis (Kim, 2009).

#### 1.2.4 OSM as a Therapeutic Target

In normal breast tissue, the expression of OSM is generally absent; however, OSM expression was present within 74% of cases of inflammatory breast carcinoma tissue (Guo, 2013). Furthermore, OSM expression induces tumor progression, cell detachment, and promotes metastasis, all of which are suggestive toward OSM as a potential therapeutic target (Queen, 2005; Bolin, 2012). Therefore, the work described in this thesis outlines the approach toward the structure-based drug design, synthesis, and preliminary testing of small molecule inhibitors (SMIs) of OSM as novel therapeutic treatment options for metastatic breast carcinomas.

### **1.3 Structure-Based Drug Design**

In 2016, it was estimated that the cost for the research and development of a new pharmaceutical drug was \$2.87 billion (2013 dollars). Furthermore, it was predicted that the cost would continue to increase yearly (DiMasi, 2016). In an effort to decrease experimental cost as well as time spent on discovery, computational techniques such as structure-based drug design (SBDD) have become increasingly popular. According to an analysis of published clinical candidates from the *Journal of Medicinal Chemistry* between 2016-2017, SBDD was employed as the lead generation strategy toward the identification of drug candidates in 14% of case studies (Brown, 2018).

The goal of SBDD is to design a small molecule that is capable of either modulating or inhibiting the function of a protein by a process that typically proceeds through multiple cycles of optimization prior to yielding a lead ready for clinical trials. The primary step in the process begins with target identification, the ideal target typically being a protein that is linked to disease and whose function can be modulated through the binding of a small molecule. Furthermore, the specified target should be unique in that there are no alternate pathways able to supplement the function of the target protein and thus overcome the inhibition provided by the SMI (Anderson, 2003).

After a target is chosen, the structural information is typically obtained using either X-ray crystallography or nuclear magnetic resonance (NMR) spectroscopy. However, in circumstances where experimentally obtained structures are not an option, homology modeling is a reliable method for target prediction in which known homologous protein structures are used to predict the structure of unknown proteins (Kalyaanamoorthy, 2011). The structural information can then be used to identify a potential binding site on the target where SMIs can bind to produce the desired modulation or inhibition of the target protein. Ideally, the binding sites identified consist of a pocket or protrusion with an assortment of hydrogen bond donors and acceptors as well as hydrophobic characteristics (Anderson, 2003).

Upon identification of the binding site, the next step of SBDD is hit discovery through the use of high-throughput virtual screening to generate a library of compounds potentially able to bind to the target. This process computationally screens large chemical databases by docking compounds into the binding site *in silico* and scoring them based upon their steric and electrostatic interactions with the binding site, resulting in an

abbreviated list of compounds with potentially high potency and selectivity (Shoichet, 2004; Śledź, 2018). Furthermore, virtual screening has yielded a 10-fold higher rate at predicting compounds exhibiting favorable interactions with the target than that of empirical screening techniques (Kalyaanamoorthy, 2011).

Leads are further evaluated based upon Lipinski's "rule of five" to estimate the drug-likeness of compounds (Lipinski, 1997). Several factors are considered when determining drug-likeness, one such factor is molecular weight, which correlates to intestinal and blood brain barrier permeability (Navia, 1996). Lipophilicity, expressed as the ratio of octanol to aqueous solubility (Log P), is another important component related to absorption. Permeability across a membrane bilayer is affected by the number of hydrogen bond donor and acceptor groups a compound contains and is also an important variable to consider (Kumar, 2016). Consequently, the "rule of five" states that poor absorption and permeation and thus poor drug-likeness are more likely when there are more than five hydrogen bond donors (expressed as the sum of OHs and NHs), more than 10 hydrogen bond acceptors (expressed as the sum of Ns and Os), the molecular weight is over 500 g/mol, and the Log P is over five (Lipinski, 1997).

After a lead has been identified *in silico* as a potential inhibitor to the target protein, it must be further evaluated *in vitro* using biochemical assays to validate its lead-likeness (Anderson, 2003). Upon *in vitro* validation of the promising lead as potentially binding to the target, the structure can then undergo additional cycles of optimization to improve the binding efficiency. Once optimization is complete, the SMI can be synthesized and evaluated via *in vitro* and *in vivo* tests with the goal of clinical trials and ultimately a commercial drug (Figure 1.5).

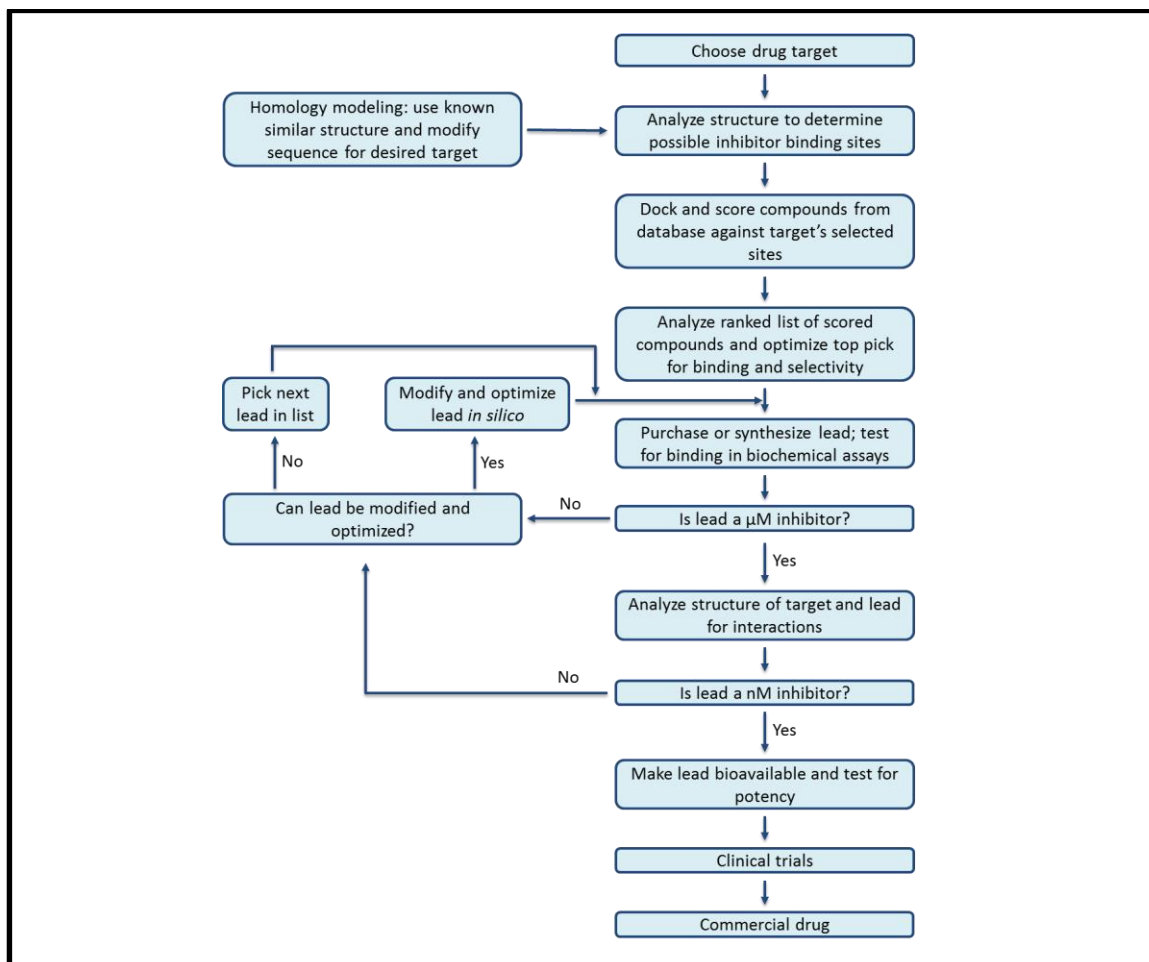


**Figure 1.5 Process of structure-based drug design.** A potential strategy for lead generation and the optimization process through which the development of commercial drugs can employ (modified from Anderson, 2003).

#### 1.4 Design of SMI-10 Analogs using SBDD

SBDD was employed in order to identify potential SMIs that inhibit metastasis through the disruption of the OSM-OSMR axis. Initially, the protein surface of the human OSM crystal structure was scanned, which identified three locations where SMIs could potentially bind to OSM. Furthermore, it was found through homology modeling that binding of SMIs at site 3 would disrupt OSM-OSMR binding directly and the other two sites were thought to interfere via allosteric effects (Figure 1.6).

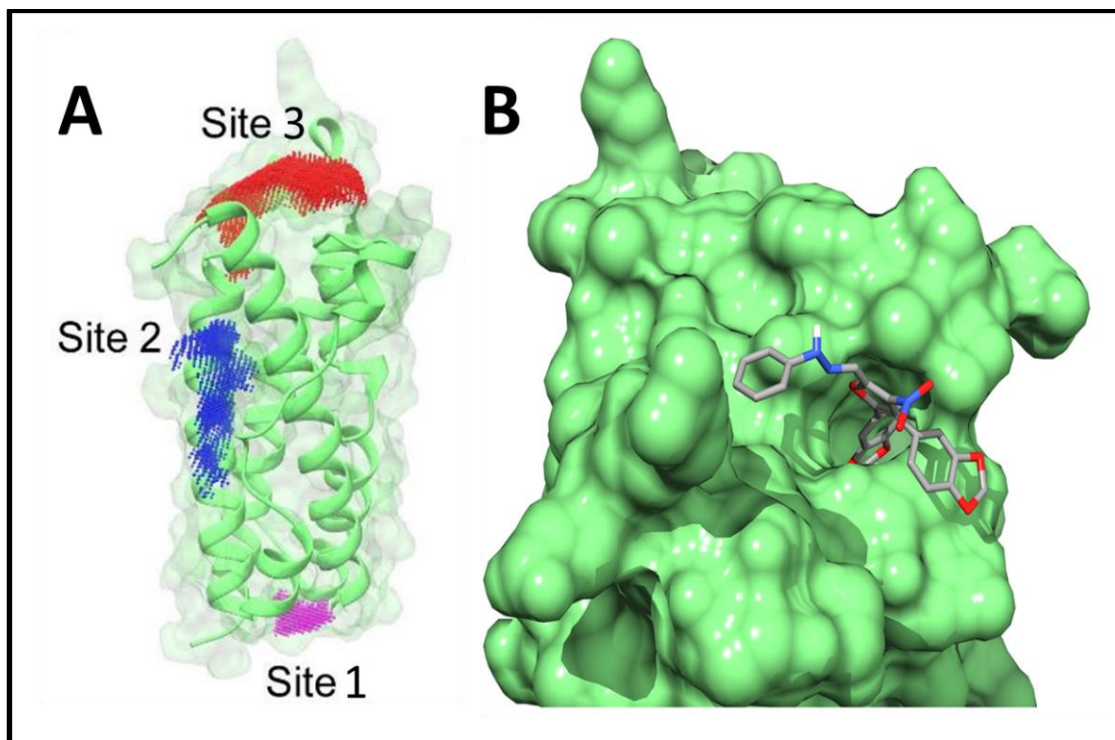


**Figure 1.6 Binding sites of OSM and SMI docked in binding pocket of OSM. A.** After scanning the OSM surface, three binding sites were located with site 3 able to directly disrupt OSM-OSMR binding. Site 2 is located within the waist region and site 1 is located at the furthest end from the binding interface. **B.** A potential SMI, available from the National Cancer Institute Diversity Set III, identified via high-throughput virtual screening is shown docked in the binding pocket of OSM at site 3 (results from Danny Xu, PhD and Matthew King, PhD; unpublished).

Using high-throughput virtual screening of the National Cancer Institute Open Database and several other accessible databases comprised of about 345,000 compounds, the top candidates were determined based upon their ability to bind to site 3. The candidates were condensed to the top 16 compounds found to have a predicted binding constant less than 10  $\mu\text{M}$  and/or binding free energies greater than -5.0 kcal/mol. Furthermore, the top compounds were assessed for their ability to inhibit OSM-induced phosphorylation of STAT3 on Tyr-705 (pSTAT3) via an enzyme-linked immunosorbent assay (ELISA). The results of the ELISA identified SMI-10 as a lead compound, with the work outlined in this thesis focused on the structural optimization of second-generation analogs of SMI-10.

Analogs were designed via a combination of synthetic accessibility and computational screening to increase binding affinity and thus improve inhibition of OSM-induced signaling. Specifically, diversity can be achieved through the modification of the heteraromatic core, the benzodioxole substituents, and the phenylhydrazone side chain. Additionally, computational experiments predicted an improved binding with the absence of the nitro group. (Figure 1.7).

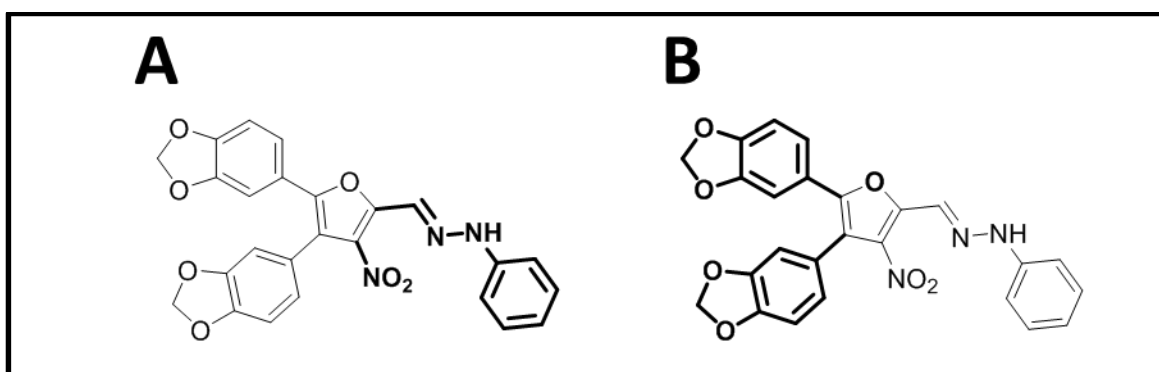


**Figure 1.7 Structure of SMI-10.** **A.** Structure of the lead compound identified for its ability to inhibit OSM-induced signaling. For the work outlined in this thesis, second-generation analogs were designed using structural optimization of the sites shown in bold to improve binding affinity toward OSM. **B.** Modification of the benzodioxole substituents and the heteraromatic core shown in bold provide additional sites for potential future optimization of analogs.

### 1.5 Concluding Remarks

The prevalence of cancer is well known, with breast cancer being the most commonly diagnosed malignancy for women. Five-year survival rates for localized breast cancer are relatively high, however, the survival rates drop by nearly 72% for metastatic breast cancer (Howlader, 2017). The work described in this thesis outlines the structure-based drug design, synthesis, and preliminary evaluation of SMI-10 analogs to be potentially used as a novel therapeutic treatment option through the inhibition of the OSM-OSMR axis.

## 1.6 References

- Anderson, A. C. (2003). The process of structure-based drug design. *Chemistry & Biology*, *10*(9), 787-797
- Anderson, K. N., Schwab, R. B., & Martinez, M. E. (2014). Reproductive risk factors and breast cancer subtypes: a review of the literature. *Breast Cancer Research and Treatment*, *144*(1), 1-10.
- Bednarz-Knoll, N., Alix-Panabières, C., & Pantel, K. (2011). Clinical relevance and biology of circulating tumor cells. *Breast Cancer Research*, *13*(6), 228.
- Bolin, C., Tawara, K., Sutherland, C., Redshaw, J., Aranda, P., Moselhy, J., Anderson, R., & Jorcyk, C. L. (2012). Oncostatin m promotes mammary tumor metastasis to bone and osteolytic bone degradation. *Genes & Cancer*, *3*(2), 117-130.
- Bos, P. D., Zhang, X. H. F., Nadal, C., Shu, W., Gomis, R. R., Nguyen, D. X., Minn, A. J., van de Vijver, M. J., Gerald, W. L., Foekens, J. A., & Massagué, J. (2009). Genes that mediate breast cancer metastasis to the brain. *Nature*, *459*(7249), 1005-1009.
- Brown, D. G., & Boström, J. (2018). Where do recent small molecule clinical development candidates come from? *Journal of Medicinal Chemistry*.
- Burstein, H. J., Polyak, K., Wong, J. S., Lester, S. C., & Kaelin, C. M. (2004). Ductal carcinoma in situ of the breast. *New England Journal of Medicine*, *350*(14), 1430-1441.
- Chaffer, C. L., Brennan, J. P., Slavin, J. L., Blick, T., Thompson, E. W., & Williams, E. D. (2006). Mesenchymal-to-epithelial transition facilitates bladder cancer metastasis: role of fibroblast growth factor receptor-2. *Cancer Research*, *66*(23), 11271-11278.
- Chen, X., Wang, H., Ou-yang, X. N., Xie, F. W., & Wu, J. J. (2013). Research on drug resistance mechanism of trastuzumab caused by activation of the PI3K/Akt signaling pathway. *Contemporary Oncology*, *17*(4), 363.
- Cowell, C. F., Weigelt, B., Sakr, R. A., Ng, C. K., Hicks, J., King, T. A., & Reis-Filho, J. S. (2013). Progression from ductal carcinoma in situ to invasive breast cancer: revisited. *Molecular Oncology*, *7*(5), 859-869.

- Cristofanilli, M., Budd, G. T., Ellis, M. J., Stopeck, A., Matera, J., Miller, M. C., Reuben, J. M., Doyle, G. V., Allard, W. J., Terstappen, L. W. M. M., & Hayes, D. F. (2004). Circulating tumor cells, disease progression, and survival in metastatic breast cancer. *New England Journal of Medicine*, 2004(351), 781-791.
- Demyanets, S., Kaun, C., Rychli, K., Pfaffenberger, S., Kastl, S. P., Hohensinner, P. J., Rega, G., Katsaros, K. M., Afonyushkin, T., Bochkov, V. N., Paireder, M., Huk, I., Maurer, G., Huber, K., & Wojta, J. (2011). Oncostatin M-enhanced vascular endothelial growth factor expression in human vascular smooth muscle cells involves PI3K-, p38 MAPK-, Erk1/2-and STAT1/STAT3-dependent pathways and is attenuated by interferon- $\gamma$ . *Basic Research in Cardiology*, 106(2), 217-231.
- DeSantis, C. E., Lin, C. C., Mariotto, A. B., Siegel, R. L., Stein, K. D., Kramer, J. L., Alteri, R., Robbins, A. S., & Jemal, A. (2014). Cancer treatment and survivorship statistics, 2014. *CA: A Cancer Journal for Clinicians*, 64(4), 252-271.
- DiMasi, J. A., Grabowski, H. G., & Hansen, R. W. (2016). Innovation in the pharmaceutical industry: new estimates of R&D costs. *Journal of Health Economics*, 47, 20-33.
- Fidler, I. J. (1970). Metastasis: quantitative analysis of distribution and fate of tumor emboli labeled with <sup>125</sup>I-5-Iodo-2'-deoxyuridine. *Journal of the National Cancer Institute*, 45(4), 773-782.
- Fossey, S. L., Bear, M. D., Kisseberth, W. C., Pennell, M., & London, C. A. (2011). Oncostatin M promotes STAT3 activation, VEGF production, and invasion in osteosarcoma cell lines. *BMC Cancer*, 11(1), 125.
- Guo, L., Chen, C., Shi, M., Wang, F., Chen, X., Diao, D., Hu, M., Yu, M., Qian, L., & Guo, N. (2013). Stat3-coordinated Lin-28–let-7–HMGA2 and miR-200–ZEB1 circuits initiate and maintain oncostatin M-driven epithelial–mesenchymal transition. *Oncogene*, 32(45), 5272-5282.
- Heinrich, P. C., Castell, J. V., & Andus, T. (1990). Interleukin-6 and the acute phase response. *Biochemical Journal*, 265(3), 621.

- Heinrich, P. C., Behrmann, I., Serge, H., Hermanns, H. M., Müller-Newen, G., & Schaper, F. (2003). Principles of interleukin (IL)-6-type cytokine signaling and its regulation. *Biochemical Journal*, *374*(1), 1-20.
- Howlader, N., Noone, A. M., & Krapcho, M. (2017). SEER Cancer Statistics Review, 1975-2014. *National Cancer Institute*.
- Jorcyk, C. L., Holzer, R. G., & Ryan, R. E. (2006). Oncostatin M induces cell detachment and enhances the metastatic capacity of T-47D human breast carcinoma cells. *Cytokine*, *33*(6), 323-336.
- Kalyaanamoorthy, S., & Chen, Y. P. P. (2011). Structure-based drug design to augment hit discovery. *Drug Discovery Today*, *16*(17-18), 831-839.
- Key, T. J., Verkasalo, P. K., & Banks, E. (2001). Epidemiology of breast cancer. *The Lancet Oncology*, *2*(3), 133-140.
- Kim, M. S., Lee, W. S., Jeong, J., Kim, S. J., & Jin, W. (2015). Induction of metastatic potential by TrkB via activation of IL6/JAK2/STAT3 and PI3K/AKT signaling in breast cancer. *Oncotarget*, *6*(37), 40158-71.
- Kim, M. Y., Oskarsson, T., Acharyya, S., Nguyen, D. X., Zhang, X. H. F., Norton, L., & Massagué, J. (2009). Tumor self-seeding by circulating cancer cells. *Cell*, *139*(7), 1315-1326.
- Knüpfner, H., & Preib, R. (2007). Significance of interleukin-6 (IL-6) in breast cancer. *Breast Cancer Research and Treatment*, *102*(2), 129-135.
- Kumar, K., & Gupta, S. C. (2016). A framework to predict uptake of trace organic compounds by plants. *Journal of Environmental Quality*, *45*(2), 555-564.
- Lipinski, C. A., Lombardo, F., Dominy, B. W., & Feeney, P. J. (1997). Experimental and computational approaches to estimate solubility and permeability in drug discovery and development settings. *Advanced Drug Delivery Reviews*, *23*, 3-25.
- Liu, J., Hadjokas, N., Mosley, B., Estrov, Z., Spence, M. J., & Vestal, R. E. (1998). Oncostatin M-specific receptor expression and function in regulating cell

- proliferation of normal and malignant mammary epithelial cells. *Cytokine*, *10*(4), 295-302.
- Malhotra, G. K., Zhao, X., Band, H., & Band, V. (2010). Histological, molecular and functional subtypes of breast cancers. *Cancer Biology & Therapy*, *10*(10), 955–960.
- Maughan, K. L., Lutterbie, M. A., & Ham, P. S. (2010). Treatment of breast cancer. *Chemotherapy*, *51*, 53.
- McPherson, K., Steel, C. M., & Dixon, J. M. (2000). Breast cancer—epidemiology, risk factors, and genetics. *BMJ: British Medical Journal*, *321*(7261), 624–628.
- Menendez, J. A., Vellon, L., Mehmi, I., Teng, P. K., Griggs, D. W., & Lupu, R. (2005). A novel CYR61-triggered ‘CYR61- $\alpha$ v $\beta$ 3 integrin loop’ regulates breast cancer cell survival and chemosensitivity through activation of ERK1/ERK2 MAPK signaling pathway. *Oncogene*, *24*(5), 761-779.
- Meng, X., Cai, C., Wu, J., Cai, S., Ye, C., Chen, H., Yang, Z., Zeng, H., Shen, Q., & Zou, F. (2013). TRPM7 mediates breast cancer cell migration and invasion through the MAPK pathway. *Cancer Letters*, *333*(1), 96-102.
- Modur, V., Feldhaus, M. J., Weyrich, A. S., Jicha, D. L., Prescott, S. M., Zimmerman, G. A., & McIntyre, T. M. (1997). Oncostatin M is a proinflammatory mediator. In vivo effects correlate with endothelial cell expression of inflammatory cytokines and adhesion molecules. *Journal of Clinical Investigation*, *100*(1), 158.
- Navia, M. A., & Chaturvedi, P. R. (1996). Design principles for orally bioavailable drugs. *Drug Discovery Today*, *1*(5), 179-189.
- Price, T. T., Burness, M. L., Sivan, A., Warner, M. J., Cheng, R., Lee, C. H., Olivere, L., Comatas, K., Magnani, J., Lysterly, H. K., Cheng, Q., McCall, C. M., & Sipkins, D. A. (2016). Dormant breast cancer micrometastases reside in specific bone marrow niches that regulate their transit to and from bone. *Science Translational Medicine*, *8*(340), 340ra73.

- Queen, M. M., Ryan, R. E., Holzer, R. G., Keller-Peck, C. R., & Jorcyk, C. L. (2005). Breast cancer cells stimulate neutrophils to produce oncostatin M: potential implications for tumor progression. *Cancer Research*, *65*(19), 8896-8904.
- Sharp, A., & Harper-Wynne, C. (2014). Treatment of advanced breast cancer (ABC): the expanding landscape of targeted therapies. *Journal of Cancer Biology & Research*, *2*, 1036.
- Shoichet, B. K. (2004). Virtual screening of chemical libraries. *Nature*, *432*(7019), 862.
- Siegel, R. L., Miller, K. D., & Jemal, A. (2018). Cancer statistics, 2018. *CA: A Cancer Journal for Clinicians*, *68*, 7-30.
- Śledź, P., & Caflisch, A. (2018). Protein structure-based drug design: from docking to molecular dynamics. *Current Opinion in Structural Biology*, *48*, 93-102.
- Sullivan, N. J., Sasser, A. K., Axel, A., Vesuna, F., Raman, V., Ramirez, N., Oberyszyn, T. M., & Hall, B. M. (2009). Interleukin-6 induces an epithelial–mesenchymal transition phenotype in human breast cancer cells. *Oncogene*, *28*(33), 2940-2947.
- Tawara, K., Bolin, C., Koncinsky, J., Kadaba, S., Covert, H., Sutherland, C., Bond, L., Kronz, J., Garbow, J., & Jorcyk, C. L. (2018). OSM potentiates preinvasion events, increases CTC counts, and promotes breast cancer metastasis to the lung. *Breast Cancer Research*, *20*(1), 53.
- Tester, A. M., Ruangpanit, N., Anderson, R. L., & Thompson, E. W. (2000). MMP-9 secretion and MMP-2 activation distinguish invasive and metastatic sublines of a mouse mammary carcinoma system showing epithelial-mesenchymal transition traits. *Clinical and Experimental Metastasis*, *18*(7), 553-560.
- van Zijl, F., Krupitza, G., & Mikulits, W. (2011). Initial steps of metastasis: cell invasion and endothelial transmigration. *Mutation Research/Reviews in Mutation Research*, *728*(1), 23-34.
- Weigelt, B., Peterse, J. L., & Van't Veer, L. J. (2005). Breast cancer metastasis: markers and models. *Nature Reviews Cancer*, *5*(8), 591-602.

Weiss, T. W., Simak, R., Kaun, C., Rega, G., Pflueger, H., Maurer, G., Huber, K., & Wojta, J. (2011). Oncostatin M and IL-6 induce u-PA and VEGF in prostate cancer cells and correlate in vivo. *Anticancer Research*, *31*(10), 3273-3278.

## CHAPTER TWO: SYNTHESIS, CHARACTERIZATION, AND EVALUATION OF SMI-10 ANALOGS

### **2.1 Introduction**

#### 2.1.1 Metastatic Breast Cancer

Cancer is a major public health concern worldwide and is the second leading cause of death in the United States. In 2018, it is estimated that there will be about 1.7 million new cases diagnosed resulting in 600,000 deaths in the United States alone (Siegel, 2018). At 30% of all cases, the most prevalent malignancy diagnosed for women is breast cancer. The five-year survival rate for localized breast cancer is 99%, however, for stage IV metastatic breast cancer the rate drops to only 27% (Howlader, 2017).

In 2017, it was estimated that nearly 155,000 women in the United States were living with metastatic breast cancer (Mariotto, 2017). Typically, women develop a metastatic form of breast cancer months or years after completing treatment for earlier stages of the malignancy, with only about 6% of women initially diagnosed with *de novo* metastatic breast cancer (Howlader, 2016). The aim of pre-metastatic breast cancer treatment is curative. In stark contrast, the primary objective of post-metastatic treatment is mainly palliative, such that symptoms are controlled and toxicity is minimized (Mestres, 2017).

Approximately 67-70% of metastatic patients are progesterone receptor (PR) and estrogen receptor (ER) positive and are typically treated with targeted therapies that block growth of new cancerous cells through the interference of molecules essential for

carcinogenesis and tumor growth (Mestres, 2017). An example of a targeted therapy includes cyclin-dependent kinase (CDK) 4/6 inhibitors capable of halting cell cycle progression and inducing cell cycle arrest (Finn, 2016). The mammalian target of rapamycin (mTOR) inhibitors are another class of targeted therapy that function via inhibition of the phosphatidylinositol-3-kinase (PI3K) pathway, which is responsible for cell survival (Hahne, 2017). Alternatively, radiation therapy and chemotherapy can also be used to help halt the growth of new tumors and potentially shrink existing tumors.

Chemotherapeutics are used for the treatment of metastatic breast cancer patients who exhibit human epidermal growth factor receptor 2 (HER2) positive expression and are either hormone receptor-negative or hormone receptor-positive, but no longer respond to hormonal therapy. Among the most common chemotherapeutic agents used for the treatment of metastatic breast cancer are taxanes, such as paclitaxel (Taxol), and anthracyclines, such as doxorubicin (Adriamycin) (Mestres, 2017). Unfortunately, the clinical usefulness of such treatment methods is limited due to toxicity that may prevent adequate dosing (O'Brien, 2004). These chemotherapeutic agents are further limited in that tumors often become resistant to treatment, which accounts for more than 90% of breast cancer deaths (Ireland, 2018; Marquette, 2012). Additional chemotherapeutics include monoclonal antibodies such as trastuzumab (Herceptin), which targets the overexpressed *HER2* gene in breast tumors that is responsible for the promotion of cancerous cell growth and division (Emens, 2004). Unfortunately, patients with triple negative breast cancer (TNBC) tend to have a poor short-term prognosis and do not respond to targeted therapies (Anderson, 2014; Sharp, 2014).

### 2.1.2 Oncostatin M as a Therapeutic Target

The interleukin-6 (IL-6) family of cytokines has been implicated in the promotion of metastasis for breast cancer patients through an increase in epithelial to mesenchymal transition (EMT), cell motility, and decrease of cellular adhesion (Sullivan, 2009; Knüpfer, 2007). A specific member of this family, oncostatin M (OSM), promotes cancer progression through the promotion of cell detachment, invasive capacity, increasing circulating tumor cell (CTC) numbers, and enhancement of angiogenesis (Queen, 2005; Jorcyk, 2006; Bolin, 2012; Tawara, 2018). Interestingly, the expression of OSM is typically absent in normal breast tissue, but was found to be elevated within malignant tissue (Guo, 2013). Due to the elevated expression and capability to promote tumor progression, OSM is a viable therapeutic target for the treatment of metastatic breast cancer.

OSM functions via binding to two types of transmembrane receptors: the leukemia inhibitory factor receptor (LIFR), composed of glycoprotein gp130 and LIFR $\beta$  subunits, and the OSM-specific receptor (OSMR), which is made up of gp130 and OSMR $\beta$  subunits (Liu, 1998; Heinrich, 2003). OSM-OSMR interactions have the potential to increase invasiveness, angiogenesis, and metastasis in malignant cells through the activation of several signaling pathways. These pathways include the signal transducer and activator of transcription 3 (STAT3), PI3K, and mitogen-activated protein kinase (MAPK) pathways (Tester, 2000; Chen, 2013; Meng, 2013; Smith, 2014) (Figure 2.1). Notably, increased OSM signaling, either by overexpression of OSM or OSMR, has been associated with poor prognosis in breast cancer patients (West, 2012).

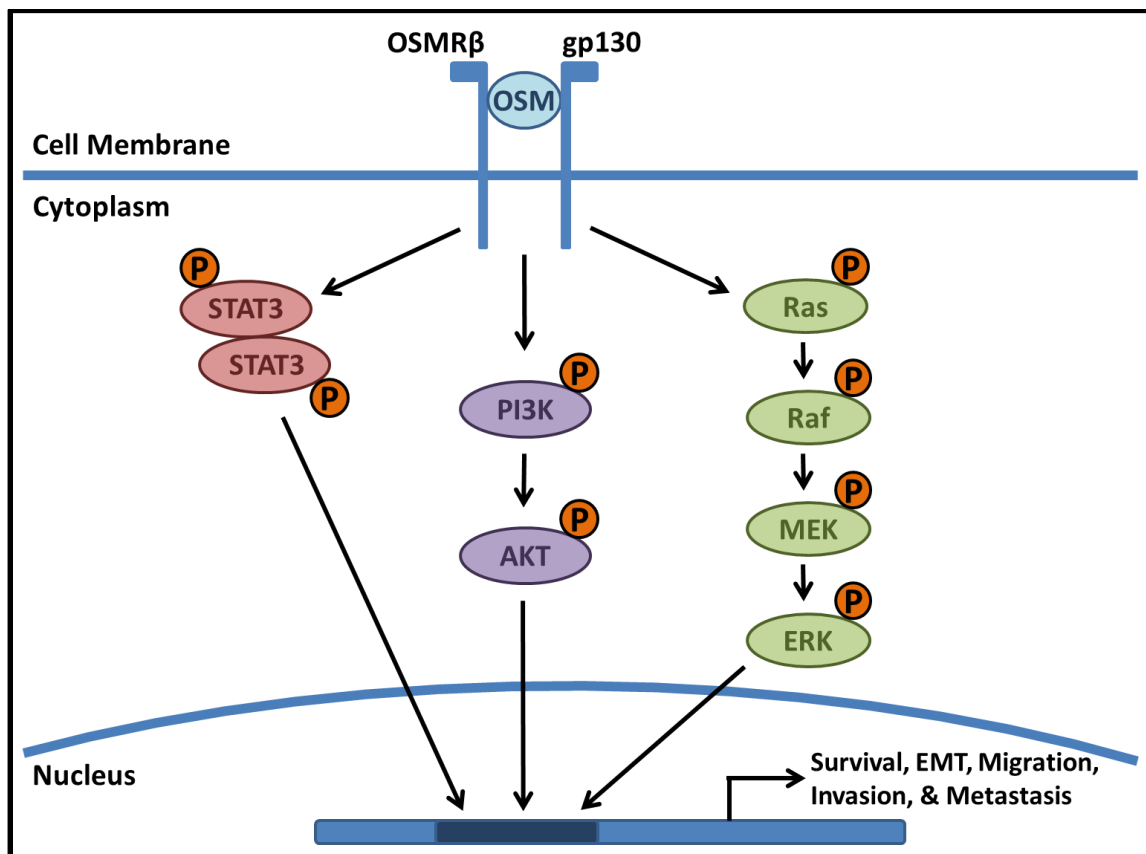


**Figure 2.1 OSM induces the STAT3, PI3K, and MAPK pathways.** OSM induces activation of several signaling pathways that include STAT3, PI3K, and MAPK. Upon activation via phosphorylation of signaling proteins, the translocation of transcription factors into the nucleus allows for transcription of target genes responsible for the promotion of cancer metastasis.

Inhibition of the OSM-OSMR axis has recently been suggested as a targeted therapy strategy. For instance, administration of OSM-bound antigen binding proteins capable of disrupting the association of OSM to the gp130 subunit of the receptor has been evaluated as a method for treating inflammatory disorders and diseases (Bembridge, 2017). Additionally, inhibition of the OSM-OSMR axis has been suggested as a targeted therapy against cervical squamous cell carcinomas (Kucia-Tran, 2017; Caffarel, 2014; Tawara, 2018). The aim of the work described in this thesis outlines the approach toward the design, synthesis, and preliminary testing of small molecule inhibitors (SMIs) that disrupt the

OSM-OSMR axis and thus prevent signal transduction of pathways promoting metastasis and angiogenesis as an approach toward the treatment of metastatic breast cancer.

## **2.2 Design of SMI-10 Analogs**

### 2.2.1 High-Throughput Virtual Screening

Computational screening was employed to identify potential SMIs that inhibit OSM using ligand shape matching (results from Danny Xu, PhD and Matthew King, PhD; unpublished). The protein surface obtained from the human OSM crystal structure (PDB ID: 1EVS) was computationally scanned via the AutoLigand program to identify potential clefts or pockets where the SMI could bind to OSM, which revealed three sites with a large enough energy to volume distribution ratio capable of SMI binding. Due to the structural similarities between OSM and the leukemia inhibitory factor (LIF), a structural alignment of OSM and the LIF-LIF receptor complex (PDB ID: 2Q7N) was performed using an AMBER force field. The results of the homology modeling indicated that binding of SMIs at site 3 would directly interrupt OSM-OSMR binding (Figure 2.2). Furthermore, it was predicted that bound SMIs at the remaining two sites might contribute to interrupted OSM-OSMR binding via allosteric effects (unpublished).

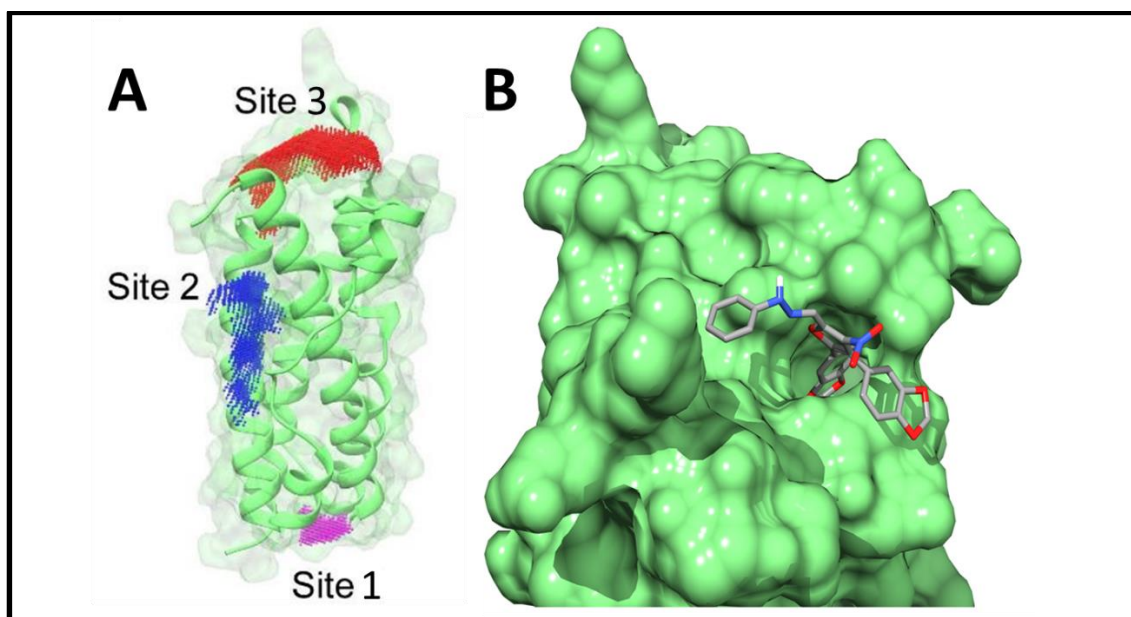


**Figure 2.2 Binding sites of OSM and SMI docked in binding pocket of OSM. A.** After scanning the OSM surface, three binding sites were located with site 3 able to directly disrupt OSM-OSMR binding. Site 2 is located within the waist region and site 1 is located at the furthest end from the binding interface. **B.** A potential SMI, available from the National Cancer Institute Diversity Set III, identified via high-throughput virtual screening is shown docked in the binding pocket of OSM at site 3 (results from Danny Xu, PhD and Matthew King, PhD; unpublished).

The top SMI candidates were identified by high-throughput virtual screening of about 345,000 compounds within the National Cancer Institute Open Database and other accessible databases. The compounds were screened for their ability to bind at site 3 of OSM, which was thought to be responsible for direct OSM-OSMR binding inhibition. The candidates were then further condensed to the top 16 compounds that were found to have a predicted binding constant less than 10  $\mu\text{M}$  and/or binding free energies greater than -5.0 kcal/mol.

### 2.2.2 OSM Inhibition Assay

OSM is able to activate several pathways associated with tumor progression, including STAT3 (Tester, 2000). In order to assess the ability of the potential SMIs identified via computational screening to disrupt signaling of OSM, inhibition of OSM-

induced phosphorylation of STAT3 on Tyr-705 (pSTAT3) was evaluated via an enzyme-linked immunosorbent assay (ELISA). Of the 16 SMIs tested via ELISA, SMI-8, -10, and -11 exhibited the greatest inhibition of pSTAT3. In addition to inhibition of the STAT3 signaling pathway, the SMIs were also shown, through Western Blot analysis, to inhibit other downstream components of OSM-induced signaling pathways such as phosphorylation of extracellular signal-regulated kinase (ERK) and protein kinase B (AKT) (Figure 2.3).

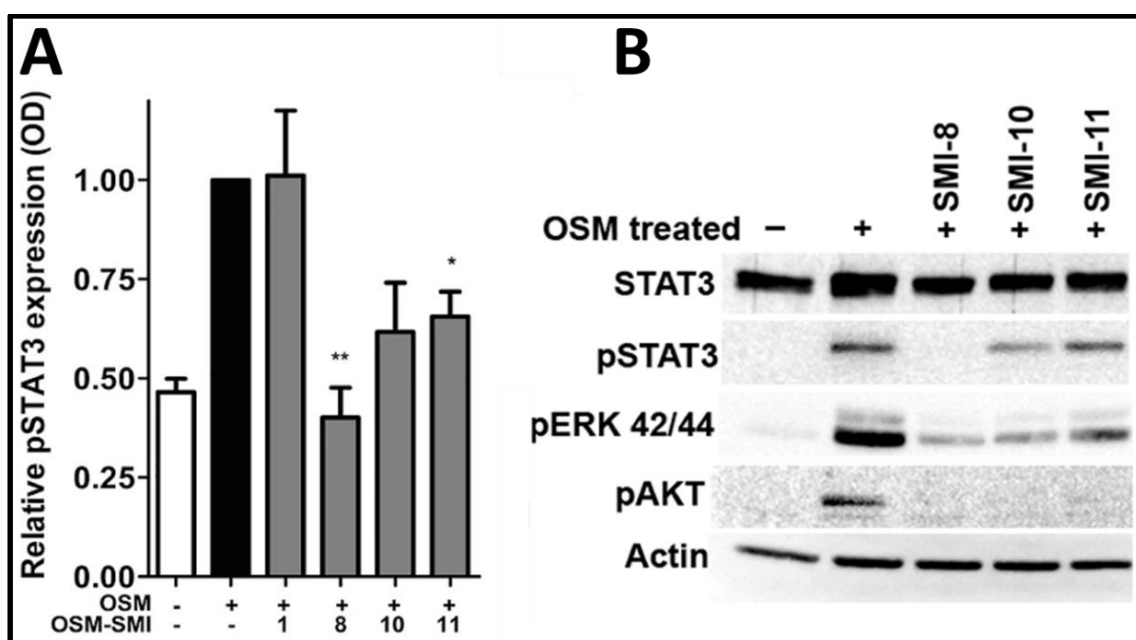


**Figure 2.3 Screening of SMIs via ELISA and Western Blot analysis.** **A.** MDA-MB-231 human breast cancer cells were treated for 30 minutes after co-incubation of each SMI-1, -8, -10, and -11 (5  $\mu$ M) with OSM (5 ng/mL) in serum-free media for 1 hour at 37  $^{\circ}$ C. The cells were lysed, collected, and pSTAT3 levels were measured by ELISA. The reduction of pSTAT3 expression by the SMIs is indicative of inhibition of OSM-induced STAT3 signaling. (mean  $\pm$  SEM; n=3; \*p<0.05; \*\*p>0.01; unpaired t-test) **B.** A Western Blot analysis was performed to assess the ability of each SMI to suppress downstream pSTAT3, pERK, and pAKT signaling in MDA-MB-231 human breast cancer cells with STAT3 and actin protein levels used as internal loading controls (results from Ken Tawara, PhD; unpublished).

### 2.2.3 Optimization of Lead Compound

Due to the ability of SMI-10 to inhibit OSM-induced signaling, it became the “lead compound” for the work outlined in this thesis. In order to improve the ability of the lead compound to inhibit signaling, second-generation analogs were designed based upon additional computational screening and structural optimization. Specifically, computational modeling of SMI-10 demonstrated a binding pose that allowed for additional structural modifications of specific regions on the SMI to potentially improve binding affinity and inhibition of OSM-induced signaling (Figure 2.4).

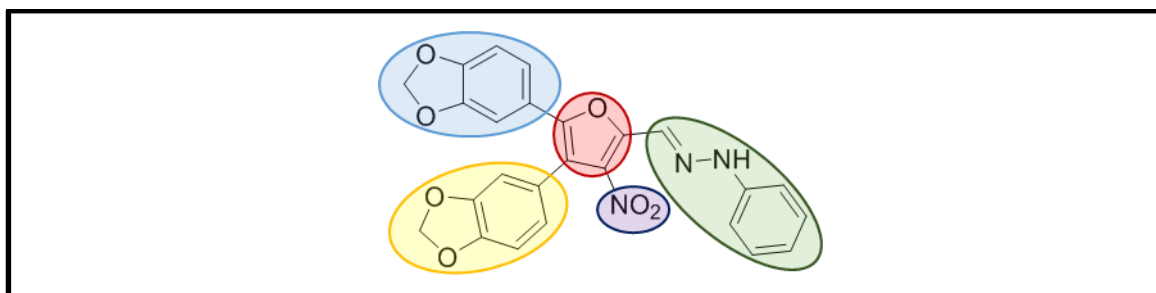


**Figure 2.4** Structure of SMI-10. Individual regions of SMI-10 are highlighted (blue = benzodioxole side group A; yellow = benzodioxole side group B; red = furan core; purple = nitro side group; green = side chain).

Through computational modeling, it was determined that there are several electrostatic interactions between OSM and SMI-10 that are potentially favorable for increased binding affinity (Figure 2.5) (results from Matthew King, PhD; unpublished). Specifically, the aldimine nitrogen atom on the side chain of SMI-10 interacts with the nearby positively charged K163 amino acid residue on OSM, resulting in an increased binding affinity. Furthermore, it was predicted that the aldimine pi bond on the side chain of SMI-10 might also be able to interact with the K163 amino acid residue to help stabilize binding with OSM. Additionally, it was predicted that the nitro side group on SMI-10 was

not directly binding to OSM and thus potentially lowering the binding affinity of the SMI as a result of increased interactions with the solvent. Due to this reason, it was projected that SMI-10 analogs with the nitro group removed would have an increased binding affinity compared to the parent SMI-10 compound.

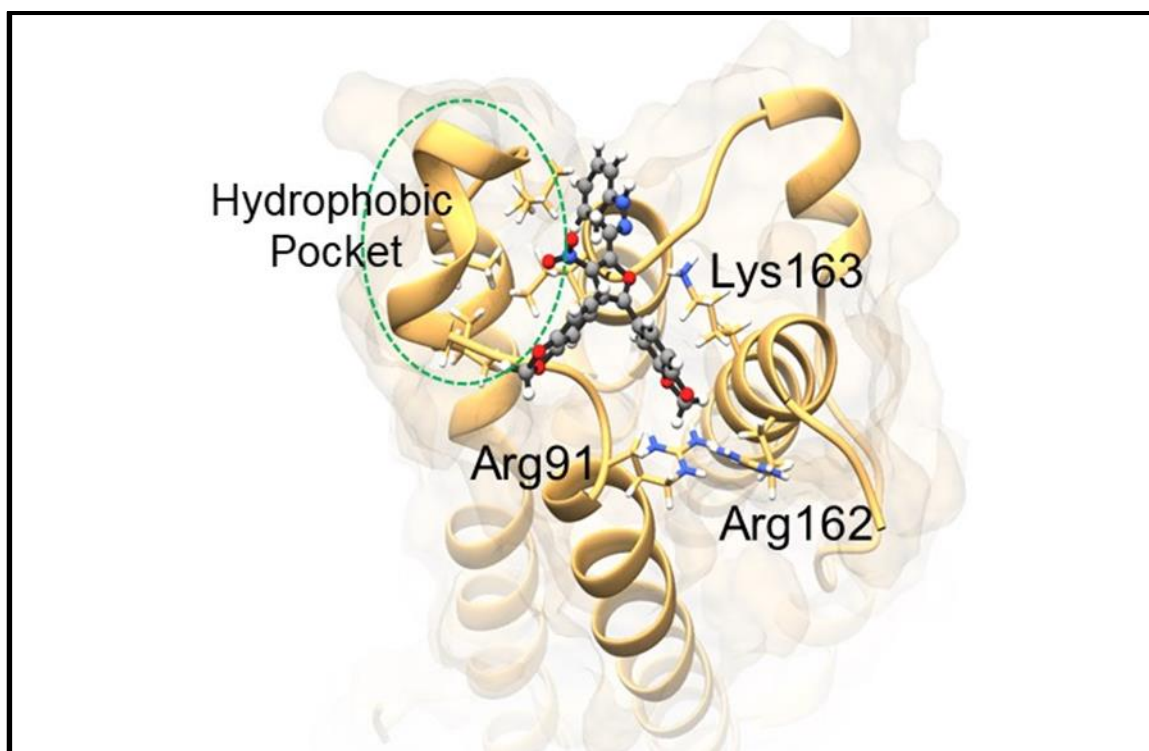


**Figure 2.5 SMI-10 in binding pocket of OSM.** Adjacent amino acid residues of OSM to bound SMI-10 that are potentially favorable for enhancement of electrostatic interactions via chemical modification of the SMI. Atom types are indicated by color: red = O, blue = N, gray = C, and white = H. (image from Matthew King, PhD; unpublished).

Another important interaction that was determined computationally revealed a hydrophobic pocket within the binding site of OSM consisting of I37, L92, P93, L98, L103, and L108 amino acid residues. This pocket is important because the aromatic phenyl ring at the end of the side chain on SMI-10 is able to fit into this space to allow for optimized binding. Therefore, structural modifications of SMI-10 that retain hydrophobic characteristics at this location should improve the binding affinity to OSM.

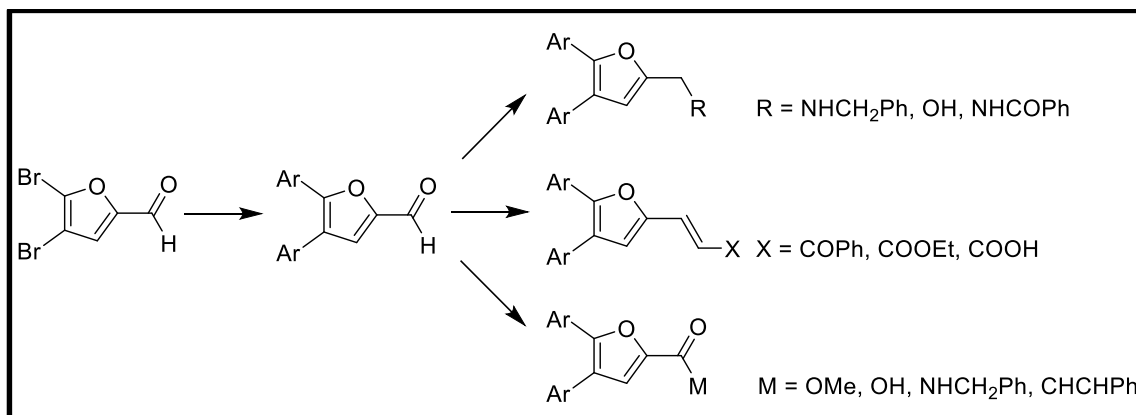
Additionally, the benzodioxole side group A on SMI-10 fits into another hydrophobic pocket in binding site 3 of OSM (L92 and A159), allowing for enhanced binding. Furthermore, at the bottom of the hydrophobic pocket are several positively charged arginine amino acid residues (R91 and R162) that stabilize the oxygen atoms present on the benzodioxole side group A within the pocket. The electrostatic interactions within this binding pocket allow for potential chemical modifications of the benzodioxole side group A to improve binding affinity.

Another important interaction between OSM and SMI-10 involves hydrogen bonding between the furan core and the adjacent positively charged K163 amino acid residue. Due to this interaction, it is feasible to alter the oxygen on SMI-10 to other electronegative atoms that would exhibit a similar electrostatic interaction to potentially enhance binding affinity between OSM and the SMI. Ultimately, based on these electrostatic interactions and synthetic accessibility, a small library of second-generation analogs was synthesized to potentially improve the ability of the lead compound to inhibit OSM-induced signaling.

## **2.3 Results and Discussion**

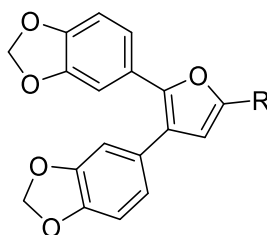
### **2.3.1 Synthesis of SMI-10 Analogs**

The overall approach toward the synthesis of the SMI-10 analogs began with a Suzuki coupling of the commercially available 4,5-dibromofuran-2-carbaldehyde with excess 3,4-methylenedioxyphenyl boronic acid. The result of this reaction was an aldehyde with aryl substituents in place of the original bromine atoms. From this product, a variety of analogs were then obtained (Scheme 2.1).



**Scheme 2.1 Overall synthetic route for SMI-10 analogs.** A Suzuki coupling of the commercially available starting material results in the aldehyde intermediate with aryl substituents. From this intermediate, a small library of second-generation analogs can then be synthesized.

The SMI-10 analogs generated were designed based upon synthetic accessibility and computational screening (Table 2.1). Specifically, the analogs were designed such that the binding affinity between the SMIs and site 3 of OSM would be optimized. Ultimately, the result of increased binding of the analogs to OSM leads to the disruption of the OSM-OSMR axis and thus inhibition of OSM-induced signaling pathways.

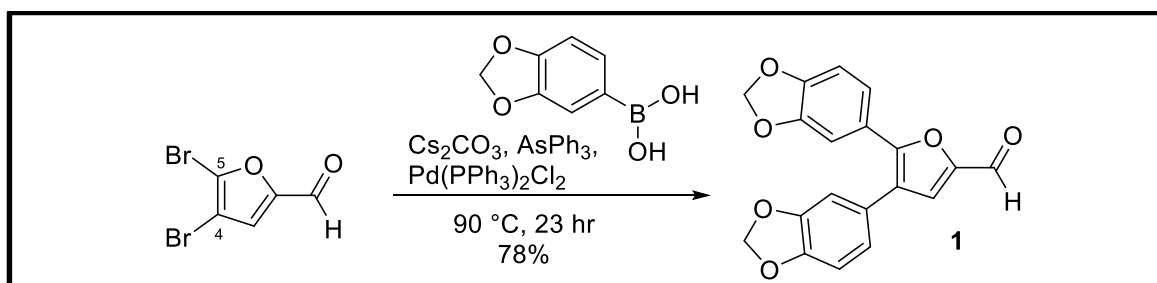
**Table 2.1 Structures of SMI-10 analogs.<sup>a</sup>**

Compound	R	Compound	R
SMI-10A		SMI-10G	
SMI-10B		SMI-10H	
SMI-10C		SMI-10I	
SMI-10D		SMI-10J	
SMI-10E		SMI-10K	
SMI-10F			

<sup>a</sup>Summary of the analogs designed via a combination of synthetic accessibility and computational screening to increase binding affinity and thus inhibition of OSM-induced signaling.

### Compound 1

The synthesis of **1** began with a Suzuki coupling of the commercially available 4,5-dibromofuran-2-carbaldehyde with 3,4-methylenedioxyphenyl boronic acid (Scheme 2.2). The reaction was heated for nearly 24 hours to allow for complete substitution of both bromine substituents with the aromatic groups despite the deactivated furan ring. Following purification of the doubly-arylated compound, **1** was obtained in a 78% yield to be used as an intermediate starting material for the synthesis of several additional SMI-10 analogs. It is worth noting that when the reaction time was decreased, mono-arylation preferentially occurred at carbon five of the furan core. This result indicates that it is feasible for future optimizations of SMI-10 analogs to contain two different aryl substituents, which could potentially enhance binding affinity to OSM.

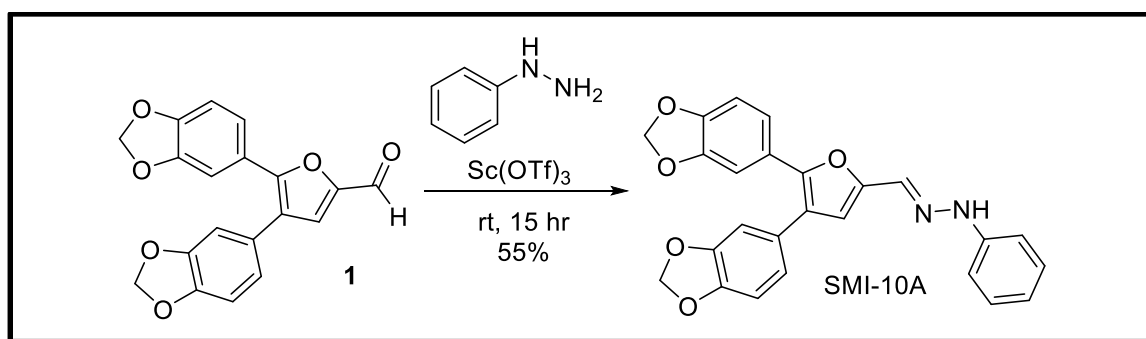


**Scheme 2.2** Synthetic route for **1**. Compound **1** was obtained through a Suzuki coupling of 4,5-dibromofuran-2-carbaldehyde with 3,4-methylenedioxyphenyl boronic acid.

### SMI-10A

Compound **1** was treated with nucleophilic phenylhydrazine to facilitate a condensation reaction via the loss of the carbonyl oxygen as water and the formation of the hydrazone product, SMI-10A (Scheme 2.3). However, initial attempts at various temperatures and with several solvents such as tetrahydrofuran, ethanol, diethyl ether, methylene chloride, and chloroform were unsuccessful and returned almost exclusively

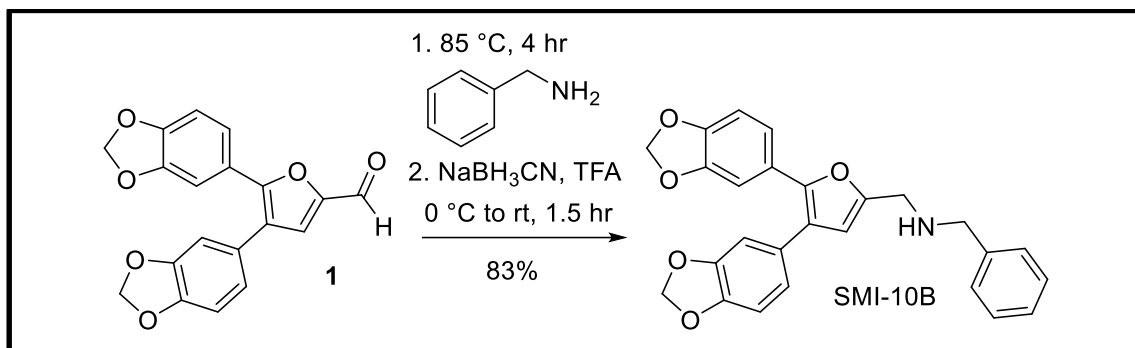
starting material. Nonetheless, the work of Furrow, et al. demonstrated the capability of using a Lewis acid catalyst such as scandium triflate to facilitate condensation reactions (Furrow, 2004). After the addition of the catalyst, the reaction occurred readily at ambient temperature with a yield of 55% after purification. However, the purified product proved to be unstable and partially decomposed over time as verified via NMR analysis.



**Scheme 2.3 Synthetic route for SMI-10A.** Condensation reaction of the aldehyde starting material with phenylhydrazine and scandium triflate to obtain the hydrazone, SMI-10A, as the product.

### SMI-10B

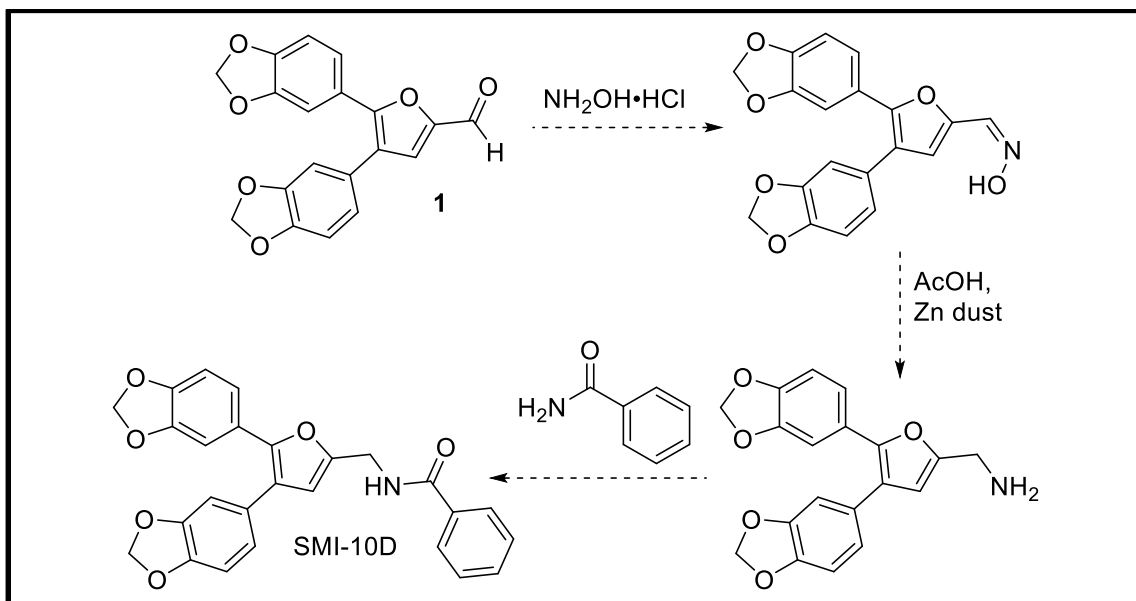
SMI-10B was obtained via a one pot synthesis by adding benzylamine to initially form the imine intermediate through the loss of water. Following the formation of the intermediate, trifluoroacetic acid was used to protonate the imine and produce the iminium ion, which was then reduced with sodium cyanoborohydride. After the reductive amination, the amine was formed with an 83% yield (Scheme 2.4).



**Scheme 2.4 Synthetic route for SMI-10B.** Addition of benzylamine to **1** resulted in the formation of an imine intermediate, which was then protonated to produce the iminium ion. The reductive amination was completed with sodium cyanoborohydride as a reducing agent to yield the final amine, SMI-10B, as the product.

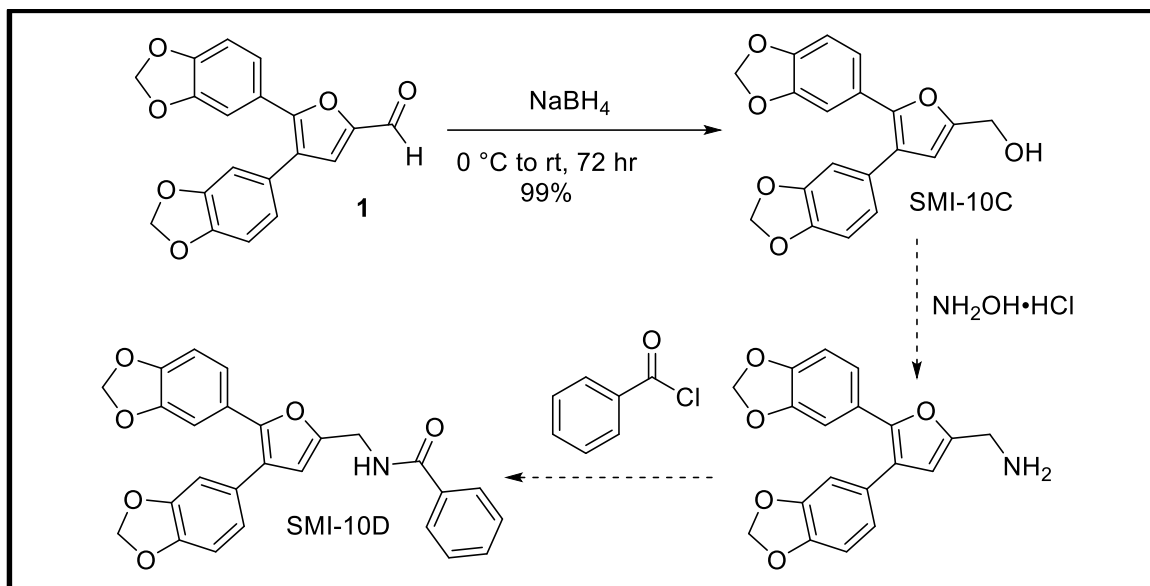
#### SMI-10C and -10D

Initially, a reductive amination was proposed in which the aldehyde of **1** would be converted to an aldoxime using hydroxylamine hydrochloride following a comparable reductive amination protocol of furfural (De Roulet, 2015). The aldoxime would then be subsequently reduced using acetic acid and zinc dust to yield the amine intermediate. Finally, after the addition of benzamide to the amine following a similar procedure described by Allen et al., the synthesis of SMI-10D would be achieved (Scheme 2.5) (Allen, 2012). However, despite alterations in temperature and molar ratios, this route was unsuccessful, which necessitated a revised synthetic route.



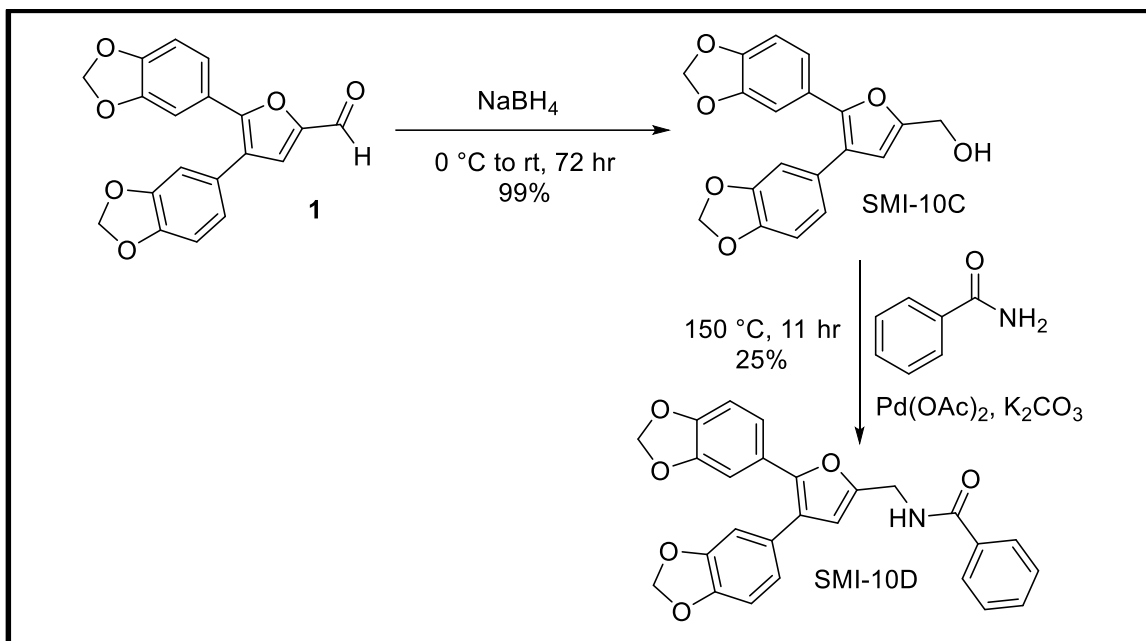
**Scheme 2.5** Proposed synthetic route for SMI-10D. Reductive amination of the starting aldehyde, **1**, to the resulting amine via an aldoxime intermediate followed by the addition of benzamide to yield SMI-10D.

The synthesis of SMI-10C begun by reducing the aldehyde moiety of **1** with sodium borohydride to yield the resulting alcohol, SMI-10C, in a yield of 99%. Upon synthesis of SMI-10C, a two-step amidation was attempted in which the alcohol would be converted to the corresponding amine following a protocol for a similar conversion (Kuang, 2005). The amine would then be treated with benzoyl chloride to yield the final product, SMI-10D, according to a comparable synthetic route (Ouairy, 2010) (Scheme 2.6). However, this route provided little success toward the synthesis of SMI-10D and was consequently abandoned in favor of a more direct route.



**Scheme 2.6** Proposed synthetic route for SMI-10C and -10D. Synthesis of SMI-10C was achieved through the reduction of the aldehyde moiety on **1**. The alcohol moiety would then be converted through an amination step to obtain the corresponding amine. The final proposed amidation step employed an acid chloride to obtain the SMI-10D product.

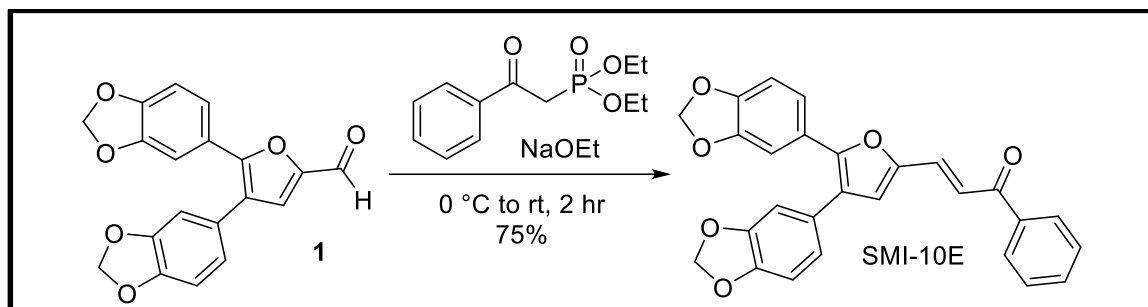
The most efficient route for the synthesis of SMI-10D was finally determined after several unsuccessful routes were attempted. The initial reduction step of **1** to the corresponding alcohol, SMI-10C, followed the same protocol as previously mentioned. The synthetic route differed in the final step which involved the direct amidation of SMI-10C to the final product, SMI-10D using benzamide and palladium(II) acetate based upon a similar protocol for the n-alkylation of carboxamides (Martínez-Asencio, 2011). Upon purification, the final amide was obtained in an un-optimized yield of 25% (Scheme 2.7).



**Scheme 2.7** Synthetic route for SMI-10C and -10D. Synthesis of SMI-10C was achieved through a reduction of the aldehyde moiety on **1**. A final amidation step using benzamide and palladium(II) acetate allowed for the obtainment of SMI-10D.

### SMI-10E

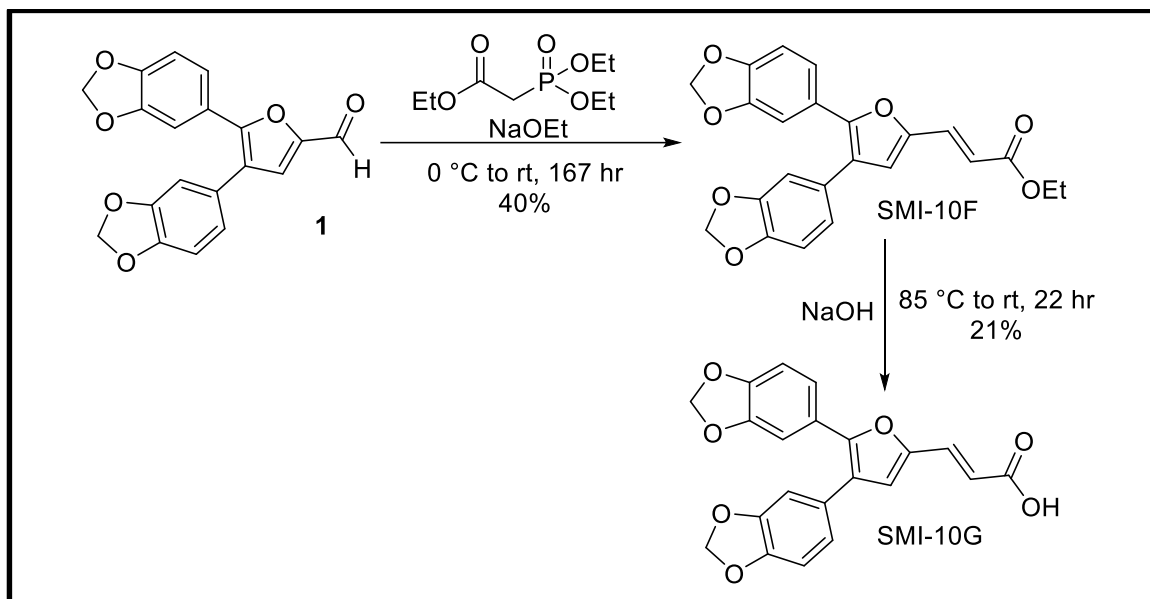
SMI-10E was synthesized via a Horner-Wadsworth-Emmons olefination reaction using commercially available diethyl (2-oxo-2-phenylethyl)phosphonate, which was initially deprotonated with sodium ethoxide using a protocol for a comparable reaction scheme (Kossler, 2015). Following deprotonation, the phosphonate carbanion underwent a nucleophilic addition to **1**. After a final elimination step and purification, SMI-10E was obtained in a 75% yield as a yellow solid (Scheme 2.8).



**Scheme 2.8** Synthetic route for SMI-10E. Horner-Wadsworth-Emmons olefination reaction between the aldehyde moiety on **1** and commercially available diethyl (2-oxo-2-phenylethyl)phosphonate to generate SMI-10E.

### SMI-10F and -10G

The synthesis of SMI-10F followed a similar synthetic route to that of SMI-10E in that it utilized a Horner-Wadsworth-Emmons olefination reaction with triethyl phosphonoacetate to obtain a yellow oil with a yield of 40%. Following the formation of SMI-10F, a saponification reaction was employed to convert the ester of SMI-10F to a carboxylic acid. The hydrolysis of SMI-10F began with the addition of 1M sodium hydroxide to produce a tetrahedral intermediate. Finally, SMI-10G was generated upon expulsion of the alkoxide ion to form the carboxylic acid in an un-optimized yield of 21% (Scheme 2.9).

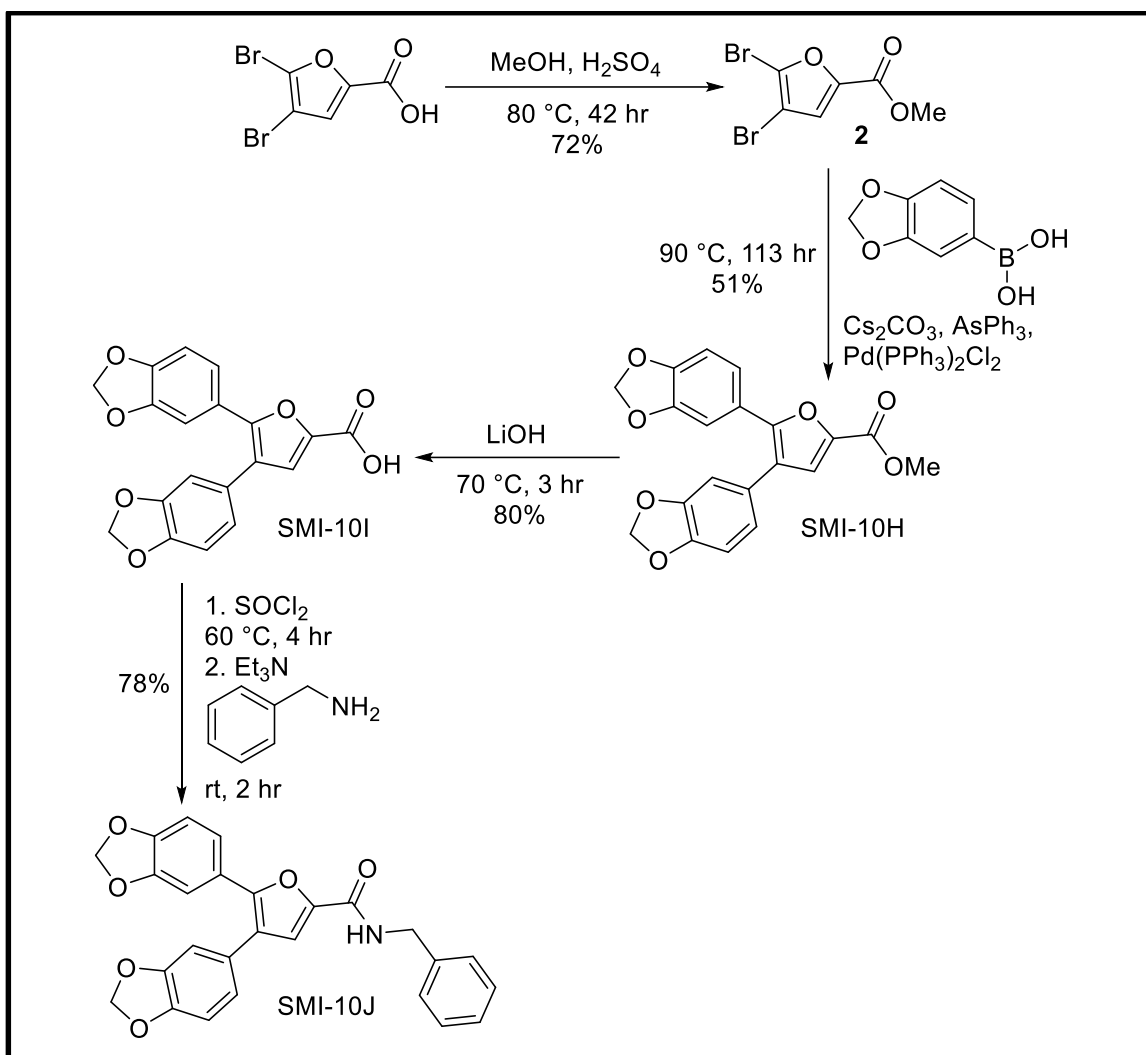


**Scheme 2.9** Synthetic route for SMI-10F and -10G. A Horner-Wadsworth-Emmons olefination reaction with triethyl phosphonoacetate and **1** generated SMI-10F in 40% yield following purification. Saponification of the ester of SMI-10F to the resultant carboxylic acid moiety resulted in the synthesis of SMI-10G.

#### SMI-10H, -10I, and -10J

After several unsuccessful attempts to employ a Suzuki coupling of the commercially available 4,5-dibromo-2-furoic acid with 3,4-methylenedioxyphenyl boronic acid to obtain SMI-10I, it became evident that a new route was necessary. As such, the carboxylic acid moiety on the furoic acid was first converted to an ester, **2**, using an acid-catalyzed Fischer esterification (Thede, 2010). Subsequently, SMI-10H could then be successfully synthesized from the newly generated ester through the aforementioned Suzuki coupling with an un-optimized yield of 51%. SMI-10I was synthesized through saponification of SMI-10H under basic conditions to regenerate the carboxylic acid moiety (Thede, 2010). Following an acidic workup and purification, the product, SMI-10I, was obtained with a yield of 80%. Finally, the synthesis of SMI-10J involved an amidation via an acid chloride intermediate using the procedure of Tang et al. (Tang, 2013). The

carboxylic acid moiety on SMI-10I was first converted to an acid chloride using thionyl chloride and then treated with benzylamine to yield the final amide product, SMI-10J, in 78% yield (Scheme 2.10).

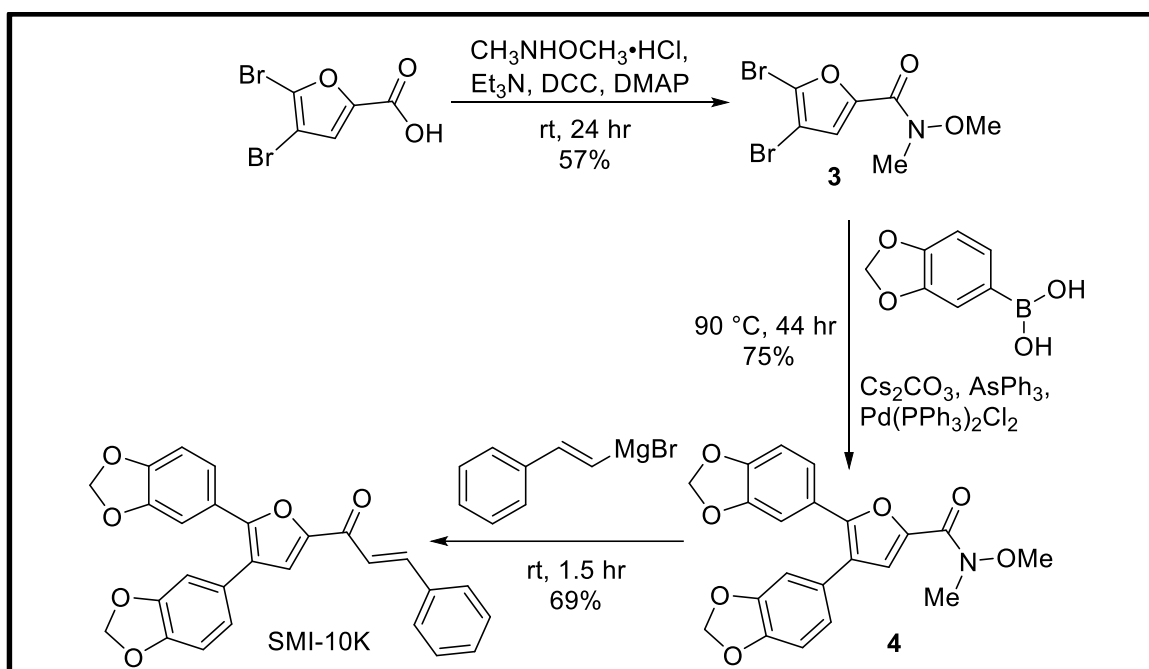


**Scheme 2.10** Synthetic route for SMI-10H, -10I, and -10J. A Fischer esterification was employed to synthesize **2** from the commercially available starting material. Following esterification, a Suzuki coupling was performed to generate SMI-10H, which was subsequently saponified to synthesize SMI-10I. Finally, an amidation reaction via an acid chloride intermediate yielded the final amide product, SMI-10J.

### SMI-10K

Using N,O-dimethylhydroxylamine hydrochloride, the commercially available 4,5-dibromo-2-furoic acid was converted to a Weinreb amide, **3**, in 57% yield. Subsequently,

synthesis of **4** employed a Suzuki coupling with 3,4-methylenedioxyphenyl boronic acid to replace the bromine substituents with benzodioxole side groups. Before synthesis of SMI-10K could be completed, the Grignard reagent was first generated using  $\beta$ -bromostyrene and magnesium. Addition of the resulting Grignard reagent to the Weinreb amide, **4**, resulted in the 69% yield of SMI-10K after purification (Scheme 2.11).



**Scheme 2.11 Synthetic route for SMI-10K.** Formation of the Weinreb amide, **3**, from the 4,5-dibromo-2-furoic acid starting material resulted in a 57% yield. Compound **4** was synthesized via a Suzuki coupling with 3,4-methylenedioxyphenyl boronic acid. After addition of the Grignard reagent synthesized from  $\beta$ -bromostyrene and magnesium, **4** was converted to the enone product, SMI-10K.

### 2.3.2 Predicted Binding Affinity of SMI-10 Analogs

All the second-generation SMI-10 analogs evaluated in the work outlined in this thesis exhibit the same furan core and benzodioxole side groups as that of the original SMI-10 compound. However, the analogs differ from the parent SMI-10 in regard to the side

chain. Therefore, alterations in binding affinity of each analog is a direct result of electrostatic interactions between the side chains and OSM.

Based upon computational modeling of the parent SMI-10 with OSM, there are several potentially important interactions between the side chain and OSM. One such interaction is the capability of the aldimine nitrogen atom on the side chain of SMI-10 to interact with the nearby positively charged K163 amino acid residue on OSM. This interaction suggested that analogs exhibiting an atom with a lone pair of electrons, such as nitrogen, at this location would also be able to interact with this lysine residue and likewise increase binding affinity. Additionally, it was proposed that analogs lacking this feature, but instead containing a pi bond within the side chain, similar to the parent SMI-10, might also be able to interact with the K163 amino acid residue to help stabilize binding, which led to the development of analogs exhibiting this same structural feature. Lastly, it was determined that the side chain of SMI-10 fit into a hydrophobic pocket to allow for better binding, which suggested that analogs designed with similar hydrophobic characteristics would allow for optimal interactions with OSM. Ultimately, analogs that exhibited at least one of these interactions should be able to bind to OSM with an increased binding affinity than that of analogs without any of these interactions (Table 2.1). Specifically, it was computationally predicted that SMI-10C, -10H, and -10I would display the poorest inhibition of OSM due to a lack of the aforementioned electrostatic interactions and the lowest predicted binding affinities of the analogs tested.

**Table 2.2 Electrostatic interactions of SMI-10 analogs.<sup>a</sup>**

SMI-10 Analog	Nitrogen and/or pi bond to interact with K163?	Hydrophobic moiety on end of side chain?	Number of electrostatic interactions?	Predicted binding affinity (kcal/mol)
SMI-10	Yes	Yes	2	-5.9
SMI-10A	Yes	Yes	2	-7.4
SMI-10B	Yes	Yes	2	-6.6
SMI-10C	No	No	0	-6.0
SMI-10D	Yes	Yes	2	-7.3
SMI-10E	Yes	Yes	2	-7.7
SMI-10F	Yes	No	1	-7.4
SMI-10G	Yes	No	1	-6.9
SMI-10H	No	No	0	-6.5
SMI-10I	No	No	0	-6.1
SMI-10J	Yes	Yes	2	-7.3
SMI-10K	Yes	Yes	2	-7.8

<sup>a</sup>Potentially important electrostatic interactions between OSM and the SMI-10 analogs as an indication toward binding affinity. It was suggested that analogs exhibiting at least one of the important interactions would bind to OSM more efficiently than analogs without any of these interactions (results from Matthew King, PhD).

### 2.3.3 OSM Inhibition Assay

The ability of the SMI-10 analogs to disrupt the OSM-OSMR axis and thus inhibit OSM-induced signaling was evaluated using an enzyme-linked immunosorbent assay (ELISA) against both MDA-MB-231 and T47D human breast cancer cell lines (results from Carsten Ashton; unpublished). Specifically, the ELISA measured the OSM-induced relative phosphorylation of STAT3 on Tyr-705 (pSTAT3), which is present within the STAT3 signaling pathway. Consequently, low levels of relative pSTAT3 expression were indicative of an inactivation of the signaling pathway and thus an inactivation of OSM itself.

Based upon the ELISA results, a majority of the second-generation analogs exhibited levels of OSM-induced signaling inhibition surpassing that of the original parent SMI-10 (Figure 2.6). Additionally, the analogs seemed to function at relatively comparable levels of inhibition with the notable exception of SMI-10C, -10H, and -10I, which were less efficient at inhibiting OSM. This exception to the general trend is important due to the fact that the analogs demonstrating the weakest disruption of OSM-induced signaling via the ELISA results were also the analogs predicted computationally to have the weakest binding affinity to OSM. Therefore, the computational predicted binding affinity corresponded well to the experimental data obtained regarding OSM inhibition.

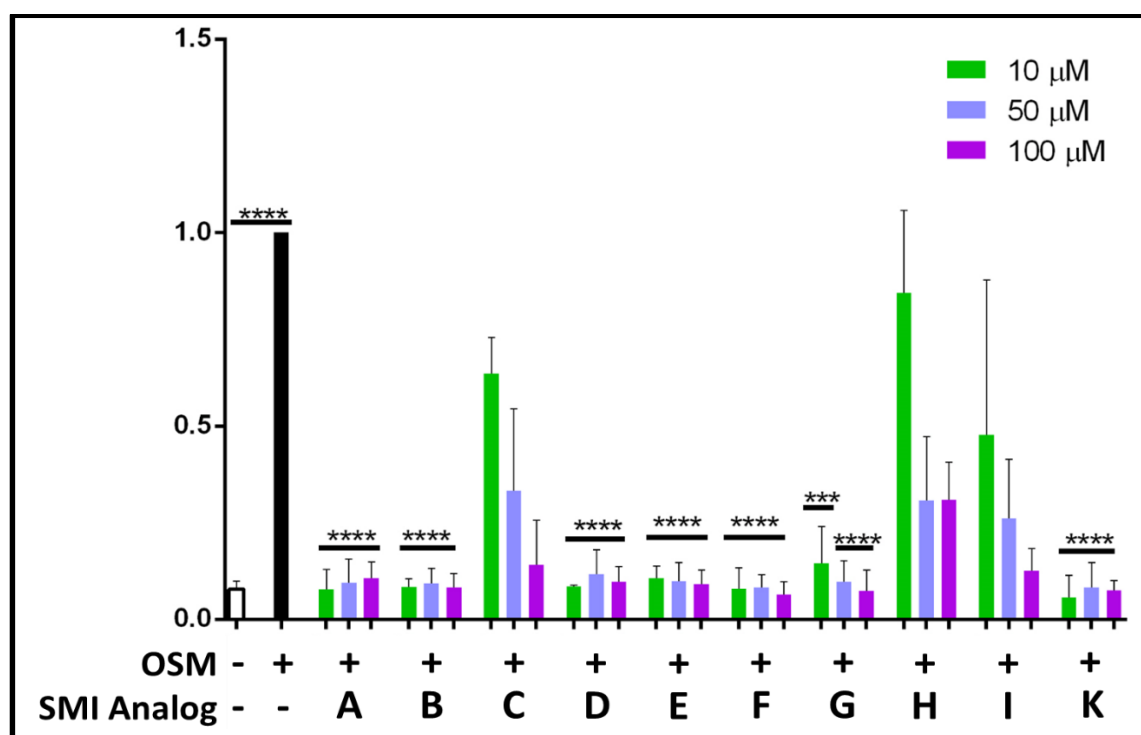


**Figure 2.6 OSM-induced inhibition assay.** T47D human breast cancer cells were treated for 30 minutes after co-incubation of each SMI-10 analog (10  $\mu$ M, 50  $\mu$ M, or 100  $\mu$ M) with OSM (10 ng/mL) in serum-free media for 1 hour at 37  $^{\circ}$ C with 5%  $\text{CO}_2$ . The cells were lysed, collected, and pSTAT3 levels were measured by ELISA. The reduction of pSTAT3 expression by the SMIs is indicative of inhibition of OSM-induced STAT3 signaling (mean  $\pm$  SEM; n=2 for 10  $\mu$ M; n=3 for 50  $\mu$ M and 100  $\mu$ M; \*\*\*p>0.0002; \*\*\*\*p>0.0001; significance determined against positive control; unpaired t-test) (results from Carsten Ashton; unpublished).

## 2.4 Concluding Remarks

Due to the potential of OSM to increase invasiveness, angiogenesis, and metastasis in malignant cells, inhibition of OSM-OSMR interactions has recently been suggested as a targeted therapy treatment method (Caffarel, 2014; Kucia-Tran, 2017; Bembridge, 2017). Based on computational analysis, it was determined that analogs possessing a hydrophobic moiety at the end of the side chain and the ability to interact with the K163 amino acid residue would exhibit an increased binding affinity compared to analogs without these characteristics. Through the use of structure-based drug design, SMI-10 second-generation analogs were designed, synthesized, and preliminarily evaluated for their ability to disrupt the OSM-OSMR axis and thus inhibit OSM-induced signaling. Several of the second-generation analogs were found both computationally and experimentally to be inhibitors of OSM to an even greater extent than that of the original SMI-10 identified through high-throughput virtual screening.

## 2.5 Materials and Methods

### 2.5.1 Materials and Reagents

For SMI-10 analogs, all solvents and reagents were obtained from Alfa Aesar, Acros Organics, Fisher Scientific, EMD Chemical, Sigma-Aldrich, VWR Analytical, Strem Chemicals, TCI Chemicals, or Oakwood Products unless otherwise specified. 4,5-dibromofuran-2-carbaldehyde was supplied from Small Molecules, Inc. 3,4-methylenedioxyphenyl boronic acid was obtained from Combi-Blocks.

For inhibition assays, SMI-10 analogs were diluted to 10  $\mu$ M stock solutions in anhydrous DMSO (obtained from Sigma-Aldrich) and stored at -20 °C. The recombinant human oncostatin M was purchased from PeproTech.

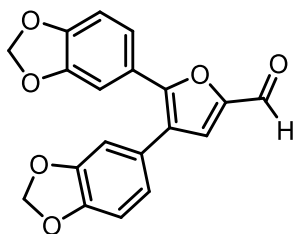
### 2.5.2 Equipment

NMR data was acquired via either a 600 MHz Bruker Avance III 600 coupled with Bruker Ultrashield 600 Plus or a 300 MHz Bruker Ultrashield 300 coupled with Bruker Avance III 300. A Bruker Daltonics maXis quadrupole time-of-flight was used for high resolution mass spectrometry analysis. IR data was obtained using a PerkinElmer FT-IR spectrometer with all samples analyzed using attenuated total reflection.

### 2.5.3 Characterization

All compounds were characterized based upon  $^1\text{H}$  NMR spectroscopy,  $^{13}\text{C}$  NMR spectroscopy, high resolution mass spectrometry (HRMS), and infrared (IR) spectroscopy (Appendix A-D).

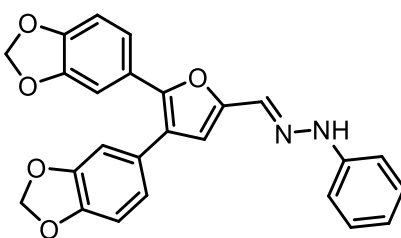
### 2.5.4 SMI-10 Analogs



**1**

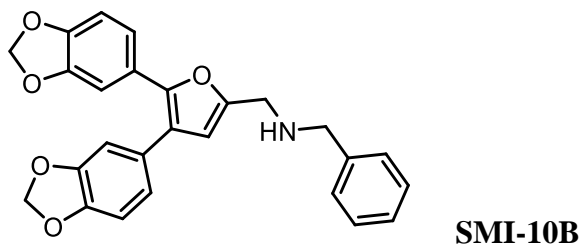
4,5-dibromofuran-2-carbaldehyde (0.990 g, 3.90 mmol) was dissolved in 26 mL dry, distilled DMF into which 3,4-methylenedioxyphenyl boronic acid (1.424 g, 8.58 mmol, 2.2 eq), cesium carbonate (7.624 g, 23.4 mmol, 6 eq), triphenylarsine (0.239 g, 0.78 mmol, 0.2 eq), and bis(triphenylphosphine)palladium(II) dichloride (0.382 g, 0.14 mmol, 0.16 eq) were added under nitrogen atmosphere. The resulting brown solution was allowed to reflux at 90 °C for 23 hours and then concentrated under reduced pressure to remove the excess DMF. The remaining residue was dissolved in 100 mL EtOAc and washed with 3 x 50 mL saturated  $\text{NaHCO}_3$  solution. The organic layer was dried with  $\text{MgSO}_4$ , filtered, and concentrated to yield a brown solid. The crude product was applied to a 7 inch (5 cm)

column containing silica gel eluted with 3:1 hexanes:EtOAc. Fractions containing pure product as determined by TLC (rf = 0.3) were combined and concentrated to yield 1.003 g of orange solid (78% yield).  $^1\text{H}$  NMR ( $\text{CDCl}_3$  with 0.03% v/v TMS, 600 MHz)  $\delta$ : 9.64 (s, 1H), 7.19 (dd, 1H,  $J = 8.3$  Hz, 1.7 Hz), 7.08 (d, 1H,  $J = 1.7$  Hz), 6.85 (s, 2H), 6.82 (s, 1H), 6.78 (d, 1H,  $J = 8.2$  Hz), 6.02 (s, 1H), 5.99 (s, 1H).  $^{13}\text{C}$  NMR ( $\text{CDCl}_3$  with 0.03% v/v TMS, 600 MHz)  $\delta$ : 177.2, 153.9, 150.5, 148.7, 148.1, 147.9, 147.5, 126.1, 125.0, 123.9, 123.3, 122.4, 122.0, 109.1, 108.9, 108.6, 107.4, 101.5, 101.3. HRMS  $m/z$ :  $[\text{M} + \text{H}]^+$  Calcd for  $\text{C}_{19}\text{H}_{12}\text{O}_6$  337.0712; Found 337.0715, Error 0.89 ppm. IR: 2919, 2853  $\text{cm}^{-1}$ .

**SMI-10A**

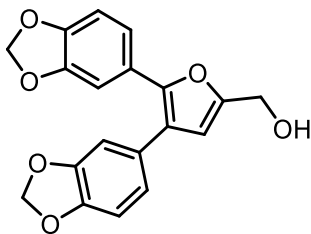
Compound **1** (73.2 mg, 0.22 mmol) was dissolved in 5 mL dry  $\text{CHCl}_3$  along with 4 Å molecular sieves. To the resulting solution was added scandium(III) triflate (1.1 mg, 0.0022 mmol, 0.01 eq) and allowed to stir at rt. After 5 minutes, phenylhydrazine (43  $\mu\text{L}$ , 0.44 mmol, 2 eq) was added and allowed to stir for 15 hours. The resulting solution was filtered using celite, washed with 5 mL  $\text{CHCl}_3$ , and concentrated to yield a red oil. The crude product was applied to a 6 inch (2 cm) column containing silica gel eluted with 6:1 hexanes:EtOAc (rf = 0.3) to yield 51.7 mg of pure product (55% yield).  $^1\text{H}$  NMR ( $\text{DMSO-d}_6$ , 600 MHz)  $\delta$ : 10.44 (s, 1H), 7.78 (s, 1H), 7.23 (t, 2H,  $J = 7.6$  Hz), 7.06-7.04 (m, 3H), 6.99-6.94 (m, 4H), 6.90 (dd, 1H,  $J = 8.0$  Hz, 1.6 Hz), 6.83 (s, 1H), 6.76 (t, 1H,  $J = 7.6$  Hz), 6.07 (s, 2H), 6.06 (s, 2H).  $^{13}\text{C}$  NMR ( $\text{DMSO-d}_6$ , 600 MHz)  $\delta$ : 149.7, 148.0, 147.9, 147.6, 147.1, 145.4, 129.6, 127.4, 127.0, 124.7, 123.4, 122.3, 120.7, 119.4, 113.8, 113.1, 112.5,

109.21, 109.16, 109.1, 106.6, 101.8, 101.6. HRMS  $m/z$ :  $[M + H]^+$  Calcd for  $C_{25}H_{18}N_2O_5$  427.1288; Found 427.1297, Error 2.11 ppm. IR: 2891, 1682, 1600  $cm^{-1}$ .



Compound **1** (60 mg, 0.18 mmol) was dissolved in 2 mL benzene. To this solution was added freshly distilled benzylamine (22  $\mu$ L, 0.20 mmol, 1.1 eq) and allowed to reflux at 85 °C under a nitrogen atmosphere for 4 hours. The reaction was then concentrated under reduced pressure to remove excess benzene and the resulting residue was dissolved in 1 mL MeOH. Sodium cyanoborohydride (17 mg, 0.27 mmol, 1.5 eq) and trifluoroacetic acid (15  $\mu$ L, 0.20 mmol, 1.1 eq) were added to the reaction and allowed to stir at 0 °C. After 30 minutes, the reaction was allowed to warm to rt and continued stirring for 1 hour. The reaction was then concentrated under reduced pressure to remove excess MeOH and the resulting residue was dissolved in 20 mL EtOAc. The solution was washed with 15 mL 1 M NaOH and 15 mL brine. The organic layer was dried with  $MgSO_4$ , filtered, and concentrated to yield a red/orange oil. The crude product was applied to a 6 inch (4 cm) column containing silica gel and eluted with 1:1 hexanes:EtOAc ( $r_f = 0.4$ ) to yield 64.2 mg of pure yellow oil (83% yield).  $^1H$  NMR ( $CDCl_3$  with 0.03% v/v TMS, 600 MHz)  $\delta$ : 7.39-7.30 (m, 4H), 7.30-7.23 (m, 1H), 7.02 (dd, 1H,  $J = 8.1$  Hz, 1.7 Hz), 6.97 (d, 1H,  $J = 1.7$  Hz), 6.87-6.82 (m, 2H), 6.80 (d, 1H,  $J = 8.0$  Hz), 6.75 (d, 1H,  $J = 8.2$  Hz), 6.28 (s, 1H), 5.97 (s, 2H), 5.94 (s, 2H), 3.88 (s, 2H), 3.83 (s, 2H), 1.98 (br, 1H).  $^{13}C$  NMR ( $CDCl_3$  with 0.03% v/v TMS, 600 MHz)  $\delta$ : 152.3, 147.8, 147.6, 147.3, 146.9, 146.7, 139.8, 128.5, 128.3, 128.24, 128.16, 127.1, 125.3, 122.0, 121.6, 120.4, 111.4, 109.1, 108.6, 108.4, 106.9, 101.0,

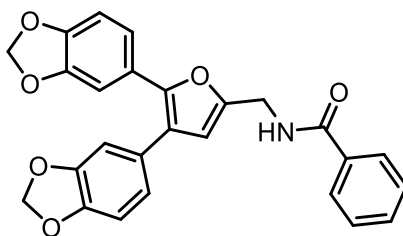
52.9, 45.4. HRMS  $m/z$ :  $[M + H]^+$  Calcd for  $C_{26}H_{21}NO_5$  428.1492; Found 428.1491, Error 0.23 ppm. IR:  $2891\text{ cm}^{-1}$ .



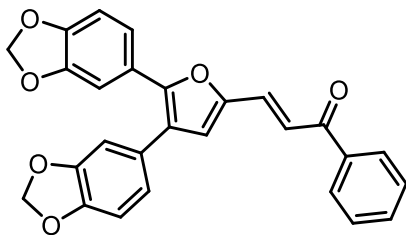
**SMI-10C**

Compound **1** (250 mg, 0.74 mmol) was dissolved in 20 mL MeOH and cooled to 0 °C in an ice bath. Sodium borohydride (33.8 mg, 0.74 mmol, 1 eq) was added portion-wise over 15 minutes. The resulting solution was then allowed to stir at rt for 1 hour. The solution was then once again cooled to 0 °C and sodium borohydride (33.8 mg, 0.74 mmol, 1 eq) was added portion-wise over 15 minutes. The resulting solution was allowed to stir at rt for 1 hour. A final equivalent of sodium borohydride (33.8 mg, 0.74 mmol, 1 eq) was added portion-wise to the solution cooled to 0 °C over 15 minutes. The resulting solution was allowed to stir at rt for 69 hours. To the solution was added 1 mL water and allowed to stir for 30 minutes. The resulting solution was concentrated under reduced pressure to remove excess MeOH and diluted with 30 mL 10% 1 M HCl in water. The reaction was extracted with 3 x 25 mL EtOAc and the organic layers were combined, dried with  $MgSO_4$ , filtered, and concentrated to yield a brown oil. The crude product was applied to a 6 inch (4 cm) column containing silica gel and eluted with 1:1 hexanes:EtOAc ( $r_f = 0.35$ ) to yield 248.0 mg of pure yellow oil (99% yield).  $^1H$  NMR ( $CDCl_3$  with 0.03% v/v TMS, 600 MHz)  $\delta$ : 7.04 (dd, 1H,  $J = 8.3$  Hz, 1.7 Hz), 6.98 (d, 1H,  $J = 1.7$  Hz), 6.85-6.81 (m, 2H), 6.80 (d, 1H,  $J = 8.0$  Hz), 6.74 (d, 1H,  $J = 8.2$  Hz), 6.38 (s, 1H), 5.98 (s, 2H), 5.95 (s, 2H), 4.65 (s, 2H), 1.87 (br, 1H).  $^{13}C$  NMR ( $CDCl_3$  with 0.03% v/v TMS, 600 MHz)  $\delta$ : 152.2, 148.1, 147.8, 147.6, 147.1, 146.8, 127.9, 125.0, 122.1, 121.7, 120.5, 112.2, 109.1, 108.6, 108.4,

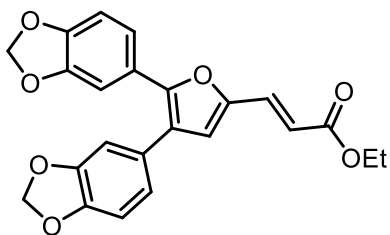
107.0, 101.10, 101.08, 57.6. HRMS  $m/z$ :  $[M + Na]^+$  Calcd for  $C_{19}H_{14}O_6$  361.0682; Found 361.0682, Error 0 ppm. IR:  $3369\text{ cm}^{-1}$ .

**SMI-10D**

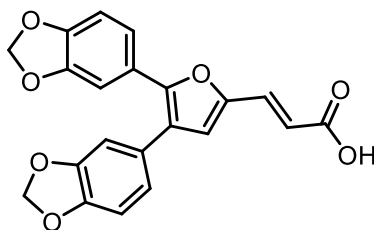
SMI-10C (25 mg, 0.07 mmol) was dissolved in 1 mL dry toluene. Palladium(II) acetate (1.6 mg, 0.007 mmol, 0.1 eq), potassium carbonate (10.6 mg, 0.08 mmol, 1.1 eq), and benzamide (26.9 mg, 0.22 mmol, 3 eq) were added and allowed to reflux at  $150\text{ }^{\circ}\text{C}$  under nitrogen for 11 hours. The reaction was hydrolyzed with 10 mL saturated ammonium chloride solution and extracted with 3 x 10 mL EtOAc. The organic layers were washed with 2 x 10 mL brine, dried with  $\text{MgSO}_4$ , filtered through celite, and concentrated. The crude product was applied to a 6 inch (5 cm) column containing silica gel that was eluted with 3:2 hexanes:EtOAc ( $r_f = 0.36$ ) to yield 27.7 mg pure product (25% yield).  $^1\text{H}$  NMR ( $\text{CDCl}_3$  with 0.03% v/v TMS, 600 MHz)  $\delta$ : 7.81 (d, 2H,  $J = 7.7$  Hz), 7.51 (t, 1H,  $J = 7.4$  Hz), 7.44 ppm (t, 2H,  $J = 7.9$  Hz), 7.02 (dd, 1H,  $J = 8.3$  Hz, 1.7 Hz), 6.96 (d, 1H,  $J = 1.7$  Hz), 6.85-6.81 (m, 2H), 6.79 (d, 1H,  $J = 8.1$  Hz), 6.75 (d, 1H,  $J = 8.3$  Hz), 6.48 (br, 1H), 6.39 (s, 1H), 5.98 (s, 2H), 5.95 (s, 2H), 4.69 (d, 2H,  $J = 5.5$  Hz).  $^{13}\text{C}$  NMR ( $\text{CDCl}_3$  with 0.03% v/v TMS, 600 MHz)  $\delta$ : 167.2, 149.5, 147.9, 147.8, 147.6, 147.2, 146.8, 134.2, 131.7, 128.6, 127.7, 127.0, 125.0, 122.0, 121.8, 120.5, 112.1, 109.1, 108.6, 108.5, 107.0, 101.10, 101.07, 37.1. HRMS  $m/z$ :  $[M + H]^+$  Calcd for  $C_{26}H_{19}NO_6$  442.1285; Found 442.1276, Error 2.04 ppm. IR: 3315,  $1645\text{ cm}^{-1}$ .

**SMI-10E**

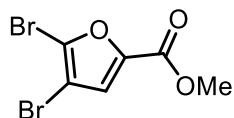
Sodium metal (6.7 mg, 0.29 mmol, 1.2 eq) dissolved in 1 mL THF was added dropwise to diethyl(2-oxo-2-phenylethyl)phosphonate (67  $\mu$ L, 0.31 mmol, 1.3 eq) cooled to 0  $^{\circ}$ C and stirred for 10 minutes. **1** (74 mg, 0.22 mmol) was added and allowed to stir at 0  $^{\circ}$ C for 30 minutes. The ice bath was removed and allowed to stir at rt for 1.5 hours. The resulting solution was diluted with 10 mL Et<sub>2</sub>O and washed with 15 mL saturated NaHCO<sub>3</sub> solution and 15 mL brine. The organic layer was dried with MgSO<sub>4</sub>, filtered, and concentrated to yield an orange solid. The crude product was applied to a 6 inch (2 cm) column containing silica gel and eluted with 3:1 hexanes:EtOAc (rf = 0.7) to yield 72.0 mg of pure yellow solid (75% yield). <sup>1</sup>H NMR (CDCl<sub>3</sub> with 0.03% v/v TMR, 600 MHz)  $\delta$ : 8.09 (d, 2H,  $J$  = 7.7 Hz), 7.64-7.60 (m, 2H), 7.55-7.51 (m, 3H), 7.18 (dd, 1H,  $J$  = 9.8 Hz, 1.6 Hz), 7.12 (d, 1H,  $J$  = 1.6 Hz), 6.90 (dd, 1H,  $J$  = 7.7 Hz, 1.9 Hz), 6.85 (d, 2H,  $J$  = 7.9 Hz), 6.81 (d, 2H,  $J$  = 9.7 Hz), 6.03 (s, 2H), 6.02 (s, 2H). <sup>13</sup>C NMR (CDCl<sub>3</sub> with 0.03% v/v TMS, 600 MHz)  $\delta$ : 189.7, 150.7, 149.7, 148.0, 147.8, 147.2, 138.3, 132.7, 130.3, 128.6, 128.4, 126.9, 124.3, 124.2, 122.2, 121.2, 120.7, 118.8, 109.1, 108.8, 108.6, 107.1, 101.3, 101.2. HRMS  $m/z$ : [M + H]<sup>+</sup> Calcd for C<sub>27</sub>H<sub>18</sub>O<sub>6</sub> 439.1176; Found 439.1171, Error 1.14 ppm. IR: 1658 cm<sup>-1</sup>.

**SMI-10F**

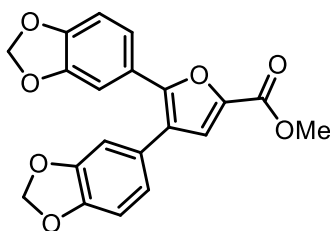
Sodium metal (15 mg, 0.66 mmol, 1.5 eq) dissolved in 5 mL EtOH was allowed to stir at 0 °C for 10 minutes. Triethyl phosphonoacetate (122  $\mu$ L, 0.62 mmol, 1.4 eq) and **1** (148 mg, 0.44 mmol) were added to the solution and allowed to stir at rt for 167 hours until disappearance of starting material as seen by TLC. The reaction was quenched with the dropwise addition of 3 mL saturated ammonium chloride solution until a precipitate formed. The resulting reaction was diluted with 15 mL water and extracted with 3 x 10 mL DCM. The organic layers were combined, dried with MgSO<sub>4</sub>, filtered, and concentrated to yield a dark yellow oil. The crude product was applied to a 6 inch (4 cm) column containing silica gel and eluted with 5:1 hexanes:Et<sub>2</sub>O (rf = 0.31) to yield 71.9 mg of yellow oil (40% yield). <sup>1</sup>H NMR (CDCl<sub>3</sub> with 0.03% v/v TMS, 600 MHz)  $\delta$ : 7.42 (d, 1H, *J* = 15.6 Hz), 7.10 (dd, 1H, *J* = 8.3 Hz, 1.6 Hz), 7.02 (d, 1H, *J* = 1.6 Hz), 6.86-6.80 (m, 3H), 6.76 (d, 1H, *J* = 8.1 Hz), 6.65 (s, 1H), 6.38 (d, 1H, *J* = 15.9 Hz), 5.99 (s, 2H), 5.97 (s, 2H), 4.26 (q, 2H, *J* = 7.0 Hz), 1.34 (t, 3H, *J* = 7.0 Hz). <sup>13</sup>C NMR (CDCl<sub>3</sub> with 0.03% v/v TMS, 600 MHz)  $\delta$ : 167.1, 150.3, 148.9, 147.9, 147.8, 147.7, 147.2, 130.5, 127.0, 124.3, 123.8, 122.2, 121.0, 119.0, 115.5, 109.1, 108.7, 108.5, 106.9, 101.3, 101.2, 60.5, 14.4. HRMS *m/z*: [M + H]<sup>+</sup> Calcd for C<sub>23</sub>H<sub>18</sub>O<sub>7</sub> 407.1125; Found 407.1117, Error 1.96 ppm. IR: 1702, 1009 cm<sup>-1</sup>.

**SMI-10G**

SMI-10F (45.4 mg, 0.11 mmol) was dissolved in 1 mL EtOH. To the resulting solution was added dropwise 1 M NaOH (0.44 mL, 0.44 mmol, 4 eq) and allowed to stir at rt for 30 minutes. The solution was allowed to reflux at 85 °C for 4 hours and continued stirring for 18 hours at rt. The reaction was quenched with 5 mL water and extracted with 2 x 5 mL Et<sub>2</sub>O. The aqueous layer was collected and acidified with 5 mL concentrated HCl until a precipitate formed. The solid was collected, dissolved in 10 mL Et<sub>2</sub>O, dried with MgSO<sub>4</sub>, filtered, and concentrated. The crude product was applied to a preparative TLC plate (20 cm x 20 cm x 1 mm) and eluted with 1:1 hexanes:EtOAc (rf = 0.3) to yield 9.5 mg of product (21% yield). <sup>1</sup>H NMR (CDCl<sub>3</sub> with 0.03% v/v TMS, 600 MHz) δ: 11.22 (br, 1H), 7.52 (d, 1H, *J* = 15.5 Hz), 7.14 (dd, 1H, *J* = 8.2 Hz, 1.5 Hz), 7.06 (d, 1H, *J* = 1.3 Hz), 6.88-6.84 (m, 3H), 6.79 (d, 1H, *J* = 8.4 Hz), 6.75 (s, 1H), 6.42 (d, 1H, *J* = 15.6 Hz), 6.03 (s, 2H), 6.01 (s, 2H). <sup>13</sup>C NMR (Acetone-d<sub>6</sub>, 600 MHz) δ: 168.1, 151.4, 150.3, 149.42, 149.37, 149.3, 148.7, 131.9, 128.3, 125.5, 125.2, 123.5, 122.2, 120.5, 116.9, 110.1, 109.9, 109.7, 107.9, 102.9, 102.7. HRMS *m/z*: [M + H]<sup>+</sup> Calcd for C<sub>21</sub>H<sub>14</sub>O<sub>7</sub> 379.0812; Found 379.0815, Error 0.79 ppm. IR: 2902 cm<sup>-1</sup>.

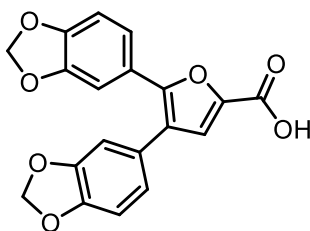
**2**

4,5-dibromo-2-furoic acid (300 mg, 1.11 mmol) was dissolved in 2.8 mL MeOH. To the resulting solution was added dropwise concentrated sulfuric acid (63  $\mu$ L, 1.22 mmol, 1.1 eq) and allowed to reflux at 80  $^{\circ}$ C under a nitrogen atmosphere for 42 hours. The solution was concentrated under reduced pressure to remove excess MeOH and quenched with 15 mL saturated NaHCO<sub>3</sub> solution until a basic pH was obtained. The aqueous layers were extracted with 2 x 20 mL EtOAc. The organic layers were combined, washed with 20 mL DI water, dried with MgSO<sub>4</sub>, filtered, and concentrated to yield a white powder. The resulting product was carried on without further purification (72% yield). <sup>1</sup>H NMR (CDCl<sub>3</sub> with 0.03% v/v TMS, 600 MHz)  $\delta$ : 7.18 (s, 1H), 3.90 (s, 3H). <sup>13</sup>C NMR (CDCl<sub>3</sub> with 0.03% v/v TMS, 600 MHz)  $\delta$ : 157.3, 145.9, 128.4, 121.9, 103.8, 52.4. HRMS m/z: [M + H]<sup>+</sup> Calcd for C<sub>6</sub>H<sub>4</sub>Br<sub>2</sub>O<sub>3</sub> 284.8580; Found 284.8586, Error 2.11 ppm. IR: 1717 cm<sup>-1</sup>.

**SMI-10H**

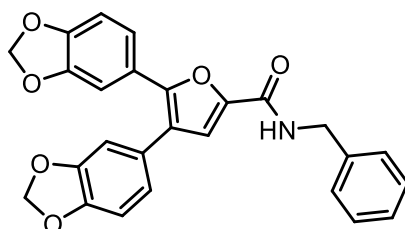
Compound **2** (0.5 g, 1.76 mmol), 3,4-methylenedioxyphenyl boronic acid (642.9 mg, 3.87 mmol, 2.2 eq), cesium carbonate (3.441 g, 10.6 mmol, 6 eq), triphenylarsine (107.8 mg, 0.35 mmol, 0.2 eq), and bis(triphenylphosphine)palladium(II) dichloride (197.7 mg, 0.28 mmol, 0.16 eq) were combined in a flask that had been evacuated and refilled with nitrogen (5 cycles). The resulting mixture was dissolved in 12 mL dry, distilled DMF

and allowed to reflux at 90 °C under an argon atmosphere for 113 hours. The reaction was concentrated under reduced pressure to remove excess DMF. The resulting residue was dissolved in 50 mL EtOAc and washed with 3 x 50 mL saturated NaHCO<sub>3</sub> solution. The aqueous layers were extracted with 3 x 30 mL EtOAc. The organic layers were combined, dried with MgSO<sub>4</sub>, filtered, and concentrated to yield a yellow/brown oil. The crude product was applied to a 6 inch (6 cm) column containing silica gel and eluted with 3:1 hexanes:EtOAc (rf = 0.3) to yield 331.3 mg of pure product (51% yield). <sup>1</sup>H NMR (CDCl<sub>3</sub> with 0.03% v/v TMS, 600 MHz) δ: 7.24 (s, 1H), 7.17 (dd, 1H, *J* = 8.2 Hz, 1.7 Hz), 7.08 (d, 1H, *J* = 1.6 Hz), 6.87 (dd, 1H, *J* = 8.0 Hz, 1.5 Hz), 6.85 (s, 1H), 6.84 (s, 1H), 6.79 (d, 1H, *J* = 8.5 Hz), 6.02 (s, 2H), 6.00 (s, 2H), 3.94 (s, 3H). <sup>13</sup>C NMR (CDCl<sub>3</sub> with 0.03% v/v TMS, 600 MHz) δ: 159.2, 151.9, 148.2, 148.0, 147.7, 147.3, 142.2, 126.6, 123.8, 123.0, 122.3, 121.7, 121.6, 109.1, 108.8, 108.5, 107.4, 101.3, 101.2, 51.9. HRMS *m/z*: [M + H]<sup>+</sup> Calcd for C<sub>20</sub>H<sub>14</sub>O<sub>7</sub> 367.0812; Found 367.0803, Error 2.45 ppm. IR: 1712 cm<sup>-1</sup>.

**SMI-10I**

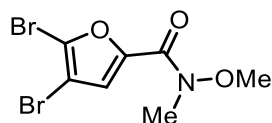
SMI-10H (180 mg, 0.49 mmol) was dissolved in 4.6 mL THF and 1.4 mL water into which was added lithium hydroxide (117 mg, 4.9 mmol, 10 eq) and allowed to reflux at 70 °C for 3 hours. The reaction was diluted with 5 mL water and quenched with 6 mL 1 M HCl until an acidic pH was obtained. The resulting solution was extracted with 3 x 15 mL EtOAc. The organic layers were combined, washed with 2 x 20 mL water, dried with MgSO<sub>4</sub>, filtered, and concentrated to yield 138.8 mg of a pale yellow solid that was carried on without further purification (80% yield). <sup>1</sup>H NMR (DMSO-d<sub>6</sub>, 600 MHz) δ: 13.18 (br,

1H), 7.36 (s, 1H), 7.03 (dd, 1H,  $J = 7.9$  Hz, 1.6 Hz), 6.99 (d, 1H,  $J = 8.4$  Hz), 6.97-6.95 (m, 3H) 6.88 (dd, 1H,  $J = 8.2$  Hz, 1.8 Hz), 6.08 (s, 2H), 6.07 (s, 2H).  $^{13}\text{C}$  NMR ( $\text{CDCl}_3$  with 0.03% v/v TMS, 600 MHz)  $\delta$ : 159.8, 151.0, 148.4, 148.1, 148.0, 147.3, 126.5, 123.9, 123.2, 122.5, 121.7, 121.2, 111.0, 109.3, 109.23, 109.19, 107.1, 102.0, 101.7. HRMS  $m/z$ :  $[\text{M} + \text{H}]^+$  Calcd for  $\text{C}_{19}\text{H}_{12}\text{O}_7$  353.0656; Found 353.0653, Error 0.85 ppm. IR: 2917, 1667, 1196  $\text{cm}^{-1}$ .

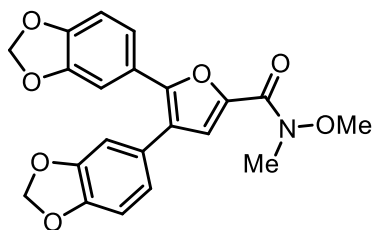
**SMI-10J**

SMI-10I (50 mg, 0.14 mmol) was dissolved in 1 mL DCM and 5 drops DMF into which was added thionyl chloride (21  $\mu\text{L}$ , 0.28 mmol, 2 eq) and allowed to reflux at 60  $^{\circ}\text{C}$  for 4 hours. The resulting solution was concentrated under reduced pressure to remove excess DCM. The resulting residue was dissolved in 1 mL  $\text{Et}_2\text{O}$ . To the reaction were added benzylamine (31  $\mu\text{L}$ , 0.28 mmol, 2 eq) and triethylamine (39  $\mu\text{L}$ , 0.28 mmol, 2 eq) and allowed to stir at rt under a nitrogen atmosphere for 2 hours. The solution was diluted with 10 mL water and extracted with 3 x 10 mL  $\text{Et}_2\text{O}$ . The organic layers were combined, dried with  $\text{MgSO}_4$ , filtered, and concentrated. The crude product was applied to a 7 inch (2 cm) column containing silica gel and eluted with 3:2 hexanes:EtOAc ( $r_f = 0.15$ ) to yield 48.2 mg of pure product (78% yield).  $^1\text{H}$  NMR ( $\text{CDCl}_3$  with 0.03% v/v TMS, 600 MHz)  $\delta$ : 7.39-7.33 (m, 4H), 7.31-7.27 (m, 1H), 7.20 (s, 1H), 7.02 (dd, 1H,  $J = 8.3$  Hz, 1.7 Hz), 6.95 (d, 1H,  $J = 1.7$  Hz), 6.84-6.78 (m, 3H), 6.77-6.72 (m, 2H), 5.97 (s, 2H), 5.94 (s, 2H), 4.65 (d, 2H,  $J = 6.1$  Hz).  $^{13}\text{C}$  NMR ( $\text{CDCl}_3$  with 0.03% v/v TMS, 600 MHz)  $\delta$ : 158.4, 149.8, 148.1, 148.0, 147.8, 147.3, 145.6, 138.2, 128.9, 128.0, 127.7, 126.7, 124.0, 123.5, 122.3, 121.4,

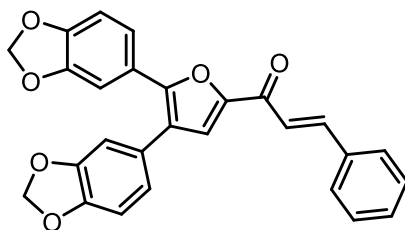
118.4, 109.1, 108.8, 108.6, 107.4, 101.4, 101.3, 43.3. HRMS  $m/z$ :  $[M + H]^+$  Calcd for  $C_{26}H_{19}NO_6$  442.1285; Found 442.1291, Error 1.36 ppm. IR:  $3252\text{ cm}^{-1}$ .

**3**

4,5-dibromo-2-furoic acid (996 mg, 3.69 mmol) was dissolved in 25 mL DCM into which were added N,O-dimethylhydroxylamine hydrochloride (414 mg, 4.24 mmol, 1.15 eq), triethylamine (0.56 mL, 4.06 mmol, 1.1 eq), 1,3-dicyclohexylcarbodiimide (761 mg, 3.69 mmol, 1 eq), and dimethylaminopyridine (235 mg, 1.85 mmol, 0.5 eq) and allowed to stir for 24 hours. The solid precipitate that formed was collected through gravity filtration, washed with DCM, and concentrated under reduced pressure. The resulting residue was dissolved in 30 mL EtOAc and washed with 25 mL brine, 25 mL saturated  $\text{NaHCO}_3$  solution, and 25 mL water. The organic layer was dried with sodium sulfate, filtered, and concentrated to yield a white solid. The crude product was applied to a 6 inch (4.5 cm) column containing silica gel and eluted with a gradient of 3:1 hexanes:EtOAc (1200 mL) followed by 1:1 hexanes:EtOAc (600 mL) ( $r_f = 0.44$ ) to yield 663 mg of pure product (57% yield).  $^1\text{H NMR}$  ( $\text{CDCl}_3$  with 0.03% v/v TMS, 600 MHz)  $\delta$ : 7.14 (s, 1H), 3.77 (s, 3H), 3.33 (s, 3H).  $^{13}\text{C NMR}$  ( $\text{CDCl}_3$  with 0.03% v/v TMS, 600 MHz)  $\delta$ : 157.1, 147.3, 127.5, 121.6, 103.4, 61.6, 33.1. HRMS  $m/z$ :  $[M + H]^+$  Calcd for  $C_7H_7Br_2NO_3$  313.8845; Found 313.8864, Error 6.05 ppm. IR:  $3165, 1639\text{ cm}^{-1}$ .

**4**

Compound **3** (313 mg, 1.0 mmol) was dissolved in 7.6 mL dry, distilled DMF. To the resulting solution were added 3,4-methylenedioxyphenyl boronic acid (365 mg, 2.2 mmol, 2.2 eq), cesium carbonate (1.95 g, 6 mmol, 6 eq), triphenylarsine (61 mg, 0.2 mmol, 0.2 eq), and bis(triphenylphosphine)palladium(II) dichloride (112 mg, 0.16 mmol, 0.16 eq) and allowed to reflux at 90 °C under a nitrogen atmosphere for 44 hours. The reaction was concentrated under reduced pressure to remove excess DMF. The resulting residue was dissolved in 100 mL EtOAc and washed with 3 x 50 mL 25% NaHCO<sub>3</sub> solution. The organic layer was dried with MgSO<sub>4</sub>, filtered, and concentrated to yield a brown solid. The crude product was applied to a 8 inch (4 cm) column containing silica gel and eluted with a gradient of 1:1 hexanes:EtOAc (600 mL) (rf = 0.3) followed by 3:1 hexanes:EtOAc (1500 mL) to yield 297.8 mg of pure yellow, solid product (75% yield). <sup>1</sup>H NMR (CDCl<sub>3</sub> with 0.03% v/v TMS, 600 MHz) δ: 7.21 (s, 1H), 7.16 (d, 1H, *J* = 8.0 Hz), 7.08 (s, 1H), 6.89-6.84 (m, 3H), 6.79 (d, 1H, *J* = 8.0 Hz), 6.02 (s, 2H), 5.99 (s, 2H), 3.84 (s, 3H), 3.39 (s, 3H). <sup>13</sup>C NMR (CDCl<sub>3</sub> with 0.03% v/v TMS, 600 MHz) δ: 159.2, 150.7, 147.9, 147.7, 147.2, 143.6, 127.0, 124.1, 122.7, 122.3, 121.44, 121.43, 109.2, 108.73, 108.69, 108.5, 107.3, 101.3, 101.2, 61.5, 33.4. HRMS *m/z*: [M + H]<sup>+</sup> Calcd for C<sub>21</sub>H<sub>17</sub>NO<sub>7</sub> 396.1078; Found 396.1092, Error 3.53. IR: 1640 cm<sup>-1</sup>.

**SMI-10K**

B-bromostyrene (0.97 mL, 7.59 mmol, 50 eq)—that was dried in a 1.5 inch (1 cm) column containing sodium sulfate and neutral alumina—was dissolved in 7 mL dry THF and purged with nitrogen. The resulting solution was cannulated to a second flask also purged with nitrogen containing 3 crystals of iodine and magnesium (199 mg, 8.19 mmol, 55 eq) that had been crushed with a mortar and pestle. The original flask was rinsed with 3 mL dry THF and cannulated to the flask containing magnesium and iodine. The resulting solution was allowed to reflux at 50 °C under a nitrogen atmosphere for 3 hours to synthesize the Grignard reagent.

Compound **4** (60 mg, 0.15 mmol) was dissolved in 3 mL of the newly synthesized Grignard reagent and allowed to stir at rt under a nitrogen atmosphere for 1.5 hours. The reaction was quenched with 10 mL saturated ammonium chloride solution. The reaction was diluted with 5 mL water and extracted with 2 x 10 mL Et<sub>2</sub>O. The organic layers were combined and washed with 10 mL saturated NaHCO<sub>3</sub> solution, 10 mL 1 M HCl, and 10 mL brine. The organic layers were then dried with MgSO<sub>4</sub>, filtered, and concentrated to yield a bright yellow oil. The crude product was applied to a 6 inch (5 cm) column containing silica gel and eluted with 3:1 hexanes:EtOAc (rf = 0.32) to yield 45.4 mg of pure yellow oil (69% yield). <sup>1</sup>H NMR (CDCl<sub>3</sub> with 0.03% v/v TMS, 600 MHz) δ: 7.90 (d, 1H, *J* = 16.0 Hz), 7.69-7.65 (m, 2H), 7.49 (d, 1H, *J* = 15.6 Hz), 7.45-7.40 (m, 3H), 7.37 (s, 1H), 7.20 (dd, 1H, *J* = 8.2 Hz, 1.7 Hz), 7.12 (d, 1H, *J* = 1.7 Hz), 6.88 (dd, 1H, *J* = 8.1 Hz, 1.8 Hz), 6.86-6.83 (m, 2H), 6.80 (d, 1H, *J* = 8.2 Hz), 6.00 (s, 2H), 5.99 (s, 2H). <sup>13</sup>C NMR

(CDCl<sub>3</sub> with 0.03% v/v TMS, 600 MHz)  $\delta$ : 177.5, 152.4, 151.4, 148.4, 148.0, 147.8, 147.4, 143.6, 134.9, 130.6, 129.0, 128.6, 126.5, 124.1, 123.7, 122.4, 121.9, 121.5, 121.2, 109.2, 108.8, 108.6, 107.4, 101.4, 101.3. HRMS m/z: [M + H]<sup>+</sup> Calcd for C<sub>27</sub>H<sub>18</sub>O<sub>6</sub> 439.1176; Found 439.1194, Error 4.10 ppm. IR: 1723 cm<sup>-1</sup>.

#### 2.5.5 Cell Cultures

Both the MDA-MB-231 and T47D cell lines were obtained from American Type Culture Collection. Cells were incubated at 37 °C in a humidified atmosphere containing 5% CO<sub>2</sub>. The cell lines were maintained in RPMI-1640 medium supplemented with 10% (v/v) fetal clone III and 1% penicillin/streptomycin.

#### 2.5.6 OSM Inhibition Assays

SMI-10 induced inhibition of pSTAT3 was determined through an ELISA against both MDA-MB-231 and T47D human breast cancer cell lines. Cells were serum starved for 4 hours. SMI-10 analogs (10  $\mu$ M, 50  $\mu$ M, or 100  $\mu$ M) and human recombinant OSM (10 ng/mL) were incubated in serum-free RPMI-1640 medium at 37 °C and 5% CO<sub>2</sub>. After incubation, the SMI-10 analogs and OSM were added to the serum starved cells for 30 minutes. Cells were lysed using a 1x PathScan Sandwich ELISA Lysis buffer (CST #7018S) for 15 minutes after which the lysates were collected and stored at -20 °C. Lysates were analyzed for pSTAT3 expression using a PathScan Phospho-Stat3 (Tyr705) Sandwich ELISA Antibody Pair kit (CST #7146). pSTAT3 expression was measured with absorbance at 450nm and quantified by comparison relative to OSM-induced pSTAT3 expression.

## 2.6 References

- Allen, C. L., Atkinson, B. N., & Williams, J. M. (2012). Transamidation of primary amides with amines using hydroxylamine hydrochloride as an inorganic catalyst. *Angewandte Chemie International Edition*, 51(6), 1383-1386.
- Anderson, K. N., Schwab, R. B., & Martinez, M. E. (2014). Reproductive risk factors and breast cancer subtypes: a review of the literature. *Breast Cancer Research and Treatment*, 144(1), 1-10.
- Bembridge, G. P., Chung, C. W., Ford, S. K., Kirby, I., McAdam, R., & Feeney, M. (2017). *U.S. Patent No. 9,605,063*. Washington, DC: U.S. Patent and Trademark Office.
- Bolin, C., Tawara, K., Sutherland, C., Redshaw, J., Aranda, P., Moselhy, J., Anderson, R., & Jorcyk, C. L. (2012). Oncostatin m promotes mammary tumor metastasis to bone and osteolytic bone degradation. *Genes & Cancer*, 3(2), 117-130.
- Caffarel, M. M., & Coleman, N. (2014). Oncostatin M receptor is a novel therapeutic target in cervical squamous cell carcinoma. *The Journal of Pathology*, 232(4), 386-390.
- Chen, X., Wang, H., Ou-yang, X. N., Xie, F. W., & Wu, J. J. (2013). Research on drug resistance mechanism of trastuzumab caused by activation of the PI3K/Akt signaling pathway. *Contemporary Oncology*, 17(4), 363.
- De Roulet, D., & DeVita, R. (2017). U.S. Patent Application No. 15/118,465.
- Emens, L. A., & Davidson, N. E. (2004). Trastuzumab in breast cancer. *Oncology*, 18(9), 1117-28.
- Finn, R. S., Aleshin, A., & Slamon, D. J. (2016). Targeting the cyclin-dependent kinases (CDK) 4/6 in estrogen receptor-positive breast cancers. *Breast Cancer Research*, 18(1), 17.
- Furrow, M. E., & Myers, A. G. (2004). Practical procedures for the preparation of N-tert-butyltrimethylsilylhydrazones and their use in modified Wolff-Kishner reductions and in the synthesis of vinyl halides and gem-dihalides. *Journal of the American Chemical Society*, 126(17), 5436-5445.

- Guo, L., Chen, C., Shi, M., Wang, F., Chen, X., Diao, D., Hu, M., Yu, M., Qian, L. & Guo, N. (2013). Stat3-coordinated Lin-28–let-7–HMGA2 and miR-200–ZEB1 circuits initiate and maintain oncostatin M-driven epithelial–mesenchymal transition. *Oncogene*, 32(45), 5272.
- Hahne, J. C., Engel, J. B., Honig, A., Meyer, S. R., Zito, D., Lampis, A., & Valeri, N. (2017). The PI3K/AKT/mTOR-signal transduction pathway as drug target in triple-negative breast cancer. *Clinical Cancer Drugs*, 4(1), 47-58.
- Heinrich, P. C., Behrmann, I., Serge, H., Hermanns, H. M., Müller-Newen, G., & Schaper, F. (2003). Principles of interleukin (IL)-6-type cytokine signalling and its regulation. *Biochemical Journal*, 374(1), 1-20.
- Howlader, N., Noone, A. M., & Krapcho, M. (2016). SEER Cancer Statistics Review, 1975-2013. *National Cancer Institute*.
- Howlader, N., Noone, A. M., & Krapcho, M. (2017). SEER Cancer Statistics Review, 1975-2014. *National Cancer Institute*.
- Ireland, L., Santos, A., Campbell, F., Figueiredo, C., Hammond, D., Ellies, L. G., Weyer-Czernilofsky, U., Bogenrieder, T., Schmid, M., & Mielgo, A. (2018). Blockade of insulin-like growth factors increases efficacy of paclitaxel in metastatic breast cancer. *Oncogene*, 37(15), 2022.
- Jorcyk, C. L., Holzer, R. G., & Ryan, R. E. (2006). Oncostatin M induces cell detachment and enhances the metastatic capacity of T-47D human breast carcinoma cells. *Cytokine*, 33(6), 323-336.
- Knüpfner, H., & Preib, R. (2007). Significance of interleukin-6 (IL-6) in breast cancer. *Breast Cancer Research and Treatment*, 102(2), 129-135.
- Kossler, D., & Cramer, N. (2015). Chiral cationic Cp<sup>x</sup>Ru(II) complexes for enantioselective yne-enone cyclizations. *Journal of the American Chemical Society*, 137(39), 12478-12481.
- Kuang, R., Blythin, D., Shih, N., Shue, H., Chen, X., Cao, J., & Wong, C. (2005). Preparation of substituted 2-quinolyl-oxazoles and their heterocyclic analogs useful as PDE4 inhibitors. *WO20055116009*.

- Kucia-Tran, J. A., Tulkki, V., Scarpini, C. G., Smith, S., Wallberg, M., Paez-Ribes, M., Araujo, A. M., Botthoff, J., Feeney, M., Hughes, K., Caffarel, M. M., & Coleman, N. (2018). Anti-oncostatin M antibody inhibits the pro-malignant effects of oncostatin M receptor overexpression in squamous cell carcinoma. *The Journal of Pathology*, *244*(3), 283-295.
- Liu, J., Hadjokas, N., Mosley, B., Estrov, Z., Spence, M. J., & Vestal, R. E. (1998). Oncostatin M-specific receptor expression and function in regulating cell proliferation of normal and malignant mammary epithelial cells. *Cytokine*, *10*(4), 295-302.
- Mariotto, A. B., Etzioni, R., Hurlbert, M., Penberthy, L., & Mayer, M. (2017). Estimation of the number of women living with metastatic breast cancer in the United States. *Cancer Epidemiology and Prevention Biomarkers*, *26*(6), 809-815.
- Marquette, C., & Nabell, L. (2012). Chemotherapy-resistant metastatic breast cancer. *Current Treatment Options in Oncology*, *13*(2), 263-275.
- Martínez-Asencio, A., Yus, M., & Ramon, D. J. (2011). Palladium (II) acetate as catalyst for the N-alkylation of aromatic amines, sulfonamides, and related nitrogenated compounds with alcohols by a hydrogen autotransfer process. *Synthesis*, *2011*(22), 3730-3740.
- Meng, X., Cai, C., Wu, J., Cai, S., Ye, C., Chen, H., Yang, Z., Zeng, H., Shen, Q., & Zou, F. (2013). TRPM7 mediates breast cancer cell migration and invasion through the MAPK pathway. *Cancer Letters*, *333*(1), 96-102.
- Mestres, J. A., iMolins, A. B., Martínez, L. C., López-Muñiz, J. I. C., Gil, E. C., de Juan Ferré, A., del Barco Berrón, S., Perez, Y. F., Mata, J. G., Palomo, A. G., Gregori, J. G., Pardo, P. G., Manas, J. J. I., Hernandez, A. L., de Duenas, E. M., Janez, N. M., Murillo, S. M., Bofill, J. S., Aunon, P. Z., & Sanchez-Rovira, P. (2017). Defining the optimal sequence for the systemic treatment of metastatic breast cancer. *Clinical and Translational Oncology*, *19*(2), 149-161.
- O'Brien, M. E. R., Wigler, N., Inbar, M., Rosso, R., Grischke, E., Santoro, A., Catane, R., Kieback, D. G., Tomczak, P., Ackland, S. P., Orlandi, F., Mellars, L., Alland, L.,

- & Tendler, C. (2004). Reduced cardiotoxicity and comparable efficacy in a phase III trial of pegylated liposomal doxorubicin HCl (CAELYX™/Doxil®) versus conventional doxorubicin for first-line treatment of metastatic breast cancer. *Annals of Oncology*, *15*(3), 440-449.
- Ouairy, C., Michel, P., Delpech, B., Crich, D., & Marazano, C. (2010). Synthesis of N-acyl-5-aminopenta-2, 4-dienals via base-induced ring-opening of N-acylated furfurylamines: scope and limitations. *Journal of Organic Chemistry*, *75*(12), 4311-4314.
- Queen, M. M., Ryan, R. E., Holzer, R. G., Keller-Peck, C. R., & Jorcyk, C. L. (2005). Breast cancer cells stimulate neutrophils to produce oncostatin M: potential implications for tumor progression. *Cancer Research*, *65*(19), 8896-8904.
- Sharp, A., & Harper-Wynne, C. (2014). Treatment of advanced breast cancer (ABC): the expanding landscape of targeted therapies. *Journal of Cancer Biology & Research*, *2*, 1036.
- Siegel, R. L., Miller, K. D., & Jemal, A. (2018). Cancer statistics, 2018. *CA: A Cancer Journal for Clinicians*.
- Smith, S. M., Lyu, Y. L., & Cai, L. (2014). NF- $\kappa$ B affects proliferation and invasiveness of breast cancer cells by regulating CD44 expression. *PloS One*, *9*(9), e106966.
- Sullivan, N. J., Sasser, A. K., Axel, A., Vesuna, F., Raman, V., Ramirez, N., Oberyszyn, T. M., & Hall, B. M. (2009). Interleukin-6 induces an epithelial–mesenchymal transition phenotype in human breast cancer cells. *Oncogene*, *28*(33), 2940-2947.
- Tang, Q., Xia, D., Jin, X., Zhang, Q., Sun, X. Q., & Wang, C. (2013). Re/Mg bimetallic tandem catalysis for [4+ 2] annulation of benzamides and alkynes via CH/NH functionalization. *Journal of the American Chemical Society*, *135*(12), 4628-4631.
- Tawara, K., Bolin, C., Koncinsky, J., Kadaba, S., Covert, H., Sutherland, C., Bond, L., Kronz, J., Garbow, J., & Jorcyk, C. L. (2018). OSM potentiates preinvasion events, increases CTC counts, and promotes breast cancer metastasis to the lung. *Breast Cancer Research*, *20*(1), 53.

- Tester, A. M., Ruangpanit, N., Anderson, R. L., & Thompson, E. W. (2000). MMP-9 secretion and MMP-2 activation distinguish invasive and metastatic sublines of a mouse mammary carcinoma system showing epithelial-mesenchymal transition traits. *Clinical and Experimental Metastasis*, *18*(7), 553-560.
- Thede, K., Greschat, S., Wildum, S., Paulsen, D., & Scheuermann, E. (2010) *PCT. Int. Appl.*, 2010075957.
- West, N. R., Murphy, L. C., & Watson, P. H. (2012). Oncostatin M suppresses oestrogen receptor- $\alpha$  expression and is associated with poor outcome in human breast cancer. *Endocrine-Related Cancer*, *19*(2), 181-195.

## CHAPTER THREE: BINDING AFFINITY OF SMI-10 ANALOGS

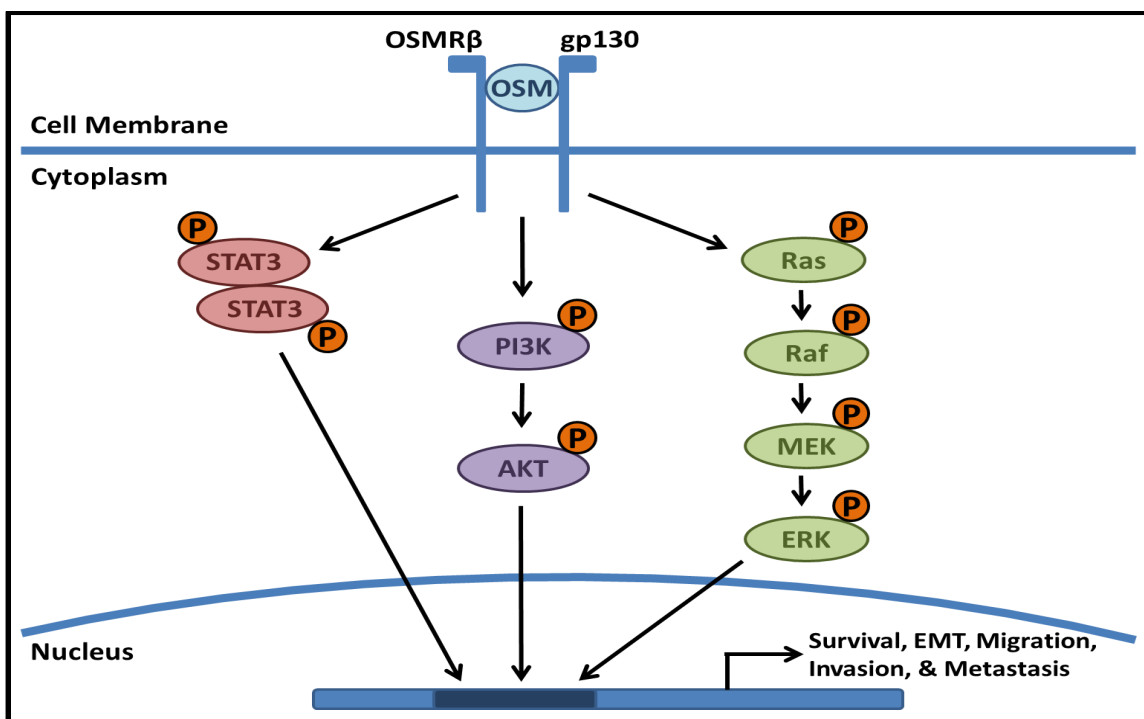
### 3.1 Introduction

#### 3.1.1 Metastatic Breast Cancer and Oncostatin M

Cancer is the second leading cause of death in the United States after heart disease. Specifically, it is estimated that about 1.7 million new cases of cancer will be diagnosed in the United States in 2018 resulting in approximately 600,000 deaths (Siegel, 2018). Breast cancer, at 30% of all new diagnoses, is the most prevalent malignancy for women. It is estimated that in 2018 alone there will be 266,000 new cases (Siegel, 2018). The five-year survival rate for localized breast cancer is 99%, however, the survival rate for distant metastatic breast cancer drops to 27% (Howlader, 2017), which is indicative of a need for a novel therapeutic treatment method

The ability of the interleukin-6 (IL-6) family of cytokines to increase epithelial to mesenchymal transition (EMT), increase cell motility, and to decrease cellular adhesion has implicated them in the promotion of metastasis for breast cancer patients (Sullivan, 2009; Knüpfer, 2007). Notably, a specific member of this family, oncostatin M (OSM), promotes cancer progression through the activation of several signaling pathways, such as the signal transducer and activator of transcription 3 (STAT3), phosphatidylinositol-3-kinase (PI3K), and the mitogen-activated protein kinase (MAPK) pathways (Tester, 2000; Chen, 2013; Meng, 2013; Smith, 2014) (Figure 3.1). Due to OSM's ability to increase metastatic potential, small molecule inhibitors (SMIs) of OSM were designed, synthesized,

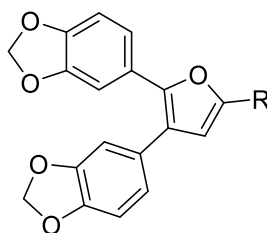
and preliminarily tested for use as novel therapeutic treatment options for metastatic breast carcinomas.



**Figure 3.1** OSM induces the STAT3, PI3K, and MAPK pathways. OSM is able to induce activation of several signaling pathways that include STAT3, PI3K, and MAPK. Upon activation via phosphorylation of signaling proteins, the translocation of transcription factors into the nucleus allows for transcription of target genes responsible for the promotion of cancer metastasis.

### 3.1.2 Design of SMI-10 Analogs

High-throughput virtual screening of multiple accessible databases comprised of about 345,000 compounds was used to identify the top candidates computationally predicted to be capable of binding to OSM. The top compounds were then further assessed based upon their ability to inhibit OSM-induced phosphorylation of STAT3 on Tyr-705 (pSTAT3) via an enzyme-linked immunosorbent assay (ELISA). The results of the ELISA identified SMI-10 as one of the “lead compounds.” Second-generation analogs of SMI-10 were subsequently designed and synthesized to potentially improve the binding affinity and inhibition of OSM-induced signaling (Table 3.1).

**Table 3.1 Structures of SMI-10 analogs.<sup>a</sup>**

Compound	R	Compound	R
SMI-10A		SMI-10G	
SMI-10B		SMI-10H	
SMI-10C		SMI-10I	
SMI-10D		SMI-10J	
SMI-10E		SMI-10K	
SMI-10F			

<sup>a</sup>Summary of the analogs designed to increase binding affinity and thus inhibition of OSM-induced signaling.

### 3.1.3 OSM Inhibition Assay

An ELISA was used to assess the ability of the second-generation SMI-10 analogs to inhibit OSM-induced signaling. The ELISA measured the relative pSTAT3 expression, which corresponded to OSM-induced activation of the STAT3 signaling pathway. Due to this, low levels of relative pSTAT3 expression are an indication of an inactivation of the STAT3 signaling pathway and thus an inactivation of OSM itself. The majority of the second-generation analogs examined by ELISA analysis exhibited levels of OSM-induced signaling inhibition surpassing that of the original parent SMI-10 (Figure 3.2). Notably, SMI-10C, -10H, and -10I displayed the poorest inhibition of OSM.

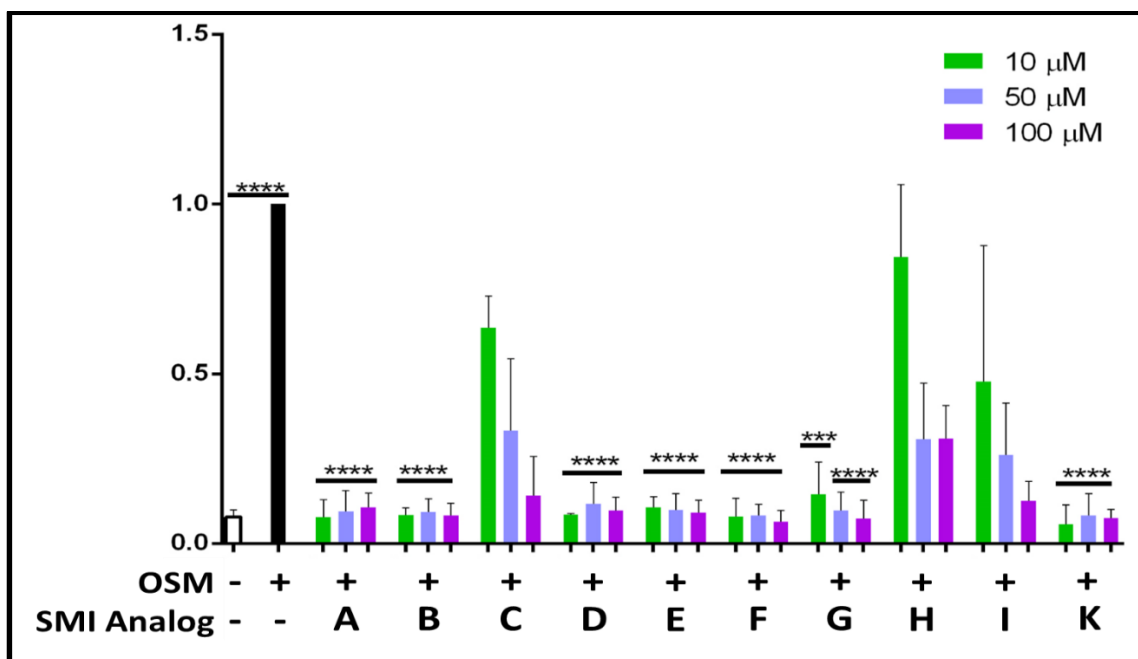


**Figure 3.2 OSM-induced inhibition assay.** T47D human breast cancer cells were treated for 30 minutes after co-incubation of each SMI-10 analog (10 μM, 50 μM, or 100 μM) with OSM (10 ng/mL) in serum-free media for 1 hour at 37 °C with 5% CO<sub>2</sub>. The cells were lysed, collected, and pSTAT3 levels were measured by ELISA. The reduction of pSTAT3 expression by the SMIs is indicative of inhibition of OSM-induced STAT3 signaling (mean ± SEM; n=2 for 10 μM; n=3 for 50 μM and 100 μM; \*\*\*p>0.0002; \*\*\*\*p>0.0001; significance determined against positive control; unpaired t-test) (results from Carsten Ashton; unpublished).

The SMIs were designed to directly bind with OSM to prevent the protein from activating signaling pathways responsible for increasing metastatic potential of breast cancer patients. Importantly, the ELISA analysis used to determine inhibition of OSM-induced signaling is an indirect assessment of SMI-OSM binding. Therefore, alternative methods for the evaluation of direct SMI-OSM binding were necessary to validate the results of the ELISA analysis as a means for detecting OSM inhibition.

#### 3.1.4 Isothermal Titration Calorimetry

Isothermal titration calorimetry (ITC) is a label-free technique capable of directly measuring the binding energetics of biological processes, such as protein-ligand binding (Freire, 1990). ITC experiments give thermodynamic information that include binding stoichiometry ( $n$ ), equilibrium dissociation constants ( $K_D$ ), changes in enthalpy ( $\Delta H$ ), Gibbs free energy ( $\Delta G$ ), and changes in entropy ( $\Delta S$ ) (Holdgate, 2005). Furthermore, the instrumentation sensitivity level allows for the direct measurement of binding processes exhibiting binding association constants as high as  $10^9 \text{ M}^{-1}$  (Freire, 1990).

Importantly, ITC has been useful in regard to drug development by answering the question of how tightly a small molecule binds at a specific interaction site (Freyer, 2008). Typically, in order for pharmaceutical drugs to be useful, the interaction between the drug and the biological target must display a  $K_D$  greater than or equal to  $1 \times 10^{-6} \text{ M}$ . Furthermore, many modern drugs exhibit nanomolar  $K_D$  values.

Due to the capacity of ITC to measure binding constants, it is a useful tool in determining the drug-likeness of compounds (Leavitt, 2001). The ability of the SMI analogs to bind to OSM as determined via ITC is of particular interest in regard to the assessment of direct SMI-OSM binding to validate the results of the previous ELISA

analyses. Ultimately, SMI-10 analogs capable of binding to OSM and exhibiting  $K_D$  values within the micromolar range or greater are viable inhibitors of OSM and thus can potentially be used as therapeutic treatment options for metastatic breast cancer.

### 3.1.5 Heteronuclear HSQC-detected Titrations

Another potential method that can be conducted to determine SMI-10 analog binding to OSM is heteronuclear single quantum correlation (HSQC)-detected titrations. In these experiments, the changes in  $^1\text{H}$ - $^{15}\text{N}$  HSQC spectra of  $^{15}\text{N}$ -labeled OSM upon addition of SMIs can be used to determine  $K_D$  values (Fielding, 2007). Furthermore, even very weak binding with  $K_D$  values in the high micromolar to low millimolar range can be detected. In addition to revealing if SMI-OSM binding is occurring, these experiments also generate information on the approximate number of residues that are affected and whether the interaction induces significant changes in the conformation of the protein (Marintchev, 2007). Moreover, the information obtained from the HSQC experiments regarding the binding of SMIs to OSM can be used in collaboration with the results of the ITC experiments to validate the  $K_D$  values obtained for each analog and to confirm the results of the ELISA analyses.

## **3.2 Results and Discussion**

### 3.2.1 Isothermal Titration Calorimetry

In order to further evaluate the SMI-10 analogs as potential inhibitors of OSM, ITC was used to determine binding affinity. This quantitative technique is often utilized as a means of studying the binding of small molecules to larger macromolecules, such as proteins. Specifically, the titration of SMI-10 analogs into human recombinant OSM protein gave values for the stoichiometry, binding affinity, and enthalpy of binding. These

values were then used to calculate the free energy and entropy associated with binding (Table 3.2; Appendix E).

**Table 3.2 Thermodynamics of SMI-10 analogs.<sup>a</sup>**

Analog	<i>n</i>	K <sub>D</sub> (μM)	ΔH (kcal/mol)	ΔG (kcal/mol)	TΔS (kcal/mol)
SMI-10F	6.03 ± 0.23	61 ± 14	-5.99 ± 0.56	-5.83	-0.15
SMI-10G	2.68 ± 0.53	28 ± 19	-1.03 ± 0.33	-6.28	5.25
SMI-10H	ND	ND	ND	ND	ND
SMI-10I	ND	ND	ND	ND	ND

<sup>a</sup>Summary of the thermodynamic values obtained via ITC experiments for the SMI-10 analogs. The results suggest that SMI-10F and -10G are capable of binding to OSM. Additionally, SMI-10H and SMI-10I are unable to bind to human recombinant OSM as determined by ITC (ND = non-determinable; n = 3).

The previous ELISA results with the second-generation SMI-10 analogs indicated that both SMI-10F and SMI-10G inhibit OSM-induced signaling of the STAT3 pathway. The ability of the SMIs to inhibit OSM-induced signaling was suggestive that the SMIs bind to OSM. However, ELISA analysis is an indirect assessment of SMI-OSM binding. Therefore, binding affinity between the SMIs and OSM was evaluated using ITC to directly measure SMI-OSM binding (Figure 3.3 and Figure 3.4).

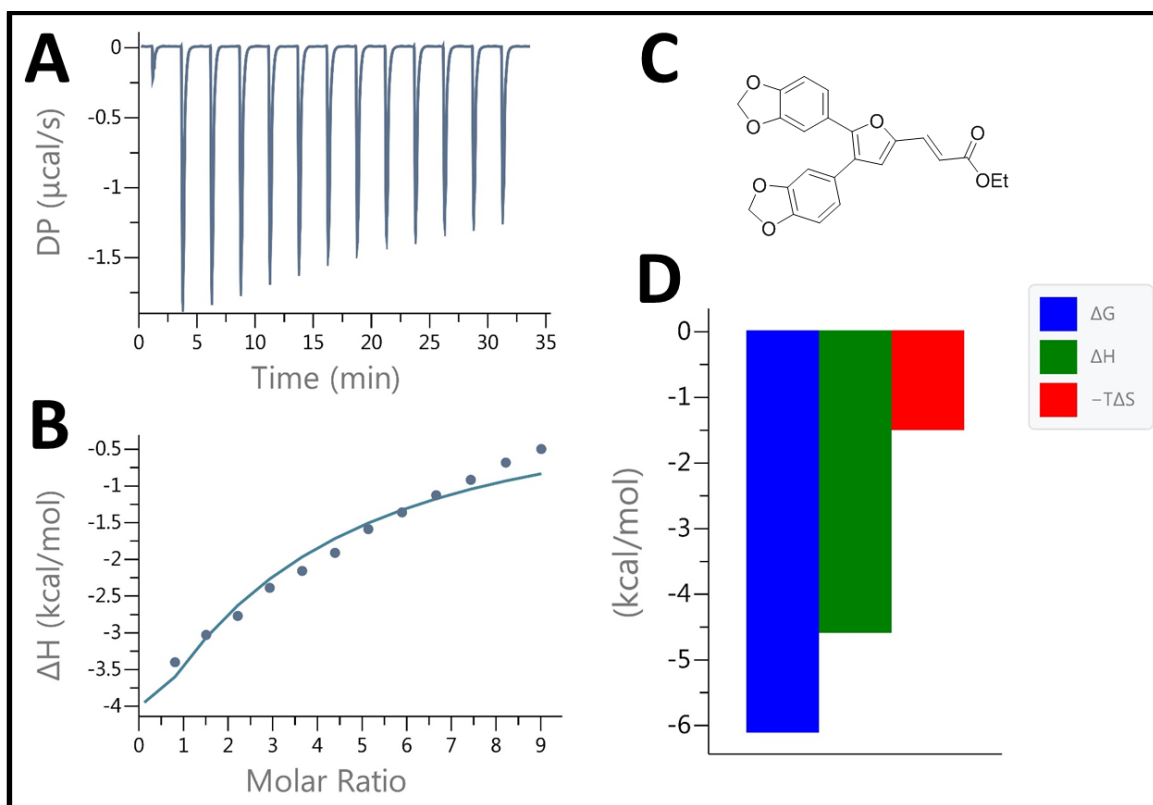


**Figure 3.3 ITC of SMI-10F.** **A.** Raw data from a representative run using SMI-10F. **B.** Normalized data from a representative run with the data fit using a fitting model. **C.** Structure of the SMI-10 second-generation analog tested. **D.** Thermodynamic data obtained from a representative run of SMI-10F, which suggested that SMI-OSM binding occurred in a favorable, exothermic, spontaneous manner.

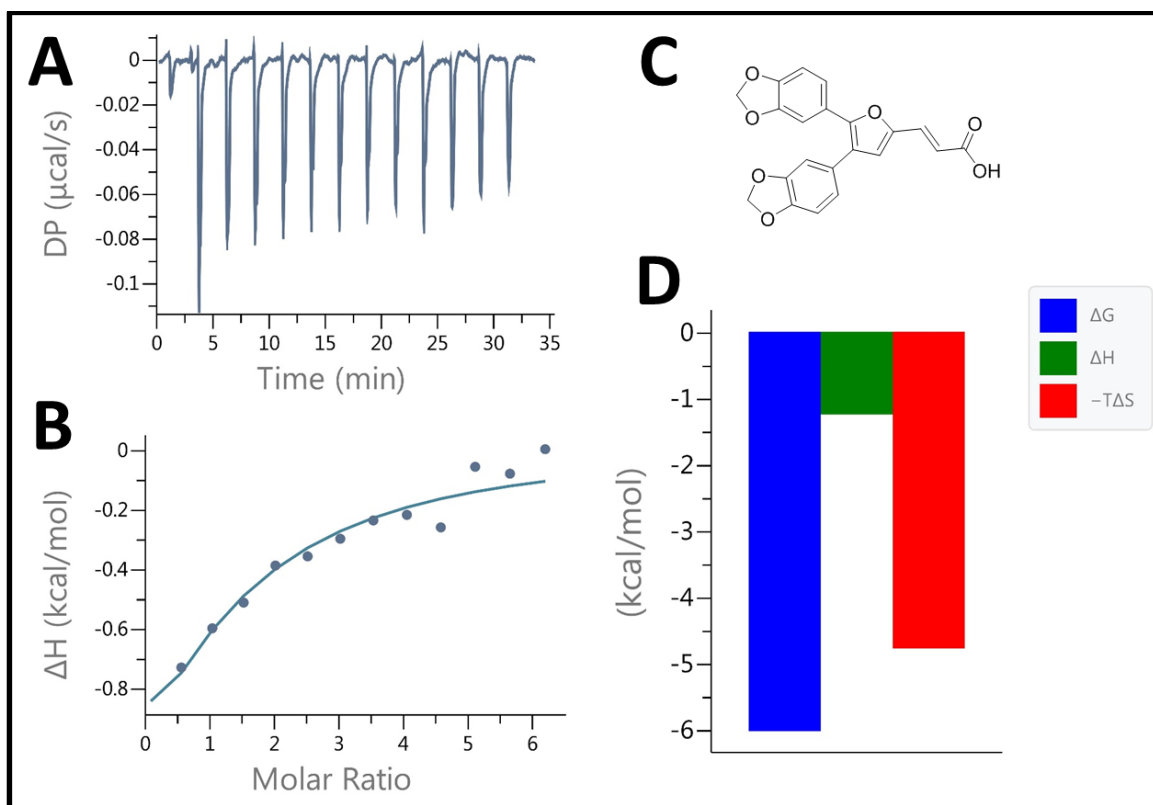


**Figure 3.4 ITC of SMI-10G.** **A.** Raw data from a representative run using SMI-10G. **B.** Normalized data from a representative run with the data fit using a fitting model. **C.** Structure of the SMI-10 second-generation analog tested. **D.** Thermodynamic data obtained from a representative run of SMI-10F, which suggested that SMI-OSM binding occurred in a favorable, exothermic, spontaneous manner.

The results for both SMI-10F and SMI-10G presented a  $K_D$  value within the micromolar range, indicating that binding occurred and thus corresponded to the ELISA results. Furthermore, both SMI-10F and SMI-10G analogs exhibited a negative  $\Delta H$  signifying that the binding was a result of an exothermic reaction. The interaction of SMI-10G was also considered spontaneous, as determined by a positive  $\Delta S$  value. Of the three experiments conducted on SMI-10F, two demonstrated a small, positive  $\Delta S$  and one exhibited a large negative  $\Delta S$ , resulting in an overall  $\Delta S$  value for SMI-10F that was negative and thus nonspontaneous. Despite the differences in  $\Delta S$  values, it was determined

from the correlation between  $\Delta H$ ,  $\Delta S$ , and  $\Delta G$  that the binding for both SMI-10F and SMI-10G had a negative value for  $\Delta G$  and thus were favorable.

The SMI-10 analogs were designed to bind at a specific site on OSM, which would presumably correspond to a 1:1 stoichiometry. However, the values obtained for  $n$  from the ITC experiments with SMI-10F and SMI-10G did not correspond to the expected value. It is worth noting that it is essential for protein and ligand concentrations to be highly accurate when obtaining ITC as any error in protein or ligand concentration will linearly change the estimated stoichiometry (Dutta, 2015). Therefore, the variations in  $n$  for SMI-10F and SMI-10G are likely a result of inaccurate concentrations.

Additionally, SMI-10H and SMI-10I, both of which exhibited poor inhibition of OSM-induced STAT3 signaling via the ELISA results, were also evaluated for binding affinity toward OSM using ITC. However, when preparing the sample of SMI-10H with 5% DMSO in an aqueous buffer for ITC, a precipitant formed. Due to the insolubility of SMI-10H, the analog was unable to be tested for binding using ITC (Figure 3.5). Furthermore, the concern with solubility in aqueous buffers is additionally problematic for the use of SMI-10H as a potential therapeutic treatment against metastatic breast cancer.

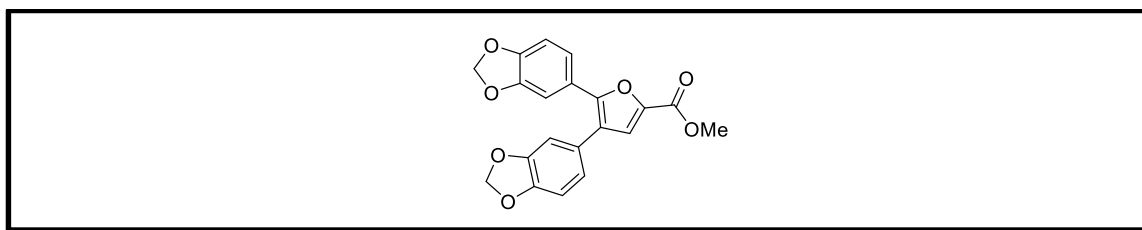


**Figure 3.5** Structure of SMI-10H. Analog was unable to be analyzed using ITC experiments due to solubility issues in an aqueous buffer.

Another poor inhibitor of OSM-induced signaling, SMI-10I, was evaluated for binding affinity with OSM using ITC (Figure 3.6). Importantly, the titration of SMI-10I into human recombinant OSM yielded results that suggested no binding was occurring. This information validates the ELISA results that were previously obtained by demonstrating that SMI-OSM binding is required for the inhibition of OSM-induced STAT3 signaling. In addition to validating the ELISA analysis, the thermodynamic parameters obtained from the ITC experiments can be useful in continued rounds of optimization for the SMI-10 analogs.

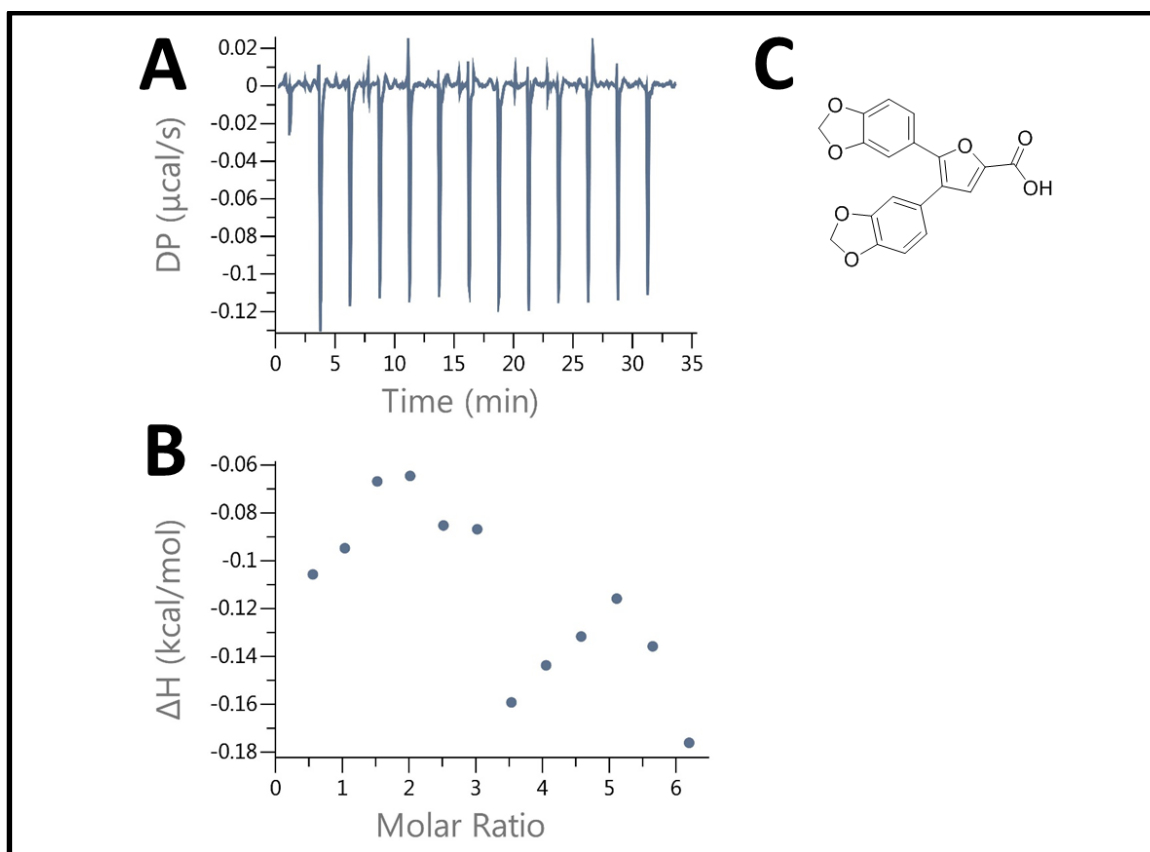


**Figure 3.6** ITC of SMI-10I. **A.** Raw data from a representative run using SMI-10I. **B.** Normalized data from a representative run, which is suggestive that no binding is occurring between SMI-10I and OSM. **C.** Structure of the SMI-10 second-generation analog tested.

### 3.2.2 Heteronuclear HSQC-detected Titrations

In order to perform the HSQC experiments,  $^{15}\text{N}$ -labeled OSM was prepared and a  $^1\text{H}$ - $^{15}\text{N}$  HSQC spectrum was collected, correlating to the chemical shifts of the backbone amide protons covalently bound to the  $^{15}\text{N}$  amide nitrogen atoms (Figure 3.7). After this initial spectrum was collected, additional spectra can be obtained following the addition of SMI-10 analogs until saturation is reached. Subsequent analysis of the chemical shift perturbations of the backbone amide within the OSM spectra as a function of ligand concentration can then be used to determine  $K_D$  values as well as indicate regions of SMI-OSM interactions (Fielding, 2007). Additionally, after assignment of the initial  $^{15}\text{N}$ -labeled OSM spectrum, the regions of perturbations would reveal the location of the SMI binding sites on OSM, which can be used to further optimize SMI analogs in the future.

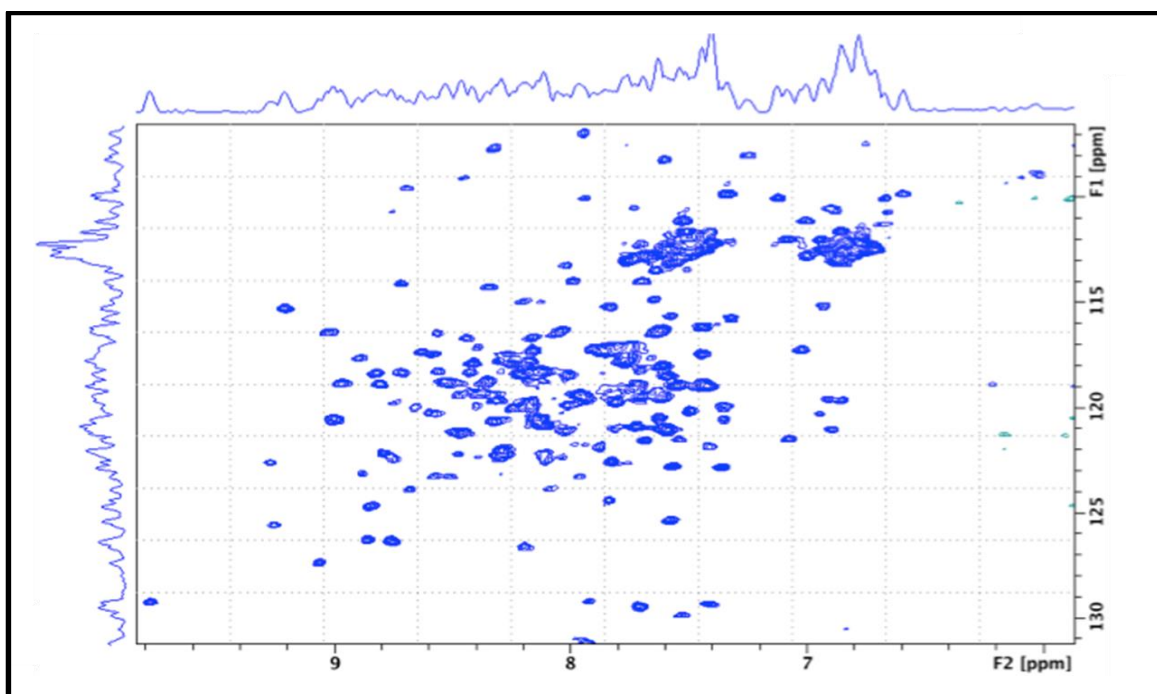


**Figure 3.7**  $^1\text{H}$ - $^{15}\text{N}$  HSQC spectrum of OSM. Preliminary spectrum of  $^{15}\text{N}$ -labeled OSM with 177 of 195 peaks picked prior to deconvolution of overlapping peaks. Subsequent spectra obtained following the addition of SMI-10 analogs can be used to obtain  $K_D$  values.

### 3.3 Concluding Remarks

The five-year survival rate for localized breast cancer is 99%, however, for distant metastatic breast cancer the survival rate drops to only 27% (Howlader, 2017), indicative of a need for a novel therapeutic treatment method. A specific inflammatory cytokine within the IL-6 family, OSM, has been shown to promote cancer progression and metastasis through the activation of several signaling pathways. The ability of OSM to induce metastasis has led to the design, synthesis, and preliminary testing of SMIs of OSM-induced signaling to be used as a potential treatment strategy for patients with metastatic breast cancer. Second-generation SMI-10 analogs were evaluated for binding affinity and other thermodynamic parameters through ITC experiments. The results indicated that SMI-10F and SMI-10G, both of which exhibited OSM-induced signaling inhibition via ELISA analysis, had  $K_D$  values within the micromolar range, suggesting specific binding occurred between the SMIs and OSM. Additionally, ITC results from analogs with poor OSM-induced signaling inhibition demonstrated that no binding occurred between the SMIs and OSM. These results—coupled with future heteronuclear HSQC-detected titration experiments—suggest specific SMI-OSM binding and thus the potential to use optimized SMIs as a therapeutic treatment for metastatic breast cancer.

### 3.4 Materials and Methods

#### 3.4.1 Materials and Reagents

For inhibition assays, SMI-10 analogs were diluted to 10  $\mu$ M stock solutions in anhydrous DMSO (obtained from Sigma-Aldrich) and stored at -20 °C. The recombinant human oncostatin M was purchased from PeproTech.

For human recombinant OSM used for ITC and HSQC experiments, D-(+)-glucose and imidazole were purchased from Acros Organics. Ammonium chloride,  $^{15}\text{N}$  ammonium chloride, D-glucose  $^{13}\text{C}_6$ , and isogro  $^{13}\text{C}$ ,  $^{15}\text{N}$  powder growth were obtained from Aldrich. From Alfa Aesar were purchased glycerol, kanamycin monosulfate cell culture grade powder, and D-(+)-biotin. Magnesium sulfate heptahydrate was purchased from EMD Millipore Corporation. Chemicals obtained from Fisher Chemical include calcium chloride, sodium chloride, thiamine hydrochloride, LB broth, tris base, and guanidine hydrochloride. Isopropyl- $\beta$ -D-thiogalactopyranoside was purchased from Gold Biotechnology. One shot BL21(DE3) chemically competent cells, NuPAGE 4-12% bis-tris gel (1.0 mm x 10 well), and NuPAGE MES SDS running buffer (20X) were obtained through Invitrogen Corporation. Both lysozyme and 2-mercaptoethanol were purchased from MP Biomedicals. Bolt LDS sample buffer (4X) was obtained from Novex by Life Technologies. Qiagen Company provided the Ni-NTA superflow. 5X M9 salts media without ammonium chloride and ammonium sulfate were purchased from Teknova. Finally, HALT protease inhibitor was obtained from Thermo Scientific.

#### 3.4.2 Equipment

$\text{OD}_{600\text{nm}}$  values were obtained using a Thermo Fisher Spectronic 200 Spectrometer. ITC data was acquired using a Malvern Microcal PEAQ-ITC. NMR data was acquired using a 600 MHz Bruker Avance III 600 coupled with Bruker Ultrashield 600 Plus.

#### 3.4.3 OSM Inhibition Assays

SMI-10 induced inhibition of pSTAT3 was determined through an ELISA against both MDA-MB-231 and T47D human breast cancer cell lines. Cells were serum starved for 4 hours. SMI-10 analogs (10  $\mu\text{M}$ ) and human recombinant OSM (10 ng/mL) were

incubated in serum-free RPMI-1640 medium at 37 °C and 5% CO<sub>2</sub>. After incubation, the SMI-10 analogs and OSM were added to the serum starved cells for 30 minutes. Cells were lysed using a 1x PathScan Sandwich ELISA Lysis buffer (CST #7018S) for 15 minutes after which the lysates were collected and stored at -20 °C. Lysates were analyzed for pSTAT3 expression using a PathScan Phospho-Stat3 (Tyr705) Sandwich ELISA Antibody Pair kit (CST #7146). pSTAT3 expression was measured with absorbance at 450nm and quantified by comparison relative to OSM-induced pSTAT3 expression.

#### 3.4.4 Human Recombinant OSM

Transformed competent cells were generated using BL21(DE3) competent cells (20-50 µL) and 6His-OSM plasmid DNA (1-5 µL) incubated on ice for 30 minutes. The cell/DNA mixture was heat shocked at 42 °C for 45-60 seconds and then placed on ice for two minutes. LB media (250-1000 µL) was added to the cell/DNA mixture and incubated at 37 °C and 250 rpm for 45 minutes. The transformation (50 µL and 450 µL, respectively) was plated on two separate 10 cm LB agar plates containing kanamycin and incubated overnight at 37 °C. The transformed cells were stored at -80 °C in 50% glycerol.

Unlabeled or uniformly labeled <sup>15</sup>N OSM protein was produced in transformed competent *Escherichia coli* BL21(DE3) with 6His-OSM plasmid DNA grown in M9 minimal medium. The cells (swiped from glycerol stock at -80 °C) were first grown in 5 mL unlabeled LB medium enriched with kanamycin (10 mg/mL, 5 µL). The cells were incubated overnight at 30 °C and 250 rpm in a 50 mL falcon tube under agitation until an OD<sub>600nm</sub> ~2.50 was obtained. The cells were centrifuged (5 min, 4000 x g, 30 °C) and the supernatant was discarded. The pre-inoculum was prepared in a 250 mL Erlenmeyer flask with the cell pellet resuspended in 50 mL of the unlabeled M9 medium prepared with 5x

M9 salts (10 mL), 10x natural abundance ammonium chloride (5 mL), 20% natural abundance glucose (750  $\mu$ L), 1 M calcium chloride (50  $\mu$ L), 1 M MgSO<sub>4</sub> (50  $\mu$ L), thiamine (10 mg/mL, 50  $\mu$ L), biotin (10 mg/mL, 50  $\mu$ L), kanamycin (10 mg/mL, 50  $\mu$ L), and water (QS 50 mL). The culture was incubated at 30 °C and 250 rpm overnight until it reached an OD<sub>600nm</sub> ~2.50. The inoculum was prepared in a 2 L Erlenmeyer flask with the equivalent of pre-inoculum necessary to obtain a starting OD<sub>600nm</sub> of 0.1 (20-50 mL). The pre-inoculum was centrifuged (5 min, 4000 x g, 30 °C) and the supernatant was discarded.

For unlabeled OSM protein, the cell pellet was resuspended in 500 mL of unlabeled M9 medium prepared with 5x M9 salts (100 mL), natural abundance ammonium chloride (0.5 g), 20% natural abundance glucose (7.5 mL), 1 M calcium chloride (500  $\mu$ L), 1 M MgSO<sub>4</sub> (500  $\mu$ L), thiamine (10 mg/mL, 500  $\mu$ L), biotin (10 mg/mL, 500  $\mu$ L), kanamycin (10 mg/mL, 500  $\mu$ L), and water (QS 500 mL). For uniformly labeled <sup>15</sup>N OSM protein, the cell pellet was resuspended in 500 mL of labeled M9 medium prepared with 5x M9 salts (100 mL), <sup>15</sup>N ammonium chloride (0.5 g), 20% natural abundance glucose (7.5 mL), 1 M calcium chloride (500  $\mu$ L), 1 M MgSO<sub>4</sub> (500  $\mu$ L), thiamine (10 mg/mL, 500  $\mu$ L), biotin (10 mg/mL, 500  $\mu$ L), kanamycin (10 mg/mL, 500  $\mu$ L), and water (QS 500 mL).

For both unlabeled or uniformly labeled <sup>15</sup>N OSM protein, the culture was then incubated at 37 °C and 250 rpm until it reached an OD<sub>600nm</sub> between 0.5 and 0.8. Protein expression was induced with 0.5 mM IPTG (1g/5mL, 500  $\mu$ L) and incubated overnight at 20 °C and 250 rpm until it reached an OD<sub>600nm</sub> between 2.0 and 2.5. The cells were harvested by centrifugation (20 min, 5000 x g, 4 °C) and the supernatant was discarded. Cell pellets were resuspended in lysis buffer containing 50 mM Tris, 100 mM NaCl (30 mL), lysozyme (10 mg/mL, 30  $\mu$ L), AEBSF (100 mM, 30  $\mu$ L), and HALT (100 mM, 30

$\mu\text{L}$ ). The cells were sonicated (30 sec pulse on, 30% amplitude; 30 sec pulse off; 8 min total cycle) and centrifuged (30 min, 18000 x g, 4 °C). The supernatant was filtered (0.45  $\mu\text{m}$ ) and shaken with Ni-beads (1.5 mL packed resin; 3 mL 50% slurry) overnight. The filtered lysate and Ni-beads were applied to column and allowed to flow through. The column was washed with 25 bed volumes (40 mL) cold lysis buffer (50 mM Tris, 100 mM NaCl, pH = 8) and with 28 bed volumes (45 mL) cold buffer (50 mM Tris, 100 mM NaCl, 25 mM Imidazole, pH = 8). The column was eluted with 12 bed volumes (17 mL) cold buffer (50 mM Tris, 100 mM NaCl, 200 mM Imidazole, pH = 8) that were collected in 1 mL, 5 mL, 5 mL, 5 mL, 1 mL fractions. Fractions containing 6His-OSM protein as determined by SDS-Page gel analysis and confirmed for activity via ELISA were combined, concentrated, dialyzed, and stored in 50 mM Tris, 100 mM NaCl, pH = 7.6 buffer.

#### 3.4.5 Isothermal Titration Calorimetry

Binding affinity of the SMI-10 analogs was determined by ITC. SMI-10 analogs were dissolved in DMSO to form a 20 mM stock solution. A 1 mM SMI-10 analog sample in 5% DMSO was then prepared using 7.5  $\mu\text{L}$  of the stock solution diluted with 142.5  $\mu\text{L}$  of 50 mM Tris, 100 mM NaCl, pH = 7.6 buffer. The OSM sample in 5% DMSO was prepared using 332.5  $\mu\text{L}$  of 21.97 or 31.34  $\mu\text{M}$  recombinant 6His-OSM in 50 mM Tris, 100 mM NaCl, pH = 7.6 buffer combined with 17.5  $\mu\text{L}$  DMSO. Parameters: a single 0.4  $\mu\text{L}$  injection followed by twelve 3  $\mu\text{L}$  injections; initial delay of 60 seconds; 150 seconds between injections; temperature at 25 °C; reference power 5 or 10  $\mu\text{Cal/sec}$ .

### 3.4.6 Heteronuclear HSQC-detected Titrations

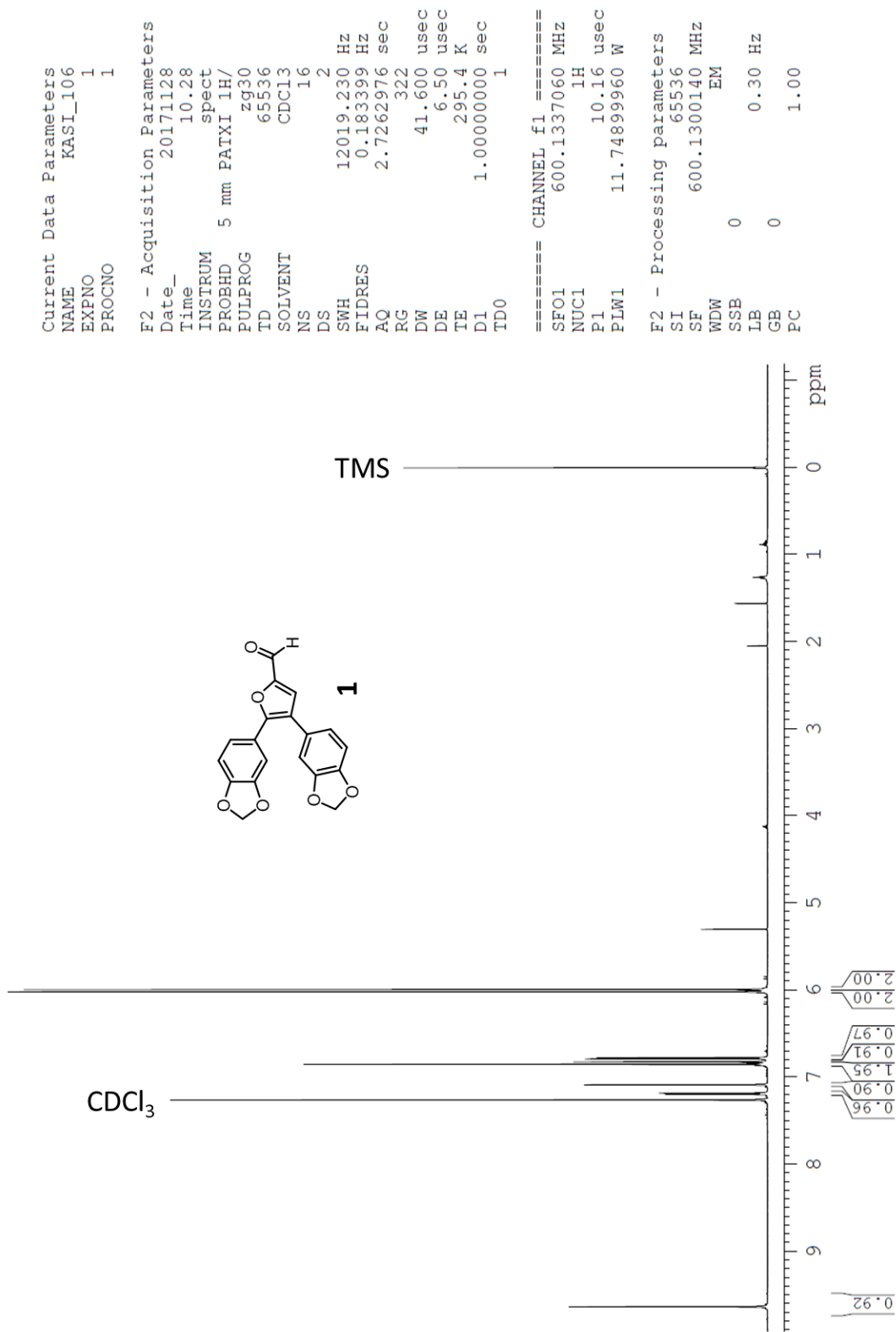
$^1\text{H}$ - $^{15}\text{N}$  HSQC spectrum of OSM was obtained using  $^{15}\text{N}$ -labeled OSM in 100 mM NaPi, 100 mM NaCl, 1x HALT protease inhibitor, pH = 7.5 buffer containing 10% D<sub>2</sub>O. The spectrum was acquired at 298 K with 176 scans.

### **3.5 References**

- Chen, X., Wang, H., Ou-yang, X. N., Xie, F. W., & Wu, J. J. (2013). Research on drug resistance mechanism of trastuzumab caused by activation of the PI3K/Akt signaling pathway. *Contemporary Oncology*, *17*(4), 363.
- Dutta, A. K., Rösgen, J., & Rajarathnam, K. (2015). Using isothermal titration calorimetry to determine thermodynamic parameters of protein–glycosaminoglycan interactions. *Methods in Molecular Biology*, *1229*, 315–324.
- Fielding, L. (2007). NMR methods for the determination of protein–ligand dissociation constants. *Progress in Nuclear Magnetic Resonance Spectroscopy*, *51*(4), 219-242.
- Freire, E., Mayorga, O. L., & Straume, M. (1990). Isothermal titration calorimetry. *Analytical Chemistry*, *62*(18), 950A-959A.
- Freyer, M. W., & Lewis, E. A. (2008). Isothermal titration calorimetry: experimental design, data analysis, and probing macromolecule/ligand binding and kinetic interactions. *Methods in Cell Biology*, *84*, 79-113.
- Holdgate, G. A., & Ward, W. H. (2005). Measurements of binding thermodynamics in drug discovery. *Drug Discovery Today*, *10*(22), 1543-1550.
- Howlander, N., Noone, A. M., & Krapcho, M. (2016). SEER Cancer Statistics Review, 1975-2013. *National Cancer Institute*.
- Howlander, N., Noone, A. M., & Krapcho, M. (2017). SEER Cancer Statistics Review, 1975-2014. *National Cancer Institute*.
- Knüpfner, H., & Preiß, R. (2007). Significance of interleukin-6 (IL-6) in breast cancer. *Breast Cancer Research and Treatment*, *102*(2), 129-135.

- Leavitt, S., & Freire, E. (2001). Direct measurement of protein binding energetics by isothermal titration calorimetry. *Current Opinion in Structural Biology*, 11(5), 560-566.
- Marintchev, A., Frueh, D., & Wagner, G. (2007). NMR methods for studying protein–protein interactions involved in translation initiation. *Methods in Enzymology*, 430, 283-331.
- Meng, X., Cai, C., Wu, J., Cai, S., Ye, C., Chen, H., Yang, Z., Zeng, H., Shen, Q., & Zou, F. (2013). TRPM7 mediates breast cancer cell migration and invasion through the MAPK pathway. *Cancer Letters*, 333(1), 96-102.
- Siegel, R. L., Miller, K. D., & Jemal, A. (2018). Cancer statistics, 2018. *CA: A Cancer Journal for Clinicians*.
- Smith, S. M., Lyu, Y. L., & Cai, L. (2014). NF- $\kappa$ B affects proliferation and invasiveness of breast cancer cells by regulating CD44 expression. *PloS One*, 9(9), e106966.
- Sullivan, N. J., Sasser, A. K., Axel, A., Vesuna, F., Raman, V., Ramirez, N., Oberyszyn, T. M., & Hall, B. M. (2009). Interleukin-6 induces an epithelial–mesenchymal transition phenotype in human breast cancer cells. *Oncogene*, 28(33), 2940-2947.
- Tester, A. M., Ruangpanit, N., Anderson, R. L., & Thompson, E. W. (2000). MMP-9 secretion and MMP-2 activation distinguish invasive and metastatic sublines of a mouse mammary carcinoma system showing epithelial-mesenchymal transition traits. *Clinical and Experimental Metastasis*, 18(7), 553-560.

APPENDIX A:  $^1\text{H}$  NMR Spectra



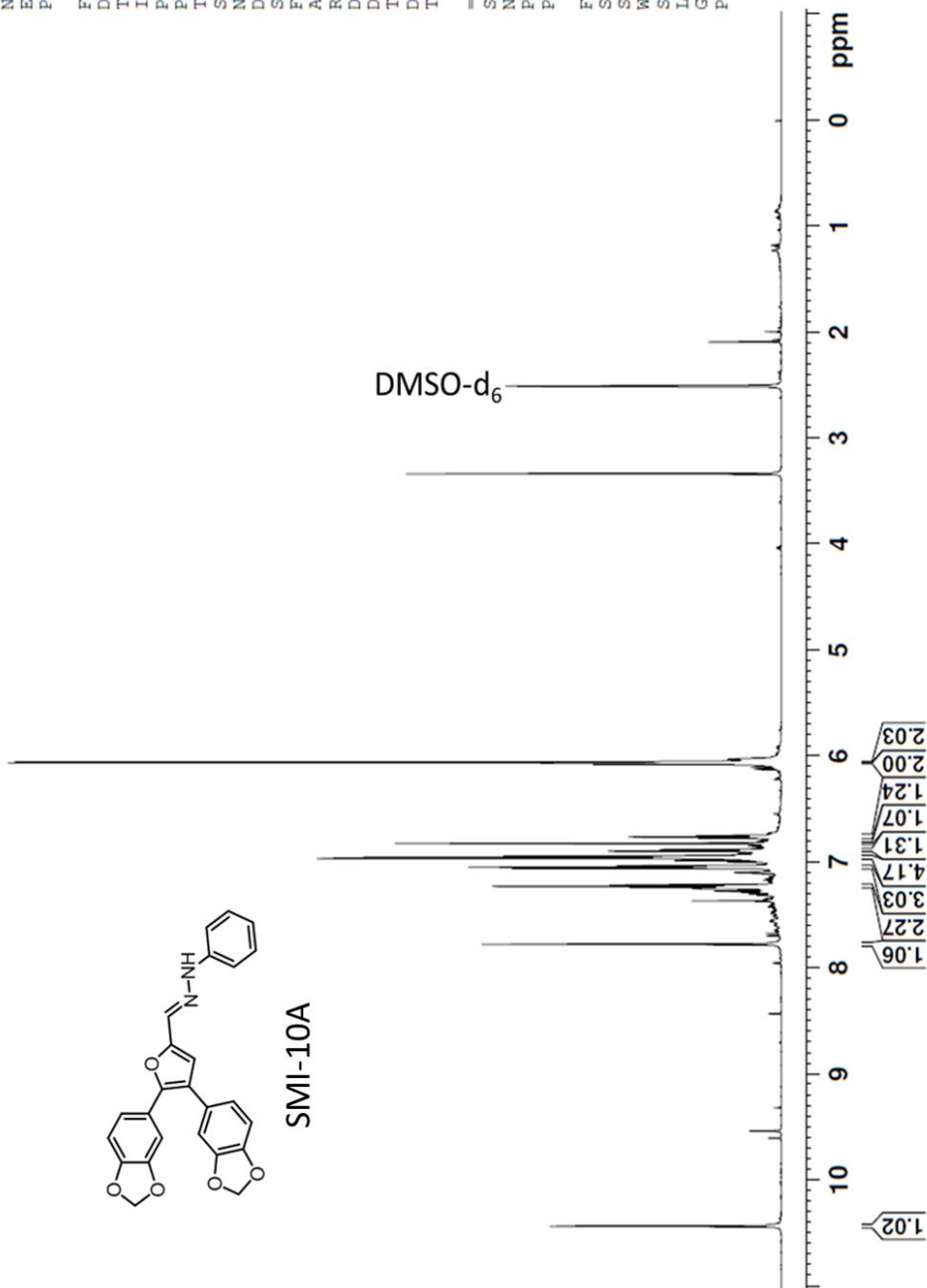
$^1\text{H}$  NMR ( $\text{CDCl}_3$  with 0.03% v/v TMS, 600 MHz)

Current Data Parameters  
 NAME TNM-IV-75-1  
 EXPNO 2  
 PROCNO 1

F2 - Acquisition Parameters  
 Date\_ 20180729  
 Time 23.26  
 INSTRUM spect  
 PROBHD 5 mm PATXI 1H/  
 PULPROG zg30  
 TD 65536  
 SOLVENT DMSO  
 NS 16  
 DS 2  
 SWH 12019.230 Hz  
 FIDRES 0.183399 Hz  
 AQ 2.7262976 sec  
 RG 90.5  
 DW 41.600 usec  
 DE 6.50 usec  
 TE 298.2 K  
 D1 1.0000000 sec  
 TD0 1

===== CHANNEL f1 =====  
 SFO1 600.1337060 MHz  
 NUC1 1H  
 P1 10.04 usec  
 PLW1 11.7489960 W

F2 - Processing parameters  
 SI 65536  
 SF 600.1300000 MHz  
 WDW EM  
 SSB 0  
 LB 0  
 GB 0  
 PC 1.00



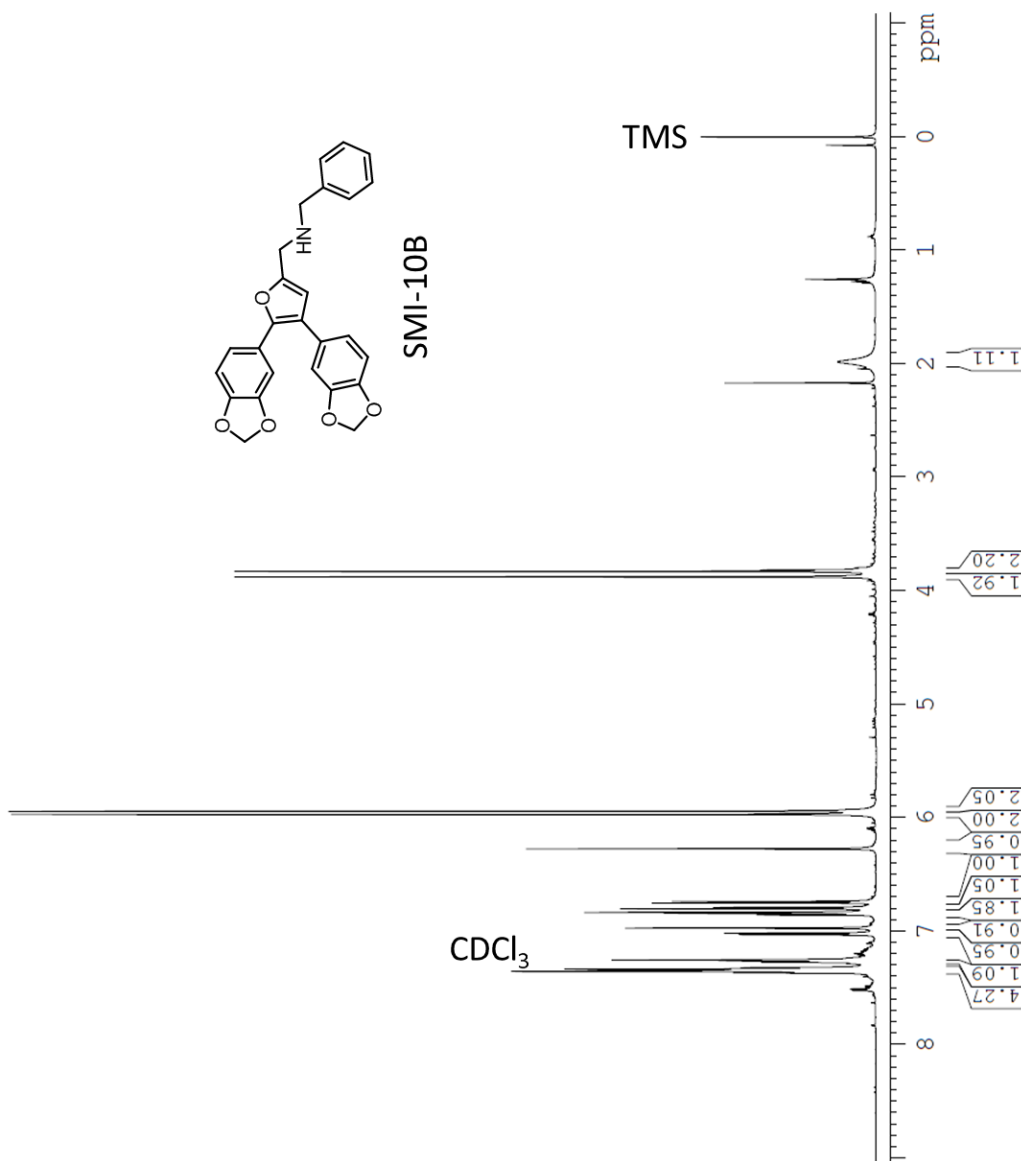
$^1\text{H}$  NMR (DMSO- $d_6$ , 600 MHz)

Current Data Parameters  
 NAME KASI\_52 pure  
 EXPNO 2  
 PROCNO 1

F2 - Acquisition Parameters  
 Date\_ 20170602  
 Time 17.51  
 INSTRUM spect  
 PROBHD 5 mm PATXI 1H/  
 PULPROG zg30  
 TD 65536  
 SOLVENT CDCl3  
 NS 1024  
 DS 2  
 SWH 12019.230 Hz  
 FIDRES 0.183399 Hz  
 AQ 2.7262976 sec  
 RG 90.5  
 DW 41.600 usec  
 DE 6.50 usec  
 TE 295.0 K  
 D1 1.00000000 sec  
 TD0 1

==== CHANNEL f1 =====  
 SF01 600.1337060 MHz  
 NUC1 1H  
 P1 10.16 usec  
 PLW1 11.74899960 W

F2 - Processing parameters  
 SI 65536  
 SF 600.1300189 MHz  
 WDW EM  
 SSB 0  
 LB 0.30 Hz  
 GB 0  
 PC 1.00



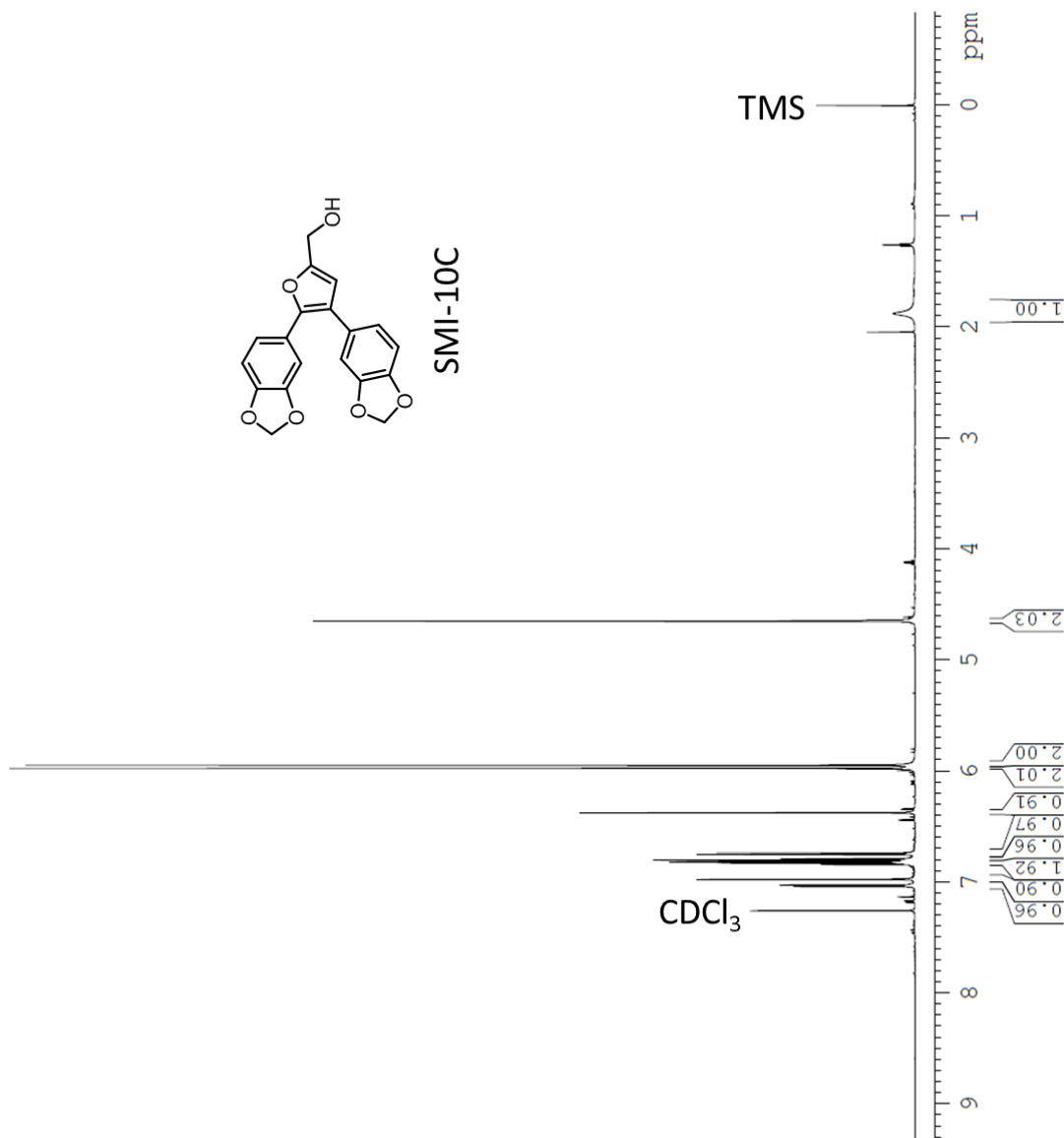
<sup>1</sup>H NMR (CDCl<sub>3</sub> with 0.03% v/v TMS, 600 MHz)

Current Data Parameters  
 NAME KASI\_66B pure  
 EXPNO 1  
 PROCNO 1

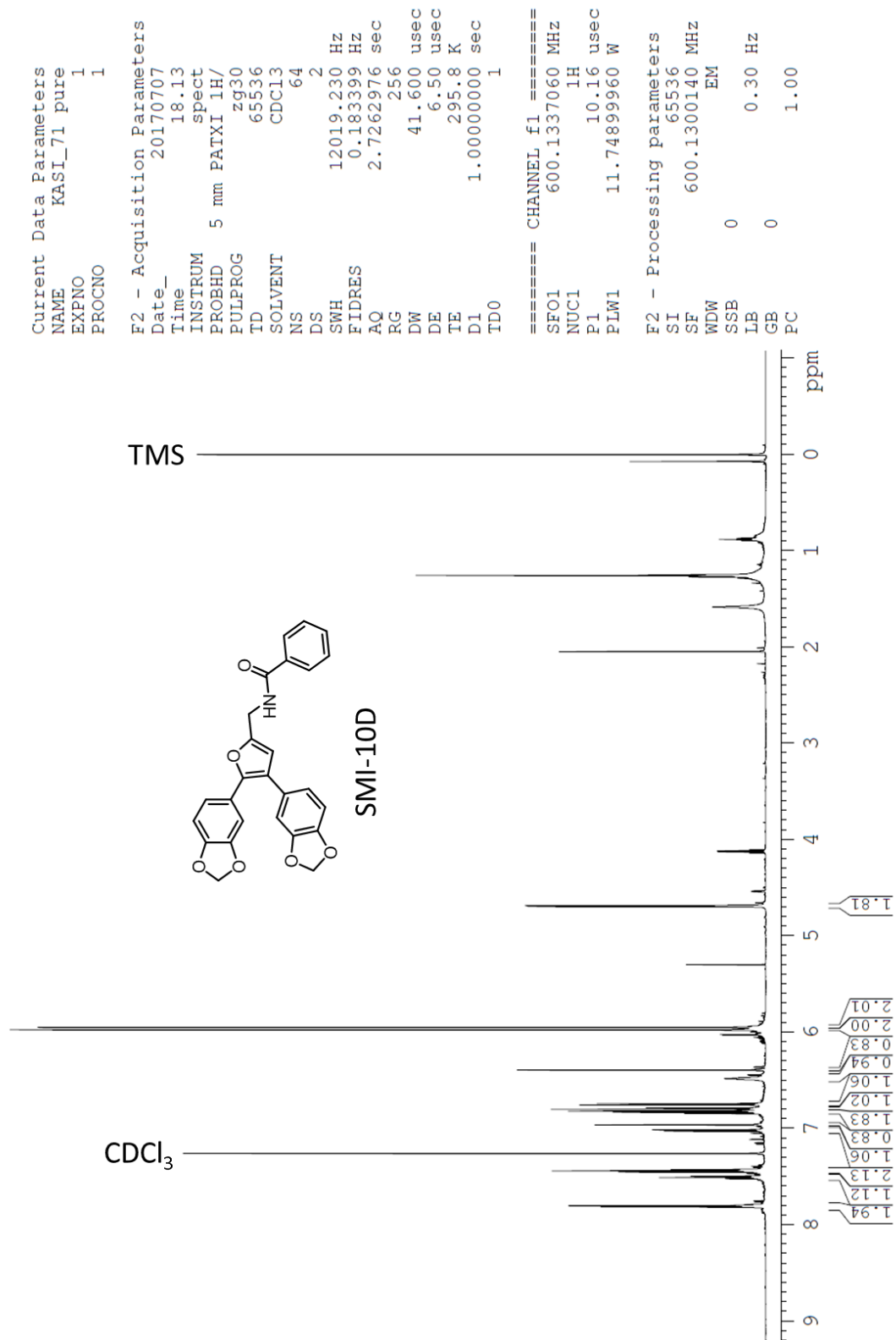
F2 - Acquisition Parameters  
 Date\_ 20170623  
 Time 18.30  
 INSTRUM spect  
 FROBHD 5 mm FAPBO BB-  
 PULPROG zg30  
 TD 65536  
 SOLVENT CDCl3  
 NS 64  
 DS 2  
 SWH 12019.230 Hz  
 FIDRES 0.183399 Hz  
 AQ 2.7262976 sec  
 RG 256  
 DW 41.600 usec  
 DE 6.50 usec  
 TE 294.3 K  
 D1 1.00000000 sec  
 TD0 1

==== CHANNEL f1 =====  
 SFO1 600.1337060 MHz  
 NUC1 1H  
 P1 15.20 usec  
 PLW1 27.98999977 W

F2 - Processing parameters  
 SI 65536  
 SF 600.1300160 MHz  
 EM  
 WDW 0  
 SSB 0 0.30 Hz  
 LB 0  
 GB 0  
 PC 1.00



<sup>1</sup>H NMR (CDCl<sub>3</sub> with 0.03% v/v TMS, 600 MHz)



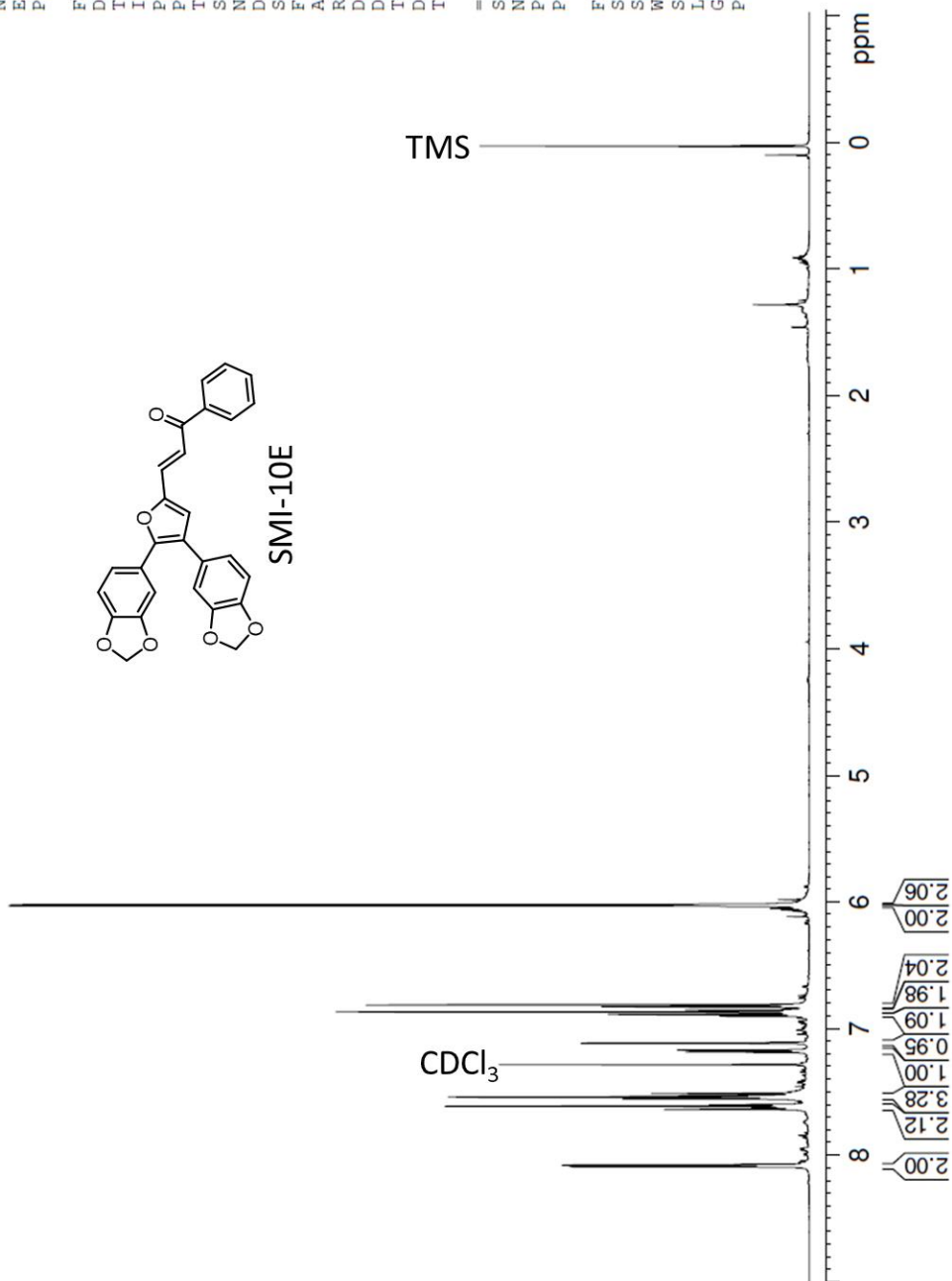
<sup>1</sup>H NMR (CDCl<sub>3</sub> with 0.03% v/v TMS, 600 MHz)

Current Data Parameters  
NAME KASI-35  
EXPNO 1  
PROCNO 1

F2 - Acquisition Parameters  
Date\_ 20180601  
Time\_ 11.52  
INSTRUM Spect  
PROBHD 5 mm PATXI 1H/  
PULPROG zg30  
TD 65536  
SOLVENT CDCl3  
NS 16  
DS 2  
SWH 12019.230 Hz  
FIDRES 0.183399 Hz  
AQ 2.7262976 sec  
RG 144  
DW 41.600 usec  
DE 6.50 usec  
TE 295.6 K  
D1 1.00000000 sec  
TD0 1

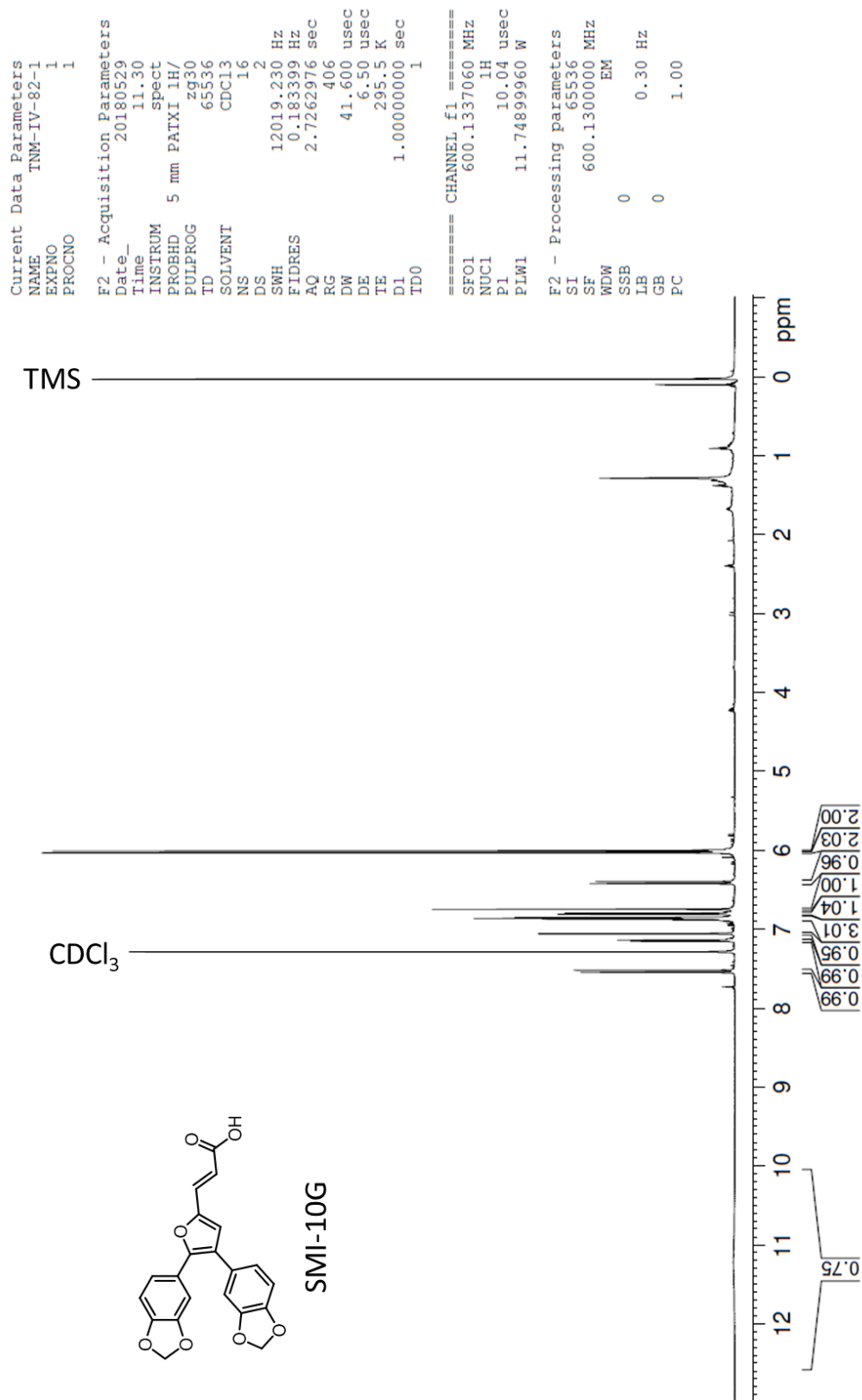
==== CHANNEL f1 =====  
SFO1 600.1337060 MHz  
NUC1 1H  
P1 10.04 usec  
PLW1 11.74899960 W

F2 - Processing parameters  
SI 65536  
SF 600.1300000 MHz  
WDW EM  
SSB 0  
LB 0.30 Hz  
GB 0  
PC 1.00



<sup>1</sup>H NMR (CDCl<sub>3</sub> with 0.03% v/v TMS, 600 MHz)





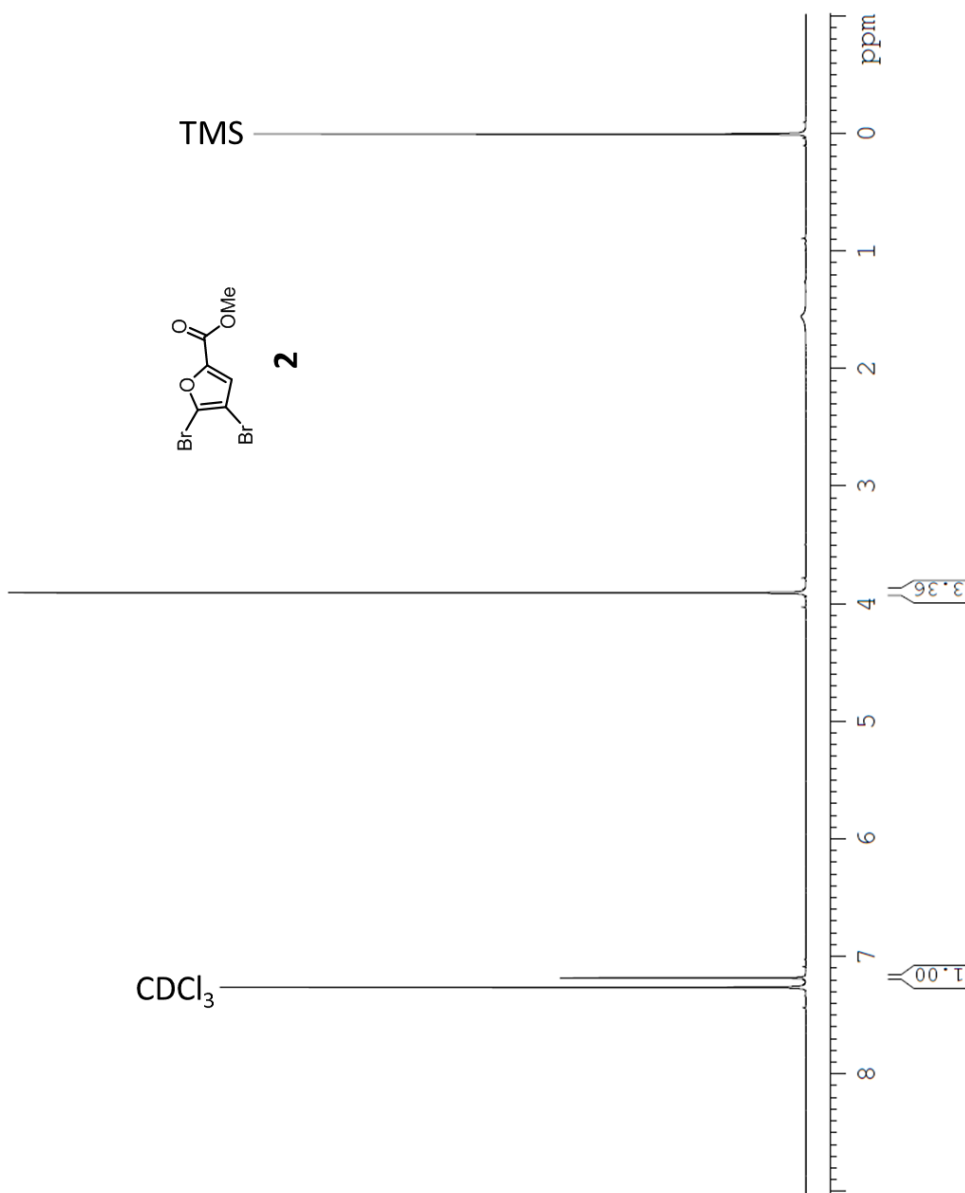
<sup>1</sup>H NMR (CDCl<sub>3</sub> with 0.03% v/v TMS, 600 MHz)

Current Data Parameters  
 NAME SJAI\_54  
 EXPNO 1  
 PROCNO 1

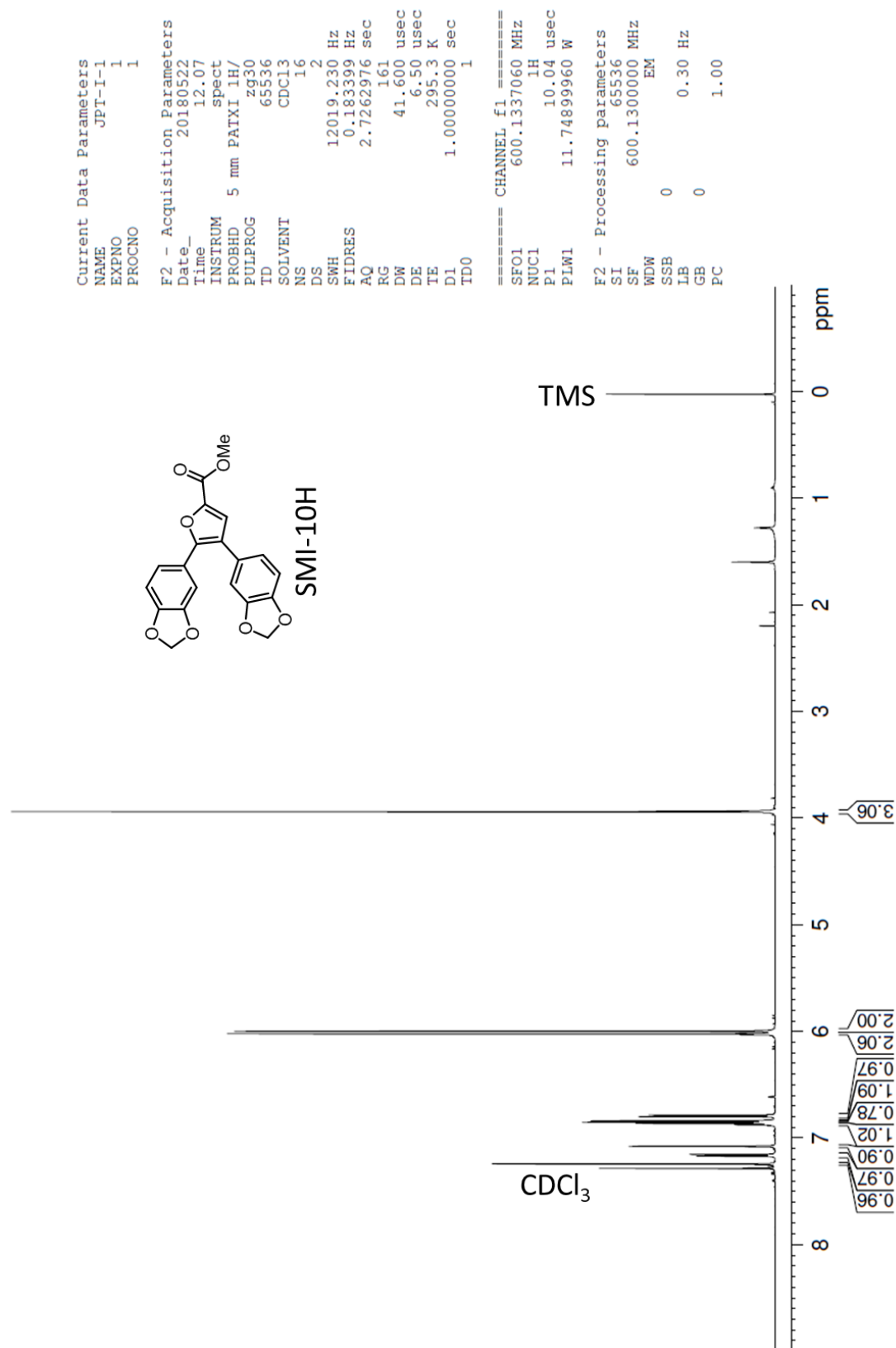
F2 - Acquisition Parameters  
 Date\_ 20170606  
 Time 12.10  
 INSTRUM spect  
 PROBHD 5 mm PATXI 1H/  
 PULPROG zg30  
 TD 65536  
 SOLVENT CDCl3  
 NS 16  
 DS 2  
 SWH 12019.230 Hz  
 FIDRES 0.183399 Hz  
 AQ 2.7262976 sec  
 RG 575  
 DW 41.600 usec  
 DE 6.50 usec  
 TE 295.0 K  
 D1 1.00000000 sec  
 TD0 1

==== CHANNEL f1 =====  
 SFO1 600.1337060 MHz  
 NUC1 1H  
 P1 10.16 usec  
 PLW1 11.74899960 W

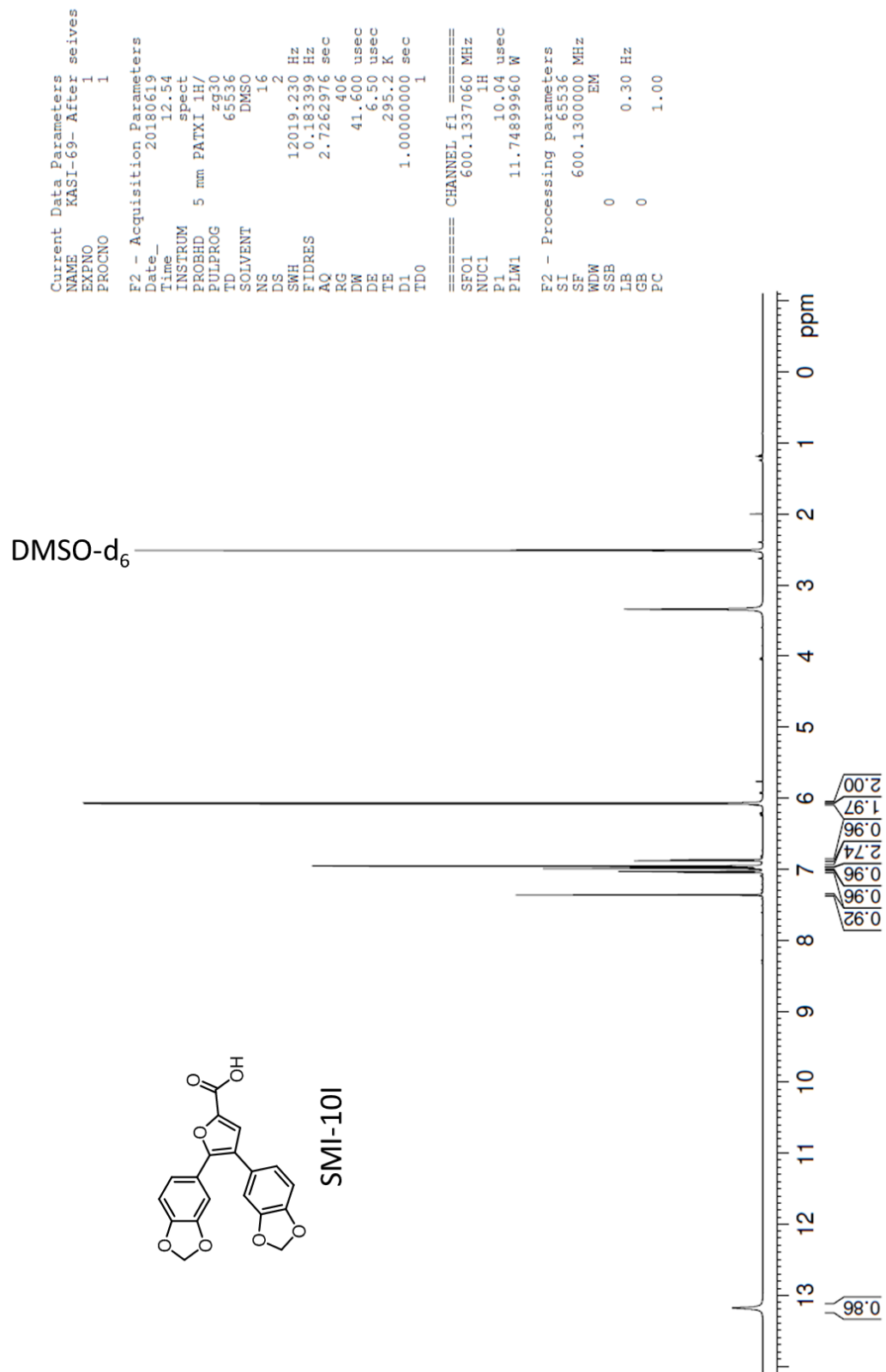
F2 - Processing parameters  
 SI 65536  
 SF 600.1300142 MHz  
 WDW EM  
 SSB 0  
 LB 0.30 Hz  
 GB 0  
 PC 1.00



$^1\text{H}$  NMR ( $\text{CDCl}_3$  with 0.03% v/v TMS, 600 MHz)



<sup>1</sup>H NMR (CDCl<sub>3</sub> with 0.03% v/v TMS, 600 MHz)



<sup>1</sup>H NMR (DMSO-d<sub>6</sub>, 600 MHz)

```

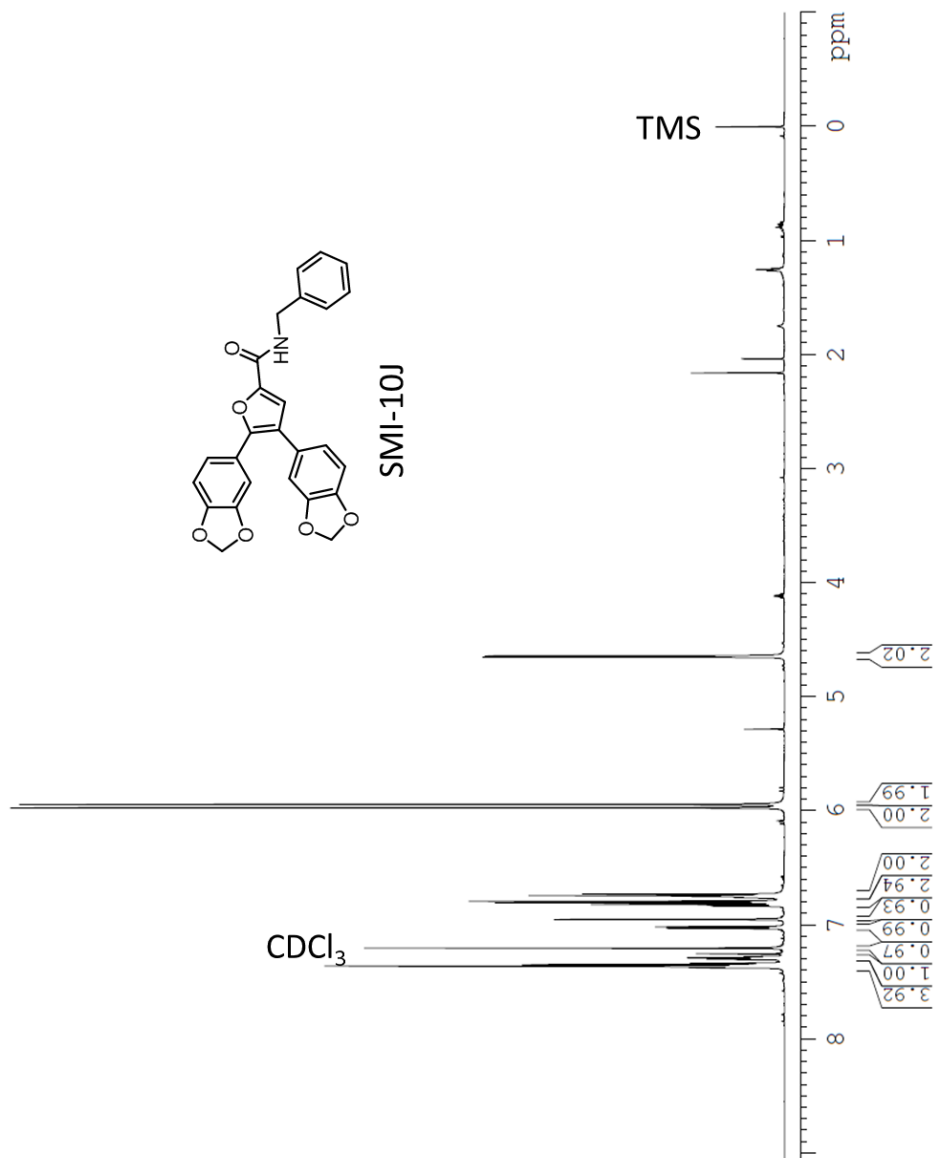
Current Data Parameters
NAME      KASI_74 test
EXPNO    1
PROCNO   1

F2 - Acquisition Parameters
Date_    20171019
Time     12.33
INSTRUM spect
PROBHD   5 mm PAXI 1H/
PULPROG zg30
TD       65536
SOLVENT  CDCl3
NS       16
DS       2
SWH      12019.230 Hz
FIDRES   0.183399 Hz
AQ       2.7262976 sec
RG       64
DW       41.600 usec
DE       6.50 usec
TE       298.2 K
D1       1.00000000 sec
TD0      1

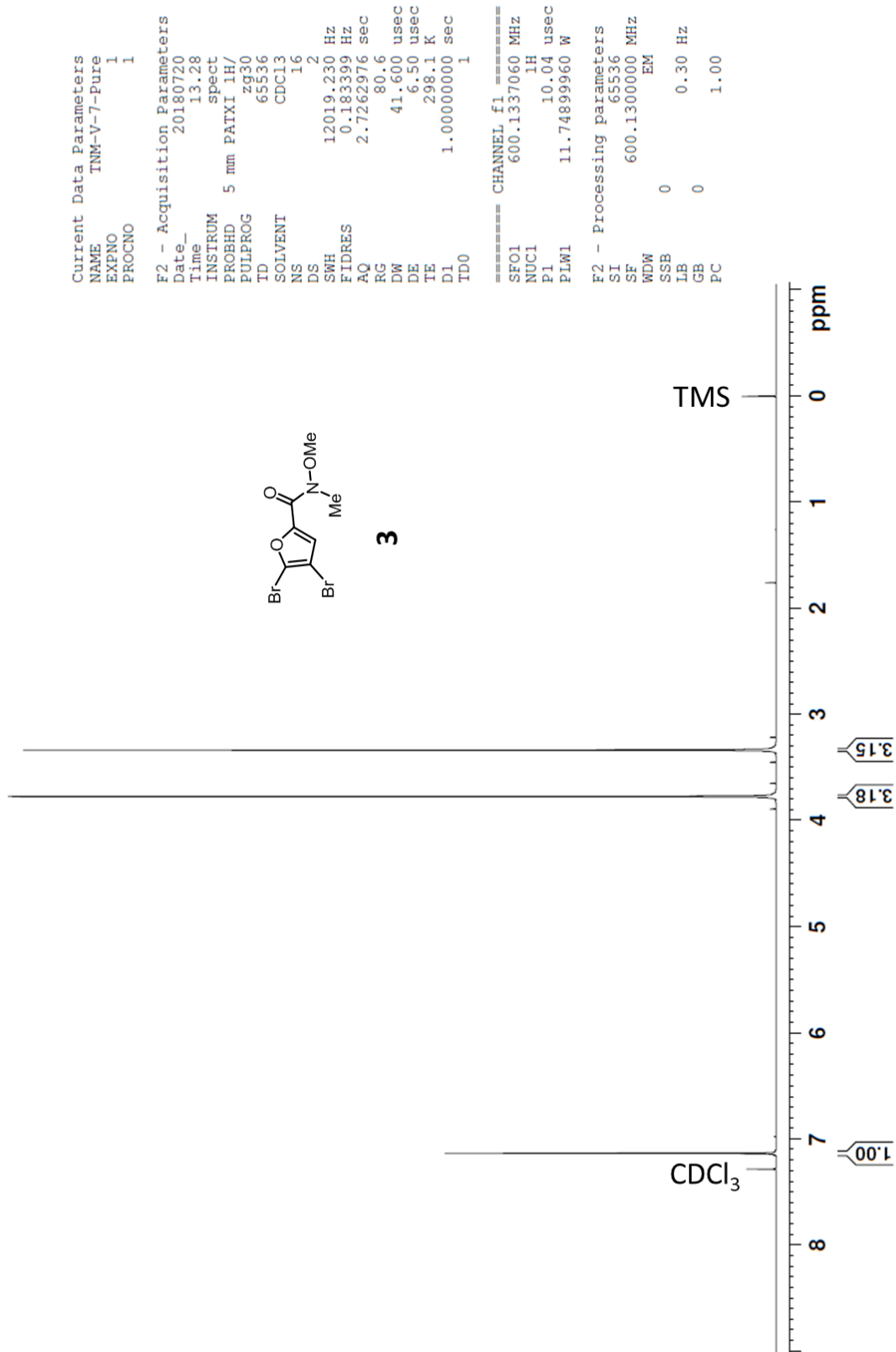
===== CHANNEL f1 =====
SF01    600.1337060 MHz
NUC1     1H
P1       10.16 usec
PLW1    11.7489960 W

F2 - Processing parameters
SI       65536
SF       600.1300185 MHz
WDW      EM
SSB      0
LB       0.30 Hz
GB       0
PC       1.00

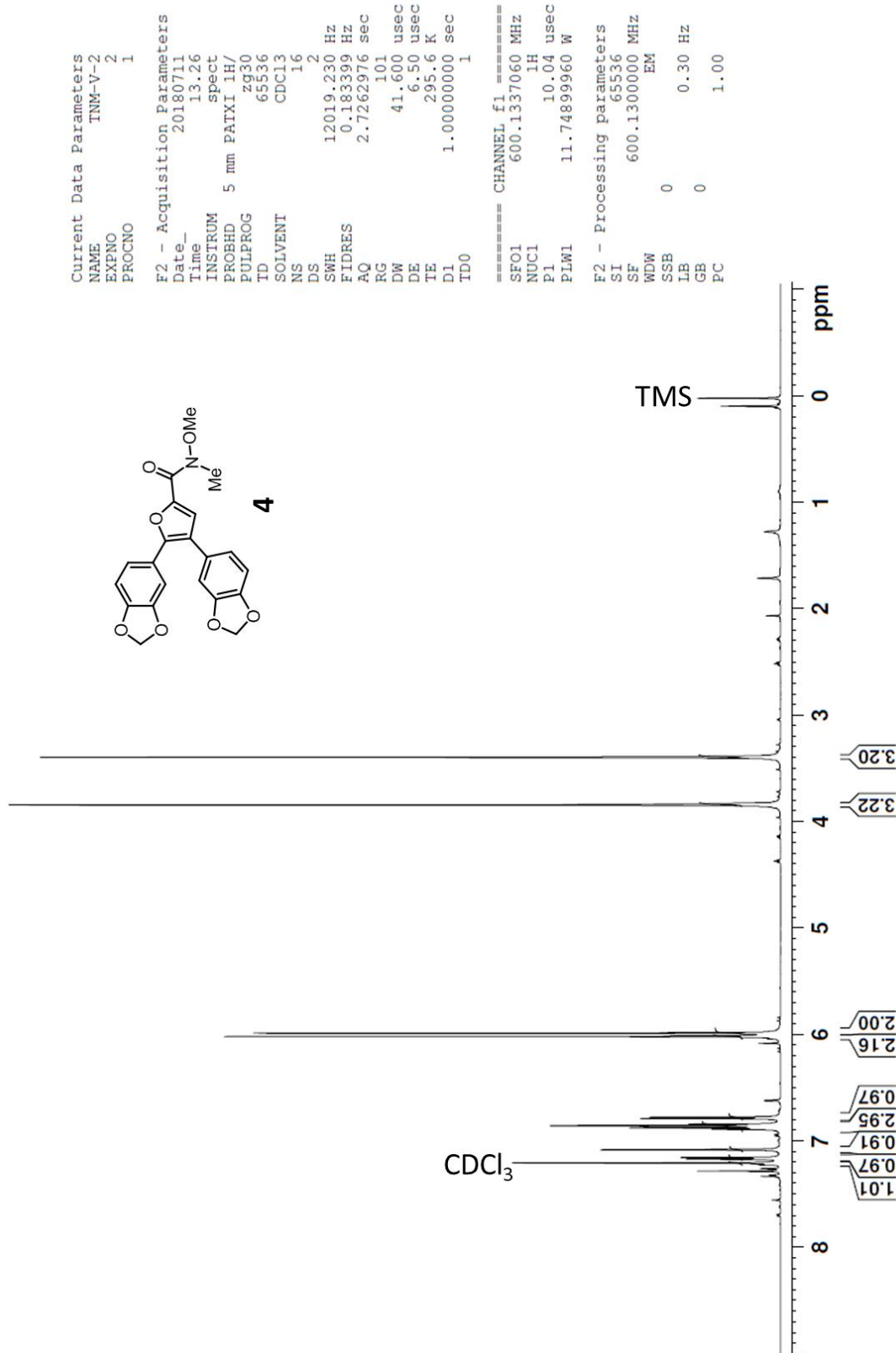
```



<sup>1</sup>H NMR (CDCl<sub>3</sub> with 0.03% v/v TMS, 600 MHz)



<sup>1</sup>H NMR (CDCl<sub>3</sub> with 0.03% v/v TMS, 600 MHz)



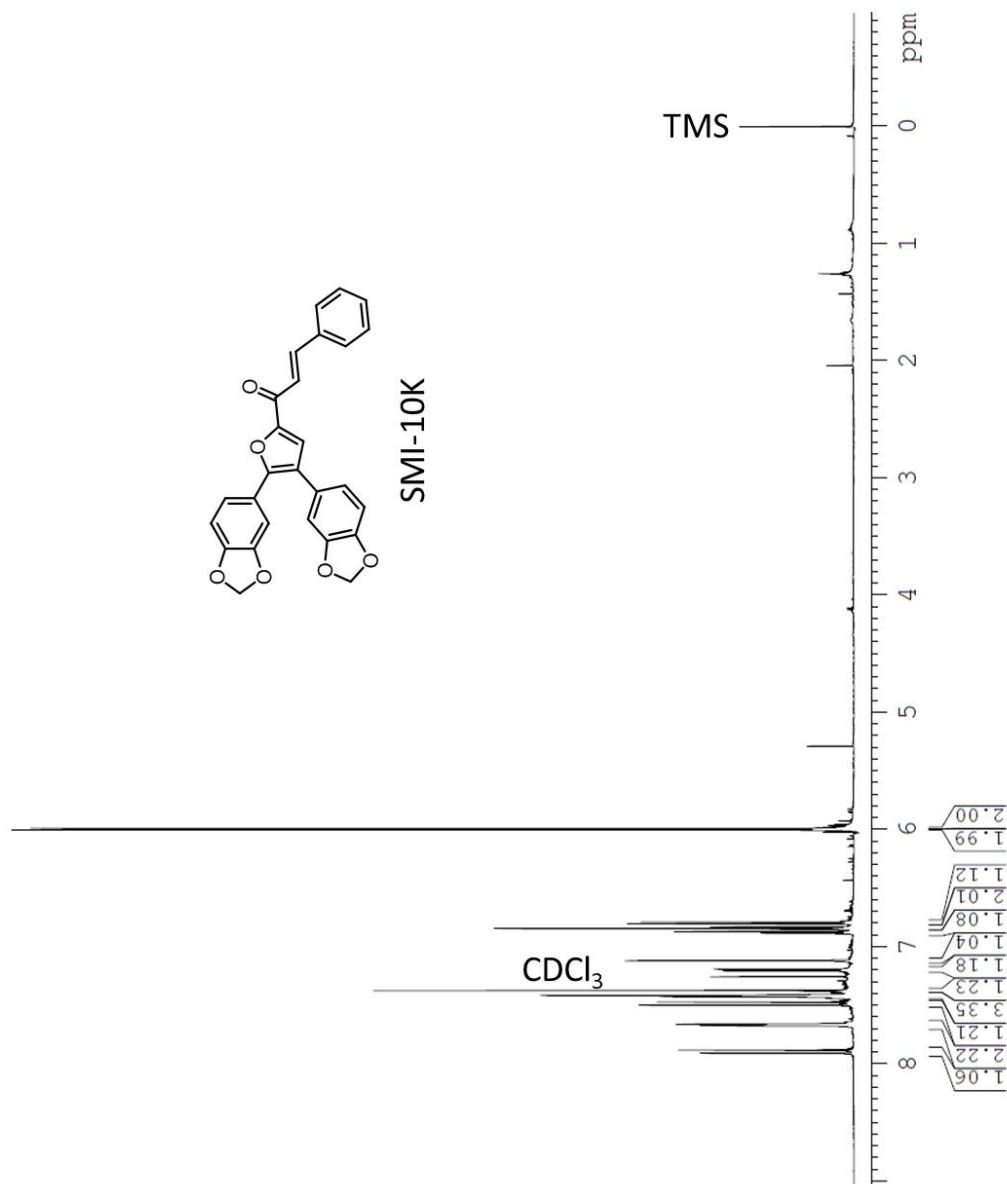
<sup>1</sup>H NMR (CDCl<sub>3</sub> with 0.03% v/v TMS, 600 MHz)

Current Data Parameters  
 NAME KASI\_81 test  
 EXPNO 1  
 PROCNO 1

F2 - Acquisition Parameters  
 Date\_ 20171019  
 Time 13.13  
 INSTRUM spect  
 PROBD 5 mm PATXI 1H/  
 PULPROG zg30  
 TD 65536  
 SOLVENT CDC13  
 NS 16  
 DS 2  
 SWH 12019.230 Hz  
 FIDRES 0.183399 Hz  
 AQ 2.7262976 sec  
 RG 71.8  
 DW 41.600 usec  
 DE 6.50 usec  
 TE 298.2 K  
 D1 1.00000000 sec  
 TD0 1

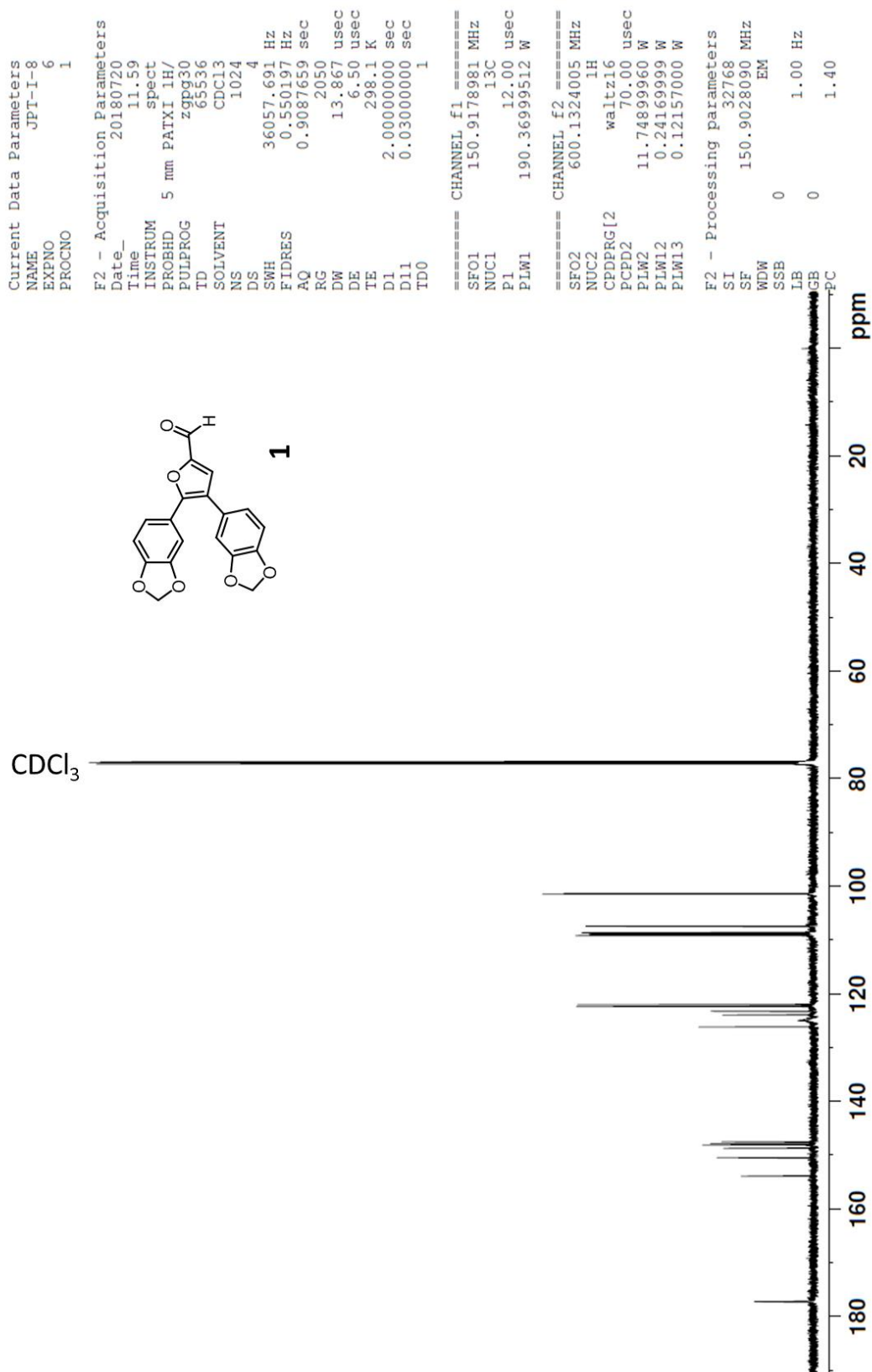
==== CHANNEL f1 =====  
 SF01 600.1337060 MHz  
 NUC1 1H  
 P1 10.16 usec  
 PLW1 11.74899960 W

F2 - Processing parameters  
 SI 65536  
 SF 600.1300169 MHz  
 WDW EM  
 SSB 0  
 LB 0.30 Hz  
 GB 0  
 PC 1.00



<sup>1</sup>H NMR (CDCl<sub>3</sub> with 0.03% v/v TMS, 600 MHz)

APPENDIX B:  $^{13}\text{C}$  NMR Spectra



<sup>13</sup>C NMR (CDCl<sub>3</sub> with 0.03% v/v TMS, 600 MHz)

Current Data Parameters  
 NAME TNM-IV-75-1  
 EXPNO 3  
 PROCNO 1

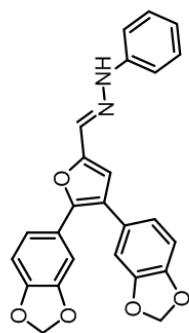
F2 - Acquisition Parameters  
 Date\_ 20180730  
 Time 7.57  
 INSTRUM spect  
 PROBHD 5 mm FATXI 1H/  
 PULPROG zgpg30  
 TD 65536  
 SOLVENT DMSO  
 NS 10240  
 DS 4  
 SWH 36057.691 Hz  
 FIDRES 0.550197 Hz  
 AQ 0.9087659 sec  
 RG 2050  
 DW 13.867 usec  
 DE 6.50 usec  
 TE 298.1 K  
 D1 2.0000000 sec  
 D11 0.0300000 sec  
 TD0 1

==== CHANNEL f1 =====  
 SFO1 150.9178981 MHz  
 NUC1 13C  
 P1 12.00 usec  
 PLW1 190.36999512 W

==== CHANNEL f2 =====  
 SFO2 600.1324005 MHz  
 NUC2 1H  
 CPDPRG[2] waltz16  
 PCPD2 70.00 usec  
 PLW2 11.74899960 W  
 PLW12 0.24169999 W  
 PLW13 0.12157000 W

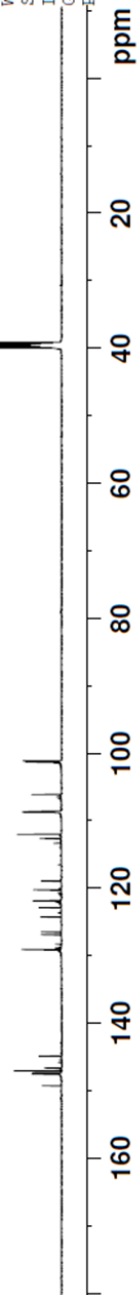
F2 - Processing parameters  
 SI 32768  
 SF 150.9028839 MHz  
 WDW EM  
 SSB 0  
 LB 0 1.00 Hz  
 GB 0  
 PC 1.40

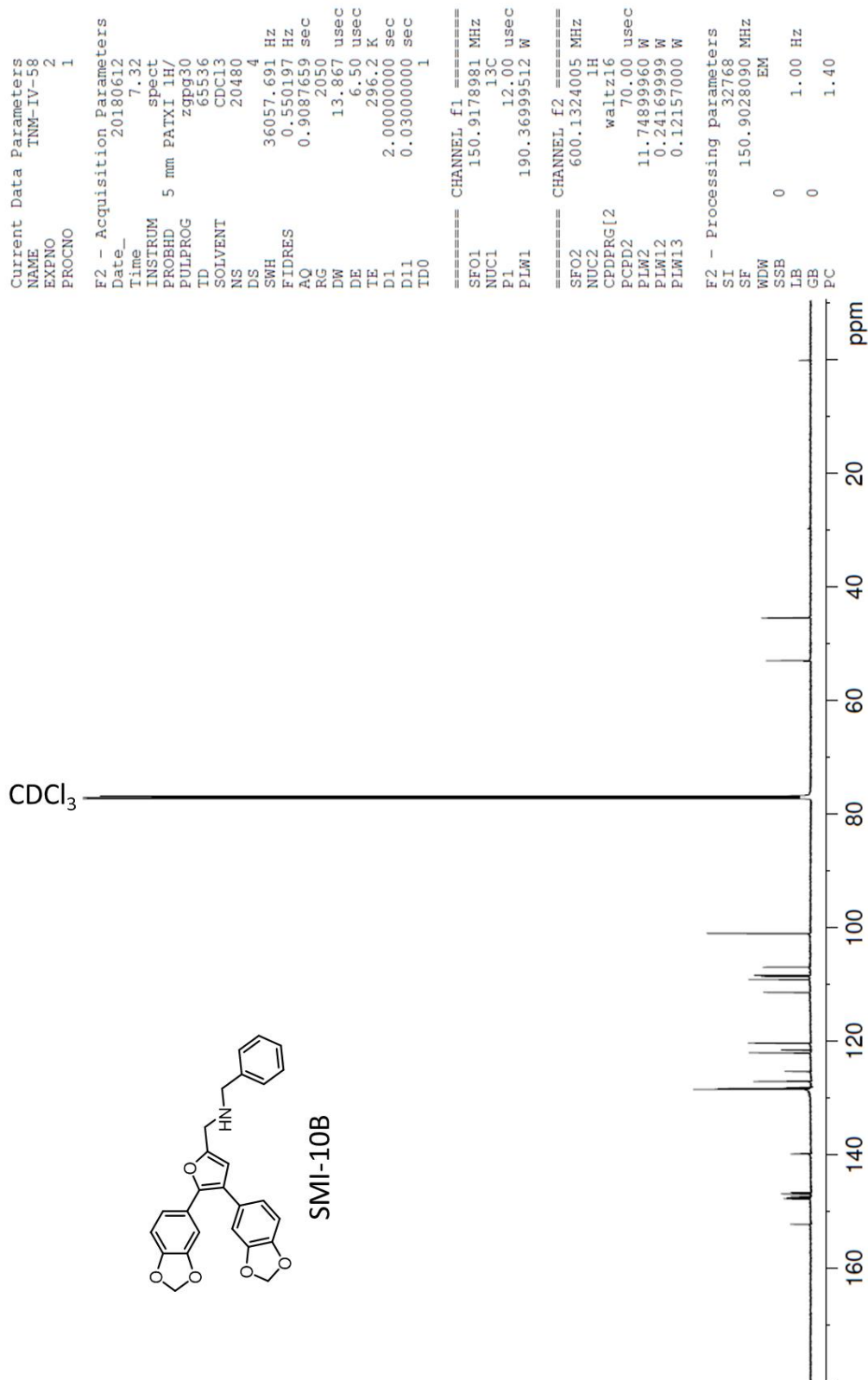
DMSO-d<sub>6</sub>



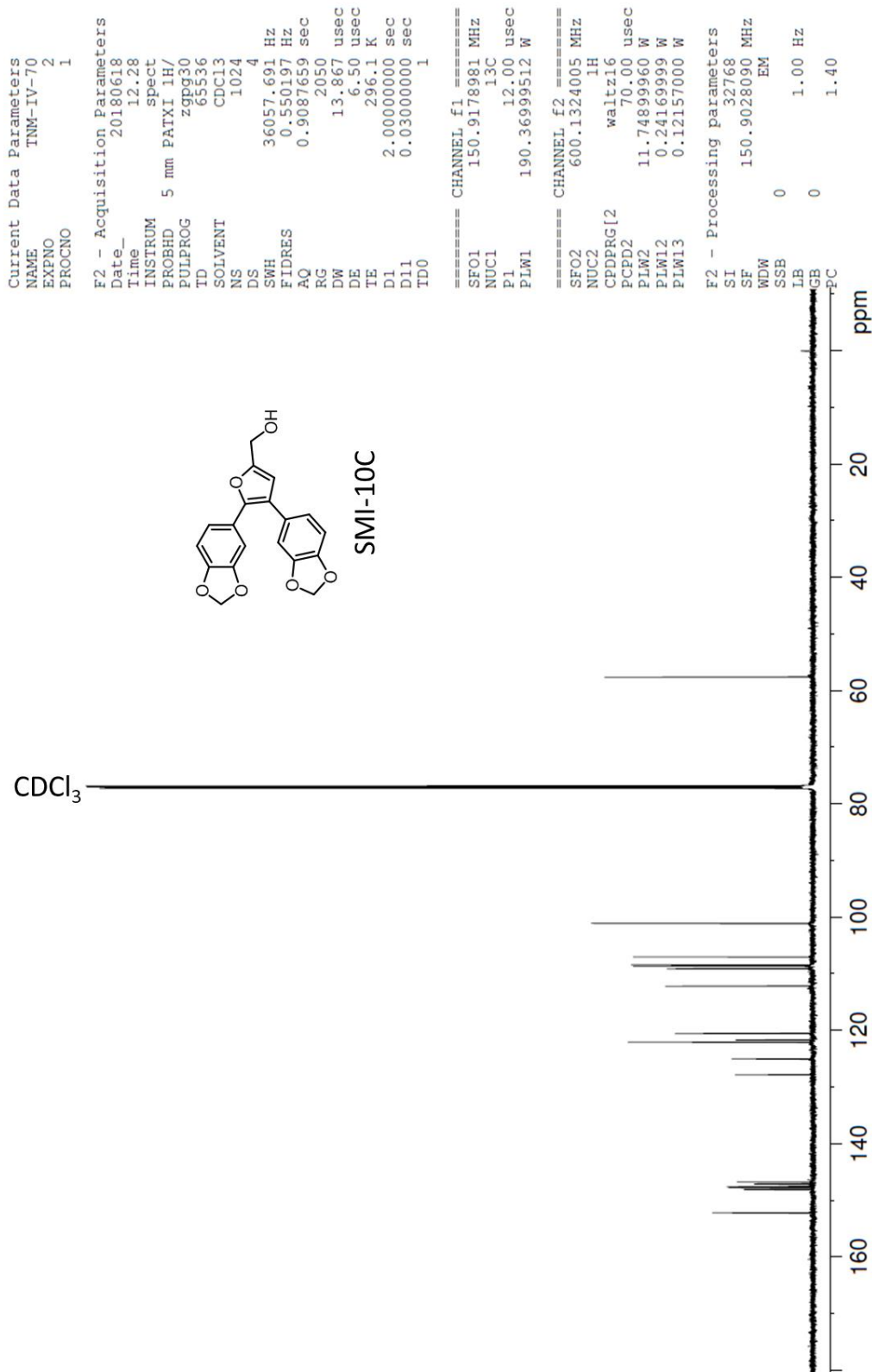
SMI-10A

<sup>13</sup>C NMR (DMSO-d<sub>6</sub>, 600 MHz)





<sup>13</sup>C NMR (CDCl<sub>3</sub> with 0.03% v/v TMS, 600 MHz)



<sup>13</sup>C NMR (CDCl<sub>3</sub> with 0.03% v/v TMS, 600 MHz)

Current Data Parameters  
 NAME TNM-IV-69-10J  
 EXPNO 2  
 PROCNO 1

F2 - Acquisition Parameters

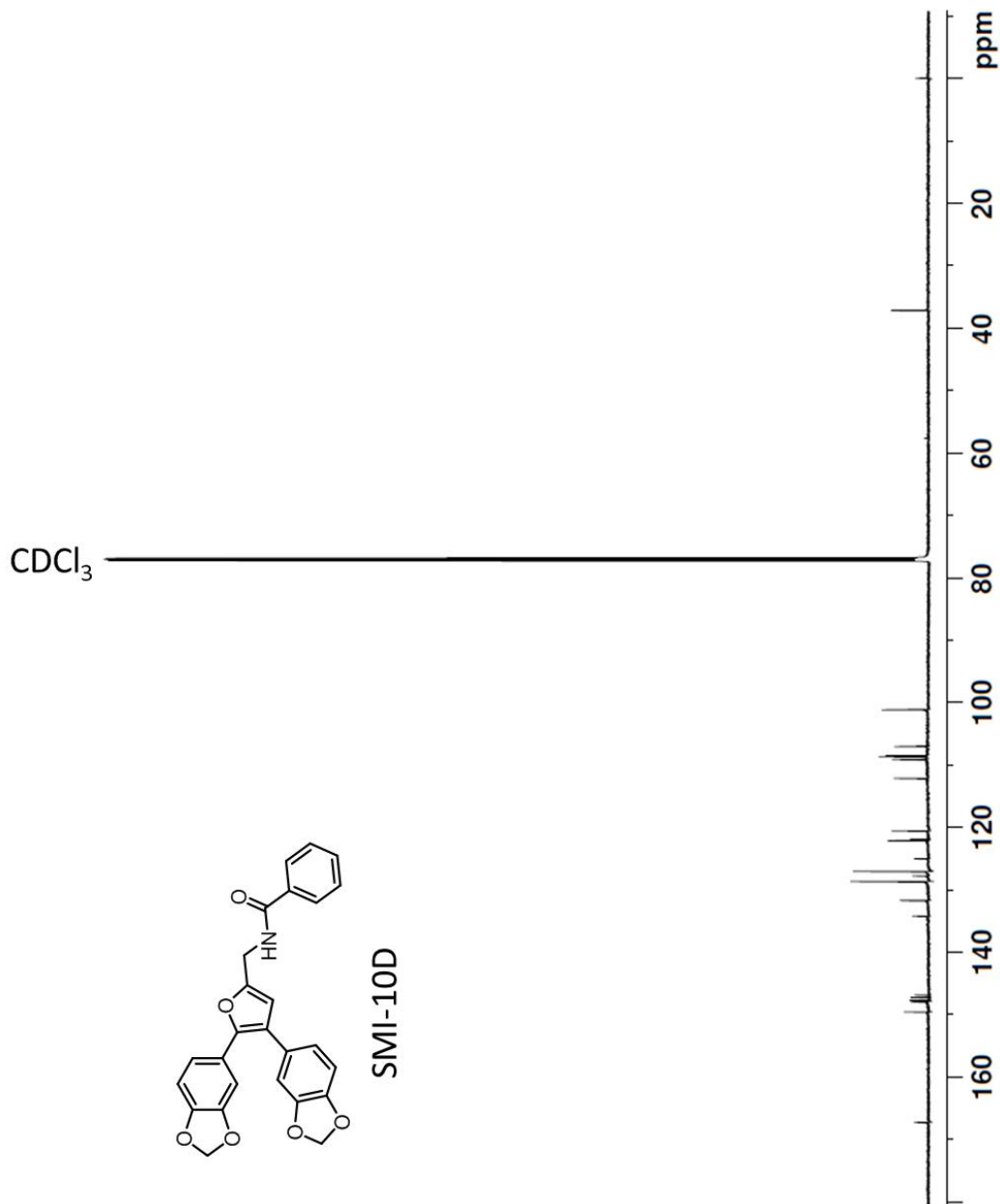
Date\_ 20180803  
 Time\_ 6.46  
 INSTRUM spect  
 PROBH 5 mm PAIXI 1H/  
 PULPROG zgpg30  
 TD 65536  
 SOLVENT CDCl3  
 NS 20480  
 DS 4  
 SWH 36057.691 Hz  
 FIDRES 0.550197 Hz  
 AQ 0.9087659 sec  
 RG 2050  
 DW 13.867 usec  
 DE 6.50 usec  
 TE 298.1 K  
 D1 2.0000000 sec  
 D11 0.0300000 sec  
 TD0 1

==== CHANNEL f1 =====  
 SFO1 150.9178981 MHz  
 NUC1 13C  
 P1 12.00 usec  
 PLW1 190.36999512 W

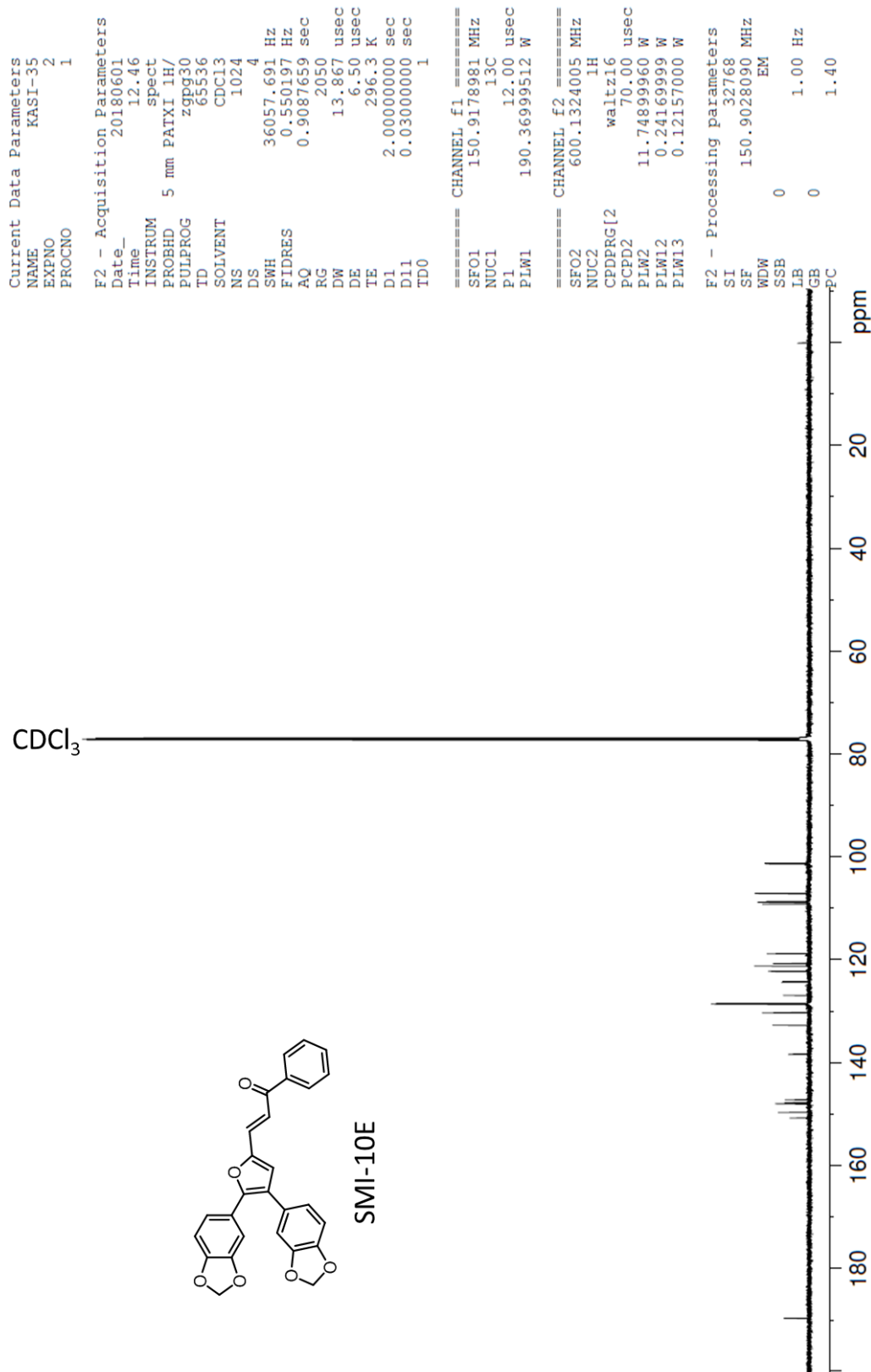
==== CHANNEL f2 =====  
 SFO2 600.1324005 MHz  
 NUC2 1H  
 CPDPRG2 waitz16  
 PCPD2 70.00 usec  
 PLW2 11.74899960 W  
 PLW12 0.24169999 W  
 PLW13 0.12157000 W

F2 - Processing parameters

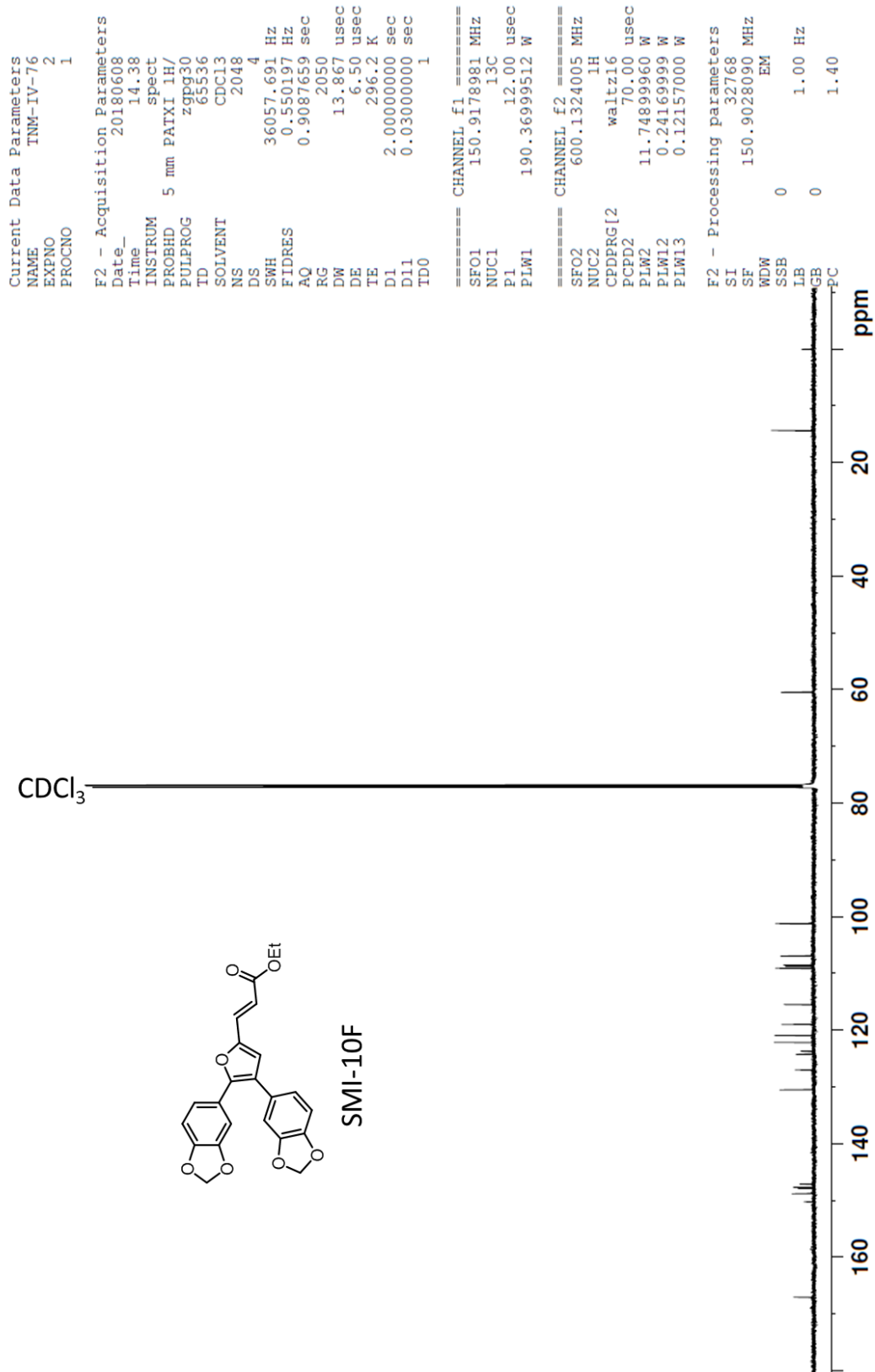
SI 32768  
 SF 150.9028090 MHz  
 WDW EM  
 SSB 0  
 LB 1.00 Hz  
 GB 0  
 PC 1.40



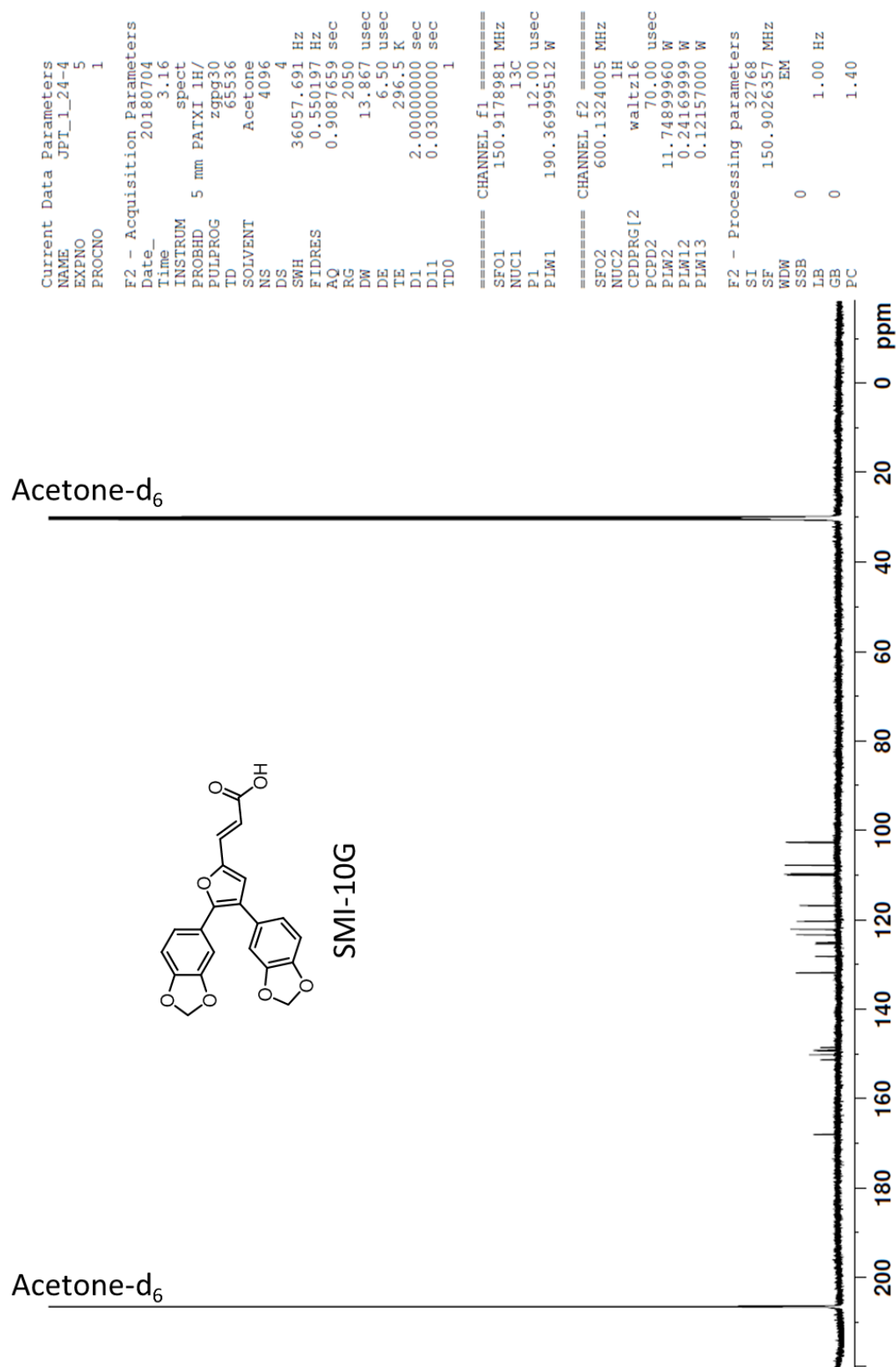
<sup>13</sup>C NMR (CDCl<sub>3</sub> with 0.03% v/v TMS, 600 MHz)



<sup>13</sup>C NMR (CDCl<sub>3</sub> with 0.03% v/v TMS, 600 MHz)



<sup>13</sup>C NMR (CDCl<sub>3</sub> with 0.03% v/v TMS, 600 MHz)



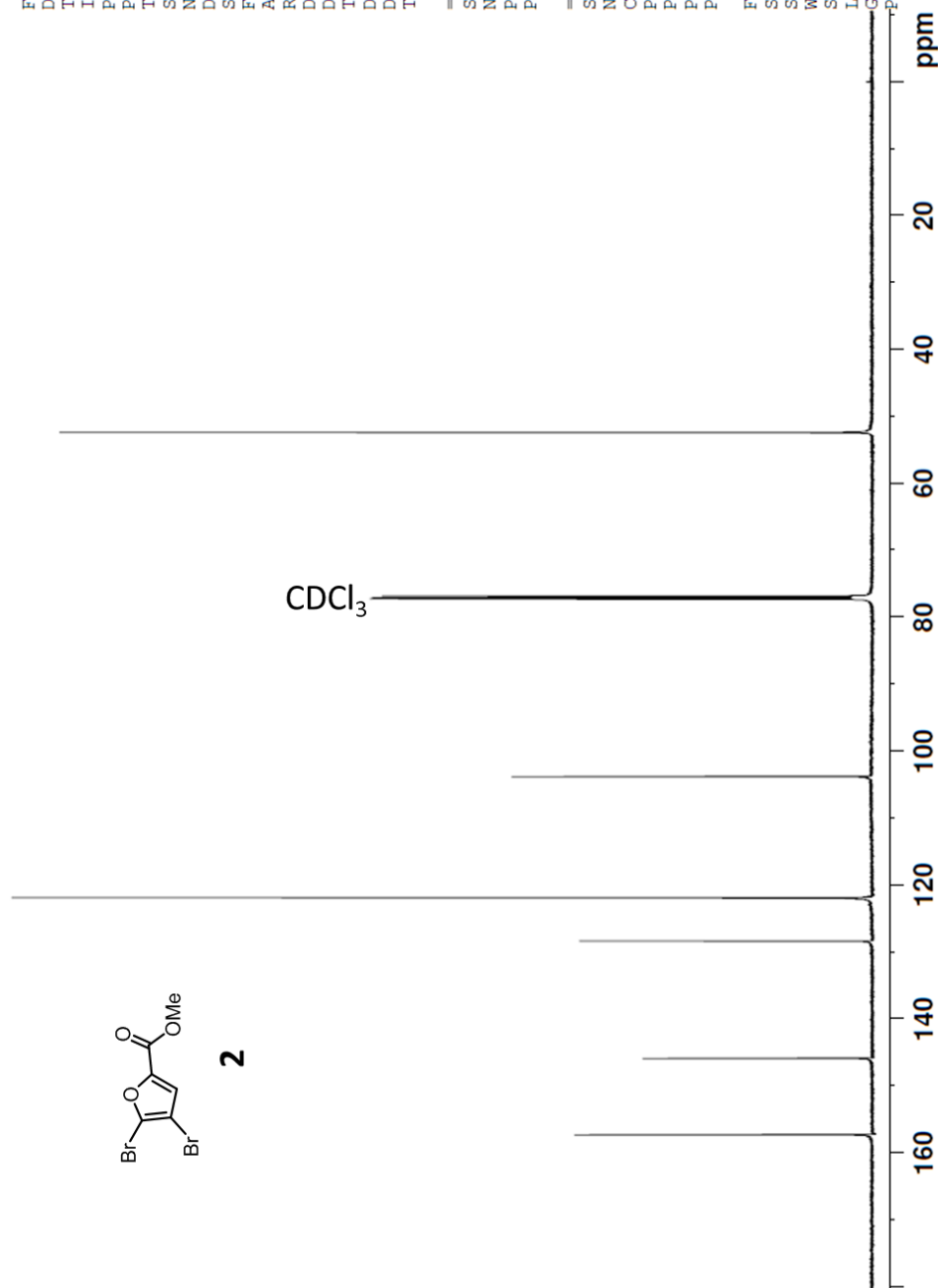
Current Data Parameters  
 NAME TNM-SJAI-54  
 EXPNO 1  
 PROCNO 1

F2 - Acquisition Parameters  
 Date\_ 20180724  
 Time 0.15  
 INSTRUM spect  
 PROBHD 5 mm PAIXI 1H/  
 PULPROG zgpg30  
 TD 65536  
 SOLVENT CDCl3  
 NS 10240  
 DS 4  
 SWH 36057.691 Hz  
 FIDRES 0.550197 Hz  
 AQ 0.9087659 sec  
 RG 2050  
 DW 13.867 usec  
 DE 6.50 usec  
 TE 298.1 K  
 D1 2.00000000 sec  
 D11 0.10300000 sec  
 ID0 1

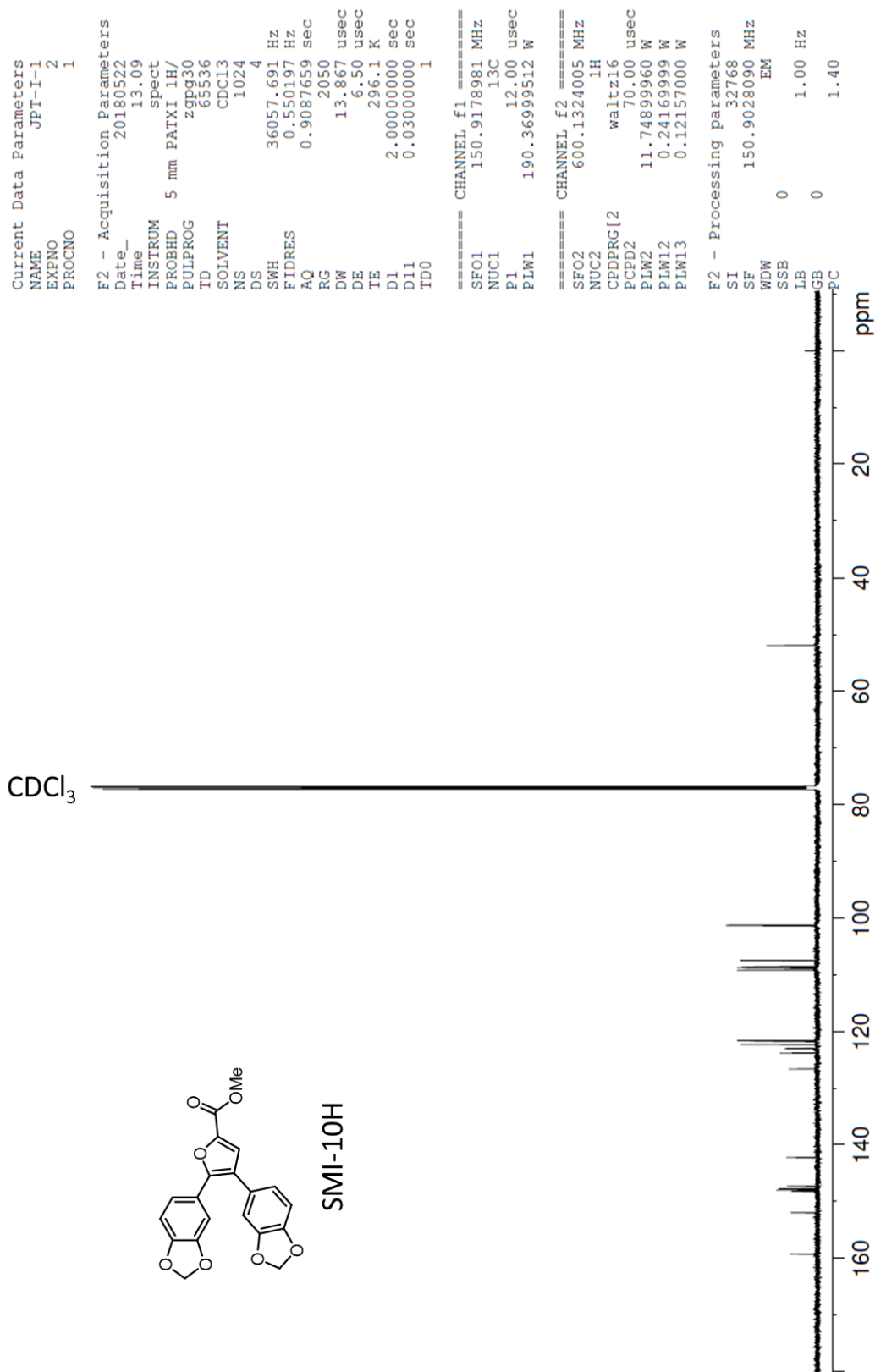
==== CHANNEL f1 =====  
 SFO1 150.9178981 MHz  
 NUC1 13C  
 P1 12.00 usec  
 PLW1 190.36999512 W

==== CHANNEL f2 =====  
 SFO2 600.1324005 MHz  
 NUC2 1H  
 CPDPRG12 waltz16  
 PCPD2 70.00 usec  
 PLW2 11.74899960 W  
 PLW12 0.24169999 W  
 PLW13 0.12157000 W

F2 - Processing parameters  
 SI 32768  
 SF 150.9028090 MHz  
 WDW EM  
 SSB 0  
 LB 1.00 Hz  
 GB 0  
 PC 1.40



<sup>13</sup>C NMR (CDCl<sub>3</sub> with 0.03% v/v TMS, 600 MHz)



<sup>13</sup>C NMR (CDCl<sub>3</sub> with 0.03% v/v TMS, 600 MHz)

Current Data Parameters  
 NAME KASI-69-Pure-101  
 EXPNO 3  
 PROCNO 1

F2 - Acquisition Parameters

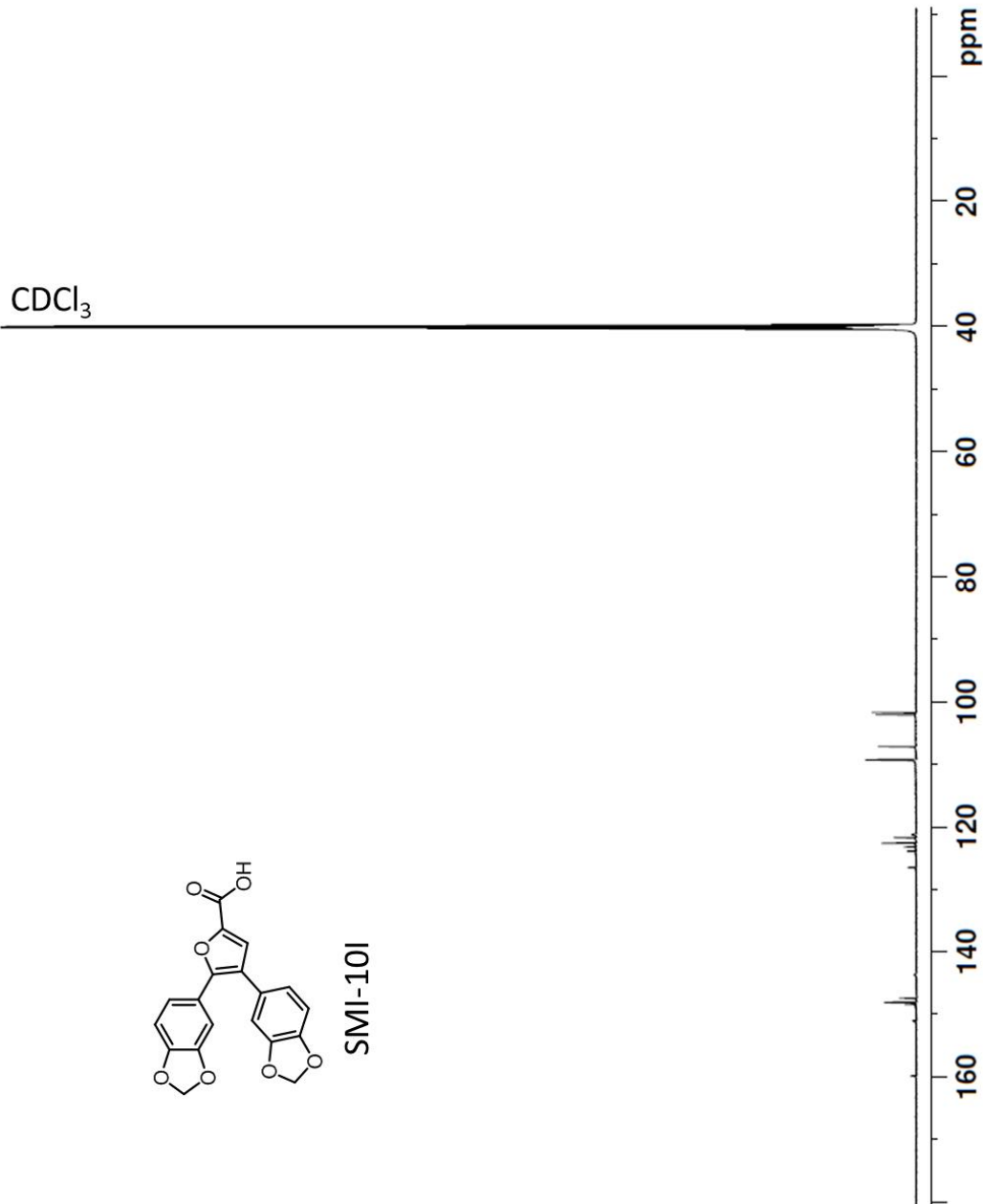
Date\_ 20180804  
 Time 8.36  
 INSTRUM spect  
 PROBHD 5 mm PATXI 1H/  
 PULPROG zgpg30  
 TD 65536  
 SOLVENT DMSO  
 NS 25600  
 DS 4  
 SWH 36057.691 Hz  
 FIDRES 0.550197 Hz  
 AQ 0.9087659 sec  
 RG 2050  
 DW 13.867 usec  
 DE 6.50 usec  
 TE 298.1 K  
 D1 2.00000000 sec  
 D11 0.03000000 sec  
 TD0 1

==== CHANNEL f1 =====  
 SFO1 150.9178981 MHz  
 NUC1 13C  
 P1 12.00 usec  
 PLW1 190.36999512 W

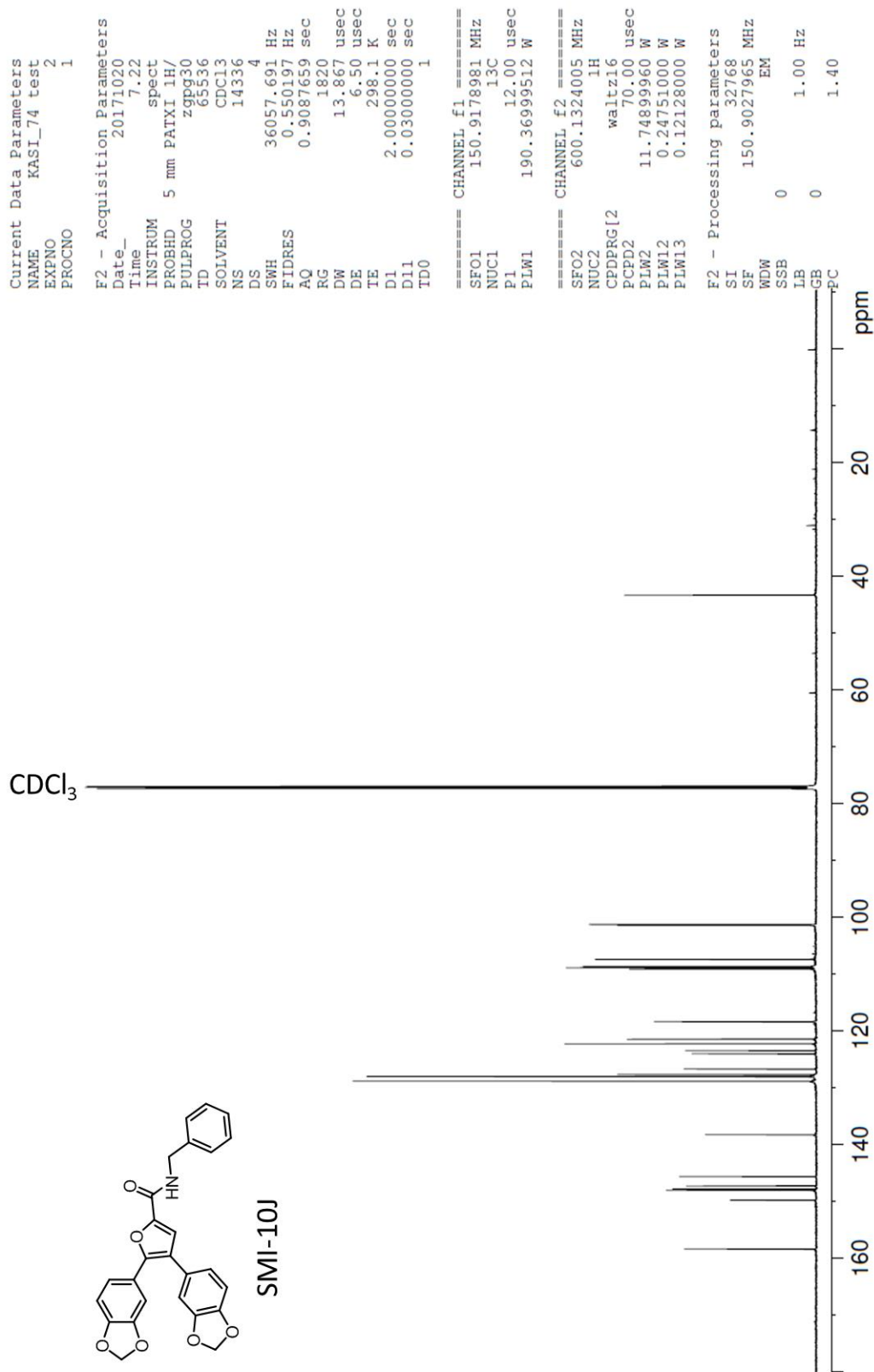
==== CHANNEL f2 =====  
 SFO2 600.1324005 MHz  
 NUC2 1H  
 CPDPRG[2] waltz16  
 PCPD2 70.00 usec  
 PLW2 11.74899960 W  
 PLW12 0.24169999 W  
 PLW13 0.12157000 W

F2 - Processing parameters

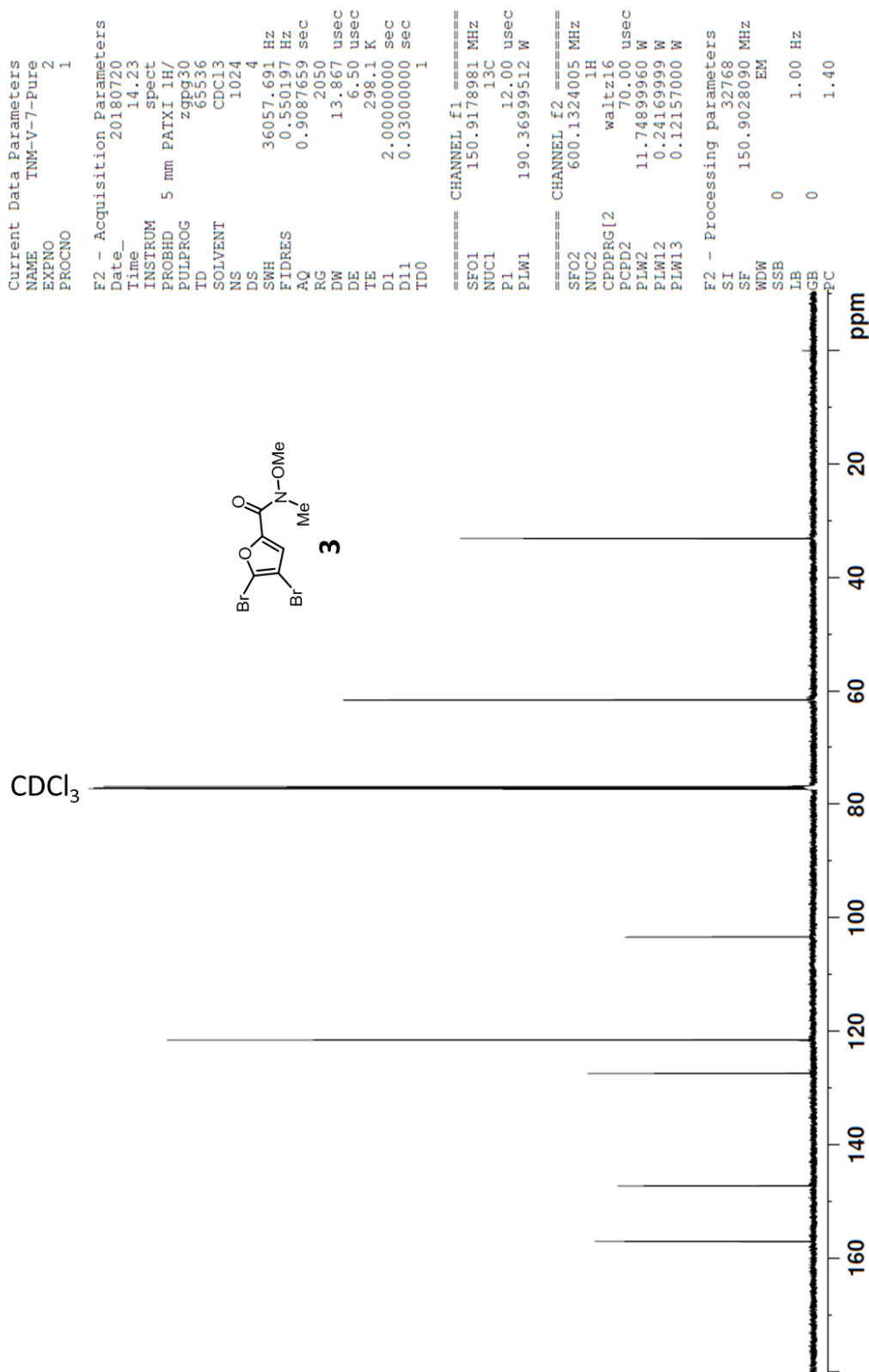
SI 32768  
 SF 150.9028090 MHz  
 WDW EM  
 SSB 0  
 LB 1.00 Hz  
 GB 0  
 PC 1.40



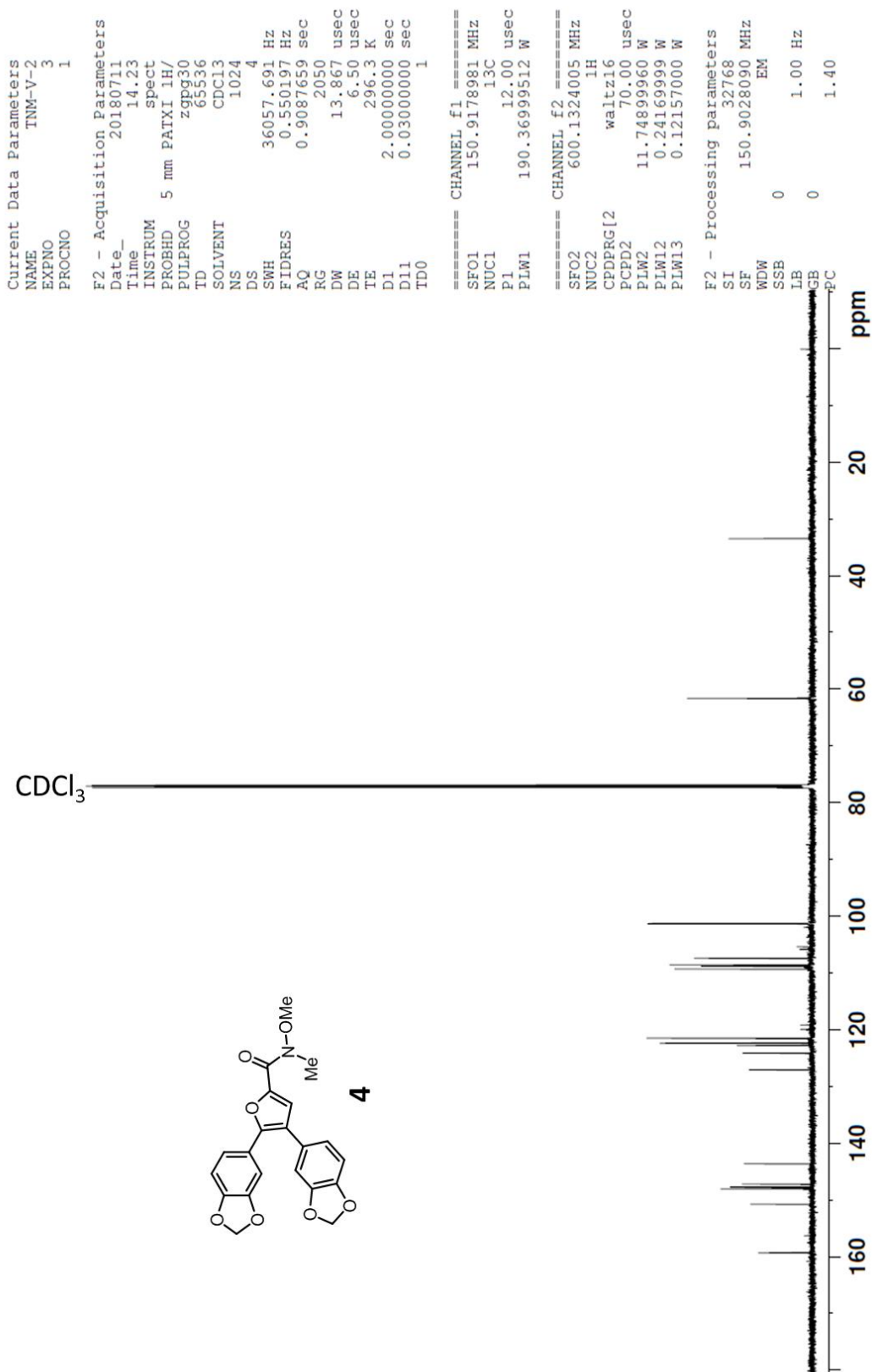
<sup>13</sup>C NMR (CDCl<sub>3</sub> with 0.03% v/v TMS, 600 MHz)



<sup>13</sup>C NMR (CDCl<sub>3</sub> with 0.03% v/v TMS, 600 MHz)



<sup>13</sup>C NMR (CDCl<sub>3</sub> with 0.03% v/v TMS, 600 MHz)



<sup>13</sup>C NMR (CDCl<sub>3</sub> with 0.03% v/v TMS, 600 MHz)

```

Current Data Parameters
NAME      TNM-IV-79
EXPNO    2
PROCNO   1

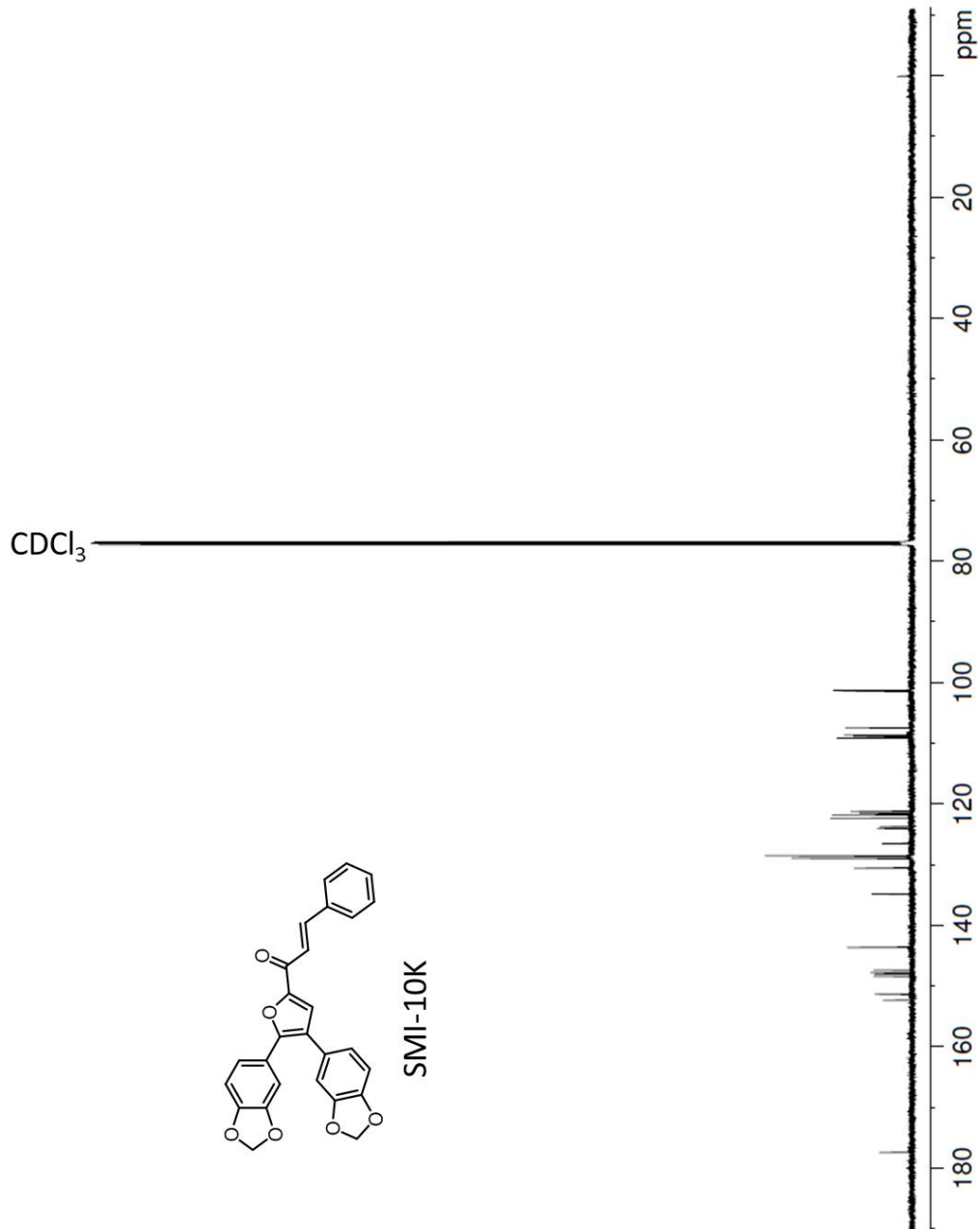
F2 - Acquisition Parameters
Date_    20180615
Time     13.17
INSTRUM  spect
PROBHD   5 mm PAXI 1H/
PULPROG  zgpg30
TD       65536
SOLVENT  CDCl3
NS       1024
DS       4
SWH      36057.691 Hz
FIDRES   0.550197 Hz
AQ       0.9087659 sec
RG       2050
DW       13.867 usec
DE       6.50 usec
TE       296.0 K
D1       2.00000000 sec
D11      0.03000000 sec
ID0      1

===== CHANNEL f1 =====
SFO1    150.9178981 MHz
NUC1     13C
P1       12.00 usec
PLW1    190.36999512 W

===== CHANNEL f2 =====
SFO2    600.1324005 MHz
NUC2     1H
CPDPRG[2] waltz16
PCPD2    70.00 usec
PLW2    11.74899960 W
PLW12   0.24169999 W
PLW13   0.12157000 W

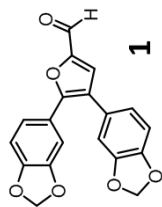
F2 - Processing parameters
SI       32768
SF       150.9028090 MHz
WDW      EM
SSB      0
LB       1.00 Hz
GB       0
PC       1.40

```

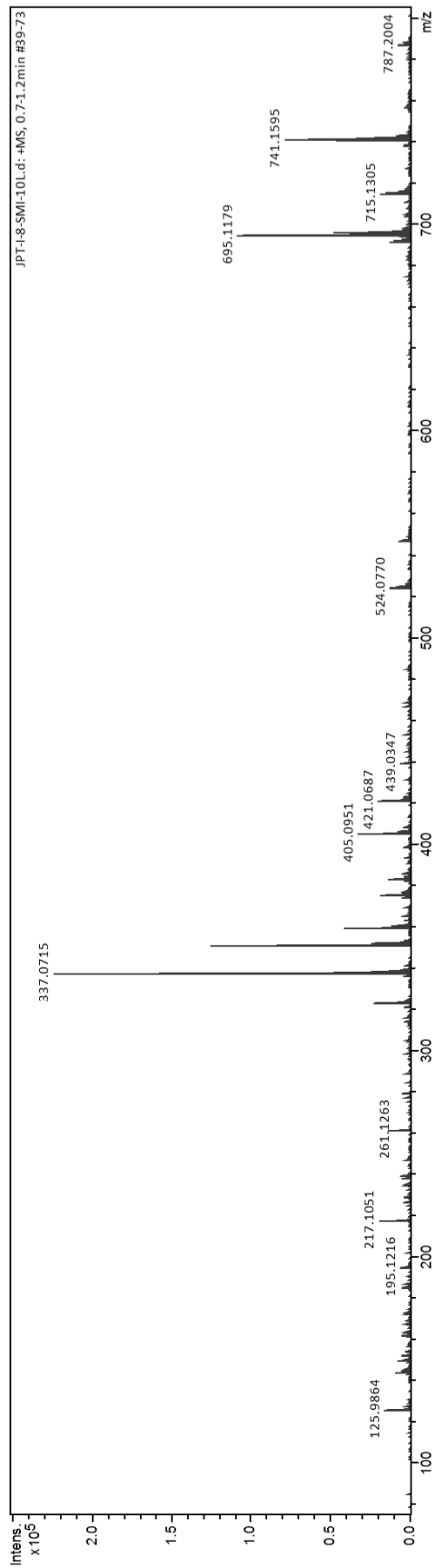


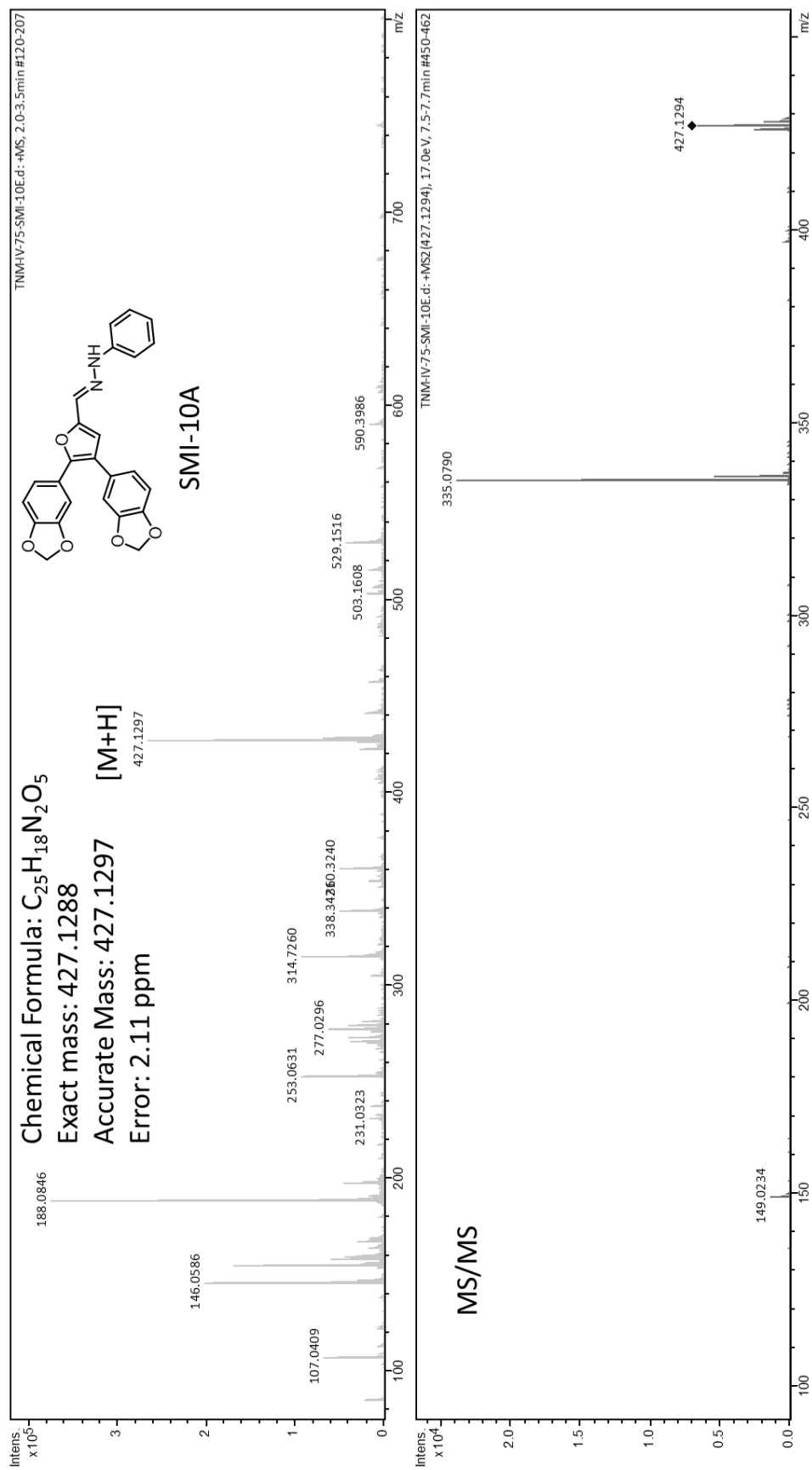
<sup>13</sup>C NMR (CDCl<sub>3</sub> with 0.03% v/v TMS, 600 MHz)

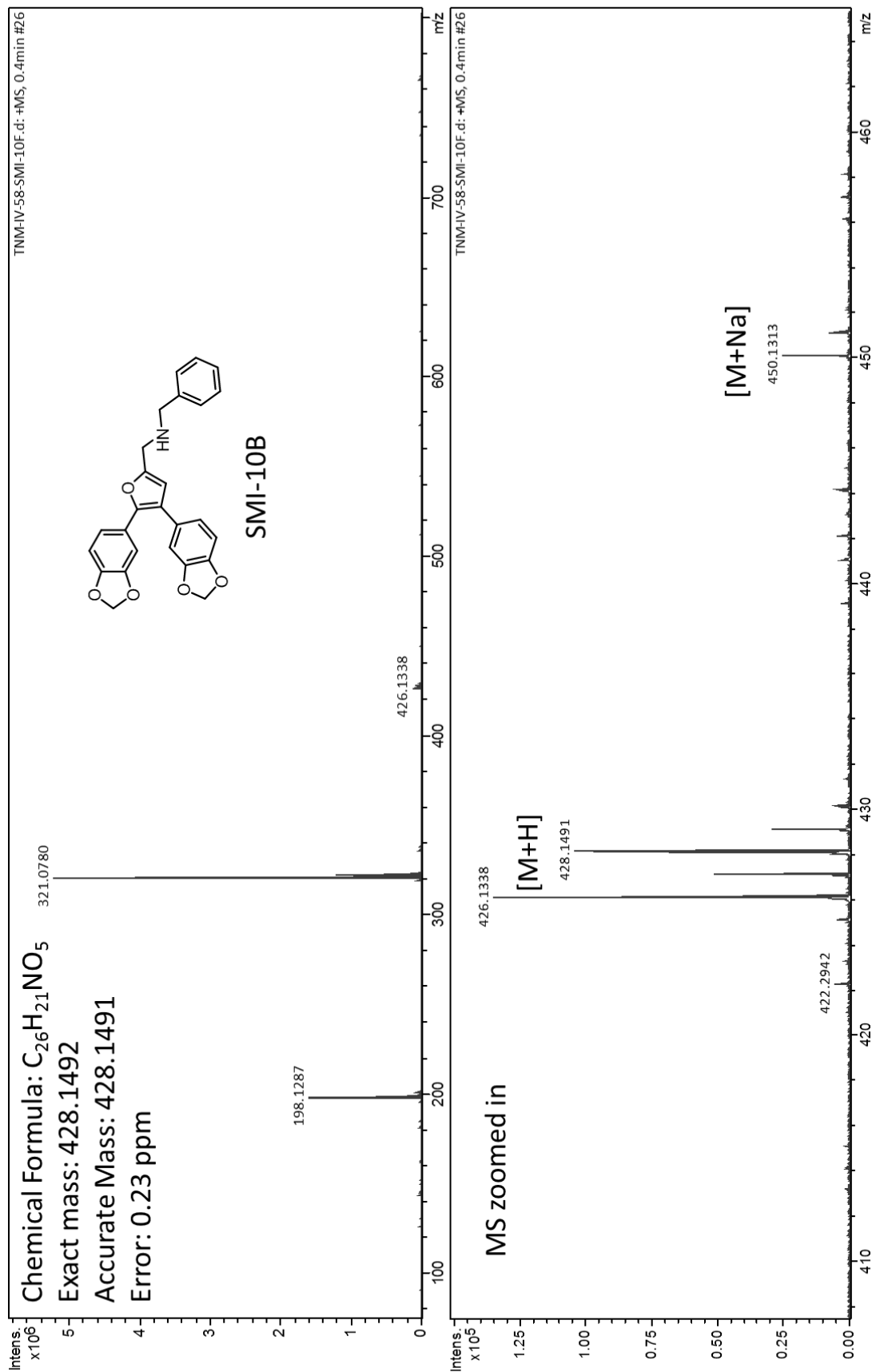
## APPENDIX C: MASS SPECTROMETRY



Chemical Formula:  $C_{19}H_{12}O_6$   
Exact mass: 337.0712  
Accurate Mass: 337.0715  
Error: 0.89 ppm







Chemical Formula:  $C_{19}H_{14}O_6$

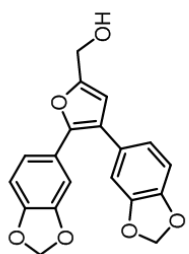
Exact mass: 339.0863

Accurate Mass [M+H]: Not Observed

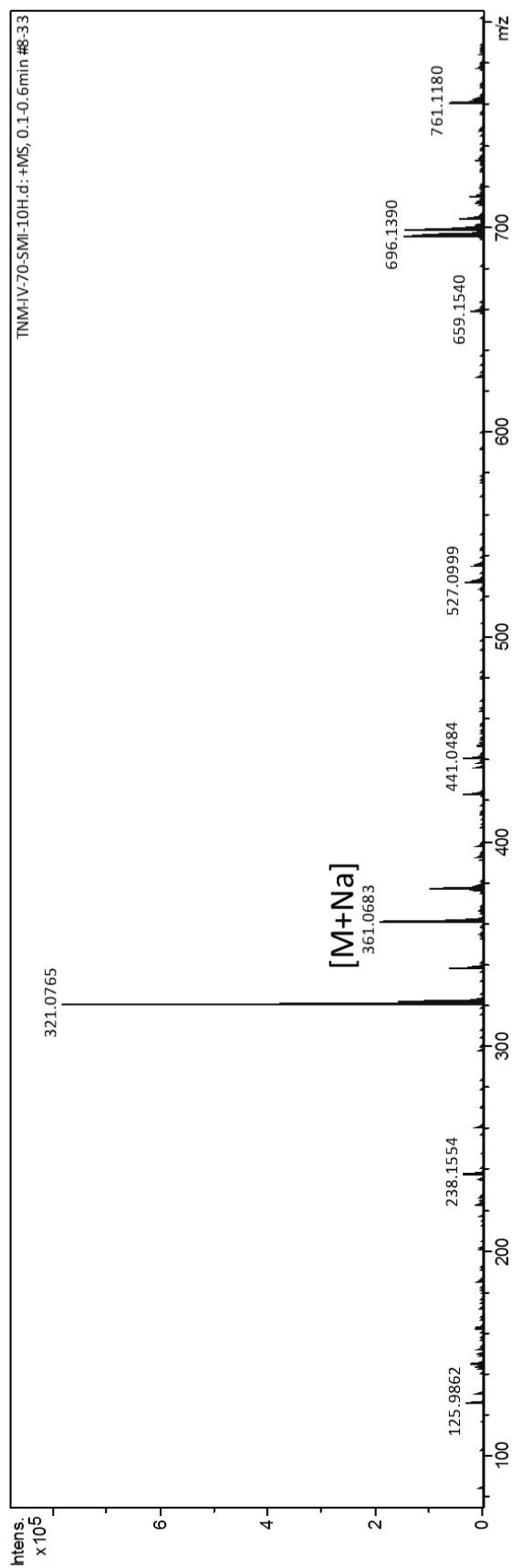
Exact Mass [M+Na]: 361.0682

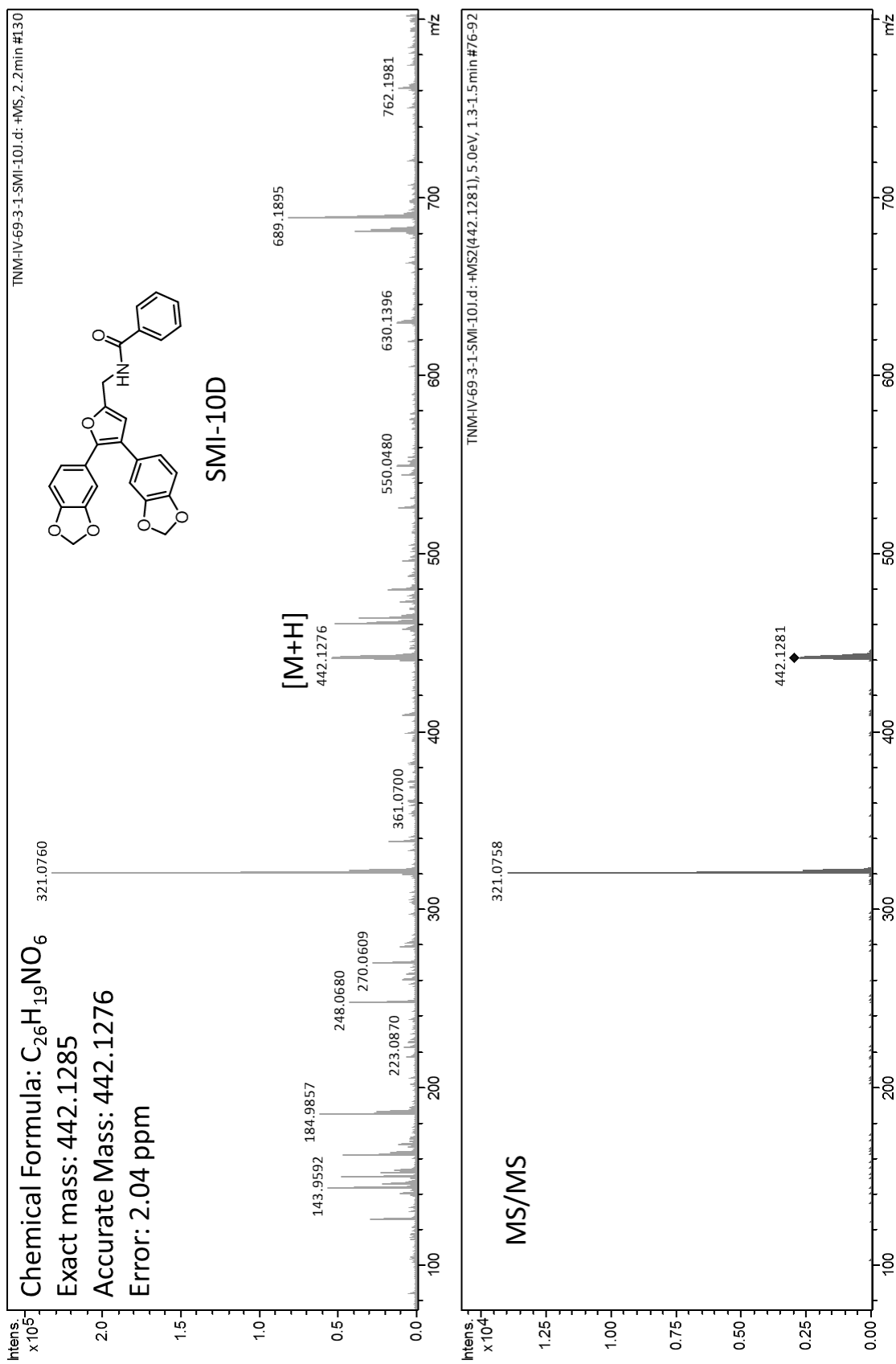
Accurate Mass [M+Na]: 361.0682

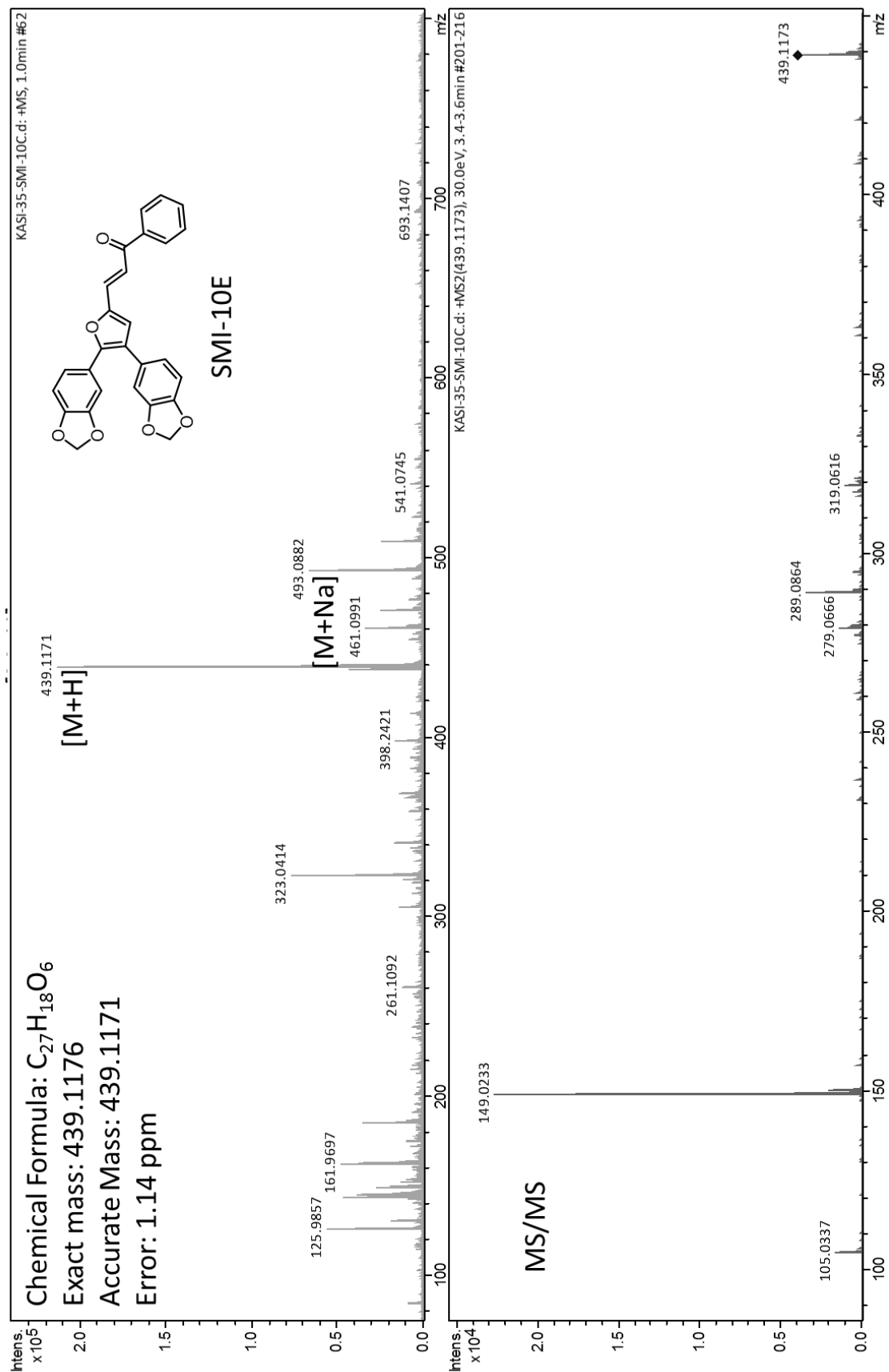
Error: 0 ppm

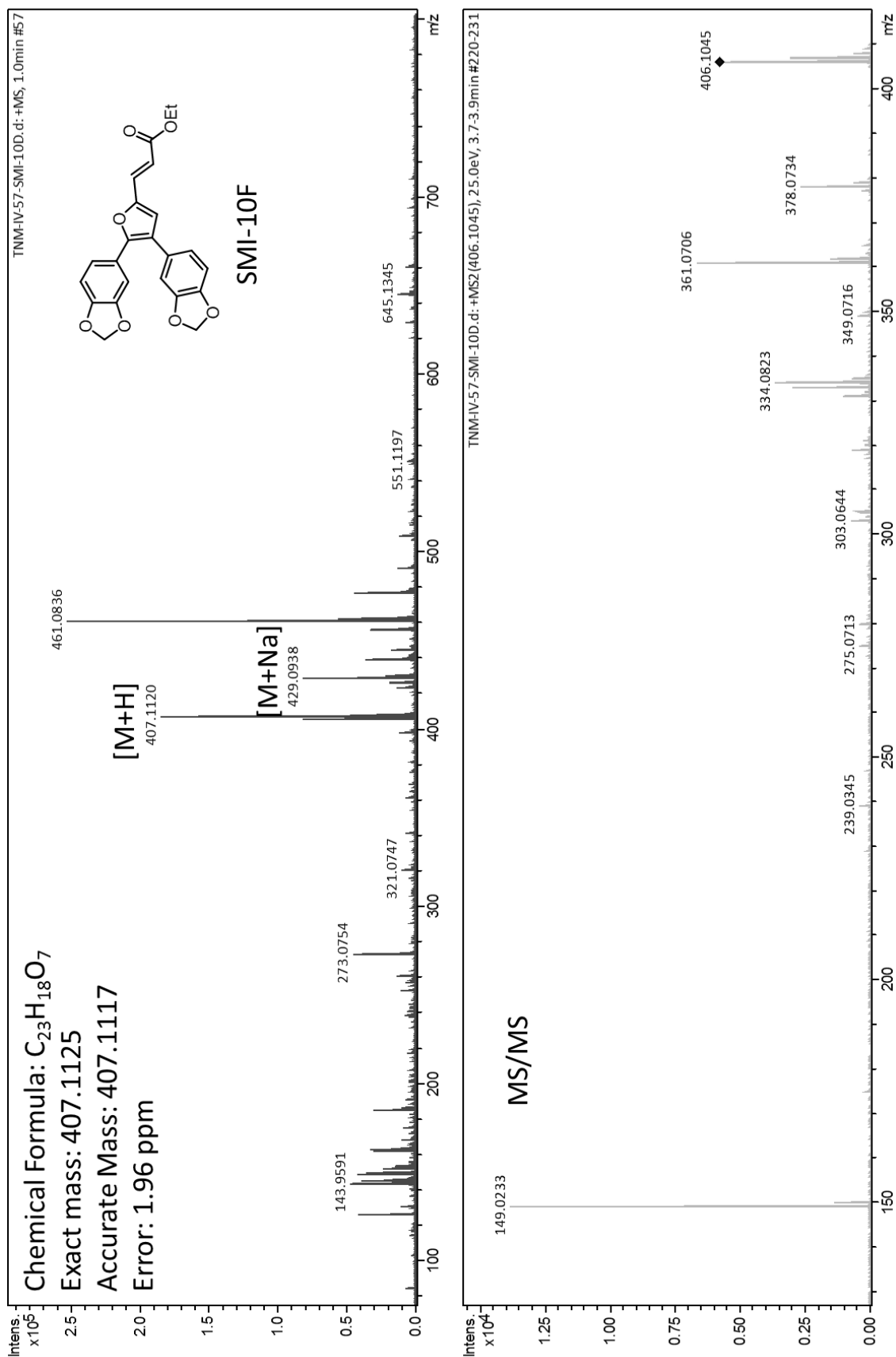


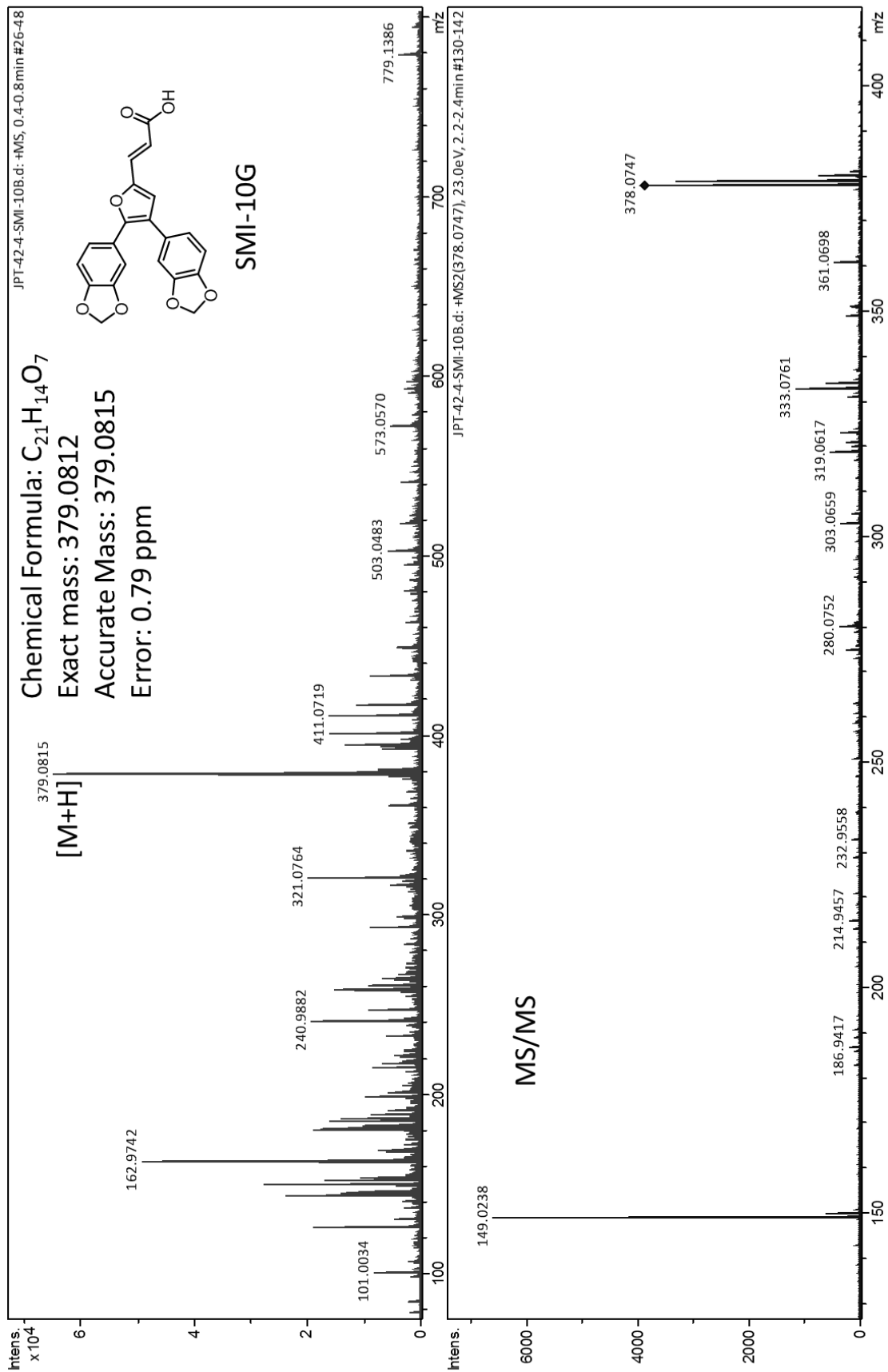
SMI-10C

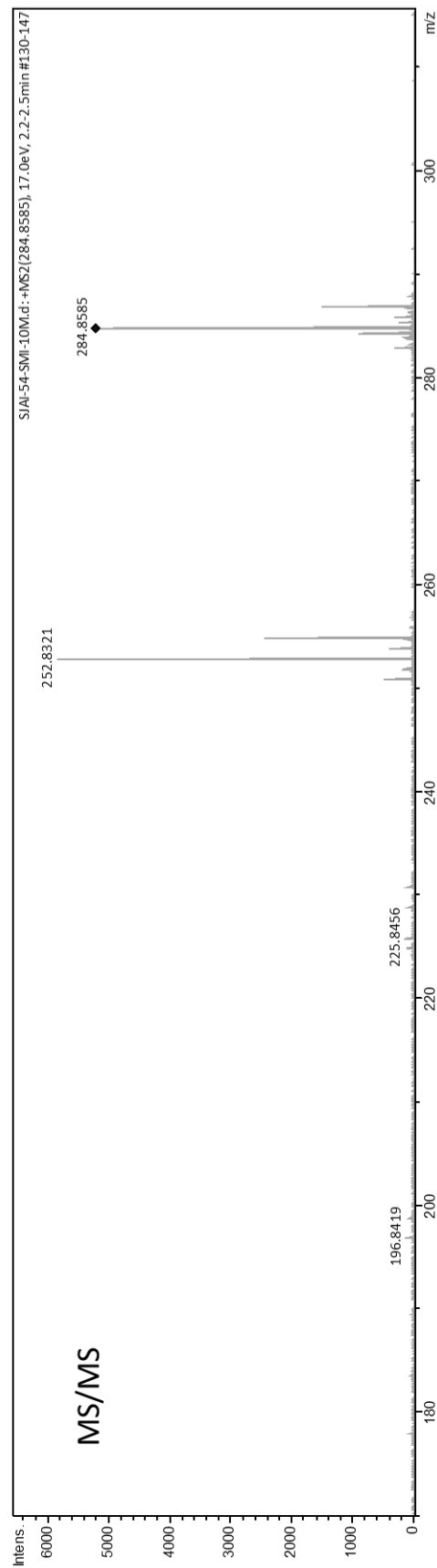
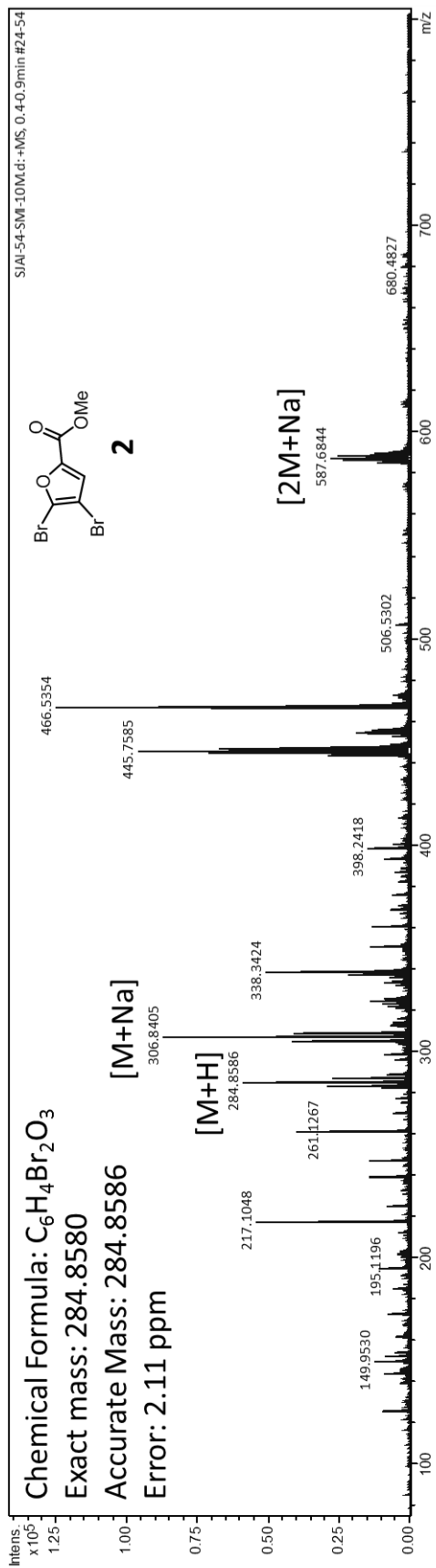


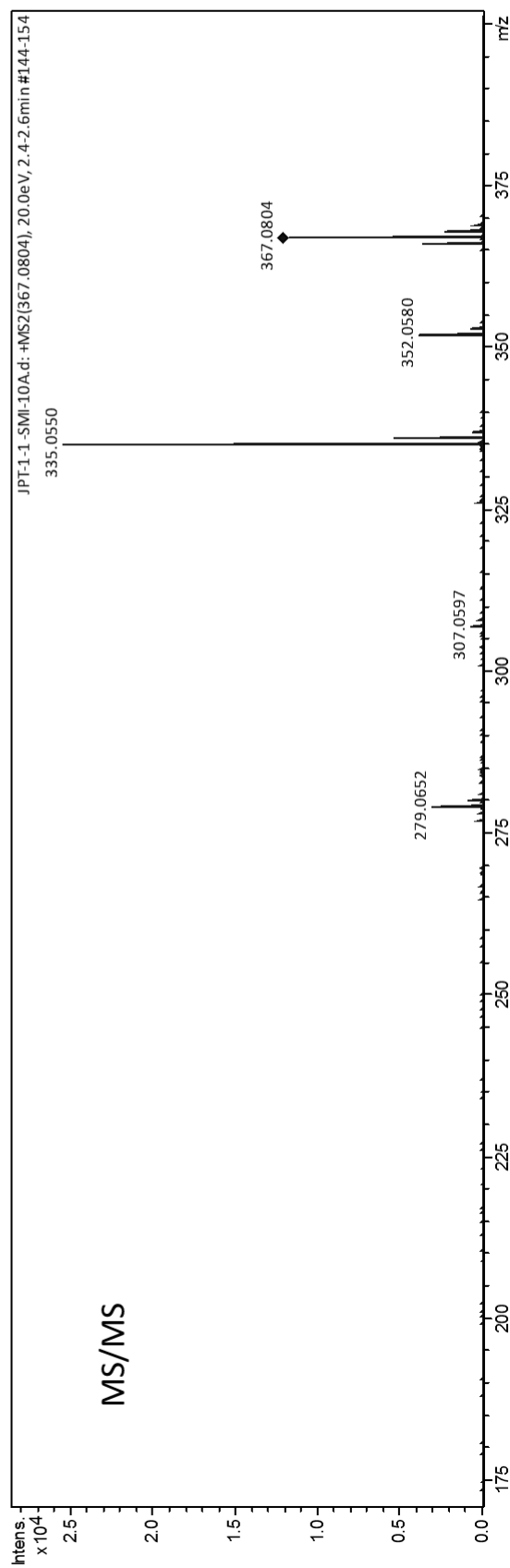
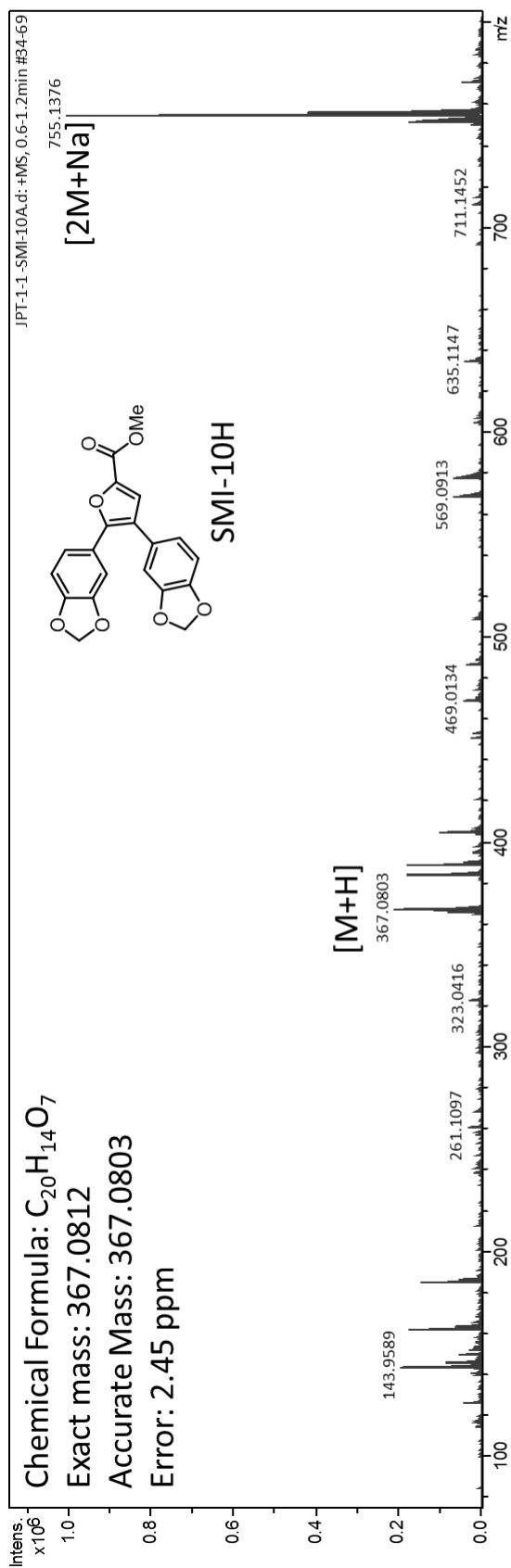


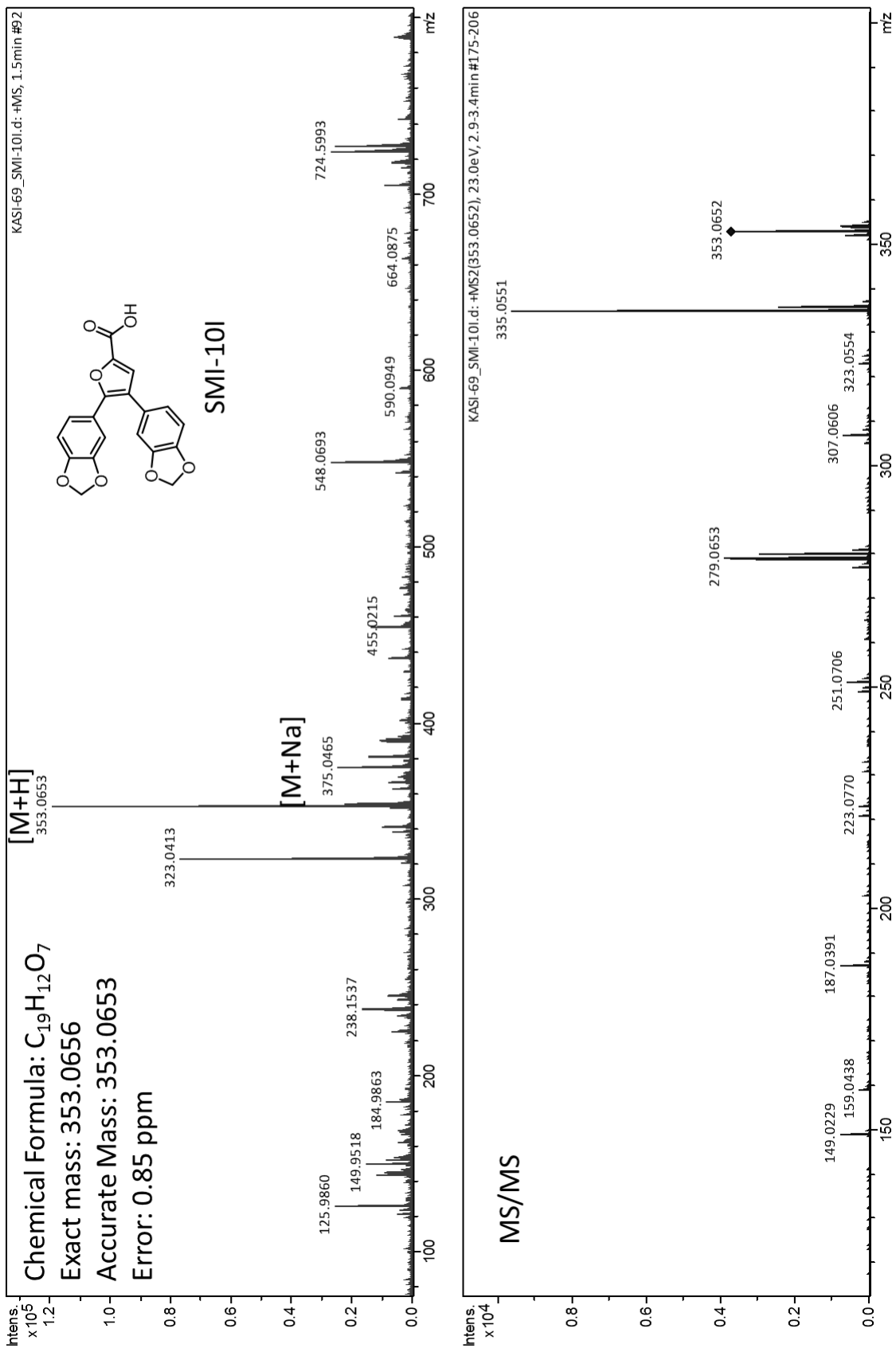


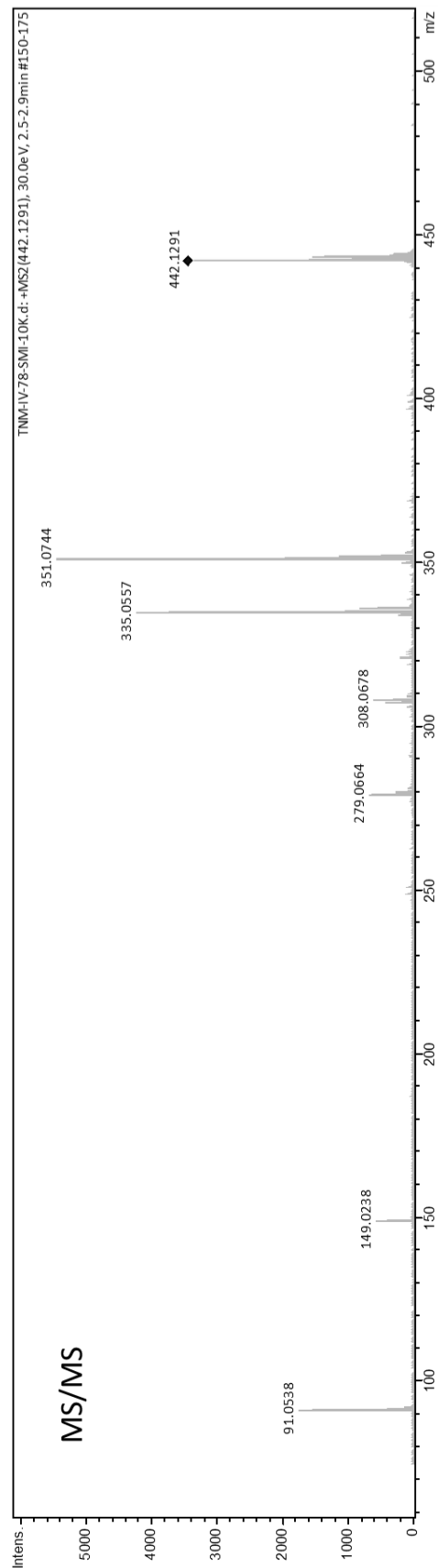
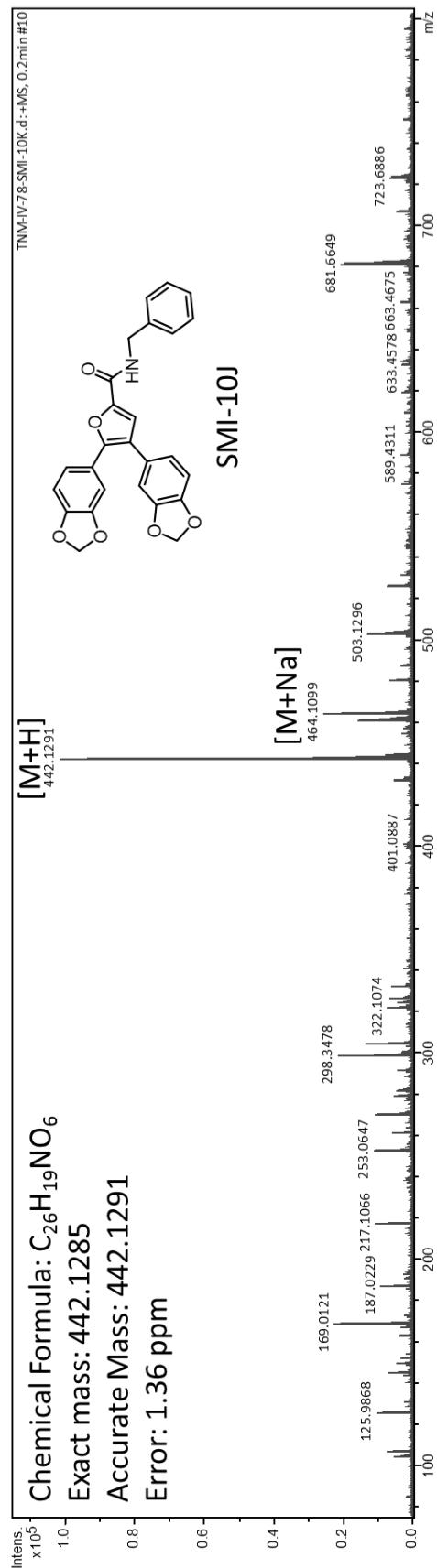


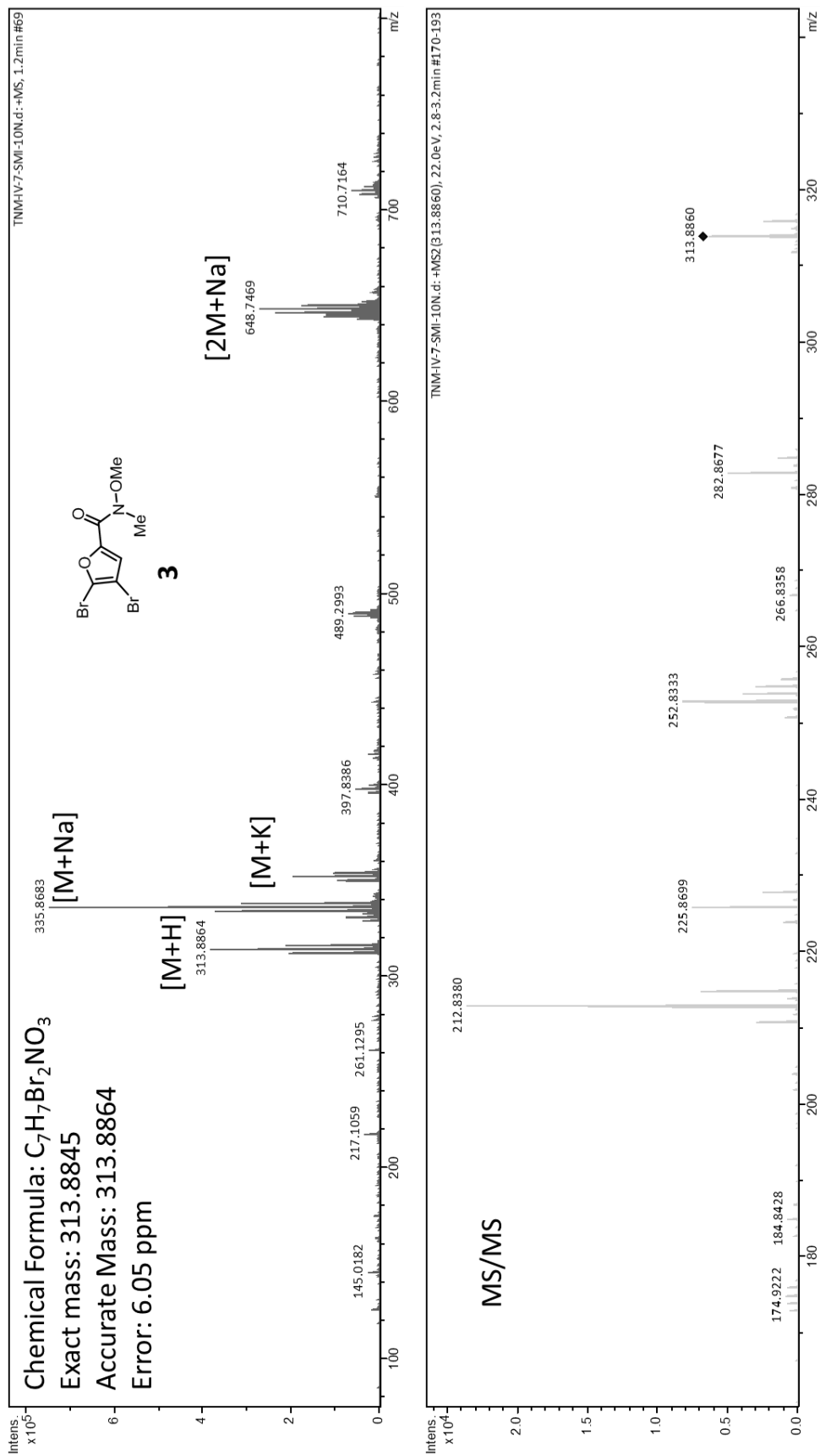


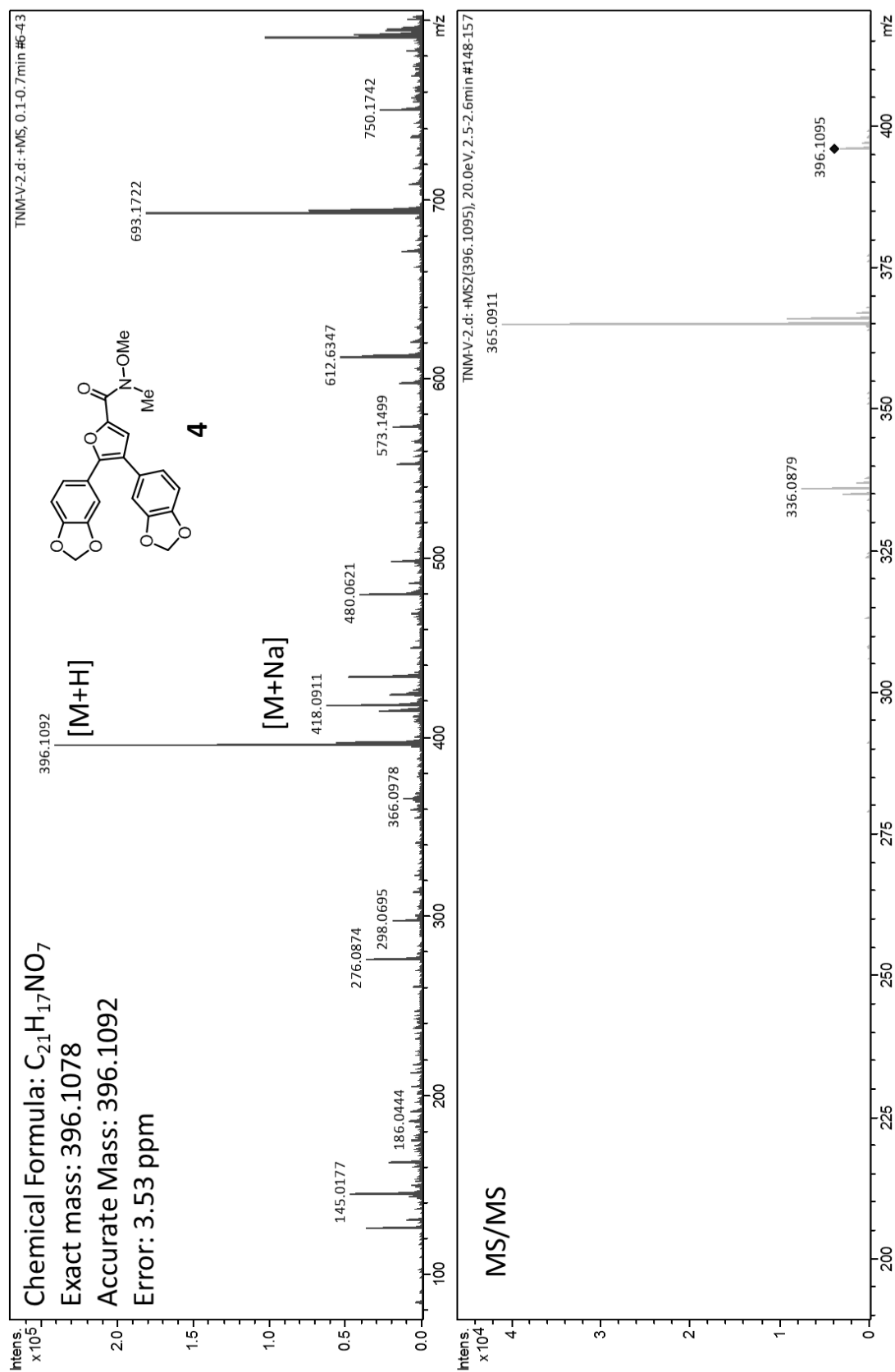


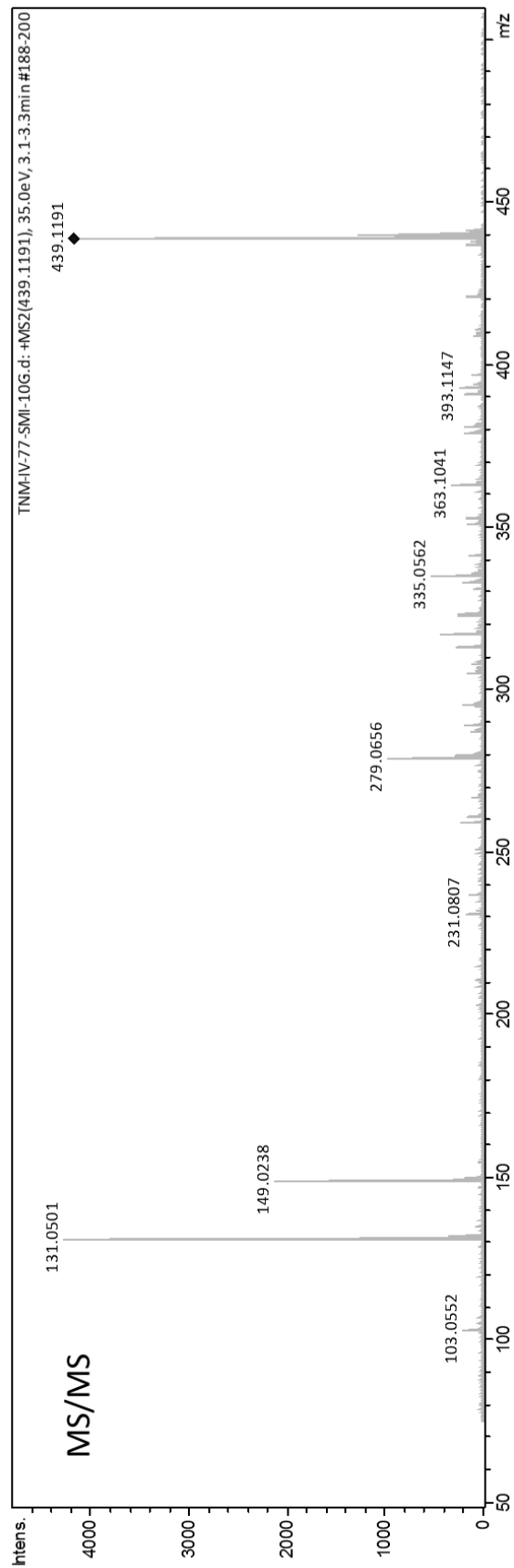
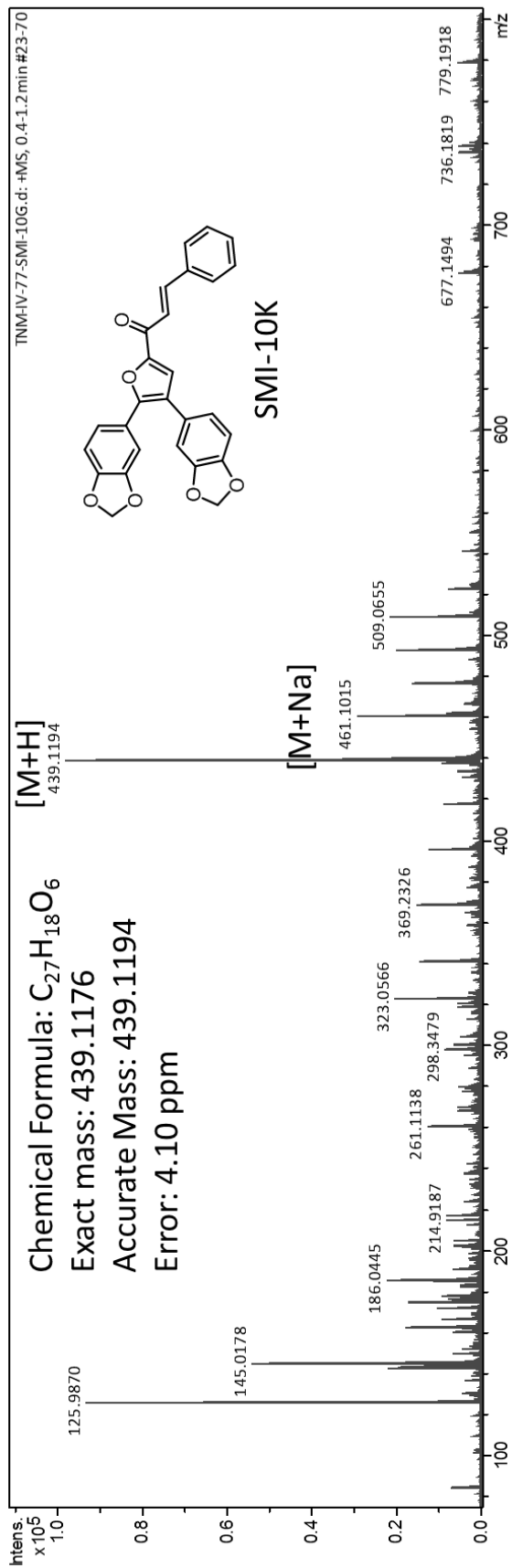




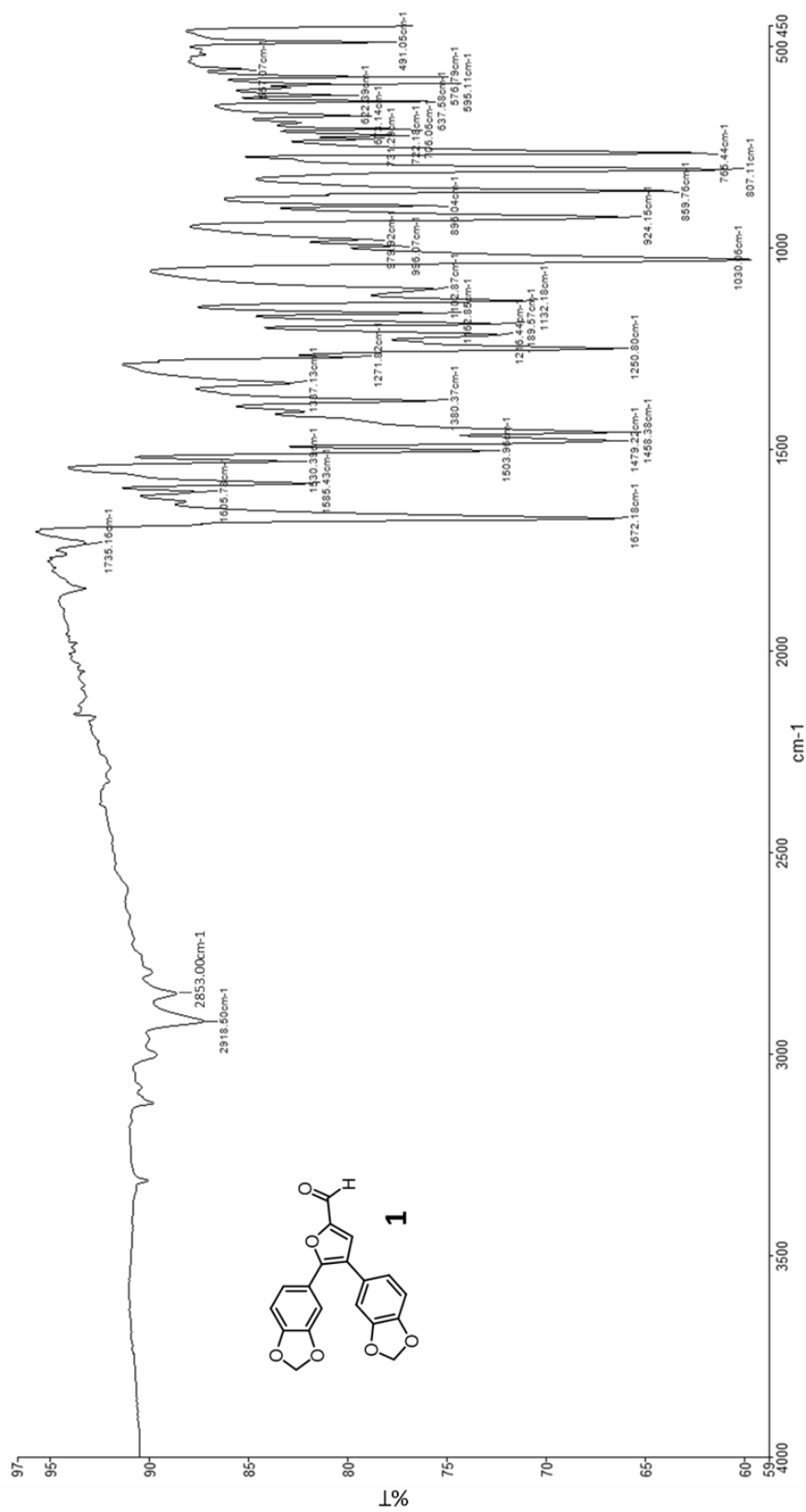


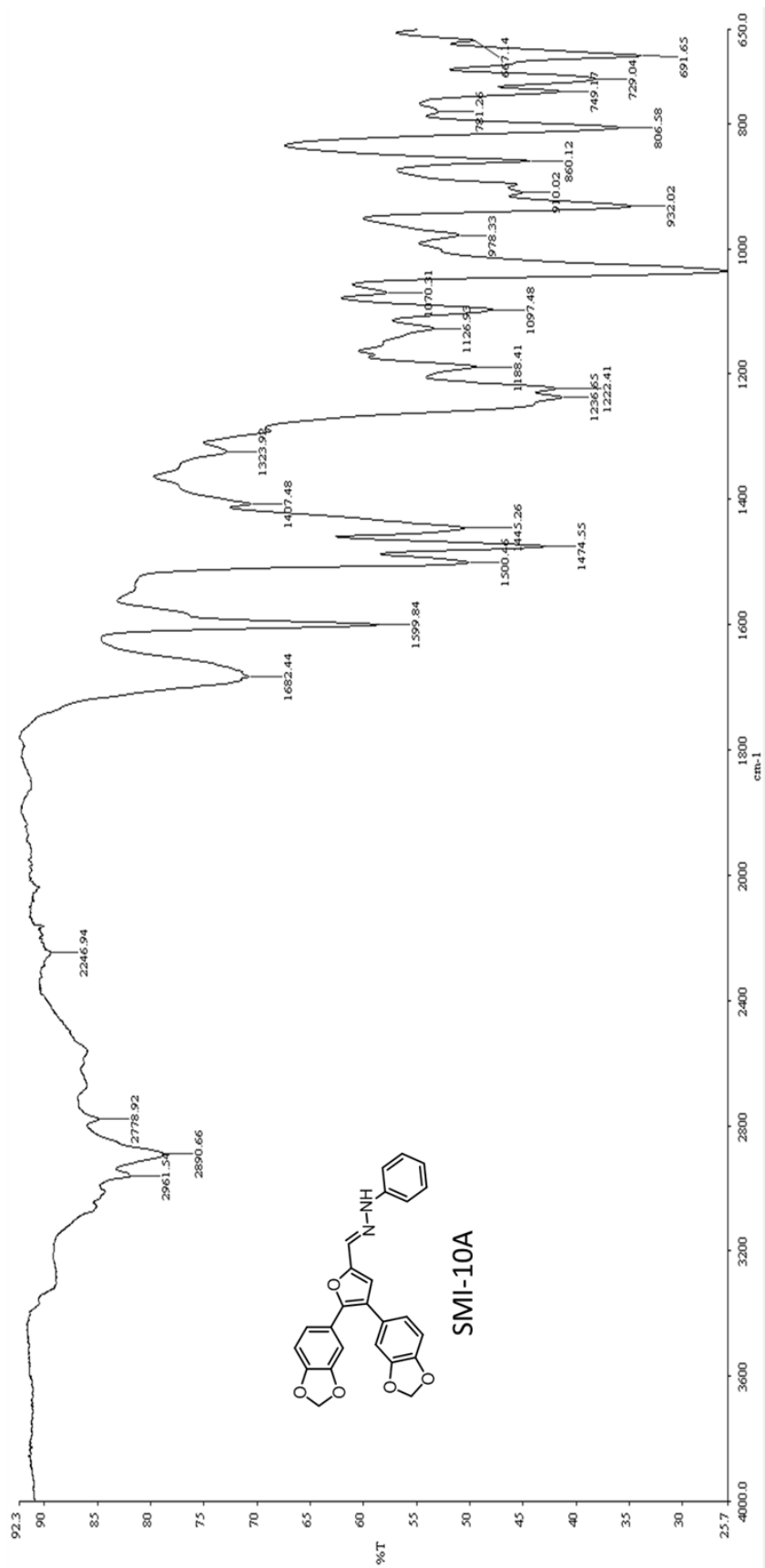


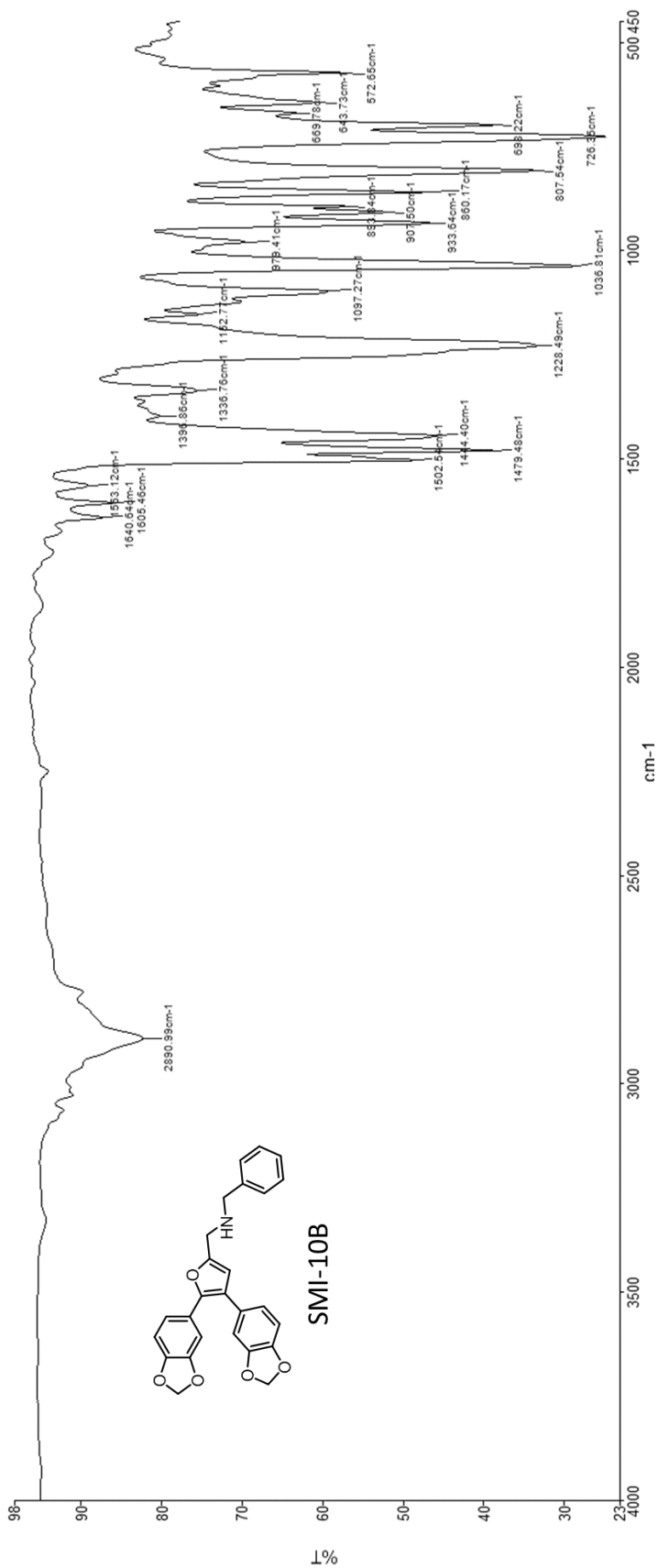


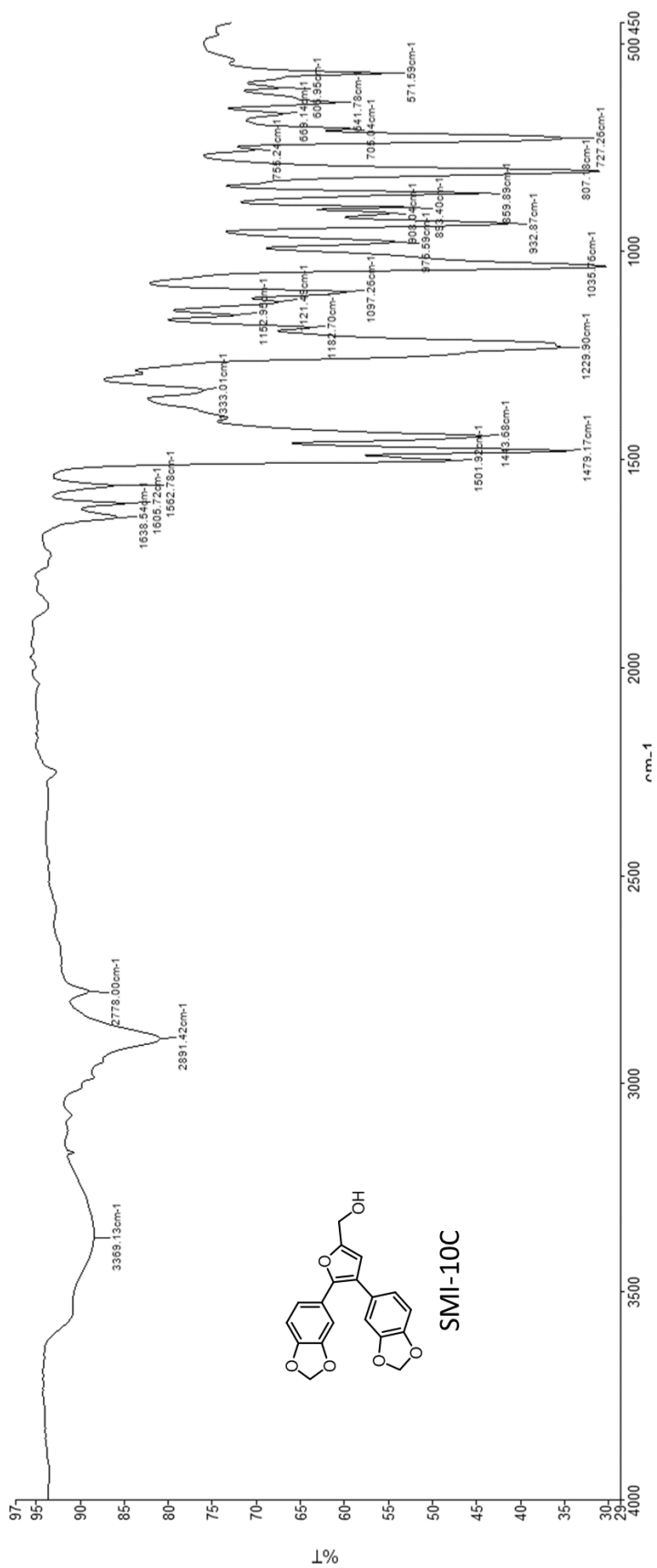


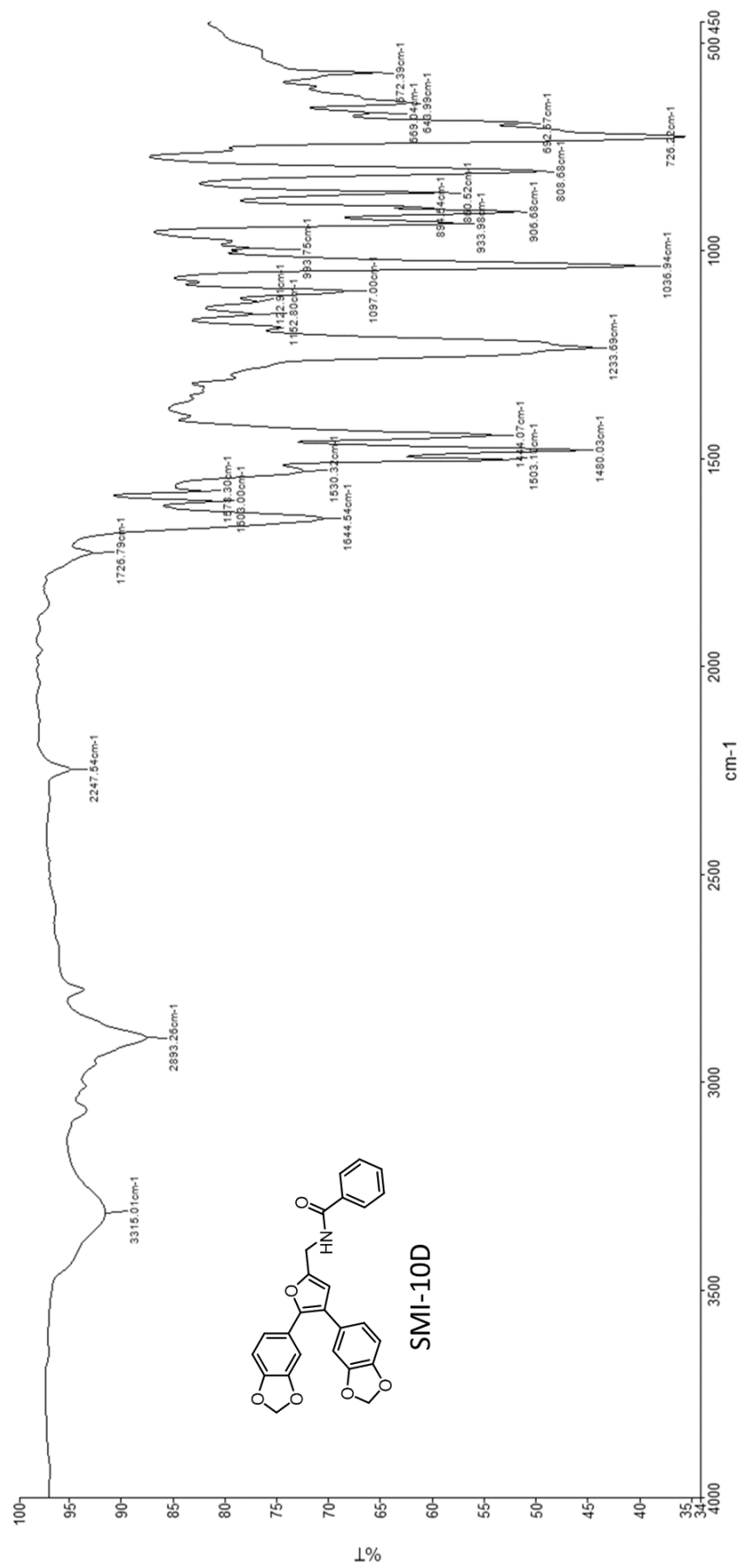
## APPENDIX D: INFRARED SPECTROSCOPY

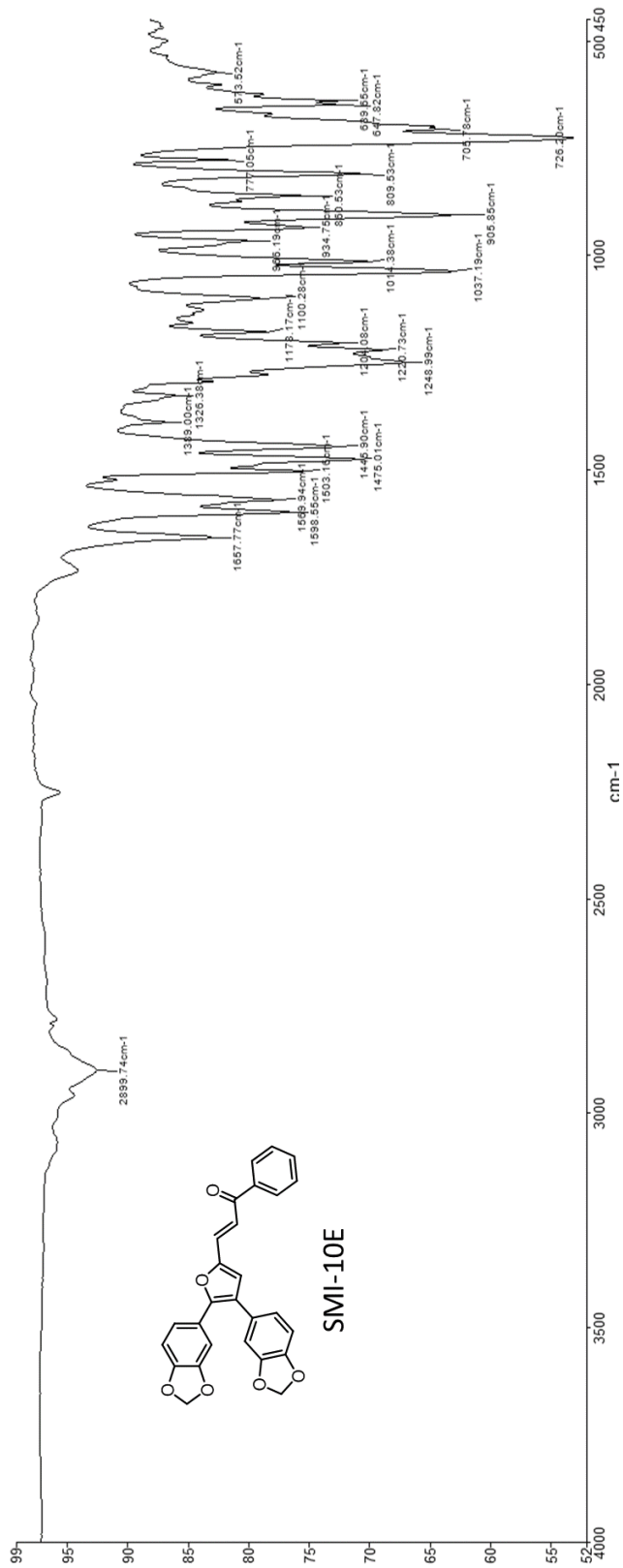


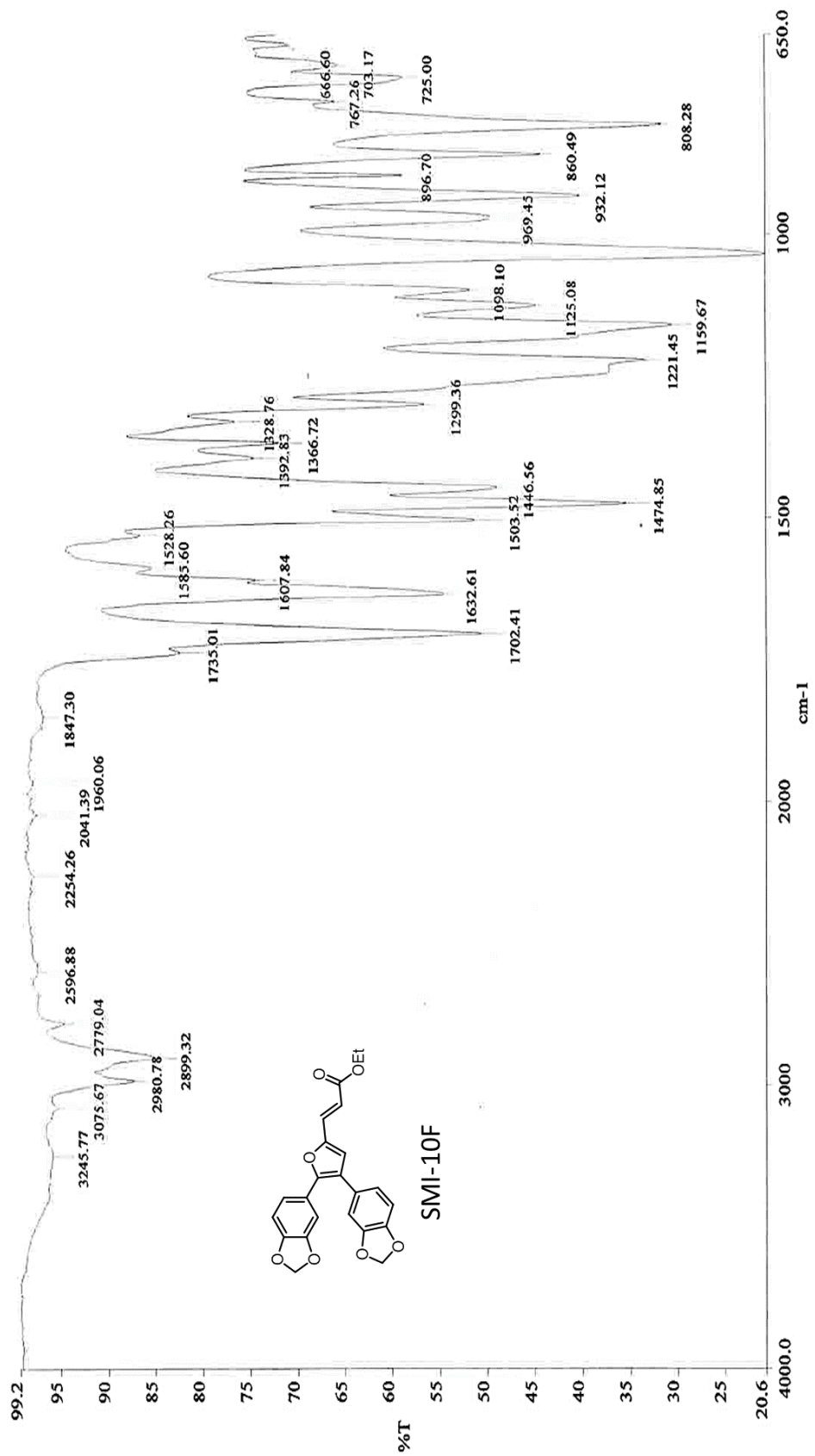


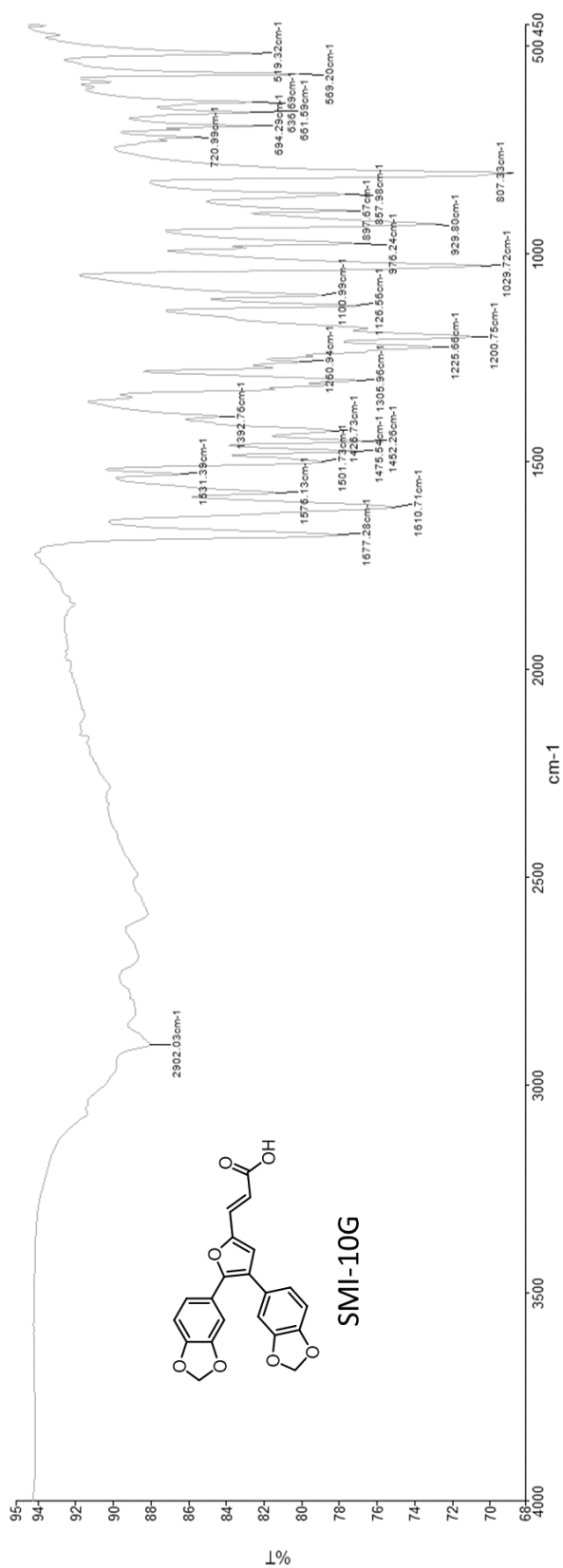


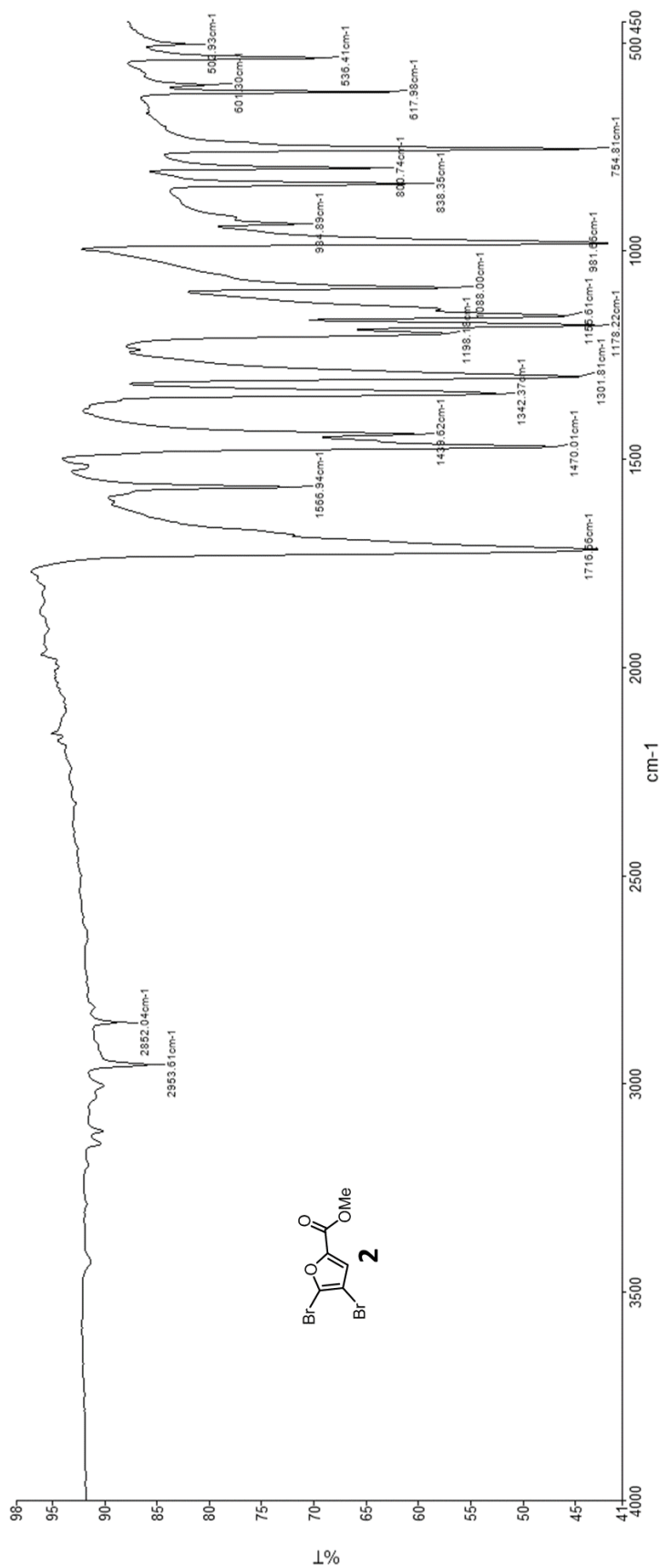


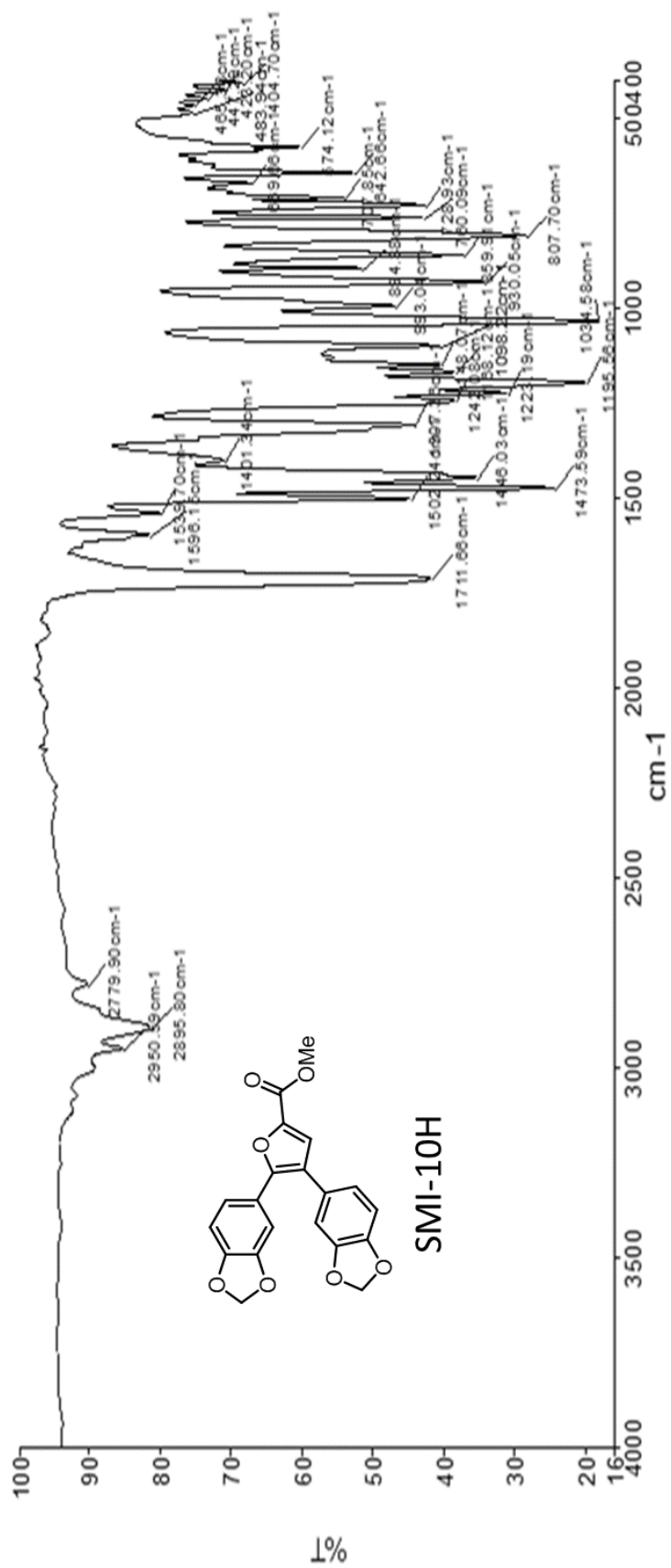


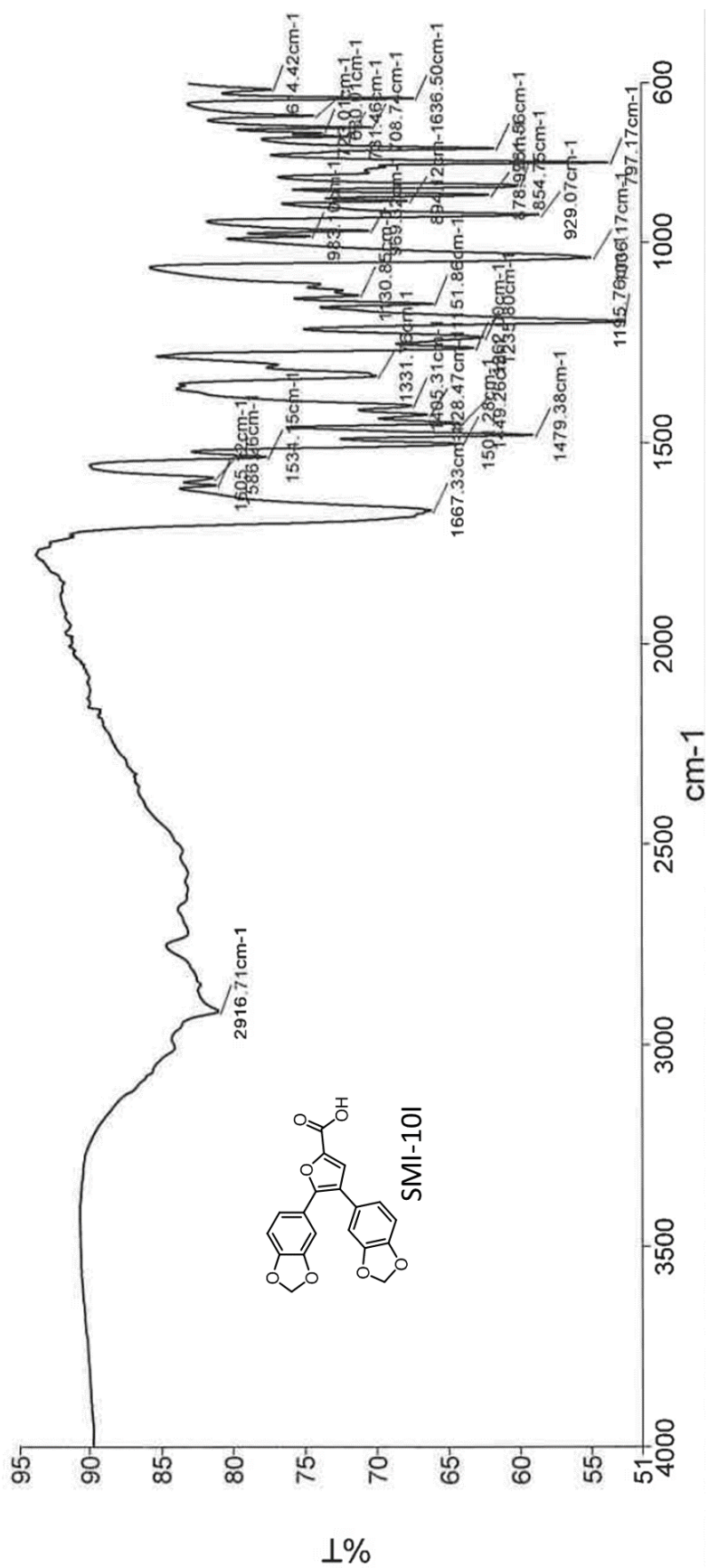


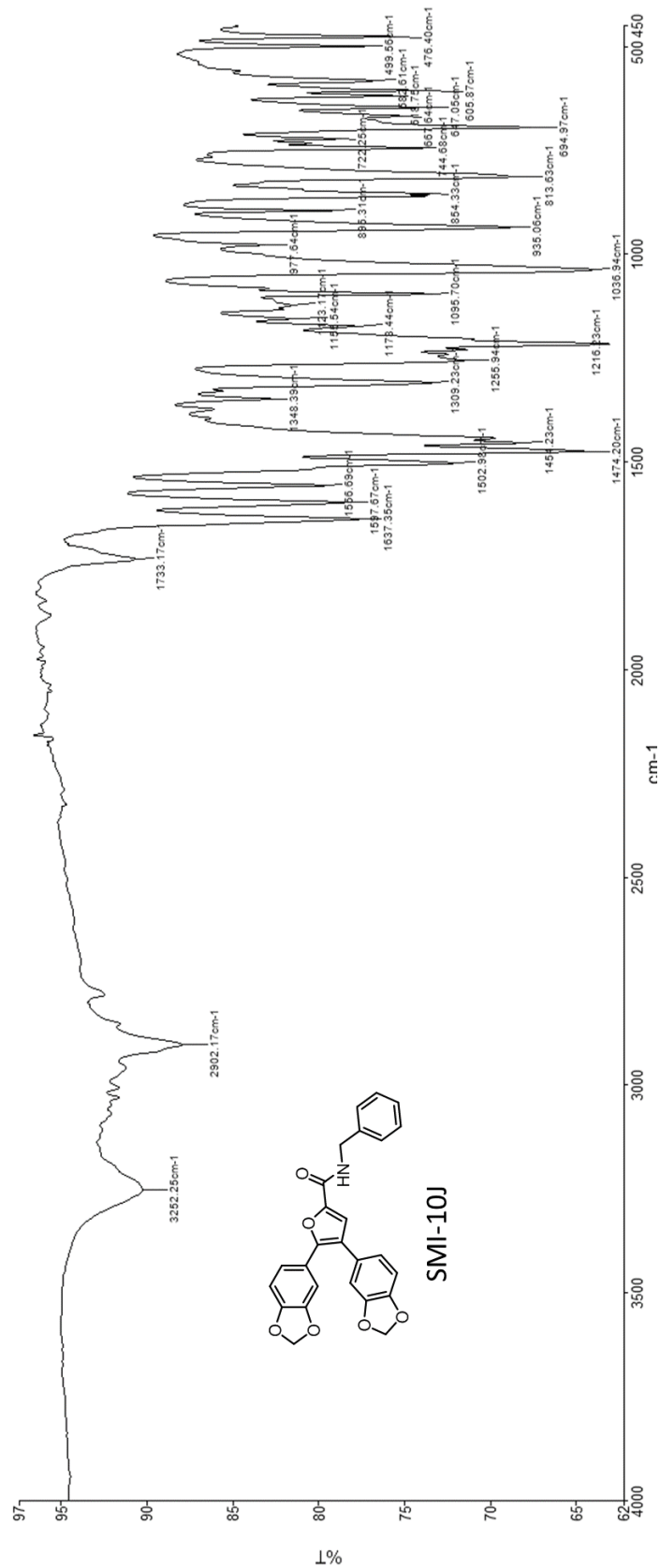


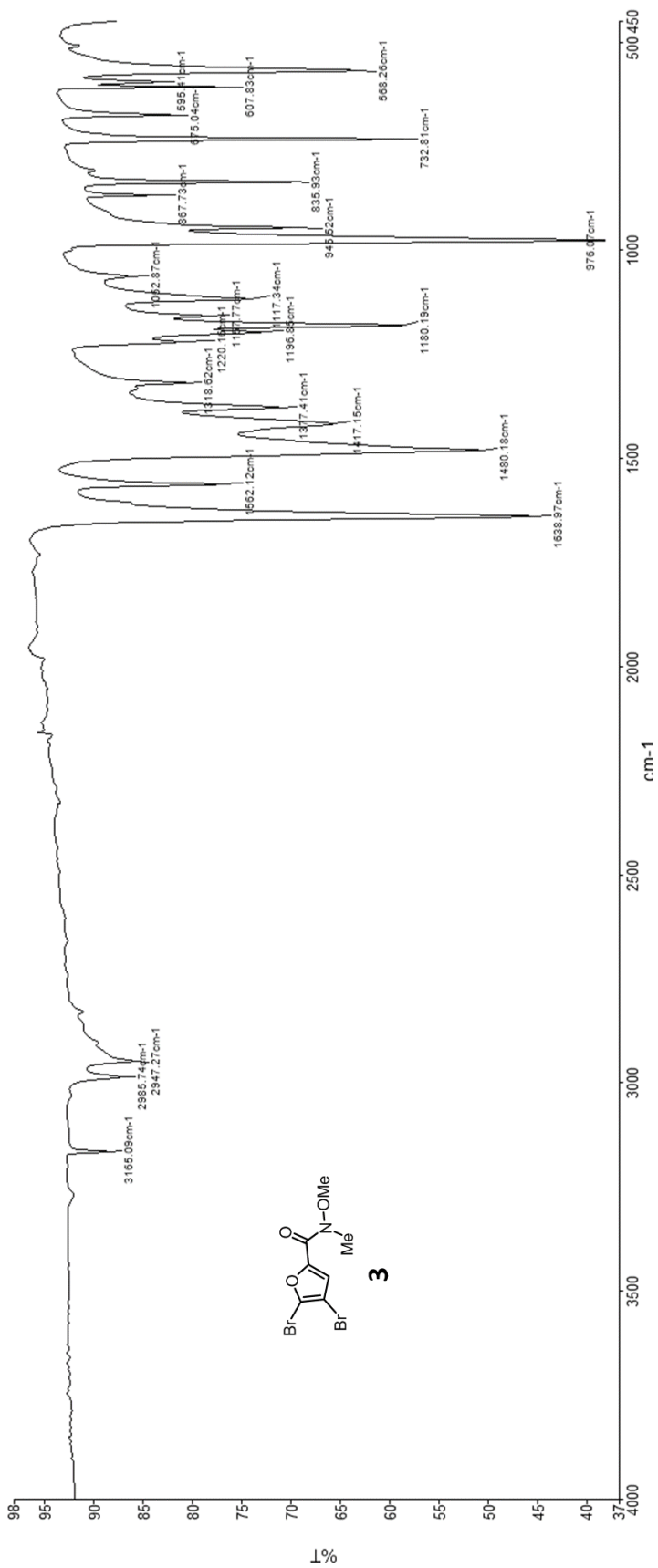
















## APPENDIX E: ISOTHERMAL TITRATION CALORIMETRY

